“ NEW METHODS FOR THE SYNTHESIS OF MAGNETIC NANOPARTICLES ”

THESIS SUBMITTED TO

UNIVERSITY OF PUNE

FOR THE DEGREE OF

DOCTOR IN PHILOSOPHY

IN

CHEMISTRY

BY

TANUSHREE BALA

PHYSICAL AND MATERIALS CHEMISTRY DIVISION
NATIONAL CHEMICAL LABORATORY
PUNE-411008
INDIA

DECEMBER 2006

Dedicated
to
my family
and
all those who
enjoy science

CERTIFICATE

This is to certify that the work discussed in the thesis entitled " **NEW METHODS FOR THE SYNTHESIS OF MAGNETIC NANOPARTICLES "** by **TANUSHREE BALA** for the degree of philosophy in chemistry was carried out under my supervision at the Physical and Materials Chemistry Division of National Chemical Laboratory, Pune. Such material as has been obtained by other sources has been duly acknowledged in this thesis. To the best of my knowledge, the present work or any part thereof, has not been submitted to any other University for the award of any other degree or diploma.

Date:

Place: Pune

Dr. Murali Sastry

(Research Guide)

CERTIFICATE

This is to certify that the work discussed in the thesis entitled " **NEW METHODS FOR THE SYNTHESIS OF MAGNETIC NANOPARTICLES "** by **TANUSHREE BALA** for the degree of philosophy in chemistry was carried out under my co-guidance at the Physical and Materials Chemistry Division of National Chemical Laboratory, Pune. Such material as has been obtained by other sources has been duly acknowledged in this thesis. To the best of my knowledge, the present work or any part thereof, has not been submitted to any other University for the award of any other degree or diploma.

Date: **Dr. B. L. V. Prasad**

Place: Pune (Research Co-guide)

CANDIDATE'S DECLARATION

I, Ms. Tanushree Bala, hereby declare that the work incorporated in this thesis entitled "**NEW METHODS FOR THE SYNTHESIS OF MAGNETIC NANOPARTICLES** " for the degree of philosophy in chemistry was carried out by me under the guidance of Dr. Murali Sastry and co-guidance of Dr. B. L. V. Prasad at the Physical and Materials Chemistry Division of National Chemical Laboratory, Pune. Such material as has been obtained by other sources has been duly acknowledged in this thesis. I declare that the present work or any part thereof, has not been submitted to any other University for the award of any other degree or diploma.

Date: **Ms. Tanushree Bala**

Place: NCL, Pune

Acknowledgements

It gives me immense contentment to extend my cordial gratitude to all those who helped me in pursuing my work presented in this thesis. To my prodigious delight I would like to convey my sincere admiration to Dr. Murali Sastry, my research guide, for directing me to the "nano-world" with his immense scientific knowledge, attention, indefatigable enthusiasm towards scientific work and over all for endowing me with the comprehensive understanding of the subject and confidence to meet the future challenges.

Abiding appreciations are due to Dr. B. L. V. Prasad, my co-guide, for his fruitful suggestions in minute problems faced during day to day work, for his discussions on the interesting yet enigmatic topic of magnetism, his "always ready to help" attitude and for valuable corrections he recommended after scrupulously reading this thesis.

My honest thanks go to Dr. S. Sivaram, the Director, NCL for providing me the opportunity to accomplish my research work in this well equipped, prestigious laboratory of India.

I am forever indebted to Dr. Sourav Pal, Head, Physical Chemistry Division, for all his support, scientific discussions and for helping me out in many of the stressful situations. Thank you so much sir...

I would like to extend my true respect and thanks to Prof. T Enoki, Tokyo Institute of Technology, Japan and Dr. P. A. Joy, Scientist, NCL, Pune for carrying out all the magnetic measurements of my samples without which I could not have presented my work in the present form. I owe special thanks for Prof. Umesh Waghmare, Jawaharlal Nehru Centre for Advanced Scientific Research, Bangalore who has performed all the theoretical calculations presented in Chapter III of this thesis. My thanks also go to Mrs. Neelima Iyer, Scientist, NCL, Pune and her group, to assist me with the Brewster Angle Microscope developed by their group. I appreciate the generous assistance I got from Marina Baidhakova, Vladimir Osipov, Shekhar D. Bhame, Rajshankar, Mousumi Upadhay Kahaly and Bhagyashree Joshi for performing some of the analyses of my samples.

With my pleasure I would like to mention the crucial role of all the scientists in Centre for Materials Characterizations (CMC) who have always been extremely helpful in all kind of characterizations whenever required. I bow my head to evince my gratitude

to Mrs. Renu Pasricha who has helped me a lot particularly in TEM analyses of all my samples and for giving me a hands-on training in the TEM instrument. I extend my thanks to Mrs. Suguna D. Adyanthaya for encouraging me to learn and operate Thermogravimeter under her kind supervision.

Interdependence seems to be more valuable to me than independence when I am accompanied by knowledgeable and friendly colleagues like my seniors who have always been a source of inspiration and my present Labmates who have helped me in every way I needed. I take this opportunity to thank Ashavani, Saikat, Sumant, Debu, Anita, Sujatha, Kannan, Shankar, Hrushi, Ambarish, Akhilesh, Manasi, Amit, Atul, Vipul, Sourabh, Deepti, Prathap, Meenakshi, Dr. Senthil, Dr. Ankamwar and all the newcomers for their constant support and for rendering a healthy scientific atmosphere in the lab to work in. Special thanks are for Ambarish and Manasi for their effort to go through the first draft of chapters and for making modification wherever necessary.

I should not forget to mention here that it gave me great enjoyment along with a sense of responsibility to work with all the project students I was assigned to. I thank their sincere efforts towards the work they have performed.

I gladly acknowledge the bountiful help and support I got in terms of scientific and non-scientific way from all the friends in NCL doling out a sweet and adorable memory ahead of me. Staff members of Physical Chemistry Division and from administrative section, NCL are also acknowledged for alleviating all the official jobs.

I take this opportunity to thank all the scientists of Physical Chemistry Division for the scientific interaction I had with them during the course work and divisional seminar in NCL. I am honored to mention about Prof. C. V. Dharmadhikari and Dr. Sourav Pal, who being the members of the evaluation-committee, offered useful suggestions regarding my work during the assessments.

Words are not enough to express my salutations to my parents and other family members for the precious support and motivation I got in every stage of my life. I wouldn't have overcome all the hurdles to achieve any goal without their blessings, care and love. I should not be parsimonious to appreciate Ambarish for his sustained help in each and every minute matters, his constructive condemnation and suggestions for the betterment of my research work.

Council of Scientific and Industrial Research (CSIR), India is gratefully acknowledged for the financial support during the course of my research.

Finally I am proud to acknowledge all my teachers in school and Jadavpur University, Kolkata for pioneering me to the fascinating world of science, introducing me to the ethics in science and encouraging me to pursue a career in scientific research activities.

December 2006 **Tanushree Bala**

Table of Contents

Chapter I: Introduction

Chapter II: Characterization techniques

Chapter III: Interaction of different metal ions with the carboxylic acid group: verification of experimental observations by quantitative approach

Chapter IV: Synthesis of magnetic metallic nanoparticles using liquid foams as template followed by their conversion to magnetic-core noble metal-shell systems via transmetallation reaction

Chapter V: Aqueous foam as a template for the synthesis of different ferrite nanoparticles

Chapter VI: Phase transfer of different nanoparticles to organic media, their assembly and transmetallation reaction in organic phase

Chapter VII: Conclusions

Chapter I

Introduction

This chapter provides an introduction to the work described in this thesis. It gives a brief outline on various aspects of nanoparticles, their synthesis by different means, assembly of the synthesized materials and their application in diverse fields. The work in this thesis is mainly based on the synthesis of magnetic nanoparticles by different methods, thus in each of the synthetic procedures special emphasis is given to the routes adapted for the production of magnetic nanoparticles. It also includes a brief outline of magnetic properties highlighting the superparamagnetic behavior of nanoparticles. The chapter finally illustrates the chapter-wise description of whole work.

1.1. INTRODUCTION:

"Imagination is more important than knowledge"

Albert Einstein

About half a century ago, in 1959, Richard Feynman put forward his view for "making, manipulating, visualizing and controlling things on a small scale" and anticipated that in decades to come it might be possible to arrange atoms "the way we want". His prophetic lecture was an inspiration to the scientific community to explore the 'small-world' of immense potential in every way it can be. Thus nanoscience and nanotechnology has evolved as an interdisciplinary branch of science where the knowledge of physics, chemistry, biology and engineering became equally important for the synthesis of new materials, to estimate their novel properties and assembling them in the way we want for the sake of different functions with special emphasis towards the biological application.

Nanoscience deals with materials in the nanometer size regime roughly within the range of 1-100 nm, but the scale length is viable only when a change in the physical and chemical properties is observed as compared to the bulk materials of the same compositions [1]. Indeed most of the nanoparticles show unusual physical and chemical properties, which make them more attractive to study [2]. Simple example of one such interesting property is optical absorption of noble metal nanoparticles in visible region known as surface plasmon resonance [3] and superparamagnetism in case of magnetic nanoparticles [4].

Nanomaterials have gained enormous importance in future technologies like electronics [5], metallurgy [6], optics [7], sensors [8], fuel cell [9], solar cell [10], catalysis [11], water purification [12] and even in the regular house-hold products [13] and cosmetics [14]. In order to characterize the nanomaterials a lot of contemporary research is devoted to the development of new instruments [15]. Nanotechnology can even be fruitful in treating some of the incurable diseases through extensive research in drug delivery and gene therapeutics [16]. A great amount of contemporary research work is going on to recognize the cause of fatal diseases like cancer and also to generate new approach towards its treatment and medicines using nanotechnology [17]. Considering all these applications, magnetic nanoparticles are found to play a very crucial role with respect to growing applications in the field of electronics [5], magnetic refrigeration [18], catalysis [19] and also in biological systems which include cell labeling and separation [20], drug targeting [21], hyperthermia [22], magnetic field assisted radionuclide therapy [23] and magnetic resonance imaging (MRI) contrast enhancement [24]. Ferrofluids are another spectacular discovery in the field of magnetic nanoparticles, which are basically colloidal solutions of ferro, or ferrimagnetic nanoparticles in a carrier fluid [25]. They behave like liquid magnets and are already in use in loudspeakers, hard discs, printer ink etc. For such a large spectrum of applications of magnetic nanoparticles, the development of new effective synthesis procedures is extremely important [26].

1.2. GENERAL APPROACHES TOWARDS THE SYNTHESIS OF NANOMATERIALS:

There are two basic approaches towards the synthesis of nanomaterials: the "top-down" and the "bottom-up" approach. The top down approach involves the breakdown of a bulk object into smaller and smaller pieces.

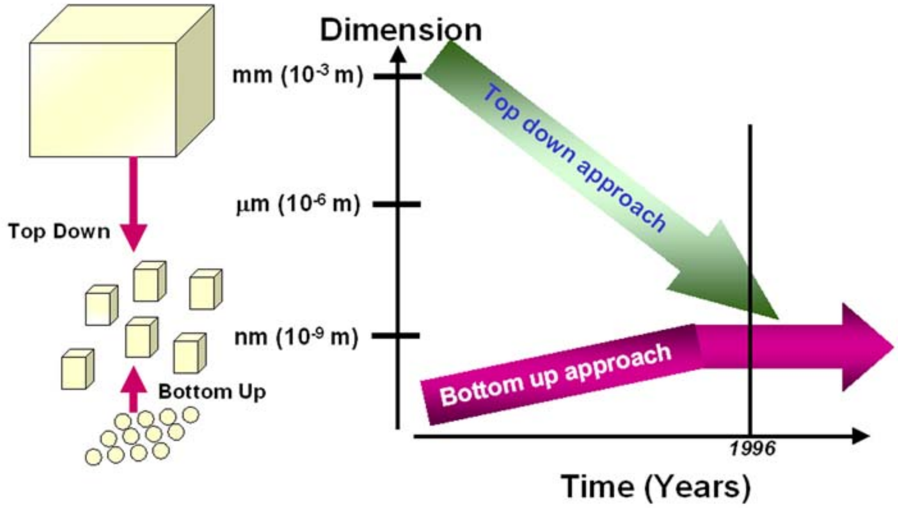

Figure 1.1. *Schematic to show the two generalized approach for the synthesis of nanomaterials [27].*

Ball milling [28 a], laser-beam induced chemical etching [28 b], lithography [28 c] are examples of this approach. These are some of the oldest routes for the synthesis of nanoparticles. But their popularity has reduced with time, as their efficiency to produce decontaminated, monodisperse materials and also very small particles of few nanometers is questionable due to the unavailability of suitable tools. The bottom-up approaches are somewhat superior and has attracted lot of interest in recent years [27] as they involve construction of matter atom by atom. The cartoon depicted in the *Figure 1.1* suggests that the bottom up approaches are still very much in vogue, whereas the top down processes have come more or less to standstill at the end of the last century due to technical difficulties. Chemical based methods like sol-gel method, precipitation, self-assembly, microemulsion based synthesis, template mediated preparation are few methods which fall under this category.

1.3. PHYSICAL AND CHEMICAL METHODS FOR SYNTHESIS OF NANOPARTICLES:

1.3.1. Vapour Deposition Technique:

Chemical vapour deposition (CVD) is a process often used for the deposition of thin films of various materials. In a typical CVD process the substrate is exposed to one or more volatile precursors, which react and/or decompose on the substrate surface as the substrate is kept at high temperature, to produce the desired deposit. Frequently, volatile byproducts are also produced, which are removed by gas flow through the reaction chamber [29]. This method has been successfully employed for the generation of thin films of ZnS [30], TiO_2 [31] etc on different substrates. Synthesis of magnetic nanostructures by this method are also common: e.g. nanowires of Fe_3B [32], Fe [33] and FeO thin film, carbon encapsulated Co nanoparticles [34] are already reported. Industries like IBM and Hitachi, for example, have used CVD to put magnetic coatings on computer hard discs [35].

Physical vapour deposition (PVD) is a similar technique to produce thin films of nanometer thickness where the reactants are taken in a heating boat and heated electrically to decompose the reactants to form the desired product. When the products come near the cool substrate surface they condense and deposit on the substrate [36]. Synthesis of nanowires of different materials like ZnO [37], Cu [38], Si [39] etc are very common by this process.

1.3.2. Laser Ablation:

Intense laser pulses when focused on a metal target leads to desorption of metal atoms present in the exposed region. In a laser ablation experiment, a bulk metal is immersed in a solvent containing surfactant. During the laser irradiation, the metal atoms will vaporize and are immediately solvated by the surfactant molecules to form nanoparticles in solution. The intensity of the laser pulse and time of exposure are two parameters, which control the size of the nanoparticles formed during laser ablation. Not only the noble metal nanoparticles such as gold [40], silver [41] and platinum [42] nanoparticles are prepared by this way with the good control over size, but nanomaterials like TiO_2 [43], ZnO/Zn [43], magnetic core-shell nanostructures of Ni/NiO [44] have also been reported. Laser ablation technique is also widely used to generate thin films of many metallic nanoparticles, semiconductors or oxides including superconducting oxides [45].

1.3.3. Sonochemical Method:

Sonochemistry is the research area where molecules undergo forceful reaction due to the application of ultra-sound radiation in the range of 20 kHz to 10 MHz. The radiation in a liquid containing precursor molecules results in cavitation (the implosive collapse of bubbles) that creates localized “hot spots” with effective temperatures of 5000 K with lifetime of a few nanoseconds or less. The extremely rapid cooling rates encountered in this process, most of the times favor the formation of amorphous products [46]. This method has been applied to prepare almost all types of nanoparticles like noble metal nanoparticles [47], oxides (e.g. TiO_2, ZrO_2, CeO_2) [48-50], multicomponent oxides (e.g. $LaNiO_3$, $LaSrMnO_3$) [51-52], bimetallic nanostructures (CdSe, AuPd, GaSb, CoCu, PbSe, RuPt etc) [53-58], magnetic ferrites [59] etc. It is also used to fabricate Fe nanoparticles of size of 8 nm by sonolysis of $Fe(CO)_5$ in presence of oleic acid which is otherwise very difficult to prepare [60]. Co [61] and Ni [62] nanoparticles are also formed from similar carbonyl precursors.

1.3.4. Photochemical Process:

These methods involve the reduction of metal salts by radiolytically produced reducing agents such as solvated electrons and free radicals. The process has been extensively used by Henglein and co-workers to generate a range of nanomaterials [63]. Alcohols are known to form radicals when they are irradiated with UV light and many times used as photolytic reaction initiator. Radicals thus generated by this way can reduce the metal ions to form nanoparticles when a mixture of aqueous metal ions and alcohols is irradiated by UV light. Sastry and coworkers have already shown that phosphotungstic or phosphomolybdic acids can be excited to their reduced state by UV light in presence of minute amount of alcohol [64 a]. These then can reduce metal ions forming spherical [64] or anisotropic [65] nanoparticles and the system can further be exploited for core-shell formation [64 b]. Even Co nanoparticles of size 2-4 nm can be routinely obtained by this process [66].

Instead of UV-radiation, microwave assisted synthetic process is also used for fabricating different types of nanomaterials starting from noble metals [67], chalcogenides [68] or even magnetic nanoparticles like Ni [69]. In this case microwave leads to rapid heating of reaction mixture and precipitation is very rapid. Generally the process is able to form very small particles with very narrow size distribution.

1.3.5. Coprecipitation Method:

1.3.5-1. Formation of Metal Nanoparticles:

Reduction of metal ions in aqueous and organic phase in presence of suitable capping agent is probably the most common and generalized chemical route for the synthesis of metal nanoparticles. H_2, hydrazine hydrate (Reduction potential –0.23 V), sodium borohydride (Reduction potential –0.48 V) are very common water-soluble reducing agents [70]. Reduction of gold ions into gold nanoparticles by citrate, where citrate acts as the capping agent also, is very popular and is known as Turkevich method [71]. Due to very high positive reduction potential, the noble metals can be reduced with many reducing agents containing amines, hydroxycarboxylic acid or alcohols. But in case of Ni^{2+} (E^0 = -0.257 V), Co^{2+} (E^0 = -0.28 V), Fe^{2+} (E^0 = -0.447 V), because of their highly negative reduction potential, reduction is mostly carried out by borohydride salts [70 b-d]. Brust's protocol [72] and the protocol reported by Sastry et al. [73] are two widely employed processes to synthesize gold nanoparticles in organic phase. In Brust's protocol two types of organic molecules are used as phase transferring and capping agent whereas the second process involves only single molecule (hexadecyl amine) that acts as phase transferring, capping and even the reducing agent. Though formation of noble metal nanoparticles in organic phase by reducing and stabilizing them with organically soluble reducing agent at room temperature is quite common [74 a], there are very few reports of such synthesis for magnetic nanoparticles. Only Ni^{2+} is reported to be reduced to form Ni nanoparticles by hydrazine hydrate in ethylene glycol solution [74 b, c]. Magnetic nanoparticles are mainly formed at very high temperature ranging from 100-300 °C in organic solvent (having high boiling points) containing different stabilizing agents among which oleic acid [75], mixture of oleic acid, lauric acid and trioctylphosphine [76] are few examples to mention. In these cases the reduction is mainly carried out by injecting superhydrides like $LiBEt_3H$ [75] or by simply decomposing the carbonyl precursors of the corresponding metals [76].

1.3.5-2. Formation of Oxide Nanoparticles:

The precipitation of oxides from both aqueous and organic solvent is less straightforward than the metals. Base induced precipitation often requires further processing like drying and calcinations to convert the intermediate hydroxides into the oxides. The direct co-precipitation of complex ternary oxides is generally performed at higher temperature (50-100 °C) to avoid subsequent calcinations. Such "one-pot" synthesis is perhaps the most practiced route for the synthesis of magnetic ferrites [77].

1.3.6. Solvothermal Process:

In a sealed vessel (bomb, autoclave, etc.), solvents can be brought to temperatures well above their boiling points by an increase in autogenous pressures resulting from heating. Performing a chemical reaction under such conditions is referred to as solvothermal processing or, in the case of water as solvent, hydrothermal processing. The critical point for water lies at 374 °C and 218 atm. Above this temperature and pressure, water is said to be supercritical. In supercritical fluids, chemical compounds can be dissolved easily that would otherwise exhibit very low solubilities under ambient conditions. Some solvothermal processes indeed involve supercritical solvents. Most, however, simply take advantage of the increased solubility and reactivity of metal salts and complexes at elevated temperatures and pressures without bringing the solvent to its critical point. In any event, solvothermal processing allows a range of crystalline inorganic materials to be prepared at temperatures substantially below those required by traditional solid-state reactions [78].

1.3.7. Sol-Gel Method:

The sol-gel process involves the conversion of a solution of molecular precursors by a chemical reaction into a sol or a gel, which is subsequently transformed into a crystalline material upon drying, densification, or calcinations. The gel is a polymer of three-dimensional network with surrounding interconnected pores. Hydrolysis and polycondensation of tetraethoxysilane (TEOS) under alkaline conditions in ethanol medium have resulted in the synthesis of SiO_2 particles having 20 nm diameters [79]. In some cases the tendency of these nanoparticles formed against aerial oxidation is inhibited by use of amino acids like alanine, tryptophan etc [80]. In some recent work, this technique has been used to prepare porous spheres of γ-Al_2O_3 [81]. However, in this case a surfactant SPAN-80 was used along with the dehydrating agent. Apart from metal oxides like silica, titania and zirconia, the sol-gel technique has been used to synthesize different ferroelectric materials like $BaTiO_3$, $PbTiO_3$, $BaSrTiO_3$ [82]. One important advantage of the sol-gel technique is the production of homogeneous ultrafine powders with the additional capability of industrially scaling up. One distinct disadvantage of surface sol-gel technique is that as a low temperature technique this might give low density or incompletely crystallized films.

1.3.8. Reverse Micelle Based Synthesis:

Most of the common surfactants are able to form reverse micelle when particular concentration of surfactants is put in oil (long chain liquid hydro carbon, alcohols or toluene etc.) in presence of small quantity of water and alcohol. The water forms small pools surrounded by surfactants with their head group towards the water pool and the hydrophobic tail towards oil. The use of alcohols is not essential but they are used very often to act as spacer molecules in between the consecutive surfactant molecules. This decreases the attraction between the consecutive head groups of the surfactants and stabilizes the reverse micelles [83].

These reverse micelles undergo collisions due to continuous Brownion motion even at room temperature and form short-lived dimer state *(Figure 1.2)*. During such collisions the reactants present in the water pools of two reverse micelles come in contact with each other and form the product, which also remains entrapped in the water pool. Hence the water pool in reverse micelles is termed as nanoreactors. Almost all types of materials have been reported to be synthesized in this system [84].

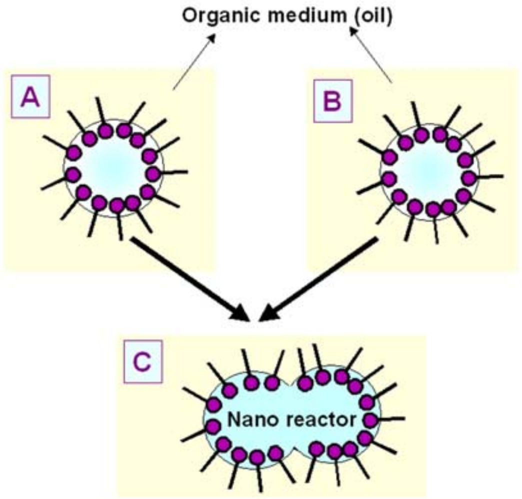

Figure 1.2. *Scheme showing the reaction mechanism in micro-emulsion based technique. The reverse micelle (A) containing one reactant dissolved in the water pool collides with micelle (B) containing the second reactant. They fuse to form the structure (C) where the reaction takes place.*

1.3.9. Synthesis at Interfaces:

1.3.9-1. Air-Water Interface:

The air-water interface has been used for in-situ synthesis of nanoparticles and their consequent assembly. Metal and semiconductor nanocrystals were grown under suitable Langmuir monolayers via the slow infusion of reactant gas (reducing agent) into the closed environment surrounding a trough containing the monolayer-coated aqueous precursor metal ion solution subphase. Formation of nanoparticulate films of cadmium sulphide [85], lead sulphide [86] zinc sulphide [87], iron oxide and cadmium selenide [88] has been established by this technique. Sastry et.al. have also reported the formation of anisotropic Au nanoparticles by spreading hydrophobized $HAuCl_4$ monolayer on a subphase containing water-soluble reducing agent [89]. Even the reverse reaction is also possible by taking water insoluble amine monolayer on aqueous $HAuCl_4$ subphase. The amine monolayer can reduce the subphase metal-ions to fabricate Au nanoparticles [90].

1.3.9-2. Liquid-Liquid Interface:

Liquid-liquid interface is also very interesting for the growth of different materials at the constrained environment. The presence of two reactants in two different phases can generate the product at the interface leading to anisotropic nanostructures or membrane in many of the cases [91]. Hele-Shaw cell, which is generally utilized for study of viscous fingering, can also be used for nanoparticle formation as already reported by Sastry and co-workers [92]. In this case when the less viscous liquid containing reactants flow over the more viscous liquid containing another reactant, react at the time of movement and generate the nanostructures at the interface of liquids having different viscosities.

1.3.10. Template Based Synthesis of Nanoparticles:

1.3.10-1. Different Types of Templates:

Template directed synthesis is an extensively used technique for the synthesis of anisotropic nanostructures. Nanowires of Ag, Au and Sn can be formed using porous alumina membrane [93]. Polycarbonate membrane has also been utilized for the purpose of nanorod formation [94]. Core-shell nanostructures and hollow structures can be made using oxides as template. In this respect Au on SiO_2, Au on TiO_2 and Ni on Al_2O_3 have already been reported [95]. There are lots of interest in the synthesis of metal and metal oxides on polymer matrix in which the nanoparticles formed are generally very small in size and are well stabilized. Co nanoparticles in polystyrene-PVP copolymer matrix have very small size of ~1-5 nm only [96]. Synthesis of $CoFe_2O_4$ and Fe_3O_4 are also achieved by this method [97]. $CoFe_2O_4$ is also prepared in the pores of Dowex, a common ion exchange resin with sulphonic acid functional group, which is estimated to a size range of 1-7 nm [98]. Lipid thin film can also be considered as template for the generation of various nanoparticles starting from metallic nanoparticles, mineral crystals, oxides or alloys. This method is well studied by Sastry and co-workers [99]. Here suitable lipid layers of desired thickness are formed on glass or Si (111) substrates in the first step, which is then dipped in metal ion solution so that metal ions are entrapped within the lipid bilayers. Subsequently the substrates are exposed to reducing agent or other suitable reactants to form the desired nanoparticles.

1.3.10-2. Foam as Template:

The foam structure has been exploited for crystal growth by Davey [100] and co-workers whereas the system was first utilized for the synthesis of different nanoparticles by Sastry et al. [101]. In this thesis this template has been extensively used for the synthesis of magnetic metallic nanoparticles and magnetic ferrites.

Aqueous foams have been a subject for scientific investigation since the 17 th century, but till date much remains to be learnt about the complex chemical and physical phenomenon that govern even in a single foamy bubble. Aqueous foams, an impermanent form of matter, are gas (often air) dispersed in an agglomeration of bubbles that are separated from one another by films of a liquid (generally water containing surfactants). Aqueous foams are typically 95% air and only 5% liquid and remarkably the liquid is often 99% water. The remaining 1% consists of surfactants and sometimes co-surfactants [102].

(A) Generation of Foam:

Foam is generally formed by injecting gas (air/ O_2/ N_2/ Ar) into the liquid containing surfactants.

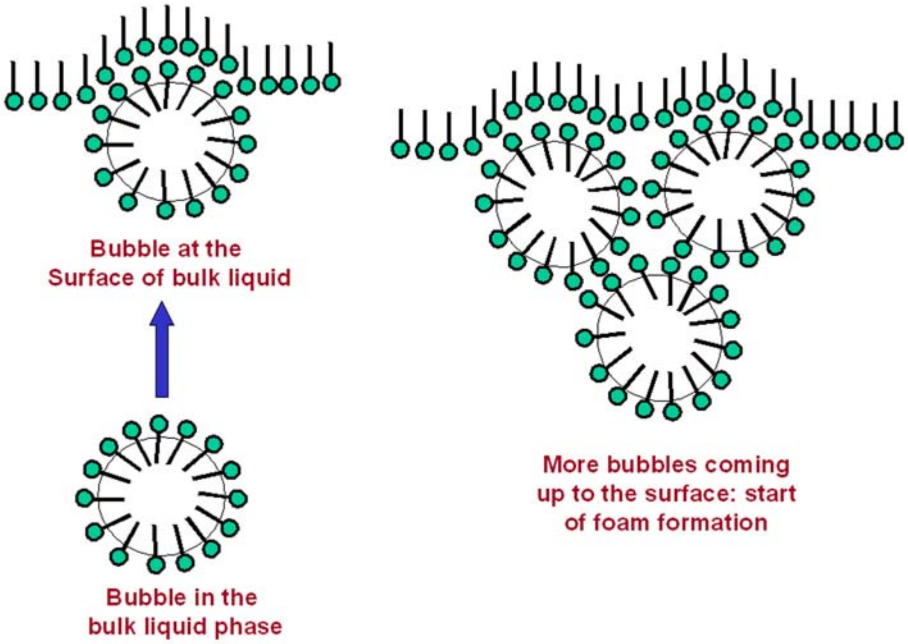

Figure 1.3. *Process of foam formation according to dispersion method [103].*

In the bulk of the solution when the first gas bubble is released, the surfactants are adsorbed at the bubble-solution interface, hence stabilizing the bubble in solution. This bubble rise to the surface of the bulk solution where it meets with the surfactant layer present there, so that a bilayer of surfactants is formed. Since air bubbles are always rising, the structure formed is lifted continuously. Successive bubbles rising to the surface either come in contact with the surface-adsorbed surfactant layer or the surfactant layer of the previous bubble. This method of generation of stable foams is known as dispersion method in analogy to the general dispersed systems [103].

(B) Structure of Foam:

Liquid foams are basically a two-phase system and depending on the liquid content their structure varies greatly. Initially just after formation, foams contain large excess of liquid and the foam bubbles take on a spherical morphology. The traditional term for a wet foam is “Kugelschaum” or “spherical foam”. The structure changes with time due to drainage of liquid from the foam by gravity and capillary action. In very dry foam the bubbles, when projected to the two dimensions, are mainly hexagonal in nature, which is named as “Polyederschaum” or “polyhedral foam”. Observation reveals that this accumulation of bubbles is not governed by chance, but is subject to law, bubbles join together in threes at equal angles in such a way that not more than four edges of three laminae pass through the same point, cutting laminae, as well as edges, at an angle of 120^{o}. The films in form of small tubes meet in triangular cross-section where most of the water in a foam is contained and are known as Plateau borders. The meeting point of three Plateau borders is called Plateau junction. The liquid content in foams is responsible for some of the characteristic visual properties of liquid foams [102].

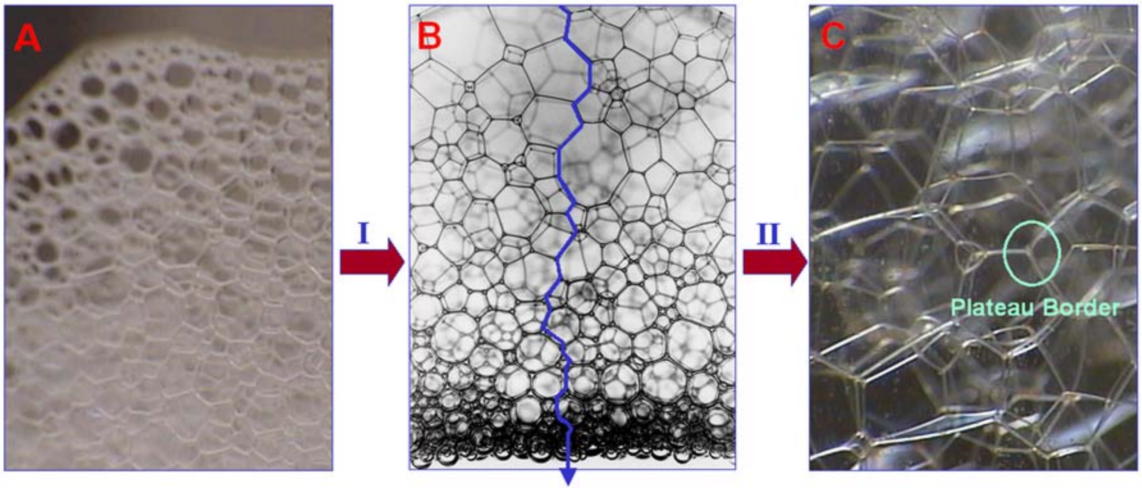

Figure 1.4. *The photograph (A) shows the initial wet foams in spherical shape. Free drainage takes place under gravity (step I) with time. After drainage very dry polyhedral foams are formed (photograph C).*

(C) Stability of Foam:

The foam owes its stability to several factors as discussed in the following sections.

(i) Role of surfactants:

Surfactants are amphiphilic surface-active molecules containing a hydrophilic head group and a hydrophobic tail having different solubilities. –OH, -COONa, $-SO_3K$, $R_3N^+Br^-$ are few hydrophilic groups whereas the typical hydrophobic tail comprises of C_nH_{2n+1} hydrocarbon chain. Due to different solubilities, surfactants can accumulate at the interface forcing the liquid molecule to go back to the bulk phase. Thus the surface tension is dropped. Without this reduction in surface tension, the liquid cannot be transformed from its bulk state, which has a minimal surface area into foam with its myriad films, which gives the liquid a far larger total surface. However after a certain concentration of surfactants at the surface, the surfactants move into the bulk liquid forming aggregates containing definite number of surfactants molecules together. Thus they hide their hydrophobic parts and project out the hydrophilic head groups towards the ionic liquid. These aggregates are typically known as micelles and the particular concentration is called critical micellar concentration (cmc) [103]. Hence the concentration of surfactants plays a major role in determining the stability of the foam.

(ii) Coarsening of the bubbles and coalescence:

The surface tension in liquids causes contracting forces along the surface of the liquid. As a result, liquids always try to minimize their surface area. The reason why a bubble remains stable and does not collapse into a drop of liquid is that there is an excess pressure inside the bubble. This produces forces acting on the bubble surface that exactly cancel the forces owing to the surface tension. The radius of curvature R of a liquid film with surface tension γ and pressure difference Δp between the bubbles it separates, is given by the Laplace-Young law:

$$R = 4\gamma / \Delta p$$

It also follows from this law that smaller bubbles have higher pressure than larger bubbles and thus the separating film between two different size bubbles will be curved towards the larger bubble.

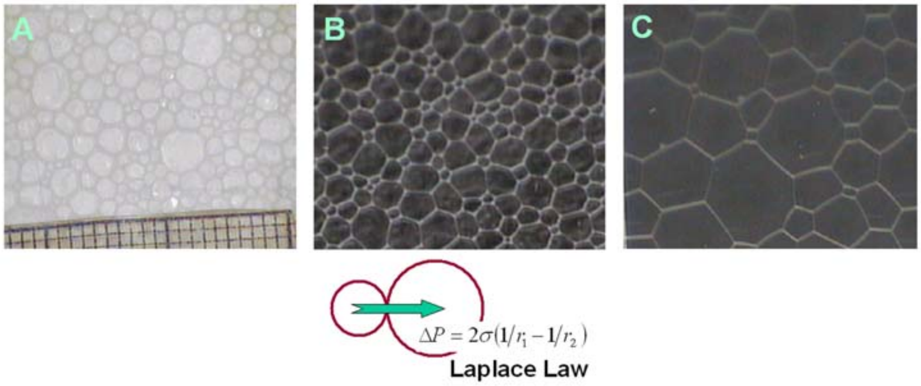

Figure 1.5. *Coarsening of foam structure by the process of coalescence.*

The gas flux goes from higher to lower pressure zone, which indicates that gas will move from smaller to bigger bubbles. Thus, smaller bubbles shrink and simultaneously bigger bubbles grow and the texture coarsens due to coalescence of two bubbles. Eventually very small bubbles evaporate and at this stage the foam consists of only bigger bubbles [102].

(iii) Film rupture:

Application of Laplace equation shows that pressure is lower towards the Plateau border than the foam film, which causes more liquid to flow towards the Plateau border and Plateau junction, promoting film drainage. Thus the film thins down and two adjacent surfactant layers come in close proximity. The disjoining pressure (the repulsion between the head groups of surfactants of the adjacent layers) then becomes effective and prevents further removal of liquid. If the disjoining pressure is not very effective the film eventually ruptures [102].

1.4. BIOLOGICAL METHODS FOR SYNTHESIS OF NANOPARTICLES:

The way biological organisms synthesize complex nanostructures is simply splendid. The examples being the eye-catching siliceous structures by diatoms and radiolarians [104] and calcareous structures synthesized by the coccoliths [105] in micro dimensions, various porous shell containing calcium carbonate and the synthesis of aligned magnetite nanoparticles in magnetotactic bacteria [106]. In recent years, materials scientists induced microorganisms to synthesize biominerals and semiconductors or metal nanoparticles because of their ability to cope with high metal ion concentration through specific resistance mechanisms. The typical resistance mechanisms include: efflux systems; alteration of solubility and toxicity by changes in the redox state of the metal ions; extra-cellular complexation or precipitation of metals; and lack of specific metal transport systems [107]. This behavior of microorganism not only helps in the synthesis of vast range nanoparticles but has also been exploited for bioremediation. There are numbers of reports by Sastry et al. where different fungal systems have been exploited for the synthesis of different nanoparticles including noble metal nanoparticles, quantum dots and mineral carbonates [108]. Even plant extracts have also been utilized for the synthesis of anisotropic metallic nanoparticles or biominerals in an eco-friendly manner [109]. Various other nanoparticles like TiO_2, SiO_2 or even iron oxides can be produced following different green approaches, which are under extensive study by Sastry and co-workers [110].

1.5. ASSEMBLY OF NANOPARTICLES:

There are several ways of assembling the nanoparticles among which self assembled monolayer (SAM) [111], electrophoretic deposition [112], spontaneous organization by solvent evaporation [113], lithography [114], magnetic field mediated ensemble of magnetic nanoparticles [115], template based assembly [116] and assembly at air-water interface by Langmuir-Blodgett technique [117] are few common routes for the purpose. Organization of nanoparticles on substrate can prevent cluster formation and thus can preserve the properties of the nanoparticles. This is also important for the formation of hierarchical nanostructures through layer by layer assembly. In fact if we can control the vertical layering process along with the lateral distribution of particles, three dimensional material with controlled shape, dimension and composition can be fabricated. Even a nanocluster is the resultant of assembled particles in a definite manner and also in definite numbers. In fact synthesis of nanomaterials is the first step and assembling these building blocks to generate super structure is a challenge to meet the future needs.

DNA is an interesting biomaterial used as a template to assemble nanoparticles and eventually to generate nanowires. First step of this process involves assembly of precursor metal ions into linear arrays through the interaction between functional groups of DNA and the metal ions. In next step, these metal ions are reduced to form string of nanoparticles along the backbone of each DNA molecule, which are further connected to generate continuous nanowires. For instance, nanowires of Au [118a,b], Ag [118c], Pt [118d] and Pd [118e] have been successfully produced by this method.

1.6. MAGNETISM IN THE NANO REGIME:

"There is nothing new under the sun, but there are lots of old things we don't know."

Ambrose Bierce

Magnetism is one such universal property, which has been studied for centuries, but till date it is considered as one of the most promising topics of research that involves synthesis of improved materials, thorough analysis of their properties and comprehensive understanding of their nature. A material is said to be "magnetic", if it has a response, when it is kept in an external magnetic field. Depending on the nature of this response, magnetic matter can be grouped into five different types, which are discussed in the subsequent sections. Magnetism exists in any matter, which is composed of spinning or moving charged particles. Atoms are made of charged particles like protons and electrons, which are moving constantly and thus they can generate their own magnetic fields. The processes, which create magnetic fields in an atom, are -

(i) Nuclear spin: Some nuclei, such as a hydrogen atom, have a net spin which creates a magnetic field.

(ii) Electron spin: An electron has two intrinsic spin states (similar to a spinning top) which we call 'up' and 'down' spins or 'alpha' and 'beta'.

(iii) Electron orbital motion: There is a magnetic field due to the electron moving around the nucleus in particular orbitals.

Interaction of the above mentioned magnetic fields with each other and with external magnetic fields gives rise to different kinds of phenomena. These interactions have different strengths; such as in most situations, interaction with nuclear spins has very minor effect. But it is taken into account to analyze compounds in nuclear magnetic resonance (NMR) and electron spin resonance (ESR) spectroscopy. Interactions between the intrinsic spin of two electrons is called spin-spin coupling and in some heavy elements like actinides, this coupling can shift the electron orbital energy levels. The interaction between an electron's intrinsic spin and it's orbital motion is called spin-orbit coupling that effects on the energy levels of the orbitals in many inorganic compounds. Macroscopic effects, such as the attraction of a piece of iron to a bar magnet are primarily due to the number of unpaired electrons in the compound and their arrangement. The various possible cases are called magnetic states of matter [119].

1.6.1. Classical view of diamagnetism:

Electrons that constitute a closed shell in an atom usually have their spins and orbitals so oriented that the atom as a whole has no net magnetic moment. Thus monoatomic inert gases, diatomic gases (H_2, N_2 etc), ionic solids (like NaCl) all possess closed shell electronic structure, in some cases due to the process of bond formation, and are expected to be diamagnetic. Covalent bonding by sharing of electrons also leads to similar closed shell structure and elements like diamond, Si, Ge are generally diamagnetic [119].

1.6.2. Classical view of paramagnetism:

Paramagnetism arises due to the presence of unpaired electrons in the atomic/molecular electronic orbitals. Theses electrons generate magnetic moments but in an ideal case of paramagnetism, the moments do not interact with each other. They are randomly oriented due to thermal agitation in absence of any external magnetic field, resulting in zero net magnetic moment. In an external magnetic field, the moments will tend to align with the applied field, resulting in a net magnetic moment in the direction of the applied field. The true origins of the alignment can only be understood via the quantum-mechanical properties of spin and angular momentum [119].

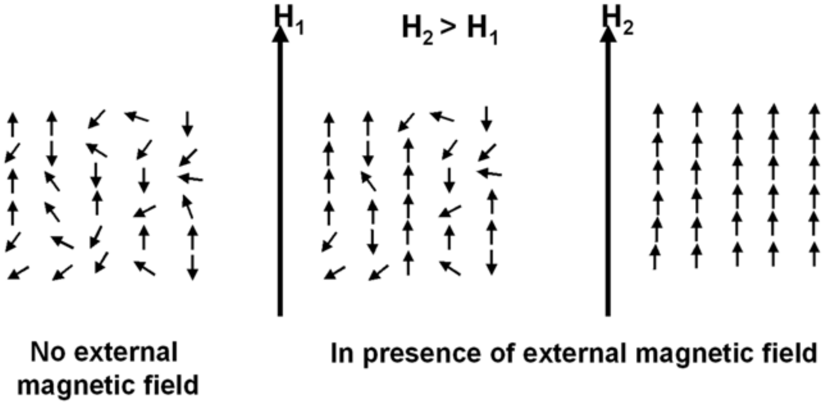

Figure 1.6. *The alignment of spin of paramagnetic substance under the influence of applied magnetic field.*

1.6.3. Classical view of ferromagnetism:

In case of ferromagnetism just like paramagnetic substance, the presence of unpaired electrons i.e. permanent magnetic moments are essential. According to classical electromagnetism, two nearby magnetic dipoles will tend to align in opposite directions which is not the case for ferromagnetic materials. In ferromagnets, they tend to align in the same direction because of direct influence of two effects from quantum mechanics: spin and the Pauli exclusion principle considering the electrons as Fermions.

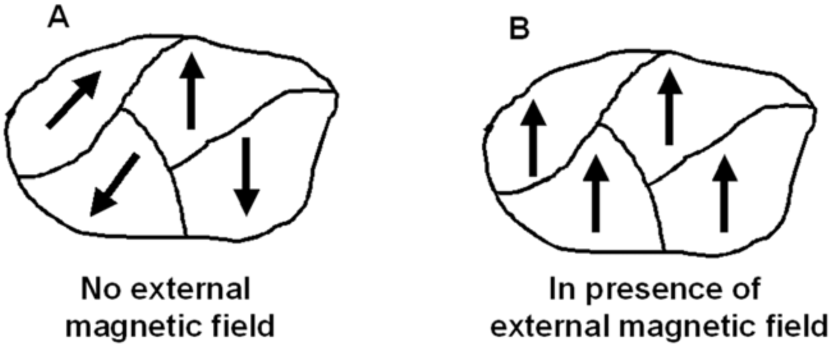

Figure 1.7. *Schematic showing different domains of a ferromagnetic substance. The arrow indicates the moment of a particular domain which is the resultant of small aligned magnetic moments within that particular domain (A). The domains of ferromagnetic material are aligned parallel in presence of magnetic field (B).*

Accordingly, total wave function of an electron system should be antisymmetric. The total wave function has two parts, one corresponding to the space coordinates of electrons and the other to their total spin. So, either the space or the spin function has to be antisymmetric such that their product gives antisymmetric total wave function. Therefore, a symmetric space function (where the electrons exists closely in the space) combines with the antisymmetric spin function (where the spins are antiparallel), and vice versa. Thus for two electrons in close proximity, due to this exchange interaction they try to align parallel to each other. At long distances (after many thousands of ions), the exchange energy advantage is overtaken by the classical tendency of dipoles to anti-align. This is why, in an equilibriated (non-magnetized) ferromagnetic material, the dipoles in the whole material are not aligned. Rather, they organize into magnetic domains (also known as Weiss domains) that are aligned (i.e. magnetized) at short range, but at long range adjacent domains are anti-aligned. The transition between two domains, where the magnetization flips, is called a Domain wall (e.g. a Bloch/Néel wall, depending upon whether the magnetization rotates parallel/perpendicular to the domain interface) [119].

1.6.4. Classical view of ferrimagnetism:

Ferrimagnetism is a situation where even though the nearest neighbor sites interact antiferromagnetically, a net magnetic moment results because the moments on the nearest neighboring states are not equal.

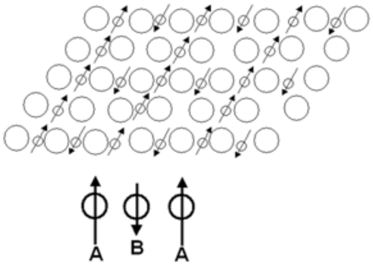

Figure 1.8. *Ferrimagnetic arrangement of spins generally observed in some ionic oxides.*

Examples of ferrimagnets are ionic oxides where the cation sites (A and B sites) are separated by oxygen. In such oxides direct exchange interaction between the cations is not possible. Thus the exchange takes place through the intervening oxygen, the phenomenon commonly called super exchange. The oxygen acts as mediator only because some sort of excited state is formed by the transfer of one *p* electron of O^{2-} to the *d* orbital of one of the neighboring cations. This makes the oxygen ion paramagnetic and can take part in magnetic interaction. The strong superexchange reaction then leads to an antiparallel arrangement of the A and B sublattices. However, as the magnetic moments on the A and B sublattices are not equal a net magnetic moment results [119].

1.6.5. Classical view of antiferromagnetism:

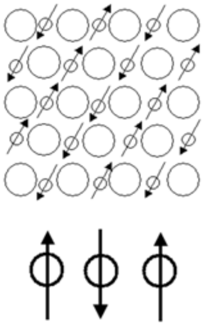

Figure 1.9. *Antiferromagnetic alignment of spins.*

If the A and B cations have moments exactly equal but opposite to each other, the net moment becomes zero. This type of magnetic ordering is called antiferromagnetism.

1.6.6. Classical view of superparamagnetism:

Superparamagnetism effect comes into the picture when the grain size decreases below a critical value, which is discussed in details as following. With reduction in the particle size, a major change occurs in the coercive force (H_c). In materials science, the coercivity of a ferromagnetic material is the intensity of the applied magnetic field to reduce the magnetization of that material to zero after the magnetization of the sample has been driven to saturation. Coercivity is usually measured in Oersted and denoted as H_c. The plot of coercivity with the particle size is shown in the *Figure 1.10.*

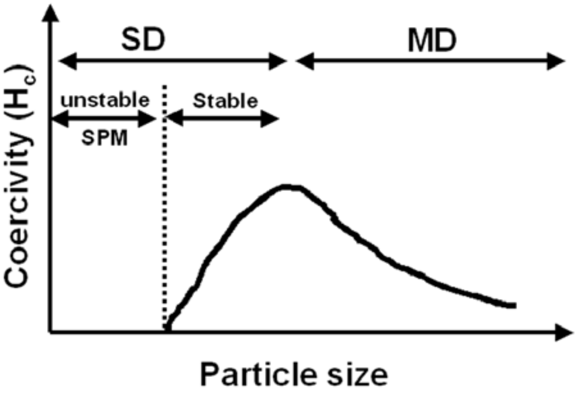

Figure 1.10. *The magnetic behaviour with respect to the grain size.*

Depending on this magnetic behaviour, the particles are broadly divided into two types:

(i) Multidomain (MD)
(ii) Single domain (SD)

Superparamagnetic (SPM) particles belong to a special class of SD entities.

To change the magnetization of a MD grain, it is required to translate the domain wall, which is an energetically easy process and can be accomplished in relatively low fields. Thus MD grains are magnetically soft with low values of coercivities and remanence magnetization. When the size reduces the number of domains also decreases and ultimately a SD grain is generated. The only way to change the magnetization of a SD grain is to rotate the magnetization itself, which is an energetically difficult process. Thus, SD grains are magnetically hard and have high coercivities and remanence. As particle size continues to decrease within the SD range, another critical threshold is reached, at which remanence and coercivity go to zero but this time it occurs due to the randomization effect of thermal energy. At this threshold, external temperature is enough to rotate the magnetic moment of the domain between two possible orientations and when this happens, the grain becomes superparamagnetic.

A SD particle of volume V has uniform magnetization directed along the easy axis of magnetization. Suppose such an assembly of uniaxial particles has been brought to initial state of magnetization (M_i) by applying external field. If the field was then withdrawn considering the moment as t = 0. Now some particles will immediately reverse their magnetization because the thermal energy is sufficient to overcome the anisotropy energy gap ($\Delta E = KV$, where K is anisotropy constant and V is volume of the particle). Hence the magnetization will start to reduce. At any moment the rate of decrease of magnetization will be proportional to the magnetization present at that instant of time and to the Boltzmann factor [exp (-KV/kT)]. The Boltzmann factor estimates the probability that in a particle thermal energy can surmount the anisotropy energy. Therefore,

$$-\frac{dM}{dt} = f_0 \, M \, e^{-KV/kT} = \frac{M}{\tau}$$

where f_0 is the frequency factor of the order 10^9 sec^{-1} and τ is the relaxation time i.e. the time within which the system try to achieve equilibrium.

Thus we can write $1/\tau = f_0 \exp(-KV/kT)$

The above concept that in response to a change in the applied field or temperature, an ensemble of SPM particles will approach an equilibrium value of magnetization with a characteristic relaxation time, was first derived by Néel. Thus it becomes possible to define an upper limit V_p for superparamagnetic behavior by arbitrarily letting a value τ = 100 sec to reach the magnetic equilibrium condition. This is basically the minimum time required to measure the remnence magnetization of a specimen. If τ changes to 1000 sec, the change in V_p is very small. Thus the approximation of τ = 100 sec is good enough for working purpose. With the value τ = 100 sec the above equation becomes,

$$10^{-2} = 10^{9} \exp(-KV_p/kT)$$

$$\text{or, } V_p = 25kT/K$$

We can thus find out the size of a particle when it will start behaving like superparamagnetic material at constant temperature. For particles with constant size there will be a particular temperature T_B called blocking temperature below which the magnetization is stable. It can be represented by,

$$T_B = KV / 25k$$

For superparamagnetic particles in an applied field, there will be a net statistical alignment of magnetic moments. This is analogous to paramagnetism, except now the magnetic moment is not that of a single atom, but belongs to a SD particle containing particular number of atoms (e.g. a spherical iron nanoparticle of 5 nm diameter contains 5560 atoms). Hence, the term superparamagnetism was first coined by Bean, which denotes a much higher susceptibility value than that for simple paramagnetism [119].

1.7. THE WORK IN THIS THESIS:

In most of the research work it has been experimentally shown that nanoparticles interact with organic molecules for their stability. However, there are very few studies that look into the fundamental aspects of such interactions. The interaction of –COOH group and metals is also important for many of the commercially available products. Here we have attempted to understand this by detailed study of carboxylic acids with metal/metal ions.

In another perspective, we have looked for different avenues for the synthesis of Co, Ni, and ferrites like $CoFe_2O_4$, $MgFe_2O_4$ nanoparticles in aqueous medium which are extremely simple yet have great potential to generate high quality materials at room temperature. In the case of Co and Ni nanoparticles extra stability and greater functionality was imparted by converting them into a magnetic-core noble metal-shell exploiting a very simple transmetallation reaction. Effort has also been put for the phase transfer of Ni nanoparticles followed by their assembly at air water interface using Langmuir-Blodgett Technique, as well as synthesizing them directly in the organic medium.

The thesis consists of seven chapters. The ***First Chapter*** presents a brief review about the different processes for formation of nanoparticles with special emphasis on the formation of magnetic nanoparticles, alteration of magnetic properties. The dependence of magnetic properties on the size and shape of the nanoparticles and the need for new approaches for the preparation of magnetic nanoparticles in aqueous and organic medium avoiding aerial oxidation with a good control over their size have been highlighted. The chapter also briefly introduces our methodology towards this goal.

In the ***Second Chapter***, the techniques such as UV-visible Spectroscopy, Fourier Transform Infrared Spectroscopy (FTIR), Transmission Electron Microscopy (TEM), Langmuir-Blodgett (LB) technique, Brewster angle Microscopy (BAM), X-ray diffraction (XRD), Energy Dispersive Analysis of X-Rays (EDAX), Thermogravimetric Analysis (TGA), X-ray photoemission spectroscopy (XPS), Atomic absorption Spectroscopy (AAS), Superconducting Quantum Interference Device (SQUID) Magnetometer, Vibrating Sample Magnetometer (VSM), Nuclear Magnetic Resonance Spectroscopy (NMR), Electron Spin Resonance Spectroscopy (ESR), Contact angle measurements and thermal evaporation of fatty lipid thin films using vacuum deposition unit etc. that are extensively used for characterization of the magnetic nanoparticles, have been discussed. The physical principles of the techniques and their applications to understand various aspects of formation of nanoparticles have also been summarized.

The ***Third Chapter*** details the results of experimental studies carried out to understand the interaction of –COOH group with different metal ions. The –COOH group and metal ion interaction assumes significance because of the unexpected experimental results that have been reported earlier that in spite of larger size Pb^{2+} have higher binding capacity compared to Cd^{2+} with arachidic acid (AA) monolayer. This as well as the fact that ligands bearing –COOH group are the preferred capping and stabilizing agents in the magnetic nanoparticles synthesis prompted us to probe this phenomenon carefully. It has been observed that there is considerable variation in the binding capacity of various metal cations complexed with AA thin films. The thin film is considered to have stacked bilayer of AA molecules and thus metal ions inside the bilayer acquire an environment to form cation-dicarboxylate linkage. The amount of intake of the cations was estimated using AAS. The results follow a trend indicating some metal ions can bind stronger than other. Similarly mixture of cations was also allowed to bind with AA monolayer on LB trough and the film was analysed to detect preferential binding of a particular cation to the AA monolayer using XPS. To have a quantitative knowledge regarding the binding capability, first-principle density functional theory calculations are applied to study the interaction of different cations with organic molecules having –COOH group with the simplest carboxylic acid i.e. acetic acid that can result in formation of metal diacetates. The molecular structures adopted by these diacetates are found to have different geometries and stabilities. By investigating the key factors like cohesive energies, bond-strengths of these metal diacetates, comparative studies of the binding of different metal ions with –COOH group are attempted in order to understand the structures, energetics and stability of these metal diacetates and a correlation between the experimental observation and theoretical calculation is established.

The ***Fourth Chapter*** demonstrates the use of foam lamellae as a dynamic template for synthesis of magnetic nanoparticles. A combination of extremely large interfacial templating area provided by the liquid lamellae in foams stabilized by ionizable surfactants and metal ions has been used successfully for the synthesis of magnetic metal nanoparticles such as Co and Ni. This was accomplished by first electrostatically complexing Co^{2+} / Ni^{2+} ions with SDS (surfactant) and oleic acid (capping agent) molecules at the air-bubble solution interface followed by reduction with $NaBH_4$ solution. These metallic magnetic nanoparticles were further utilized for the formation of magnetic-core noble metal-shell type nanocomposites, which not only increased the functionality but also the stability of the core from aerial oxidation. Detailed magnetic characterization based on the variation of magnetization with temperature and applied field are presented. The utility of ESR spectroscopic study in characterizing the magnetic metal nanoparticles and their core-shell analogues is described.

The ***Fifth Chapter*** describes the synthesis of cobalt and magnesium ferrite nanoparticles using liquid foam as templates. The foam is formed from an aqueous mixture of an anionic surfactant and the desired metal ions, where the metal ions are electrostatically entrapped by the surfactant at the thin borders between the air bubbles and their junctions. The hydrolysis is carried out using alkali resulting in the formation of desired nanoparticles with the foam playing the role of a template. However, in the formation of ferrites with the formula MFe_2O_4 where the metal ion and iron possess oxidation states of +2 and +3, respectively, if a foam is formed from a 1:2 mixture of the desired ionic solutions a foam composition at variance with the original solution mixture is resulted due to greater electrostatic binding of ions possessing higher charge with the surfactant. In our procedure we circumvent this problem by preparing the foam from a 1:2 mixture of M^{2+} and Fe^{2+} ions and then utilizing the *in-situ* conversion of Fe^{2+} to Fe^{3+} under basic conditions inside the foam matrix to get the desired composition of the metal ions with the required oxidation states. The fact that we could prepare both $CoFe_2O_4$ and $MgFe_2O_4$ particles shows the vast scope of this method for making even multi component oxides. The magnetic nanoparticles so obtained exhibit good crystalline nature and are characterized by superparamagnetic properties.

The ***Sixth Chapter*** discusses the phase transfer of nanoparticles synthesized in aqueous phase to organic phase like toluene. Pristine Ni nanoparticles were transferred into organic medium containing stearic acid (STA) after their synthesis in the aqueous medium where oleic acid is used as the capping agent. The space exchange between the oleic acid and STA has probably directed this phase transfer. These Ni nanoparticles were then assembled at the air-water interface in the form of Langmuir monolayer, which resulted in the long-range 2D arrangement of the nanoparticles. The Ni-core Ag-shell nanoparticles were also phase-transferred exploiting the orientational flexibility of the capping agent oleic acid to organic medium only in presence of ortho phosphoric acid. This approach has its genesis on the finding that oleic acid when bound to Ag nanoparticles exhibits excellent orientational flexibility both in aqueous and organic environment. Therefore, a silver shell on Ni surface makes it possible to obtain this orientation flexibility and phase transfer the core-shell system to the organic phase. Subsequently this work was extended to other amphiphilic molecules such as AOT. It was shown that AOT capped Ag nanoparticles obtained from the initial preparative conditions as a powder through centrifuging and removal of solvent, can be dispersed both in non-polar organic media as well as polar media such as water. In both the above cases it was conclusively shown, based on the FTIR spectra and ^1H NMR studies, that a change in the orientation of capping molecules (oleic acid or AOT) imparts the desired surface functionality so that the nanoparticles surface becomes hydrophilic or hydrophobic. In comparison to Ni nanoparticles prepared by an aqueous medium based technique, Co nanoparticles prepared by the same technique can be easily redispersed in organic phase. Accordingly the organic solvent dispersible Co particles have been further utilized to carry out transmetallation reaction in order to form core-shell nanoparticles. The transmetallation was achieved with hydrophobized $HAuCl_4$, which is efficiently phase transferred with benzyl di stearyl ammonium chloride (BDSAC) in toluene. The addition of different volume of chloroaurate ions into cobalt solution in toluene results in the formation of shell with varied thickness. As the reduction of chloroaurate ions occur by means of transmetallation reaction i.e. by consuming the surface Co atoms of cobalt nanoparticles, a phase pure core-shell system is expected. The magnetic properties of these core-shell systems have been characterized in detail and have been discussed in this chapter.

The ***Seventh Chapter*** summarizes the work presented in the thesis and emphasizes on possible further research in this area. The protocols developed by us have been compared with other protocols currently in vogue, and the advantages brought out.

1.8. REFERENCES:

[1]. Ozin, G. A.; Arsenault, A. C. Nanochemistry, A Chemical Approach to Nanomaterials, RSC Publishing, **2005.**

[2]. (a) Klabunde, K. J. Nanoscale Materials In Chemistry, A John Wiley & Sons, Inc., Publication, **2001**. (b) El-Sayed, M. A. *Acc. Chem. Res.* **2001,** *34,* 257.

[3]. Kelly, K. L.; Coronado, E.; Zhao, L. L.; Schatz, G. C. *J. Phys. Chem. B* **2003,** *107,* 668.

[4]. Sellmyer, D.; Skomski, R. *Advanced Magnetic Nanostructure*, Springer Publishing, **2006.**

[5]. (a) Mene´ndez, J. L.; Besco´s, B.; Armelles, G.; Serna, R.; Gonzalo, J.; Doole, R.; Petford-Long, A. K.; Alonso, M. I. *Phys. Rev. B*, **2002**, *65*, 205413. (b) Yakushiji, K.; Mitani, S.; Takanashi, K.; Takahashi, S.; Maekawa, S.; Imamura, H.; Fujimori, H. *Appl. Phys. Lett.*, **2001,** *78*, 515. (c) Fiete, G. A.; Zarand, G.; Halperin, B. I.; Oreg, Y.; *Phys. Rev. B* **2002**, *66*, 024431 (d) Aktsipetrov, O. A. *Coll. Surf. A* **2002**, *202*, 165. (e) Graf, H.; Vancea, J.; Hoffmann, H. **2002**, *80*, 1264.

[6]. Charles, S.C.; Popplewell J. *In Ferromagnetic Material,* Wohlharth E.P. Ed. North Holland Amersterdam, **1980.**

[7]. (a) Moran, C. E.; Steele, J. M.; Halas, N. J. *Nano Lett.* **2004,** *4*, 1497. (b) Maier, S. A.; Brongersma, M. L.; Kik, P. G.; Meltzer, S.; Requicha, A. A. G.; Atwater, H. A. *Adv.*

Mater. **2001,** *13*, 1501. (c) Maier, S. A.; Brongersma, M. L.; Kik, P. G.; Atwater, H. A. *Phys. Rev. B*, **2002,** *65*, 193408. (d) Wang, Y. *Acc. Chem. Res.* **1991,** *24*, 133. (e) Yoffe, A. D. *Adv. Phys.* **1993,** *42*, 173. (f) Radloff, C.; Halas, N. J. *Nano Lett.* **2004,** *4*, 1323. (f) Jackson, J. B.; Halas, N. J. *J. Phys. Chem. B* **2001,** *105,* 2743.

[8]. (a) Liu, G.; Lin, Y. *Anal. Chem.* **2005,** *77*, 5894. (b) Liu, J.; Lu,Y. *Anal. Chem.* **2004,** *76,* 1627. (c) Matsui, J.; Akamatsu, K.; Hara, N.; Miyoshi, D.; Nawafune, H.; Tamaki, K.; Sugimoto, N. *Anal. Chem.* **2005,** *77*, 4282. (d) Spadavecchia, J.; Prete, P.; Lovergine, N.; Tapfer, L.; Rella, R. *J. Phys. Chem. B* **2005,** *109,* 17347. (e) Nath, N.; Chilkoti, A. *Anal. Chem.* **2004,** *76,* 5370. (f) Bishnoi, S.W.; Rozell, C. J.; Levin, C. S.; Gheith, M. K.; Johnson, B. R.; Johnson, D. H.; Halas, N. J. *Nano Lett.* **2006,** *6,* 1687.

[9]. Fichtner, M. *Adv. Eng. Mater.* **2005,** *7*, 443.

[10]. (a) Hagfeldt, A.; Graetzel, M. *Acc. Chem. Res.* **2000**, *33*, 269. (b) Bueno, J. T.; Shchukina, N.; Ramos, A. A. *Nature* **2004**, *430*, 326.

[11]. (a) Roucoux, A.; Schulz, J.; Patin, H. *Chem. Rev.* **2002,** *102,* 3757. (b) Lewis, L. N. *Chem. Rev.* **1993**, *93*, 2693.

[12]. Boronina, T.; Klabunde, K. J.; Sergeev, G. B. *Environ. Sci. Technol.* **1995**, *29*, 1511.

[13].http://www.nanoforum.org/dateien/temp/Nanotechnology%20in%20consumer%20products.pdf?26102006234613.

[14]. http://www.azonano.com/news.asp?newsID=1344

[15]. Wang, Z. L. *Characterization of Nanophase Materials,* Wiley-VCH, Weinhein, **2000.**

[16]. Nori, A.; Jensen, K. D.; † Tijerina, M.; Kopecˇkova, P.; Kopecek, J.; *Bioconjugate Chem.* **2003,** *14,* 44.

[17]. (a) Kohler, N.; Sun, C.; Wang, J.; Zhang, M.; *Langmuir* **2005,** *21,* 8858. (b) Huh, Y. M.; Jun, Y. W.; Song, H. T.; Kim, S.; Choi, J.; Lee, J. H.; Yoon, S.; Kim, K. S.; Shin, J. S.; Suh, J. S.; Cheon, J. *J. Am. Chem. Soc***.** **2005**, *127*, 12387. (c) Zhou, J.; Leuschner C.; Kumar, C.; Hormes, J.; Soboyejo, W. O. *Materials Science and Engineering C* **2006**, 26, 1451. (d) Loo, C.; Lowery, A.; Halas, N.; West, J.; Drezek, R. *Nano lett.* **2005**, *5*, 709.

[18]. (a) Nelson, J. A.; Bennett, L. H.; Wagner, M. J. *J. Am. Chem. Soc.* **2002***, 124*, 2979. (b) Hariharan, S.; Gass, J. *Rev. Adv. Mater. Sci.* **2005,** *10*, 298.

[19]. (a) Li, X. K.; Ji, W. J.; Zhao, J.; Wang, S. J.; Au, C. T . *J. Catal.* **2005**, *236*, 181. (b) Heracleous, E.; Lee, A. F.; Wilson, K.; Lemonidou, A. A. *J. Catal.* **2005**, *231*, 159. (c) Fatsikostas, A. N.; Verykios, X. E. *J. Catal.* **2004**, *225*, 439. (d) Molina, A. I.; Robles, J. M.; Garcia, P. B.; Castellan, E. R.; Finoechio, E.; Busca, G.; Torres, P. M.; Lopez, A. J.; *J. Catal.* **2004**, *225*, 479. (e) Li, Y.; Zhang, B.; Xie, X.; Liu, J.; Xu, Y.; Shen, W. *J. Catal.* **2006**, *238*, 412. (f) Chen, D.; Christensen, K. O.; Fernandaz, E. O.; Yu, Z.; Totdal, B.; Latorre, N.; Monzon, A.; Holmen, A. *J. Catal.* **2005**, *229*, 82.

[20]. (a) Vuu, K.; Xie, J.; McDonald, M. A.; Bernardo, M.; Hunter, F.; Zhang, Y.; Li, K.; Bednarski, M.; Guccione, S. *Bioconjugate Chem.* **2005,** 16, 995. (b) Wang, D.; He, J.; Rosenzweig, N.; Rosenzweig, Z. *Nano Lett*. **2004,** *4*, 409. (c) Son, S. J.; Reichel, J.; He, B.; Schuchman, M.; Lee, S. B. *J. Am. Chem. Soc***.** **2005**, *127,* 7316.

[21]. Petri-Fink, A.; Chastellain, M.; Juillerat-Jeanneret, L.; A. Hofmann, F. H. *Biomaterials*, **2005**, *26*, 2685.

[22]. (a) Hilger, I.; Andra, W.; Hergt, R.; Hiergeist, R.; Schubert, H.; Kaiser, W. A.; *Radiology,* **1997**, *218,* 570. (b) Jordan, A.; Wust, P.; Fahling, H.; Jonh, W.; Hinz, A.; Felix, R. *International Journal of Hyperthermia,* **1997**, *9*, 51. (c) Moroz, P.; Jones, S. K.; Gray, B.N. *International Journal of Hyperthermia,* **2002**, *18,* 267.

[23]. (a) Scherer, F.; Anton, M.; Schillinger, U.; Hanke, J.; Kruger, A.; Gansbacher, B.; Plank, C.; *Gene Therapy*, **2002**, *9*, 102. (b) Alexiou, C.; Arnold, W.G.; Klein, R. J.; Parak, F. G.; Hulin, P. R.; Bergemann, C.; Erhardt, W.; Wagenpfeil, S.; Lubbe, A. S. *Cancer Research*, **2000**, *60*, 6641.

[24]. (a) Bulte, J. W. M.; Cuyper, M.; Despres, D.; Frank, J. A. *J. Magn. Magn. Mater.* **1999**, *194,* 204. (b) Kim, D. K.; Mikhaylova, M.; Wang, F. H.; Kehr, J.; Bjelke, B.; Zhang, Y.; Tsakalakos, T.; Muhammed, M. *Chem. Mater.* **2003,** *15,* 4343. (c) Mikawa, M.; Kato, H.; Okumura, M.; Narazaki, M.; Kanazawa, Y.; Miwa, N.; Shinohara, H. *Bioconjugate Chem.* **2001,** *12,* 510.

[25]. Buscher, K.; Helm, C. A.; Gross, C.; Glockl, G.; Romanus, E.; Weitschies, W. *Langmuir* **2004,** *20,* 2435.

[26]. http://www.answers.com/topic/ferrofluid

[27]. www.nanotechnology.ethz.ch/Introduction.html

[28]. (a) Koch, C. C. *Adv. Mater. Sc.* **2003**, *5*, 99. (b) Stellacci, F.; Bauer, C. A.; Meyer-Friedrichsen, T.; Wenseleers, W.; Alain, V.; Kuebler, S. M.; Pond, S. J. K.; Zhang, Y.; Marder, S. R.; Perry, J. W. *Adv. Mater.* **2002**, *14,* 194. (c) Li, J.; Lu, C.; Maynor, B.; Huang, S.; Liu, *J. Chem. Mater.* **2004**, *16*, 1633.

[29]. http://en.wikipedia.org/wiki/Chemical_vapor_deposition

[30]. Lee, E. Y. M.; Tran, N. H.; Russell, J. J.; Lamb, R. N. *J. Phys. Chem. B* **2003**, *107,* 5208.

[31]. Tsapatsis, M.; Vlachos, D. G.; Kim, S.; Ramanan, H.; Gavalas, G. R. *J. Am. Chem. Soc.* **2000**, *122,* 12864.

[32]. Li, Y.; Tevaarwerk, E.; Chang, R. P. H. *Chem. Mater.* **2006**, *18,* 2552.

[33]. Park, S.; Lim, S.; Choi, H. *Chem. Mater.* **2006**, *18,* 5150.

[34]. Flahaut, E.; Agnoli, F.; Sloan, J.; O'Connor, C.; Green, M. L. H. *Chem. Mater.* **2002,** *14,* 2553.

[35]. www.ieee-virtual-museum.org/collection/tech.p...

[36]. (a) http://www.pvi.com.tw/4_2en.htm (b) Mattox, D.M. *Handbook of Physical Vapor Deposition (PVD) Processing* , William Andrew Publishing/Noyes, **1998**.

[37]. Lyu, S. C.; Zhang, Y.; Lee, C. J.; Ruh, H.; Lee, H. J. *Chem. Mater.* 2003, *15,* 3294.

[38]. Wang, J.; Huang, H.; Kesapragada, S. V.; Gall, D. *Nano Lett*. **2005,** *5*, 2505.

[39]. Yu, D. P.; Bai, Z. G.; Ding, Y.; Hang, Q. L.; Zhang, H. Z.; Wang, J. J.; Zou, Y. H.; Qian, W.; Xiong, G. C.; Zhou, H. T.; Feng, S. Q. *Appl. Phys. Lett*. **1998,** *72,* 3458.

[40]. (a) Mafune´, F.; Kohno, J.; Takeda, Y.; Kondow, T. *J. Phys. Chem. B* **2003**, *107,* 12589. (b) Amendola, V.; Polizzi, S.; Meneghetti, M. *J. Phys. Chem. B* **2006**, *110,* 7232.

[41]. Mafune´, F.; Kohno, J.; Takeda, Y.; Kondow, T. *J. Phys. Chem. B* **2000,** *104,* 9111.

[42]. Mafune´, F.; Kohno, J.; Takeda, Y.; Kondow, T. *J. Phys. Chem. B* **2003,** *107,* 4218.

[43]. (a) Golightly, J. S.; Castleman, A. W. Jr. *J. Phys. Chem. B* **2006**, *110,* 19979. (b) Zeng, H.; Cai, W.; Li, Y.; Hu, J.; Liu, P. *J. Phys. Chem.* , **2005,** *109,* 18260.

[44]. Sakiyama, K.; Koga, K.; Seto, T.; Hirasawa, M.; Orii, T. *J. Phys. Chem. B* **2004**, *108,* 523.

[45]. (a) Paszti, Z.; Peto, G.; Horvath, Z. E.; Karacs, A.; Guczi, L. *J. Phys. Chem. B* **1997,** *101,* 2109. (b) Chimmalgi, A.; Hwang, D. J.; Grigoropoulos, C. P. *Nano Lett.* **2005,** *5,* 1924. (c) Fan, H.; Reid, S. A. *Chem. Mater.* **2003,** *15,* 564. (d) Ramana, C. V.;

Utsunomiya, S.; Ewing, R. C.; Julien, C. M.; Becker, U. *J. Phys. Chem. B* **2006,** *110,* 10430. (e) Lees, S. T.; Gameson, I.; Jones, M. O.; Edwards, P. P. Slaski, M. *Chem. Mater.* **1998,** *10,* 3146.

[46]. (a) Suslick, K. S. *Science,* **1990**, *247*, 1439. (b) Flint, E. B.; Suslick, K. S. *Science,* **1991**, *253*, 1397. (c) Atchley, A. A.; Crum, L. A. In *Ultrasound*; Suslick, K. S., Ed.; VCH: New York, **1988.**

[47]. Pol, V. G.; Grisaru, H.; Gedanken, A. *Langmuir* **2005,** *21,* 3635.

[48]. Zhu, Y.; Li, H.; Koltypin, Y.; Hacohen, Y. R.; Gedanken, A. *Chem Commun*. **2001,** 2616.

[49]. Liang, J.; Jiang, X.; Liu, G.; Deng, Z.; Zhuang, J.; Li, F.; Li, Y. *Mater. Res. Bull.* **2003**, *38*, 161.

[50]. Kumar, E. V.; Mastai, Y.; Gedanken, A. *Chem. Mater.* **2000**, *12*, 3892.

[51]. Jeevanandam, P.; Koltypin, Y.; Gedanken, A. *Nano Lett.* **2001**, *1*, 263.

[52]. Xia, X.; Shen, L.L.; Guo, J. P. et.al. *J. Nanosci. Nanotechnol,* **2002**, *2,* 45.

[53]. Zheng, X.; Xie, Y.; Zhu, L.; Jiang, X.; Yan, A. *Ultrason. Sonochem.* **2002,** *9*, 311.

[54]. Mizukoshi, Y.; Okitsu, K.; Maeda, Y.; Yamamoto, T. A.; Oshima, R.; Nagata, Y.; *J. Phys. Chem. B,* **1997***, 101,* 7033.

[55]. Li, H. -L.; Zhu, Y. C.; Palchik, O.; Koltypin, Y.; Gedanken, A.; Palchik, V.; Slifkin, M.; Weiss, A. *Inorg. Chem.* **2002**, *41*, 637.

[56]. Jia, Y.; Niu, H.; Wu, M.; Ning, M.; Zhu, H.; Chen, Q. *Mater. Res. Bull.* **2005,** *40,* 1623.

[57]. Zhu, J. J.; Wang, H.; Xu, S.; Chen, H. Y. *Langmuir,* **2002,** *18,* 3306.

[58]. Basnayake, R.; Li, Z.; Katar, S.; Zhou, W.; Rivera, H.; Smotkin, E. S.; Casadonte, D. J. Jr.; Korzeniewski, C. *Langmuir,* **2006,** DOI 10.1021/la061274

[59]. (a) Sivakumar, M.; Gedanken, A.; Bhattacharya, D.; Brukental, I.; Yeshurun, Y.; Zhong, W.; Du, Y. W.; Felner, I.; Nowik, I. *Chem. Mater.* **2004**, *16,* 3623. (b) Sivakumar, M.; Takami, T.; Ikuta, H.; Towata, A.; Yasui, K.; Tuziuti, T.; Kozuka, T.; Bhattacharya, D.; Iida, Y. *J. Phys. Chem. B* **2006**, *110,* 15234.

[60]. Shafi, K. V. P. M.; Koltypin, Y.; Gedanken, A.; Prozorov, R.; Balogh, J.; Lendavi, J.; Felner, I. *J. Phys. Chem. B,* **1997,** *101*, 6409.

[61]. Suslick, K. S.; Fang, M.; Hyeon, M. T.; Cichowlas, A. A. *Mater. Res. Soc. Symp. Proc.* 1994*, 351*, 443.

[62]. (a) Grinstaff, M.W.; Cichowlas, A.A.; Choe,S. B.; Suslick, K. S. *Ultrasonics* **1992***, 30*, 168. (b) Koltypin, Y.; Katabi, G.; Cao, X.; Prozorov, R.; Gedanken, A. *J. Non Cryst. Solids* **1996**, *201*,159.

[63]. (a) Henglein, A. *J. Phys. Chem. B* **2000**, *104,* 1206. (b) Hodak, J. H.; Henglein, A.; Giersig, M.; Hartland, G. V. *J. Phys. Chem. B* **2000,** *104,* 11708. (c) Gutierrez, M.; Henglein, A. *J. Phys. Chem.* **1996**, *100,* 7656. (d) Henglein, A.; Meisel, D. *Langmuir* **1998,** *14,* 7392. (e) Henglein, A. *Chem. Mater.* **1998,** *10,* 444.

[64]. (a) Yonezawa, Y.; Sato, T.; Ohno, M.; Hada, H. *J. Chem. Soc., Faraday Trans.* 1, **1987**, 83, 1559. (b) Mandal, S.; Selvakannan, PR.; Pasricha, R.; Sastry, M. *J. Am. Chem. Soc.* **2003***, 125,* 8440. (c) Mandal, S.; Rautaray, D.; Sanyal, A.; Sastry, M. *J. Phys. Chem. B* **2004**, *108*, 7126. (d) Sanyal, A.; Mandal, S.; Sastry, M. *Adv. Func. Mater.* **2005**, *15*, 273.

[65]. Sanyal, A.; Sastry, M. *Langmuir,* **2006** (communicated)

[66]. Ershov, B. G.; Sukhov, N. L.; Janata, E. *J. Phys. Chem. B,* **2000**, *104*, 6138.

[67]. Yu, W.; Tu, W.; Liu, H. *Langmuir* **1999,** *15*, 6.

[68]. (a) Palchik, O.; Avivi, S.; Pinkert, D.; Gedanken, A. *Nanostruct. Mater.* **1999,** *11*, 415. (b) Zhu, J.; Palchik, O.; Chen, S.; Gedanken, A. *J. Phys. Chem. B,* **2000,** *104*, 7344.

[69]. Tsuji, M.; Hashimoto, M.; Tsuji, T. *Chem. Lett.* **2002**, 1232.

[70]. (a) Cushing, B. L.; Kolesnichenko, V. L.; O'Connor, C. J. *Chem. Rev.* **2004,** *104,* 3893. (b) Glavee, G. N.; Klabunde, K. J.; Sorensen, C. M.; Hadjipanayis, G. C. *Langmuir* **1993**, *9*, 162. (c) Glavee, G. N.; Klabunde, K. J.; Sorensen, C. M.; Hadjipanayis, G. C. *Inorg. Chem.* **1995**, *34*, 28. (d) Glavee, G. N.; Klabunde, K. J.; Sorensen, C. M.; Hadjipanayis, G. C.; Tang, Z. X.; Yiping, L. *Nanostruct. Mater.* **1993**, *3*, 391. (e) Glavee, G. N.; Klabunde, K. J.; Sorensen, C. M.; Hadjipanayis, G. C. *Langmuir* **1994**, *10*, 4726 (f) Atkins, P. W. *Physical Chemistry* (Sixth Edition), Oxford University Press, **1998.**

[71]. (a) Enustun, B. V.; Turkevich, J. *J. Am. Chem. Soc.* **1963**, *85*, 3317. (b) Turkevich, J.; Stevenson, P. S.; Hillier, J. *Discuss. Faraday Soc.* **1951**, *11*, 58.

[72]. (a) Brust, M.; Walker, M.; Bethell, D.; Schiffrin, D. J.; Whyman, R. *Chem. Commun.* **1994**, 801. (b) Brust, M.; Fink, J.; Bethell, D.; Schiffrin, J.; Kiely, C. *Chem. Commun.* **1995**, 1655.

[73]. Selvakannan, PR.; Mandal, S.; Pasricha, R.; Adyanthaya, S. D.; Sastry, M. Chem.Commun. **2002**, 1334.

[74]. (a) Pham, T.; Jackson, J. B.; Halas, N. J.; Lee, T. R. *Langmuir,* **2002,** *18*, 4915. (b) Wu, S.-H.; Chen, D.-H. *J. Colloid Interface Sci.* **2003**, *259*, 282. (c) Duan, Y.; Li, J. *Mater. Chem. Phys.* **2004**, *87*, 452.

[75]. Sun, S.; Murray, C. B. *J. Appl. Phys.*, **1999**, *85*, 4325.

[76]. Puntes, V. F.; Krishnan, K. M.; Alivisatos, A. P. *Appl. Phys. Lett.* **2001**, *78*, 2187.

[77]. (a) Rao, C. N. R.; Raveau, B. *Transition Metal Oxides*, Wiley-VCH, New York, 2nd edn., **1998.** (b) Cornell, R. M.; Schwertmann, U. *The iron oxides*, VCH, Weinheim, **1996**. (c) Rockenberger, J.; Scher, E. C.; Alivisatos, A. P. *J. Am. Chem. Soc.* **1999**, *121*, 11595. (d) Hyeon, T.; Chung, Y.; Park, J.; Lee, S. S.; Kim, Y.-W.; Park, B. H.; *J. Phys. Chem. B*, **2002**, *106,* 6831. (*e*) Moumen, N.; Pileni, M. P. *Chem. Mater.* **1996,** *8*, 1128; (*f*) Moumen, N.; Pileni, M. P. *J. Phys. Chem.* **1996**, *100,* 1867. (g) Chen, J. P.; Lee, K. M.; Sorensen, C. M.; Klabunde, K. J.; Hadjipanayis, G. C. *J. Appl. Phys.* **1994**, *75*, 5876. (h) Liu, C.; Zou, B.; Rondinone, A. J.; Zhang, Z. J. *J. Am. Chem. Soc.* **2000**, *122*, 6263. (i) Rondinone, A. J.; Samia, A. C. S.; Zhang, Z. J. *J. Phys. Chem.* **1999,** *103*, 6876. (j) Fried, T.; Shemer, G.; Markovich, G. *Adv. Mater.* **2001**, *13,* 1158. (k) Sun, S.; Zeng, H. *J. Am. Chem. Soc.* **2002,** *124*, 8204.

[78]. Demazeau, G. *J. Mater. Chem,* **1999**, *9,* 15.

[79]. Buining, P. A.; Liz-Marzan, L. M.; Philipse, A. P. *J. Colloid Interface Sci.* **1996**, *179***,** 318.

[80]. Zhang, L.; Coffer, J. L. *Chem. Mater.* **1997,** *9,* 2249.

[81]. Palkar, V.R. *Nanostruc. Mater.* **1999**, *11*, 369.

[82]. (a) Hernandez, B. A.; Chang, K.; Fisher, E. R.; Dorhout, P. K. *Chem. Mater.* **2002,** *14,* 480. (b) Sharma, P. K.; Varadan, V. V.; Varadan, V. K. *Chem. Mater.* **2000,** *12,* 2590.

[83]. Tadros, T. F. *Applied Surfactants: Principles and Application,* Wiley-VCH Verlag GmbH & Co. KgaA, **2005.**

[84]. (a) Quinlan, F. T.; Kuther, J.; Tremel, W.; Knoll, W.; Risbud, S.; Stroeve, P. *Langmuir* **2000,** *16,* 4049. (b) Calandra, P.; Longo, A.; Liveri, V. T. *J. Phys. Chem. B* **2003,** *107,* 25. (c) Morrison, S. A.; Cahill, C. L.; Carpenter, E. E.; Harris, V. G. *Ind. Eng. Chem. Res.* **2006,** *45,* 1217. (d) Lisiecki, I. *J. Phys. Chem. B* **2005,** *109,* 12231. (e) Koo, H. Y.; Chang, S. T.; Choi, W. S.; Park, J. H.; Kim, D.Y.; Velev, O. D. *Chem. Mater.* **2006,** *18,* 3308. (f) Lemyre, J. L.; Ritcey, M. *Chem. Mater.* **2005,** *17,* 3040. (g) Vestal, C. R.; Zhang, Z. J. *Nano Letters***, 2003,** *3,* 1739. (h) Tartaj, P.; Tartaj, J. *Chem. Mater.* **2002,** *14,* 536. (i) Kitchens, C. L.; McLeod, M. C.; Roberts, C. B. *J. Phys. Chem. B* **2003,** *107,* 11331. (j) Cason, J. P.; Roberts, C. B. *J. Phys. Chem. B* **2000,** *104,* 1217. (k) Hirai, T.; Bando, Y.; Komasawa, I. *J. Phys. Chem. B* **2002,** *106,* 8967. (l) Li, M.; Mann, S. *Langmuir* **2000,** *16,* 7088. (m) Wu, M. L.; Chen, D. H.; Huang, T. C. *Langmuir* **2001,** *17,* 3877. (n) Doolittle, J. W. Jr.; Dutta, P. K. *Langmuir* **2006,** *22,* 4825. (o) Sugimoto, T.; Kimijima, K. *J. Phys. Chem. B* **2003,** *107,* 10753. (p) Sangregorio, C.; Galeotti, M.; Bardi, U.; Baglioni, P. *Langmuir* **1996,** *12,* 5800. (q) Bagwe, R. P.; Khilar, K. C. *Langmuir* **2000,** *16,* 905.

[85]. (a) Kyunghee, C. Y.; Fendler, J. H. *Langmuir* **1990**, *6,* 1519. (b) Yang, J.; Meldrum, F.C.; Fendler, J. H. *J. Phys. Chem.* **1995**, *99*, 5500. (c) Zhao, X. K.; Xu, S.; Fendler, J. H. *Langmuir* **1991**, *7*, 520. (d) Zhao, X. K.; Fendler, J. H. *Chem. Mater***. 1991,** *3***,** 168. (e) Zhao, X. K.; Fendler, J. H. *J. Phys. Chem.* **1991**, *95*, 3716. (f) Zhao, X. K.; McCormick, L. D.; Fendler, J. H. *Chem. Mater.* **1991**, *3*, 922. (g) Yuan, Y.; Cabasso, I.; Fendler, J. H.; *Chem. Mater***. 1990**, *2*, 226. (h) Yang, J.; Meldrum, F.C.; Fendler J. H. *J. Phys. Chem.* **1995**, *99,* 5500.

[86]. Zhao, X. K.; Yang, J. L.; McCormick, D.; Fendler, J. H. *J. Phys. Chem.* **1992**, *96*, 9933.

[87]. Yang, J.; Fendler, J. H. *J. Phys. Chem.* **1995**, *99*, 5505.

[88]. Zhao, X. K.; McCormick, L. D.; Fendler J. H. *Langmuir* **1991**, *7*, 1255.

[89]. (a) Swami, A.; Kasture, M.; Pasricha, R.; Sastry, M. *J. Mater.Chem.* **2004**, *14,* 709.

[90]. (a) Swami**,** A.; Kumar, A.; Selvakannan, PR.; Mandal, S.; Pasricha, R.; Sastry, M.; *Chem. Mater.* **2003,** *15*, 17. (b) Swami, A.; Kumar, A.; D`Costa, M.; Sastry, M. *J. Mater.Chem.* **2004**, *14,* 2696. (c) Swami, A.; Selvakannan, PR.; Pasricha, R.; Sastry, M. *J. Phys. Chem. B,* **2004**, *108*, 19269.

[91]. (a) Selvakannan, PR.; Senthilkumar, P.; More, A. S.; Shingte, R. S.; Wadgaonkar, P. P.; Sastry, M. *Adv.Mater.* **2004**, *16*, 966. (b) Sanyal, A.; Sastry, M. *Chem. Commun.* **2003**, 1236.

[92]. (a) Rautaray, D.; Kumar, A.; Reddy, S.; Sainkar, S. R.; Pavaskar, N. R.; Sastry, M. *CrystEngComm* **2001**, *45*,1. (b) Reddy, S.; Rautaray, D.; Sainkar, S. R.; Sastry, M. *Bull. Mater. Sci.* **2003**, *26*, 283. (c) Rautaray, D.; Banpurkar, A.; Sainkar, S. R.; Limaye, A. V.; Ogale, S.; Sastry, M. *Crystal Growth & Design* **2003**, *3*, 449. (d) Rautaray, D.; Banpurkar, A.; Sainkar, S. R.; Limaye, A. V.; Pavaskar, N. R.; Ogale, S.; Sastry, M. *Adv. Mater.* **2003**, *15*, 1273. (e) Rautaray, D.; Kavathekar, R.; Sastry, M. *Faraday Discuss.* **2005**, *129*, 205.

[93]. (a) Qu, L.; Shi, G.; Wu, X.; Fan, B. *Adv. Mater.* **2004**, *16,* 1200. (b) Hou, S.; Harrell, C. C.; Trofin, L.; Kohli, P.; Martin, C. R. *J. Am. Chem. Soc.* **2004**, *126,* 5674. (c) Go1ring, P.; Pippel, E.; Hofmeister, H.; Wehrspohn, R. B.; Steinhart, M.; Go1sele, U. *Nano Lett.* **2004**, *4*, 1121. (d) Choi, J.; Sauer, G.; Nielsch, K.; Wehrspohn, R.B.; Gosele, U. *Chem. Mater.* **2003**, *15,* 776. (e) Zheng, M.; Li, G.; Zhang, X.; Huang, S.; Lei, Y.; Zhang, L. *Chem. Mater.* **2001**, *13*, 3859. (f) Zong, R.-L.; Zhou, J.; Li, Q.; Du, B.; Li, B.; Fu, M.; Qi, X.-W.; Li, L.-T.; Buddhudu, S. *J. Phys. Chem. B.* **2004**, *108*, 16713.

[94]. Cepak, V. M.; Martin, C. R. *J. Phys. Chem. B* **1998**, *102*, 9985.

[95]. (a) Pol, V. G.; Grisaru, H.; Gedanken, A. *Langmuir* **2005,** *21,* 3635. (b) Zanella, R.; Giorgio, S.; Henry, C. R.; Louis, C. *J. Phys. Chem. B* **2002**, *106*, 7634. (c) Michalski, J.; Konopka, K.; Trzaska, M. *Acta Phys. Pol., A* **2002**, *102*, 181.

[96]. Platonova, O. A.; Bronstein, L. M.; Solodovnikov, S. P.; Yanovskaya, I. M.; Obolonkova, E. S.; Valetsky, P. M.; Wenz, E.; Antonietti, M. *Colloid Polym. Sci.* **1997**, *275*, 426.

[97]. (a) Ahmed, S. R.; Kofinas, P. *Macromolecules* **2002**, *35*, 3338. (b) Rabelo, D.; Lima, E. C. D.; Reis, A. C.; Nunes, W. C.; Novak, M. A.; Garg, V. K.; Oliveira, A. C.; Morais, P. C. *Nano Lett.* **2001**, *1*, 105.

[98]. Hoh, J. C.; Yaacob, I. I. *J. Mater. Res.* **2002**, *17*, 3105.

[99]. (a) Mandal, S.; Sastry, M. *Mater. Res. Bull.* **2002**, *37*, 1613. (b) Mandal, S.; Damle, C.; Sainkar, S.R.; Sastry, M. *J. Nanosci. Nanotech,* **2001**, 1, 281. (c) Rautaray, D.; Sainkar, S. R.; Sastry, M. *Langmuir* **2003**, *19*, 888. (d) Rautaray, D.; Sainkar, S. R.;

Sastry, M. *Chem. Mater.* **2003**, *15*, 2809. (e) Shankar, S. S.; Rautaray, D.; Pasricha, R.; Pavaskar, N. R.; Mandale, A. B.; Sastry, M. *J. Mater. Chem.* **2003**, 1*3*, 1108 (f) Shankar, S. S.; Joshi, H.; Pasricha, R.; Pavaskar, N. R.; Mandale, A. B.; Sastry, M. *J. Colloid Interface Sci.* **2004**, *269*, 126. (g) Mandal, S.; Sainkar, S. R.; Sastry, M. *Nanotechnology,* **2001**,12, 358. (h) Mandal, S.; Phadtare, S., Selvakannan, PR.; Pasricha, R.; Sastry, M. *Nanotechnology,* **2003**,14, 878. (i) Shankar, S. S.; Ahmad, A.; Pasricha, R.; Khan, M. I.; Kumar, R.; Sastry, M. *J. Colloid Interface Sci.* **2004**, *274*, 69. (j) Shankar, S. S.; Chatterjee, S.; Sastry, M. *PhysChemComm,* **2003**, *6*, 36.

[100]. Chen, B.-D.; Cilliers, J. J.; Davey, R. J.; Garside J.; Woodburn, E. T. *J. Am. Chem. Soc.,* **1998**, *120*, 1625.

[101]. (a) Rautaray, D.; Sinha, K.; Shiv Shankar, S.; Adyanthaya, S. D.; Sastry, M. *Chem. Mater.* **2004**, *16*, 1356. (b) Rautaray, D.; Sastry, M. *CrystEngComm.* **2004** (Communicated). (c) Mandal, S.; Arumugam, S. K.; Adyanthaya, S. D.; Sastry, M. *J. Mater. Chem.* **2004**, *14*, 43. (d) Mandal, S.; Arumugam, S. K.; Pasricha, R.; Sastry, M. *Bull. Mater. Sci.* **2005,** *28*, 503. (e) Shankar, S. S.; Patil, U. S.; Prasad, B. L. V.; Sastry, M. *Langmuir* **2004**, *20*, 8853.

[102]. (a) Berkman, S.; Egloff, G. "The Physical Chemistry of Foams" *Eighty Fifth Meeting of the American Chemical Society, Washington, D. C.* March **1933**. (b) Gardiner, B. S.; Dlugogorski, B. Z.; Jameson, G. J. *Ind. Eng. Chem. Res.* **1999**, *38*, 1099. (c) Weaire, D.; Hutzler, S. *"The Physics of Foam"* Clarendon Press, Oxford, **1999**. (d) Hedreul, C.; Frens, G. *Colloids and Surfaces A: Physicochem. Eng. Aspects* **2001**, *186*, 73. (e) Neethling, S. J.; Lee, H. T. Cilliers, J. J. *J. Phys.: Condens. Matter* **2002**, *14*, 331. (f) Stein, H. N.; Laven, J. *J. Colloid Interface Sci.* **2001**, *244***,** 436. (g) Jalmes, A.; Lagevin, D. *J. Phys.: Condens. Matter* **2002**, *14*, 9397. (h) Koehler, S. A.; Hilgenfeldt, S. Stone, H. A. *Langmuir* **2000,** *16,* 6327. (i) Hilgenfeldt, S.; Koehler, S. A.; Stone, H. A. *Phys. Rev. Lett.* **2001**, *86*, 4704.

[103]. Barnes, G.; Gentls, I. *Interfacial Science An Intrduction,* Oxford University Press, **2005.**

[104]. (a) Mann, S.; *Nature*, **1993**, *365*, 499. (b) Oliver, S.; Kupermann, A.; Coombs, N.; Lough, A; Ozin, G. A., *Nature*, **1995,** *378*, 47. (c) Kroger, N.; Deutzmann, R.; Sumper, M., *Science*, **1999**, *286*, 1129. c) Parkinson, J.; Gordon, R. *Trends Biotech.* **1999**, *17*, 190.

[105]. Young, J. R.; Davis, S. A.; Bown, P. R.; Mann, S. *J. Struct. Biol.* **1999**, *126***,** 195.

[106]. (a) Lovley, D. R., Stolz, J. F., Nord, G. L. and Phillips, E. J. P., *Nature* **1987**, *330*, 252. (b) Spring, H. and Schleifer, K. H., *Sys. Appl. Microbiol*. **1995**, *18*, 147. (c) Dickson, D. P. E., *J. Magn. Magn. Mater.* **1999**, *203*, 46.

[107]. (a) Beveridge, J. T.; Hughes, M. N.; Lee, H.; Leung, K. T.; Poole, R. K.; Savvaides, I.; Silver, S.; Trevors, J. T. *Adv. Microb. Physiol.* **1997**, 38, 178. (b) Silver, S. *Gene* **1996**, *179*, 9. (c) Rouch, D.A. Lee, B. T.; Morby, A. T. *J. Ind. Micro.* **1995**,*14*, 132.

[108]. Mukherjee, P.; Ahmad, A.; Mandal, D.; Senapati, S.; Sainkar, S. R.; Khan, M. I.; Ramani, R.; Pasricha, R.; Ajayakumar, P. V.; Alam, M.; Sastry, M.; Kumar, R. *Angew. Chem. Int. Ed.* **2001**, *40*, 3585. (b) Mukherjee, P.; Senapati, S.; Mandal, D.; Ahmad, A.; Khan, M. I.; Kumar, R.; Sastry, M. C*hemBioChem* **2002**, *3*, 461. (c) Ahmad, A.; Mukherjee, P.; Mandal, D.; Senapati, S.; Khan, M. I.; Kumar, R.; Sastry, M. *J. Am. Chem. Soc*. **2002,** *124*, 12108. (d) Sanyal, A.; Rautaray, D.; Bansal, V.; Ahmad, A.; Sastry, M.; *Langmuir* **2005,** *21*, 7220. (e) Rautaray, D.; Sanyal, A.; Adyanthaya, S. D.; Ahmad, A.; Sastry, M. *Langmuir* **2004,** *20***,** 6827. (f) Rautaray, D.; Ahmad, A.; Sastry, M. *J. Am. Chem. Soc.***2003,** *125*, 14656.

[109]. (a) Shankar, S. S.; Rai, A.; Ankamwar, B.; Singh, A.; Ahmad, A.; Sastry, M. *Nat. Mater*. **2004**, *3*, 482. (b) Shankar, S. S.; Ahmad, A.; Pasricha, R.; Sastry, M. *J. Mater. Chem.* **2003**, *13*, 1822. (c) Shankar, S. S.; Ahmad, A.; Sastry, M. *Biotechnol. Prog.*, **2003**, *19*, 1627. (d) Shankar, S. S.; Rai, A.; Ahmad, A.; Sastry, M. *Applied Nanoscience* **2004**, *1*, 69. (e) Shankar, S. S.; Rai, A.; Ahmad, A.; Sastry, M. *J. Colloid Interface Sci.*, **2004**, *275*, 496. (f) Rautaray, D.; Sanyal, A.; Ahmad, A.; Sastry, M. *Cryst.Growth & Des.* **2005**, *5*, 399. (g) Sanyal, A.; Ahmad, A.; Sastry, M. *Curr. Sci.* **2005,** *89***,** 1742.

[110]. (a) Bansal, V.; Rautaray, D.; Bharde, A.; Ahire, K.; Sanyal, A.; Ahmad, A.; Sastry, M. *J. Mater. Chem.* **2005**, *15***,** 2583. (b) Bansal, V.; Sanyal, A.; Rautaray, D.; Ahmad, A.; Sastry, M. *Adv. Mater.* **2005**, *17*, 889. (c) Bansal, V.; Ahmad, A.; Sastry, M. *J. Am. Chem. Soc.* **2006,** *128*, 14059. (d) Bharde, A.; Wani, A.; Shouche, Y.; Joy, P. A.; Prasad, B. L. V.; Sastry, M. *J. Am. Chem. Soc.* **2005,** *127*, 9326.

[111]. (a) Jiang, P.; Liu, Z. F.; Cai, S. M. *Langmuir* **2002,** *18,* 4495. (b) Wanunu, M.; Vaskevich, A.; Cohen, S. R.; Cohen, H.; Yellin, R. A.; Shanzer, A.; Rubinstein, I. *J. Am. Chem. Soc.* **2005**, *127,* 17877. (c) Patrone, L.; Palacin, S.; Bourgoin, J. P.; Werts, M. H.

V. *Langmuir* **2004,** *20,* 11577. (d) Hata, K.; Yoshida, S.; Fujita, M.; Yasuda, S.; Makimura, T.; Murakami, K.; Shigekawa, H. *J. Phys. Chem. B* **2001,** *105,* 10842. (e) Ang, T. P.; Wee, T. S. A.; Chin, W. S. *J. Phys. Chem. B* **2004,** *108,* 11001. (f) He, H. X.; Zhang, H.; Li, Q. G.; Zhu, T.; Li, S. F. Y.; Liu, Z. F. *Langmuir* **2000,** *16,* 3846. (g) Santhanam, V.; Liu, J.; Agarwal, R.; Andres, R. P. *Langmuir* **2003,** *19,* 7881. (h) Fresco, Z. M.; Frechet, J. M. J. *J. Am. Chem. Soc.* **2005**, *127,* 8302. (i) Zhou, N.; Wang, J.; Chen, T.; Yu, Z.; Li, G. *Anal. Chem.* **2006,** *78,* 5227.

[112]. (a) Trou, M.; Saville, D. A.; Aksay, I. A. *Science* **1996**, *272*, 706. (b) Giersig, M.; Mulvaney, P. *J. Phys. Chem.* **1993**, *97*, 6334. (c) Giersig, M.; Mulvaney, P. *Langmuir* **1993**, *9,* 3408. (d) Teranishi, T.; Hosoe, M.; Tanaka, T.; Miyake, M. *J. Phys. Chem. B* **1999**, *103,* 3818. (e) Chandrasekharan, N.; Kamat, P. V. *Nano Lett.* **2001**, *1,* 67.

[113]. (a) Korgel, B. A.; Fullam, S.; Connoly, S.; Fitzmaurice, D. *J. Phys. Chem. B* **1998**, *122,* 4640. (b) Harfenist, S. A.; Wang, Z. L.; Alvarez, M. M.; Vezmar, I.; Whetten R. L. *J. Phys. Chem.* **1996**, *100,* 13904. (c) Pileni, M. P. *Langmuir* **1997**, *13,* 3266. (d) Pileni, M. P. *New J. Chem.* **1998**, *22,* 693. (e) Pileni, M. P. *J. Phys. Chem. B* **2001**, *105,* 3358. (f) Selvakannan, PR.; Mandal, S.; Pasricha, R.; Sastry, M. *J. Colloid Int. Sci.* **2004**, *279,* 124. (g) Sarathy, K. V.; Raina, G.; Yadav, R. T.; Kulkarni, G. U.; Rao, C. N. R. *J. Phys. Chem. B* **1997**, *101,* 9876. (h) Brown, L. O.; Hutchison, J. E. *J. Phys. Chem. B* **2001**, *105*, 8911. (i) He, S.; Yao, J.; Jiang, P.; Shi, D.; Zhang, H.; Xie, S.; Pang, S.; Gao, H.; *Langmuir* **2001**, *17,* 1571. (j) Zhao, S.Y.; Wang, S.; Kimura, K. *Langmuir* **2004**, *20,* 1977. (k) Stoeva, S.; Klabunde, K. J.; Sorensen, C.M.; Dragieva, I. *J. Am. Chem. Soc.* **2002**, *124,* 2305. (l) Liu, S.; Zhu, T.; Hu, R.; Liu, Z. *Phys. Chem. Chem. Phys.* **2002**, *4*, 6059. (m) Kiely, C. J.; Fink, J.; Brust, M.; Bethell D.; Schiffrin, D. J. *Nature* **1998**, *396,* 444. (n) Kiely, C. J.; Fink, J., Zheng, J. G.; Brust, M.; Bethell D.; Schiffrin, D. J. *Adv. Mater.* **2000**, *12,* 640.

[114]. (a) Hulteen, J. C.; van Duybe, R. P. *J. Vac. Sci. Tech. A* **1995**, *13,* 1533. (b) Haynes, C. L.; van Duybe, R. P. *J. Phys. Chem. B* **2001**, *105,* 5599. (c) Hulteen, J. C.; Treichel, D. A.; Smith, M.T.; Duval, M. L.; Jensen, T.R.; van Duyne, R. P. *J. Phys. Chem. B* **1999**, *103,* 3854. (d) Haynes, C. L.; McFarland, A. D.; Smith, M.T.; Hulteen, J. C.; van Duyne R. P. *J. Phys. Chem B* **2002**, *106,* 1898. (e) Ormonde, A. D.; Hicks, E. C. M.; Castillo, J.; van Duyne, R. P. *Langmuir* **2004**, *20,* 6927. (f) Grunes, J.; Zhu, J.;

Anderson, E. A.; Somorjai, G. A. *J. Phys. Chem. B* **2002**, *106,* 11463. (g) Guo, Q.; Teng, X.; Rahman, S.; Yang, H. *J. Am. Chem. Soc.* **2003**, *125*, 630. (h) Garno, J. C.; Yang, Y.; Amro, N. A.; Dupeyrat, S. C.; Chen, S.; Liu, G. Y.; *Nano Lett.* **2003**, *3*, 389. (i) Kim, K.; Lee, I. *Langmuir* **2004,** *20,* 7351. (j) Bullen, H. A.; Garrett, S. J. *Nano Lett.* **2002, *2*,** 739.

[115]. (a) Tripp, S. L.; Pusztay, S. V.; Ribbe, A. E.; Wei, A. *J. Am. Chem. Soc***. 2002**, *124,* 7914. (b) Love, J. C.; Urbach, A. R.; Prentiss, M. G.; Whitesides, G. M. *J. Am. Chem. Soc.* **2003**, *125*, 12696.

[116]. (a) Lim, I. I. S.; Maye, M. M.; Luo, J.; Zhong, C. J. *J. Phys. Chem. B* **2005,** *109,* 2578. (b) Zhang, M.; Drechsler, M.; Muller, A. H. E. *Chem. Mater.* **2004,** *16,* 537. (c) Herna´ndez, R. M.; Richter, L.; Semancik, S.; Stranick, S.; Mallouk, T. E. *Chem. Mater.* **2004,** *16,* 3431.

[117]. (a) Meldrum, F. C.; Kotov, N. A.; Fendler, J. H. *Langmuir* **1994**, *10*, 2035. (b) Meldrum, F.C.; Kotov, N. A.; Fendler, J. H. *Chem. Mater.* **1995**, *7,* 1112. (c) Ganguly, P.; Paranjape, D. V.; Patil, K.R.; Chaudhari, S. K.; Kshirsagar, S. T. *Indian J. Chem. A* **1992**, *31,* F42. (d) Sastry, M.; Patil, V.; Mayya, K. S.; Paranjape, D. V.; Singh, P.; Sainkar, S. R. *Thin Solid Films* **1998**, *324,* 239. (e) Damle, C.; Gole A.; Sastry, M. *J. Mater. Chem.* **2000**, *10*, 1389. (f) Swami, A.; Kumar, A.; Selvakannan, PR.; Mandal, S.; Sastry, M. *J. Colloid Int. Sci.* **2003**, *260*, 367. (g) Selvakannan, PR.; Swami, A.; Srisathiyanarayanan, D.; Shirude, P. S.; Pasricha, R.; Mandale, A. B.; Sastry, M. *Langmuir* **2004**, *20*, 7829.

[118]. (a) Patolsky, F.; Weizmann, Y.; Lioubashevski, O.; Willner, I. *Angew. Chem. Int. Ed.* **2002**, *41*, 2323. (b) Keren, K.; Gilad, K.R.; Yoseph, G. B.; Sivan, U.; Braun, E. *Science* **2002**, *297*, 72. (c) Braun, E.; Eichen, Y.; Sivan, U.; Yoseph, G. B. *Nature* **1998**, *391*, 775. (d) Ford, W. E.; Harnack, O.; Yasuda, A.; Wessels, J. M. *Adv. Mater.* **2001**, *13*, 1793. (e) Deng, Z.; Mao, C. *Nano Lett.* **2003**, *3,* 1545.

[119]. (a) Cullity, B. D.; *Introduction to Magnetic Materials,* Addison-Wesley Publishing, Reading, **1972.** (b) http://www.irm.umn.edu/hg2m/hg2m_index.html (c) O'Handley, R. C. *Modern Magnetic Materials: Principles and Application,* John Wiley & Sons, Inc., **2000**.

Chapter II

Characterization techniques

The different characterization techniques used in the course of the research work along with their guiding principles and their specifications are discussed in this chapter.

2.1. INTRODUCTION:

Nanoparticles in the true sense are often present as stable dispersion in a solution and are not perceptible to our normal naked eye. Property measurements and characterization have thus always been a challenging task to various researchers over the decades. However this situation has changed quite remarkably in recent years and special instrumental techniques have been developed in order to characterize the nanoparticles. This chapter highlights the basic principles of various characterization techniques which have been used in the present thesis work namely UV-Vis spectroscopy, X-Ray Diffraction (XRD), Transmission Electron Microscopy (TEM), Energy Dispersive Analysis of X-rays (EDAX), Fourier Transform Infrared Spectroscopy (FTIR), Langmuir-Blodgett technique (LB), Brewster Angle Microscopy (BAM), Nuclear Magnetic Resonance Spectroscopy (NMR), Contact Angle Measurement, X-Ray Photoelectron Spectroscopy (XPS), Atomic Absorption Spectroscopy (AAS), Thermogravimetric Analysis (TGA), Vibrating Sample Magnetometer (VSM), Superconducting Quantum Interference Device (SQUID) and Electron Spin Resonance Spectroscopy (ESR).

2.2. UV-VIS SPECTROSCOPY:

UV–Visible absorption spectroscopy is one of the very important and primary characterization tool to study the metal nanoparticles formation, particularly noble metals like Au, Ag, Cu etc. This is because in nanometer regime, visible radiation can initiate the generation of surface plasmon resonance in the particles, thus showing very prominent peak in this electromagnetic region [1a, b].

As depicted in the *Figure 2.1* the light from the source is alternatively split into one of two beams by a rotating mirror called a chopper; one beam is passed through the sample and the other through the reference. The detector alternately sees the beam from the sample and then the reference. Its output that ideally would be an oscillating square-wave gives the ratio of I to I_o directly i.e. the reference correction is made automatically. Array-detector spectrophotometers allow rapid recording of absorption spectra. Dispersing the source light after it passes through a sample allows the use of an array detector to simultaneously record the transmitted light power at multiple wavelengths. These spectrometers use photodiode arrays as the detector. The light source is a continuum source such as a tungsten lamp. All wavelengths pass through the sample. The light is dispersed by a diffraction grating after the sample and the separated wavelengths fall on different pixels of the array detector. The resolution depends on the grating, spectrometer design and pixel size and is usually fixed for a given instrument. Besides allowing rapid spectral recording, these instruments are relatively small and robust. Portable spectrometers have been developed that use optical fibers to deliver light to and from a sample. These instruments use only a single light beam, so reference spectrum is recorded and stored in memory to produce transmittance or absorbance spectra after recording the sample spectrum.

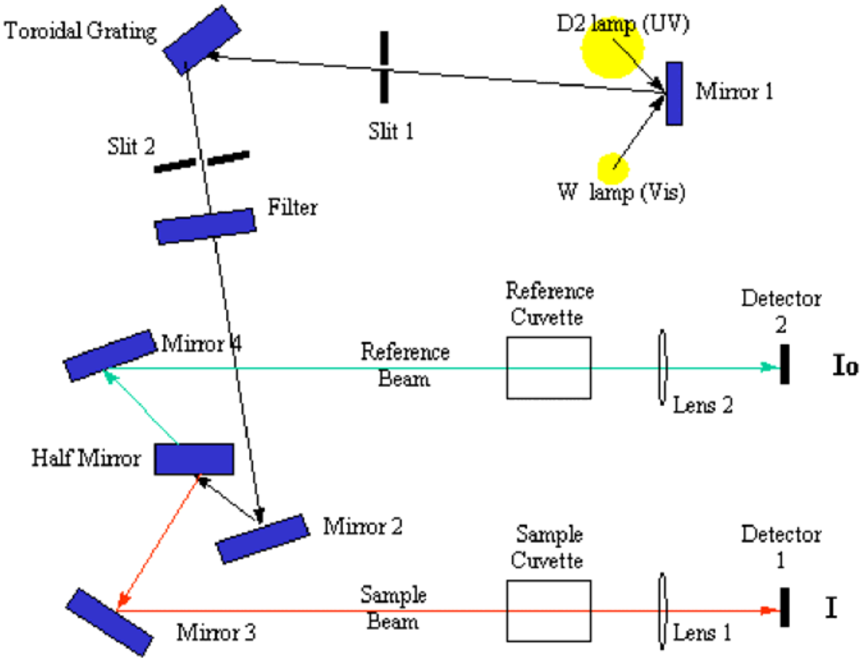

Figure 2.1. *A pictorial representation of the principle of UV-Vis spectrophotometer [1d].*

All the UV–Visible absorption spectra presented in the thesis were carried out on Jasco V-570 dual beam spectrophotometer and HP diode array spectrophotometer operated at a resolution of 2 nm [1c].

2.3. X-RAY DIFFRACTION (XRD):

X-rays, which are electromagnetic radiation with wavelengths of the order of 10^{-10} m, are typically generated by bombarding a metal target with high-energy electrons. The electrons decelarate as they undergo elastic and inelastic collisions and generate radiation with a continuous range of wavelengths known as Bremsstrahlung. After the discovery of X-ray by Roentgen, Laue in 1912 suggested that X-rays can be diffracted when passed through a crystal. Thus a technique came into existence which had immense potential for detection of samples.

Diffraction of X-rays occurs in a crystal, as the distance between the planes of the crystal is comparable to the wavelength of X-rays. When X-rays strike a crystal, it interacts with the arrays of atoms (electrons) and undergoes elastic and inelastic scattering. It is the elastically scattered beam that we are interested as that contains the information about the arrangement of the atoms in the crystal lattice. The diffracted beam coming from a set of planes either combine constructively or destructively depending on the phase difference. They follow a relation as was given by Bragg and is commonly known as Bragg's law where,

$$2d \sin\theta = n \lambda$$

where θ= angle of incidence, d= interplanar distance, λ= wavelength of X-rays (1.54 Å for Cu K_α) and n= order of reflection (integer values of 1, 2, 3…). This suggests that only for integral value of n, the equation satisfies the appearance of bright spots on the screen, thus constructive interference occurs. Bragg's diffraction pattern is schematically shown in *Figure 2.2.*

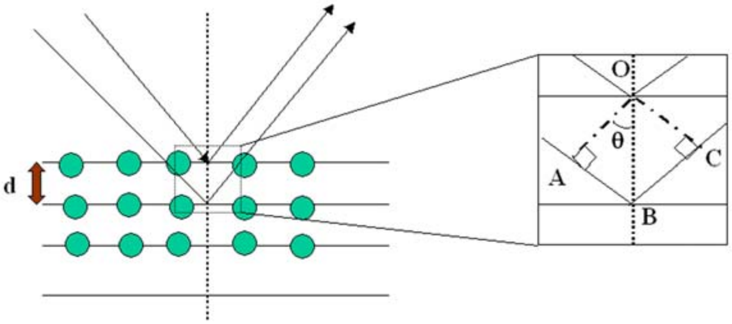

Path difference= AB+BC

AB=BC=d cos (90-θ)= d sin θ

Hence AB+BC=2d sin θ= nλ

Figure 2.2: *Pictorial representation of Bragg's law.*

An alternative method to Laue's technique is the powder diffractometer in which monochromatic X-rays are focused on a sample pellet or on slide containing sample film mounted on rotating stage. Since sample is powder, all possible diffractions are recorded simultaneously from hypothetical randomly oriented grains. Mount is then rotated to ensure all diffractions are obtained. Powder diffraction technique is used to identify a sample of a solid substance by comparison of the position of the diffraction line and the corresponding intensity with a large data bank. Intensity of the diffracted line depends on the scattering strengths of the individual atoms which in turn depends on the electron density. The phase difference between the *hkl* reflections of two atoms, one of which is located at the origin and the other located at the coordinates (*xa*, yb, zc) is given by,

$$\phi_{hkl} = 2\pi (hx+ky+lz)$$

The total intensity is thus the integration of the scattering strengths of all the atoms taken together. Hence the **structure factor** of a unit cell containing n atoms with scattering factors f_n is given by;

$$F_{hkl} = \Sigma f_j \exp\{ i(\phi_{hkl}) \}$$

Thus the intensity is proportional to F_{hkl}^{2}.

For practical reasons the diffractometer measures an angle twice that of the incident theta (θ) angle. All the XRD data presented here in the thesis were carried out on a Philips PW 1830 instrument operating at a voltage of 40 kV and a current of 30 mA with Cu Kα radiation. Most of the XRD samples were made either by drop coating the sample on a glass plate or by drying the samples to make powder [2].

2.4. TRANSMISSION ELECTRON MICROSCOPY (TEM):

Although some structural features can be revealed by X-Ray diffraction, for direct imaging of nanoparticles transmission electron microscope is an extremely important tool that operates on the same basic principles as the light microscope but uses electrons instead of light [3]. The development of the transmission electron microscope (TEM) in the late 1930's primarily as an imaging device, which exceeds the resolution power of the light microscope, by several orders of magnitude. Since the de Broglie wavelength of electrons decreases with their kinetic energies, fast moving electrons have very short wavelength associated with them and so are capable of very high resolution if that wavelength can be used in an appropriately designed instrument. Resolving power of a microscope is given by the following formula

$$d \approx 0.5\,\lambda / \sin\alpha$$

Where λ represents the wavelength and α equals the one-half of the angular aperture.

In TEM analysis, a thin specimen is illuminated with electrons in which the electron intensity is uniform over the illuminated area. As the electrons travel through the specimen, depending on the density of the material present, some of the electrons are scattered and disappear from the beam and some remain unaffected. At the bottom of the microscope the un-scattered electrons hit a fluorescent screen, which gives rise to a "shadow image" of the specimen with its different parts displayed in varied darkness according to their density and it thus contains all the structural and chemical information about the specimen.

When we form images in TEM, we either form an image using the central spot, or we use some or all of the scattered electrons. In the case of bright-field imaging an aperture is inserted into the back focal plane of the objective lens, thus blocking out most of the diffraction pattern except that which is visible through the aperture whereas in dark-field imaging one or more of the diffracted beams is allowed to pass through and the direct beam is blocked by the aperture. Some useful information like planar defects, stacking faults can be obtained through dark-field imaging. Bright field imaging depends on the mass-thickness of the sample. Areas of the sample that are thicker will have fewer transmitted (unscattered) electrons, hence will appear darker. In selected area electron diffraction (SAED), an aperture is used to define the area from which a diffraction pattern is formed in a TEM specimen. The resulting patterns contain information about the lattice spacing measurement and sample orientation.

All the TEM images presented in the thesis were recorded on a JEOL model 1200EX instrument at an accelerating voltage of 120 kV equipped with LaB_6 as the electron source. Samples for TEM have been made by drop coating the sample on the carbon coated copper grids and allowing the solvent to evaporate.

2.5. ENERGY DISPERSIVE ANALYSIS OF X-RAYS (EDAX):

Energy Dispersive Analysis of X-rays (EDAX) is a chemical microanalysis technique. It is also sometimes referred to as EDX or EDS analysis. It is a technique to identify the elemental composition of the specimen or for an area of interest. It generally works as an integrated feature with Scanning Electron Microscope (SEM). During EDAX analysis the specimen is bombarded with the incident electron beam. When a voltage of 10-20 keV is used in SEM, the incident electrons knock out the inner core level electrons of the sample. The electrons from the higher energy levels fill up the vacancy thus created. During this transition X-ray is emitted which is plotted as no. of counts (intensity) with respect to the binding energy. The detector generally used in EDAX analysis is different from SEM and is the Lithium drifted Silicon detector, known as SiLi detector. This detector must be operated at liquid nitrogen temperatures. The photoelectron emitted is drawn into the Si detector, which creates electron-hole pairs. These electron-hole pairs are attracted towards the opposite ends of the detector by a strong electric field. The SiLi detector is often protected by Beryllium window, hence it protects detection of soft X-rays of elements having low atomic number.

An EDAX spectrum also shows the nature of X-rays emitted which means that a transition from L-level to K-level is known as K-alpha peak, transition from M-level to K-level is known as the K-β peak and so on. This is shown in the cartoon of *Figure 2.3.*

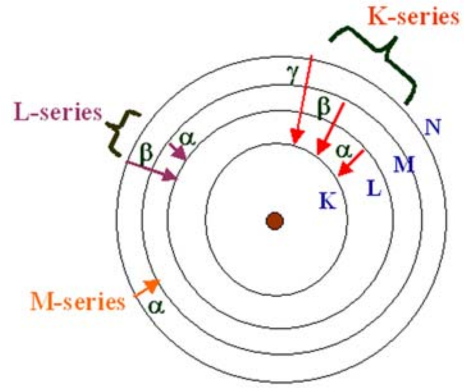

Figure 2.3. *Schematic showing the possible transition lines to form an EDAX spectrum.*

EDAX measurements described in this thesis were performed on a Leica Stereoscan-440 scanning electron microscope instrument equipped with a Phoenix EDAX attachment. Samples for EDAX analysis were made by drop coating the solutions onto Si (111) wafers. In some cases powder samples were also used directly on the sample-holder for the measurement.

2.6. FOURIER TRANSFORM INFRA-RED SPECTROSCOPY (FTIR):

The atoms in a molecule do not remain in a fixed relative position and vibrate about the mean position. Due to this vibrational motion, if there is a periodic alternation in the dipole moment then such mode of vibration is infrared (IR) active. The 100 μm – 1 μm wavelength region of the electromagnetic spectrum is called the IR region. The vibrating molecule absorbs energy only from radiation with which it can coherently interact, i.e. the radiation of its own oscillation frequency. The appearance or non-appearance of certain vibrational frequencies gives valuable information about the structure of a particular molecule [4]. Each functional group has specific range of vibrational frequencies and is very sensitive to the chemical environment and the neighboring groups, thus providing valuable information regarding the presence of certain functional groups in the specific sample for their further characterization and identification. The frequency of vibration is given by the relation:

$$\omega_{osc} = \frac{1}{2\pi}\sqrt{\frac{k}{\mu}} \text{ cm}^{-1}$$

where, k is force constant related to the particular vibration and μ is reduced mass of the atoms present in a compound.

Silicon is the most commonly used substrate for IR measurements, for variety of reasons. It is chemically very stable and generally not very reactive even at high temperatures. It is excellent for optical studies of deposited films in the visible region using reflection techniques. It does not have strong lattice absorption bands in the useful regions of the infrared and thus can be used for transmission studies in this region. To correct for the lattice absorption bands in silicon, a reference silicon sample is used as a reference. FTIR measurements of the films of nanoparticles in the present study were carried out in the diffuse reflectance mode at a resolution of 4 cm^{-1} on a Perkin-Elmer FTIR Spectrum One spectrophotometer.

2.7. LANGMUIR BLODGETT (LB) TECHNIQUE:

LB technique is one of the most promising techniques for preparing organic thin films [5] as it enables (a) the precise control of the monolayer thickness, (b) homogenous deposition of the monolayer over large areas on almost any kind of solid substrate and (c) the possibility to make multilayer structures with varying layer composition. For the work discussed in this thesis, LB technique has been extensively used to organize the hydrophobized Ni nanoparticles on the subphase of water and study their assembly by subsequent formation of monolayer and multilayer films on different substrates.

Langmuir films: Langmuir films consist of surface-active materials or ‘surfactants’ trapped at the interface between two dissimilar phases, either liquid-liquid or liquid-gas. Surfactants are molecules, which are amphiphilic in nature and consist of a hydrophilic (water soluble) and hydrophobic (water insoluble) part as explained in details in Chapter I. The hydrophobic part usually consists of hydrocarbon or fluorocarbon chains and the forces acting upon them are predominantly Van-der Waal's type ($1/r^{12}$ and $1/r^{6}$), while the hydrophilic part consists of a polar group (-OH, -COOH, $-NH_3^+$, $-PO_4^-(CH_2)_2NH_3^+$ etc.) and the forces acting upon them are predominantly coulomb type ($1/r^{2}$). Amphiphilic molecules are trapped at the interface because they possess two very different types of bonding with the two constituents of the interface. The driving force behind the association is the reduction of the free energy of the system. Therefore, when a surfactant comes in contact with water at the air-water interface it accumulates at the interface causing a decrease in the surface tension of water. Many of these amphiphilic molecules, insoluble in water, can (with the help of a volatile and water insoluble solvent) be easily spread on water surface with hydrophilic 'head' groups pulling the molecule into the bulk of the water and the hydrophobic 'tail' groups pointing into the air. One molecule thick surface monolayer will only be achieved if the amphiphatic balance (that is balance between hydrophilic and hydrophobic parts) of the molecule is correct. Sweeping a barrier over the water surface causes the molecules to come closer together and eventually form a compressed, ordered monolayer. The film produced by such a method is known as a Langmuir film.

Pressure-Area Isotherm (π-A isotherm): The most important indicator of the monolayer formation of an amphiphilic molecule is given by measuring the changes in surface tension upon compressing the monolayer. The reduction of surface tension is known as the surface pressure i.e. surface pressure is the lateral pressure that must be applied to prevent the film from spreading. Pressure readings are made by means of Wilhelmy plate attached to a microbalance. The plot of surface pressure versus area occupied per molecule is known as a 'pressure-area isotherm' – isotherm because compression takes place at constant temperature *(Figure 2.4)*.

The shape of isotherm is characteristic of the molecules making up the film and hence provides a two-dimensional 'fingerprint'. π-A isotherm gives information about the stability of the molecules in the two dimensional system, phase transitions and conformational transitions. It also gives some idea of the amount of pressure that has to be applied to the film on the sub phase, to enable deposition of the LB film in the solid-like phase. Thus at appropriate pressure, the film can be transferred to the substrate.

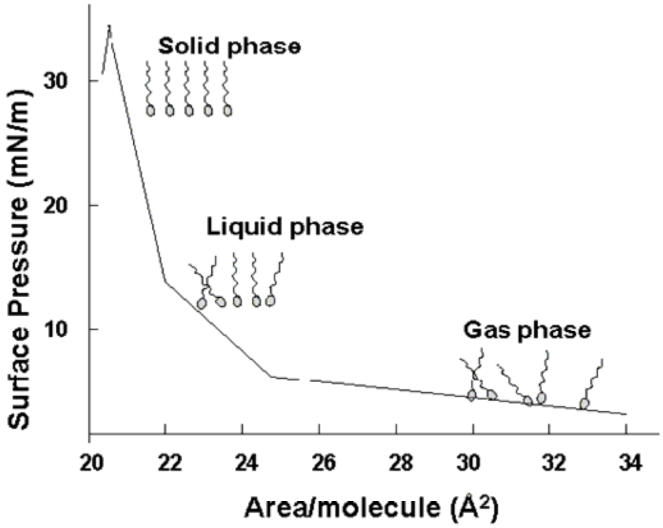

Figure 2.4. *A typical pressure area (π-A) isotherm showing the various phase transitions of the floating monolayer.*

Deposition of LB films: Langmuir film balance can also be used for building up highly organised multilayers of the amphiphile. This is accomplished by successively dipping a solid substrate up and down through the monolayer while simultaneously keeping the surface pressure constant by a computer controlled feedback system between the electrobalance measuring the surface pressure and the barrier moving mechanism. Consequently the floating monolayer is adsorbed to the solid substrate. In this way multilayer structures of hundreds of layers can be produced. These multilayer structures are commonly called Langmuir-Blodgett or simply LB films. The LB deposition is traditionally carried out in the 'solid' phase. The surface pressure is then high enough to ensure sufficient cohesion in the monolayer so that the monolayer does not fall apart during transfer to the solid substrate. This also ensures the build up of homogeneous multilayers. The surface pressure value that gives the best results depends on the nature of the monolayer. When the solid substrate is hydrophilic (glass, SiO_2 etc.) the first layer is deposited by raising the solid substrate from the subphase through the monolayer, whereas if the substrate is hydrophobic (HOPG, silanized SiO_2 etc.) the first layer is deposited by lowering the substrate into the subphase through the monolayer.

There are several parameters that affect on what type of LB film is produced. These are nature of the spread film, the subphase composition and temperature, the surface pressure during the deposition and the deposition speed, the type and nature of the solid substrate and the time the solid substrate is stored in air or in the subphase between the deposition cycles.

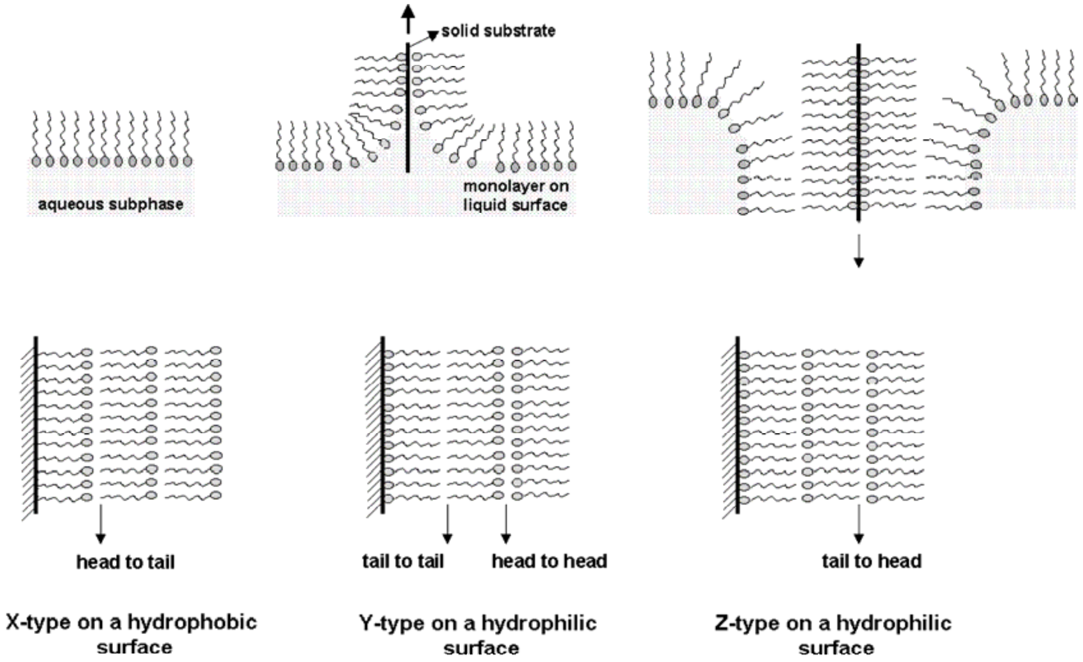

Figure 2.5. *A schematic showing different types of deposition of LB films [4].*

The quantity and the quality of the deposited monolayer on a solid support is measured by a transfer ratio, given by:

$$TR = \frac{area\ of\ monolayer\ removed\ from\ the\ subphase\ at\ particular\ pressure}{area\ of\ substrate\ immersed\ in\ water}$$

For ideal transfer the TR is 1. Different kind of LB multilayers can be produced and/or obtained by successive deposition of monolayers on the same substrate. The most common type is Y-type multilayer, which is produced when the monolayer deposits on the solid substrate in both upward and downward movement of the substrate. When the monolayer deposits only during upward or downward movement, the multilayer structure is called either Z-type or X-type *(Figure 2.5)*. An alternative way to deposit the monolayer is the Langmuir-Schaeffer (LS) technique. This technique differs from the vertical deposition technique described above only in the sense that the solid substrate is horizontally lowered in contact with the monolayer.

Nima LB trough Model 611 was used for the present work. The photograph of the setup is shown in the *Figure 2.6* below.

Figure 2.6. *Photograph of the Nima LB trough.*

Pressure–area (π–A) isotherms were recorded at room temperature as a function of time from spreading the monolayer at a compression and expansion rate of 100 cm^2/min. A standard Wilhelmy plate was used for surface pressure sensing. Multilayer films of the nanoparticles of different thickness were formed by the LB technique at a constant surface pressure and deposition rate of 20 mm/min with a waiting time of 180 s between dips on quartz slides, Si (111) wafers, gold-coated AT-cut quartz crystals and carbon-coated transmission electron microscopy (TEM) grids for UV–vis spectroscopy, Fourier transform infrared spectroscopy (FTIR), quartz crystal microgravimetry (QCM) and transmission electron microscopy measurements, respectively. The quartz and Si (111) substrates were hydrophobized by depositing three monolayers of lead arachidate prior to transfer of the nanoparticle monolayers. The hydrophobization of the support resulted in better transfer ratios of the nanoparticle monolayers. For the LB films grown on different substrates, monolayer transfer was observed both during the upward and downward strokes of the substrate at close to unity transfer ratio.

2.8. BREWSTER ANGLE MICROSCOPY (BAM):

Brewster Angle: Sir David Brewster, a Scottish physicist, in his studies on polarized light discovered that when light strikes a reflective surface at a certain angle, the light reflected from that surface is polarized into a single plane. This angle is commonly referred to as Brewster angle as shown in *Figure 2.7* [6]. When the beam arrives on the surface at this critical angle, the polarization degree of the reflected beam is 100 percent with the orientation of the electric vectors lying perpendicular to the plane of incidence and parallel to the reflected surface. The refracted ray is oriented at an angle of 90° from the reflected ray and is only partially polarized.

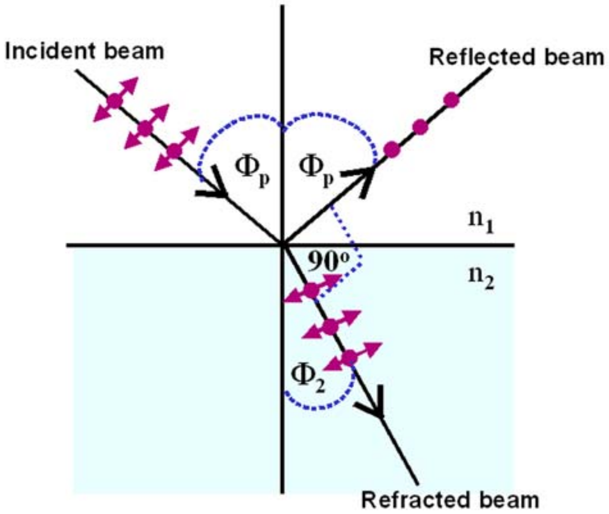

If μ is the refractive index, then, by Snell's law:

$$\frac{\eta_2}{\eta_1} = \mu = \frac{\sin\Phi_p}{\sin\Phi_2}$$

$$\mu = \frac{\sin\Phi_p}{\sin(90-\Phi_p)}$$

$$\mu = \frac{\sin\Phi_p}{\cos\Phi_p}$$

$$\Phi_p = \tan^{-1}\mu$$

Φ_p = Brewster Angle

Figure 2.7. *Generation of Brewster Angle (Φ_p) shown by the ray diagram.*

Brewster angle microscopy: The principle behind the Brewster Angle Microscope (BAM) makes use of the zero reflectance from an air-water interface or dielectric substrate for vertically linearly polarized light at the Brewster angle of incidence. Brewster angle is determined by the formula ($\Phi_p = \tan^{-1}\mu$) described above. For example, for air-water interface (refractive index of 1.333), air-glass interface (refractive index of 1.515), and air-diamond interface (refractive index of 2.417), the critical angles (Brewster angles) are 53, 57 and 67.5 respectively.

When a beam of plane polarized light is incident at air water interface at the Brewster angle ($\Phi_B = 53^o$) there will be no reflection from the surface making it appears black. But when a condensed phase of a monolayer with different refractive index is spread or deposited at the interface of interest, a measurable change in reflectivity will occur. The reflected light can then be used to form a high contrast image of the lateral morphology of the spread or deposited layer *(Figure 2.8)*. The microscopy is used in the thesis work for imaging hydrophobized Ni nanoparticles spread at air-water interface on a LB trough [6b].

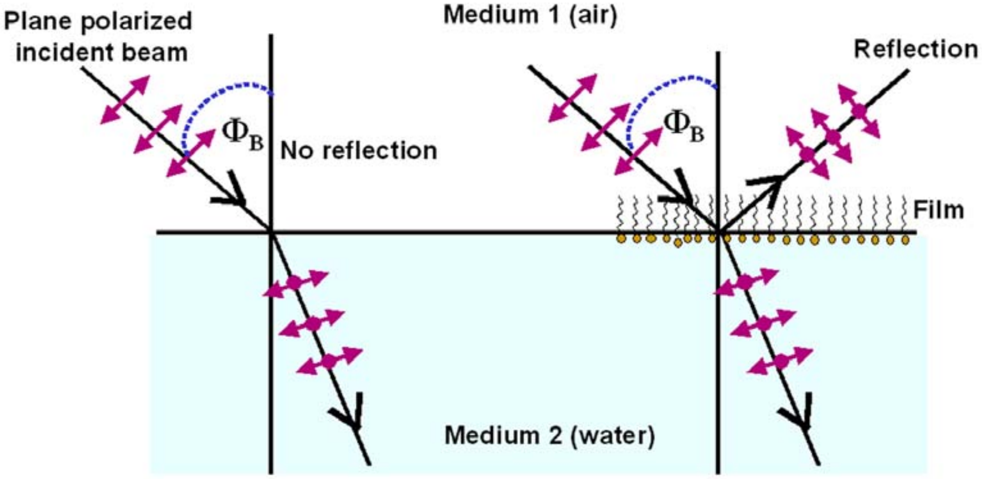

Figure 2.8. *Principle of Brewster Angle Microscopy.*

2.9. NUCLEAR MAGNETIC RESONANCE SPECTROSCOPY (^{1}H NMR):

Magnetic properties of nuclei: All atomic nuclei possess nuclear spin, I, which may be integral (i.e. 1, 2, 3 etc.) or half integral (i.e 1/2, 3/2, 5/2 etc.) Since nucleus possesses an electric charge, the spinning nucleus gives rise to a magnetic field whose axis coincides with the axis of spin. Thus each nucleus can be thought of being equivalent to a minute magnet having magnetic moment μ. Each nucleus with $I > 0$ has magnetic moment. If a magnetic nucleus is placed in a uniform magnetic field, it is found that the magnetic dipole assumes only a discrete set of orientations. The system is said to be quantized. The magnetic nucleus may assume any one of $(2I + 1)$ orientations with respect to the direction of the applied magnetic field. Thus, a proton ($I = ½$) will be able to assume only one of two possible orientations that correspond to energy levels of $\pm \mu H$ in a applied magnetic field, where H is the strength of the external magnetic field. The transition of a proton from one possible orientation to another may be affected by the absorption or emission of a discrete amount of energy such that

$$E = h\nu = 2\mu H,$$

where ν is the frequency of electromagnetic radiation absorbed or emitted.

Unless the axis of the nuclear magnet is oriented exactly parallel or antiparallel with the applied magnetic field, there will be a certain force by the external field to orient it likewise. But because the nucleus is spinning, the effect is that its rotational axis draws out a circle perpendicular to the applied field. This motion of nucleus is called precessional motion and is of exceptional importance in the nuclear resonance phenomenon [4].

***Theory of nuclear resonance*:** The precessional frequency of the spinning nucleus is exactly equal to the frequency of electromagnetic radiation necessary to induce a transition from one nuclear spin state to another. The nucler transition corresponds to a change in the angle that the axis of the nuclear magnet makes with the applied magnetic field. This change can be brought about through the application of electromagnetic radiation whose magnetic vector component is rotating in a plane perpendicular to the main magnetic field. When the frequency of the rotating magnetic field and the frequency of the precessing nucleus become equal, they are said to be in resonance, and absorption or emission of energy by the nucleus can occur [4].

Chemical shift: If the resonance frequencies for all protons in a molecule were the same, the nuclear resonance technique would be of little use and one would observe only one peak for a compound, regardless of number or nature of protons present. The utility of the nuclear resonance phenomenon depends on the fact that nuclear magnetic resonane frequencies are to a small degree dependent on the molecular environment of the nucleus. The surrounding electrons shield the nucleus, so the effective magnetic field felt by the nucleus is not quite the same as the applied field. Electronic shielding arises from an induced circulation of electrons about a nucleus. These circulations are induced by the applied field and are in a plane perpendicular to the applied magnetic field. They produce a magnetic field that, in the region of the nucleus, is usually in a direction opposed to the direction of the applied field. The magnitude of the induced field is directly proportional to the magnitude of the applied field. The effective magnetic field experienced by the nucleus is changed by this small local field such that

$$H_{eff} = H_0 - \sigma H_0$$

where, σH_0 is the induced field owing to electronic circulations. Protons in different environments are shielded by the circulations of surrounding electrons to different extents. Hence, different values of σH_0 are obtained, each dependent on the magnitude of the applied field H_0 for different protons. Because the strength of the applied magnetic field cannot be determined to the required degree of accuracy, the absolute position of absorption cannot be obtained directly from the instrument. However relative proton frequencies can readily be determined. The separation of resonance frequencies of nuclei in different structural environments from some arbitrarily chosen standard is termed as chemical shift [4].

Proton NMR spectra of the samples in D_2O solutions in the current study were recorded on a Bruker AC 200 MHz instrument and scanned in the range 0–15 ppm.

2.10. CONTACT ANGLE MEASUREMENTS:

Definition: Contact angle, θ, is a quantitative measure of the wetting of a solid by a liquid. It is defined geometrically as the angle formed by a liquid at the three phase boundary where a liquid, gas and solid intersect as shown in *Figure 2.9*. It can be seen from this figure that low values of θ indicate that the liquid spreads on the solid substrate, or wets well, while high values indicate poor wetting. If the angle θ is less than 90 the liquid is said to wet the solid. If it is greater than 90 it is said to be non-wetting. A zero contact angle represents complete wetting [5].

Measurement of contact angle: Two different approaches are commonly used to measure contact angles of non-porous solids, goniometry and tensiometry. Goniometry involves the observation of a sessile drop of test liquid on a solid substrate. Tensiometry involves measuring the forces of interaction as a solid is contacted with a test liquid.

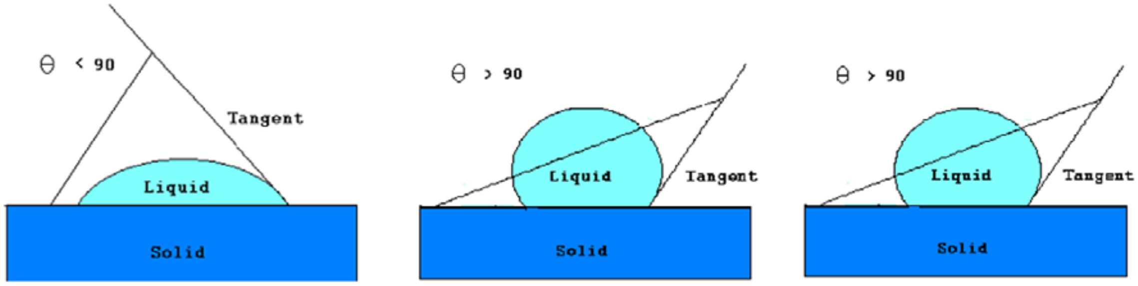

Figure 2.9. *Schematic showing the different contact angles of a liquid drops on solid substrate.*

Goniometry: Analysis of the shape of a drop of test liquid placed on a solid is the basis for goniometry. The basic elements of a goniometer include a light source, sample stage, lens and image capture. Contact angle can be assessed directly by measuring the angle formed between the solid and the tangent drawn to the drop surface. Goniometry can be used in many situations where tensiometry cannot. One can use a great variety of solid substrates provided they have a relatively flat portion for testing and can fit on the stage of the instrument. Substrates with regular curvature, such as contact lenses are also easily analyzed. Testing can be done using very small quantities of liquid. It is also easy to test high temperature liquids such as polymer melts [5].

In the present study contact angle measurements of a sessile water drop (1 μL) were carried out on the nanoparticle multilayer films deposited on quartz substrates using a Rame-Hart 100 goniometer.

2.11. X-RAY PHOTOELECTRON SPECTROSCOPY (XPS):

X-ray Photoelectron Spectroscopy known as XPS has been developed from the fifties by Professor K. Siegbahn for which he was awarded the Physics Nobel Prize in 1981 [7a]. XPS is surface science technique used to study the composition and electronic state of the surface region of a sample. Since, the technique provides a quantitative analysis of the surface composition is sometimes known by the alternative acronym, ESCA (**E**lectron **S**pectroscopy for **C**hemical **A**nalysis).

Working Principle: XPS is based on well-known photoelectric effect (a single photon in/electron out process) first explained by Einstein in 1905. Photoelectron spectroscopy uses monochromatic sources of radiation (i.e. photons of fixed energy given by relation, $E = h\nu$). In XPS the photon is absorbed by an atom in a molecule or solid, leading to ionization and the emission of a core (inner shell) electron. The kinetic energy distribution of the emitted photoelectrons (i.e. the number of emitted photoelectrons as a function of their kinetic energy) can be measured using any appropriate electron energy analyzer and a photoelectron spectrum can thus be recorded [7b]. One way to look at the overall process of photoionization is follows :

$$\mathbf{A} + h\nu = \mathbf{A}^{+} + \mathbf{e}^{-}$$

Conservation of energy then requires that:

$$\mathbf{E(A)} + h\nu = \mathbf{E(A^{+})} + \mathbf{E(e^{-})}$$

Since the electron's energy is present solely as kinetic energy (KE) this can be rearranged to give the following expression for the KE of the photoelectron:

$$\mathbf{KE} = h\nu - (\mathbf{E(A^{+})} - \mathbf{E(A)})$$

The final term in brackets, representing the difference in energy between the ionized and neutral atoms and is generally called the binding energy (BE) of the electron. This then leads to the following commonly quoted equation:

$$\mathbf{KE} = h\nu - \mathbf{BE}$$

the binding energies (BE) of energy levels in solids are conventionally measured with respect to the Fermi-level of the solid, rather than the vacuum level. This involves a small correction to the equation given above in order to account for the work function (φ) of the solid,

$$\mathbf{KE} = h\nu - \mathbf{BE} - \varphi$$

Employing photons with fixed energy *hν*, it is obvious that if kinetic energy KE and work function φ of the sample are measured, it is possible to measure binding energy of electron in solid. The picture becomes more evident from the cartoon in *Figure 2.10.*

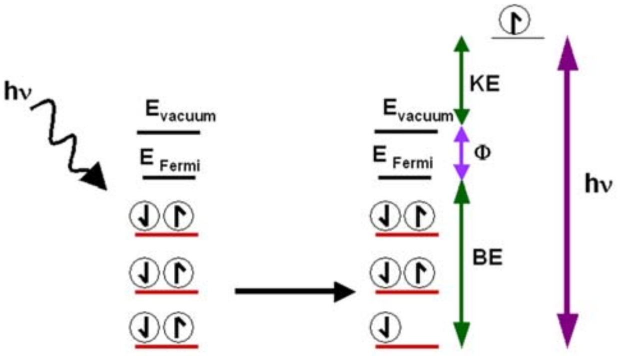

Figure 2.10. *Principle of X-ray photoelectron spectroscopy.*

Binding energies being characteristic of atoms, different elements present in the sample under investigation are identified. Electrons traveling through a material have a relatively high probability of experiencing inelastic collisions with locally bound electrons as a result of which they suffer energy loss and contribute to the background of the spectrum rather than a specific peak. Due to inelastic scattering process, the flux of photoelectrons emerging from the sample is much attenuated. Generally electrons from penultimate shell of an atom are knocked out by X-rays for characterization purpose. A closer look at the spectra from the core levels of *p, d and f levels* (example Co 2p, Ag 3d or Au 4f) shows the presence of a photoemission doublet. The reason for the formation of the doublet is the mixing of the spin and the angular momentum, commonly known as the spin-orbit coupling, it can be the Russell- Saunders (*l-s*) coupling or the *j-j* coupling. For example since the value of *l* for d orbital is 2 hence the coupling will result in the *j value of* 5/2 (2+1/2) and 3/2 (2-1/2). Thus there will be 2 states of $d_{5/2}$ and $d_{3/2}$, the intensity of which depends on the multiplicity.

$$\text{Multiplicity} = 2j+1$$

Hence, for $d_{5/2}$, multiplicity = 2*(5/2)+1= 6 and for $d_{3/2}$, multiplicity = 2*(3/2)+1= 4 and the ratio of the intensities of the peak will be 6:4 or 1.5:1.

Same is true for other orbitals too. Routinely used X-ray sources are Mg Kα (hγ = 1253.6 eV), Al Kα (hγ = 1486.3 eV). The overall resolution was ~1 eV for XPS measurements. The core level spectra were background corrected using the Shirley algorithm [7c] and the chemically distinct species resolved using a non-linear least squares fitting procedure. The core level binding energies (BE) were aligned with the adventitious carbon binding energy of 285 eV.

Instrumentation: In contrast to the valence electrons, which are delocalized in molecules and condensed matter, the core electrons are localized, that is, they are atomic like in all matter. Therefore, the electron binding energy associated with a given orbital is essentially the same; independent of which system the atom happens to be a part of. X-rays illuminate an area of a sample causing electrons to be ejected with a range of energies and directions [7d]. The electron optics, which may be a set of electrostatic and/or magnetic lens units, collect a proportion of these emitted electrons defined by those rays that can be transferred through the apertures and focused onto the analyzer entrance slit. Electrostatic fields within the hemispherical analyzer (HSA) are established to allow electrons of a given energy (Pass Energy) to arrive at the detector slits and onto the detectors themselves.

A hemispherical analyzer and transfer lenses can be operated commonly in the mode called Fixed Analyzer Transmission (FAT), also known as Constant Analyzer Energy (CAE), or Fix Retard Ratio (FRR) also known as Constant Retard Ratio (CRR). In FAT mode, the pass energy of the analyzer is held at a constant value and it is entirely the job of the transfer lens system to retard the given kinetic energy channel to the range accepted by the analyzer. Most XPS spectra are acquired using FAT. A way of measuring the kinetic energy of the photoelectrons is to let them pass through a spherically symmetric field that is created between two hemispherical electrodes. In this field, electrons with different energies will follow paths with different radii, that is, the electrons are energy dispersed and an energy spectrum can be recorded [7d].

For the work described in this thesis, the X-ray photoelectron spectra of samples were recorded on a VG Microtech ESCA 3000 instrument at a base pressure better than 1×10^{-9} Torr with un-monochromatized Mg Kα radiation (1253.6 eV energy). The measurements were made in the constant analyzer energy (CAE) mode at a pass energy of 50 eV and electron takeoff angle (angle between electron emission direction and surface plane) of 60°. This leads to an overall resolution of ~ 1 eV in the measurements. The chemically distinct components in the core level spectra were resolved by a nonlinear least squares fitting algorithm after background removal by the Shirley method [9]. The core level binding energies (BE) were aligned with the adventitious carbon binding energy of 285 eV. The Samples were prepared by drop-coating the solution on Si (111) substrate.

2.12. THERMAL DEPOSITION OF ORGANIC THIN FILMS:

Thermally evaporated stearic acid (STA) thin films used for the entrapment of different metal ions inside the stacked bilayers of the lipids, have been deposited using Edwards E306 coating unit. The coating unit consists of a rotary pump used for backing and roughing the chamber where deposition is done and can produce a vacuum upto 10^{-3} Torr. Below this pressure, oil diffusion pump is employed to produce high vacuum of 10^{-7} Torr [8] and the deposition rate was 10 Å /min. Both these pumps are used in conjunction for backing and roughing of the deposition chamber. A liquid nitrogen trap was also used. Deposition of organic thin films is done under vacuum due to the following reasons: 1) The quality of deposition is better due to the increased mean free path of a molecule under vacuum as compared to atmosphere, resulting in a linear trajectory of the thermally evaporated molecule. 2) The melting point of fatty acids is reduced under vacuum, enabling low current requirements for thermal evaporation. The fatty acid (amphiphilic molecules) used for deposition, was taken in a molybdenum boat and subjected to low tension DC of about 20 amps under 10^{-7} Torr vacuum and heated. The substrates such as Si(111), glass and quartz were kept at a suitable distance above the molybdenum boat. The molecules when heated evaporated and condensed onto these substrates giving nearly uniform thickness of the uniform films on each substrate. The rate of deposition and the thickness of the lipid films was monitored in-situ using Edwards FTM5 quartz crystal microbalance. The films were tested for stability by using infrared spectroscopy, and it was found that the films did not decompose on deposition in vacuum.

2.13. ATOMIC ABSORPTION SPECTROSCOPY (AAS):

Atomic absorption spectroscopy (AAS) is one of the common chemical analyses methods for qualitative and quantitative determination of sample composition. We have used AAS, in order to estimate the amount of metal ions present in the samples.

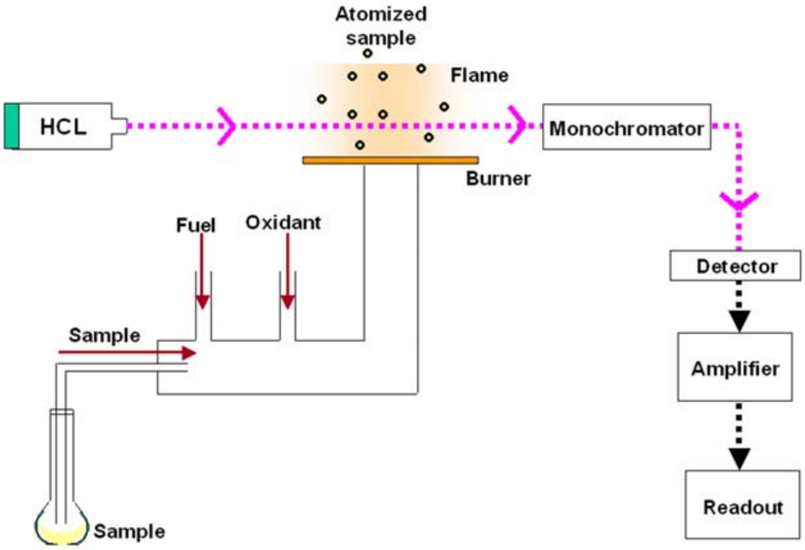

Figure 2.11. *The experimental set-up of AAS [9].*

Operating principles: The main parts of the AAS system are a hollow cathode lamp, nebulizer, air/acetylene flame, and optical system [9]. The jobs of each are detailed below:

The hollow cathode lamp (HCL) uses a cathode made of the element of interest with a low internal pressure of an inert gas. A low electrical current (~ 10 mA) is imposed in such a way that the metal is excited and emits a few spectral lines characteristic of that element. The light is emitted directionally through the lamp's window, made of a glass transparent in the UV and visible wavelengths. It provides the analytical light line for the element of interest. The nebulizer chamber suck up liquid sample at a controlled rate and create a fine aerosol for introduction into the flame. The nebulizer mix the aerosol and fuel and oxidant thoroughly for introduction into the flame. The flame destroys any analyte ions and breakdown complexes create atoms (the elemental form) of the element of interest. The atoms absorb the characteristic ultraviolet or visible light from the source and make transitions to higher electronic energy levels. The analyte concentration is determined from the amount of absorption. Applying the Concentration measurements are usually determined from a working curve after calibrating the instrument with standards of known concentration. The monochromator isolate analytical lines' photons passing through the flame. It also removes scattered light of other wavelengths from the flame. In doing this, only a narrow spectral line impinges on the photomultiplier tube (PMT). As a detector, PMT determines the intensity of photons of the analytical line exiting the monochromator [9].

2.14. THERMO GRAVIMETRIC ANALYSIS (TGA):

Thermal analysis includes a group of techniques in which a physical property of a substance is measured as a function of temperature while the substance is subjected to a controlled temperature program. Thermogravimetry provides a quantitative measurement of any weight change associated with a transition and the photograph of the instrument along with the working principle is pictorially represented in *Figure 2.12* [10].

For TGA, the sample is continuously weighed as it is heated to elevated temperatures. Samples are placed in a crucible or shallow dish that is attached to an automatic recording balance. The automatic null-type balance incorporates a sensing element, which detects a deviation of the balance beam from its null position. Once an initial balance has been established, any changes in sample weight cause the balance to rotate. This moves the flag so that the light falling on each photocell is no longer equal. The resulting nonzero signal is amplified and fed back as a current to a taut-band torque motor to restore the balance to equilibrium. This current is proportional to the weight change and is recorded on the y-axis of the recorder. The sample container is mounted inside a quartz or pyrex housing which is located inside the furnace. Furnace temperature is continuously monitored by a thermocouple whose signal is applied to the x-axis of the recorder. Linear heating rates from 5 ^{o}C/min to 100 ^{o}C/min are generally employed in the temperature range of room temperature to 1000 ^{o}C.

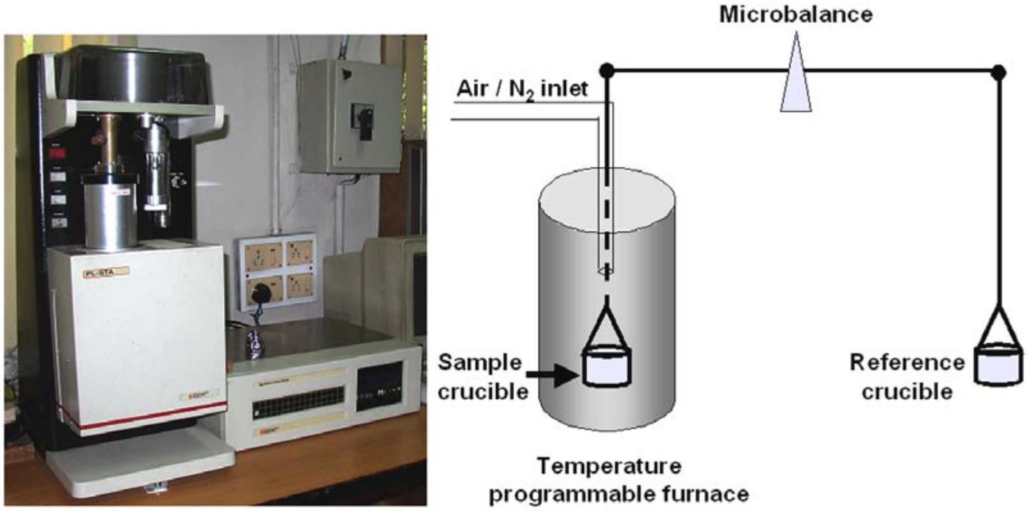

Figure 2.12. *The actual photograph of TGA instrument along with the pictorial representation [10].*

All TGA measurements of the nanoparticle samples in the form of purified powders were recorded on a Seiko instruments model TG / DTA 32 instrument at a heating rate of 10 ^{o}C per minute.

2.15. VIBRATING SAMPLE MAGNETOMETER (VSM):

The VMS, first developed by Foner in the late 1950s, is a basic research tool for determining magnetic properties in a variety of studies of the structure of paramagnetic, ferromagnetic, antiferromagnetic, diamagnetic and ferrimagnetic materials. If any material is placed in a uniform magnetic field, a dipole moment will be induced in the sample proportional to the product of the sample susceptibility and the applied field. If the sample is made to undergo sinusoidal motion, the resulting magnetic flux changes near the sample will induce an electrical signal in suitably placed stationary coils. This signal will be proportional to the moment, amplitude, and frequency of vibration [11].

Figure 2.13 shows a typical VSM setup. The material under study in the VSM is inserted in the sample holder so that it rests centered in a pair of pickup coils between the poles of an electro magnet. The sample holder is mounted using a sample rod in a transducer assembly, which passes through the center of a driving coil. The transducer is driven by a power amplifier which itself is driven by an oscillator. The magnetic sample under study is constraint to vibrate only along the vertical axis. As it does so, it induces a signal in the sample pickup coils as described above. The magnitude of this signal is dependent on the magnetic properties of the sample itself.

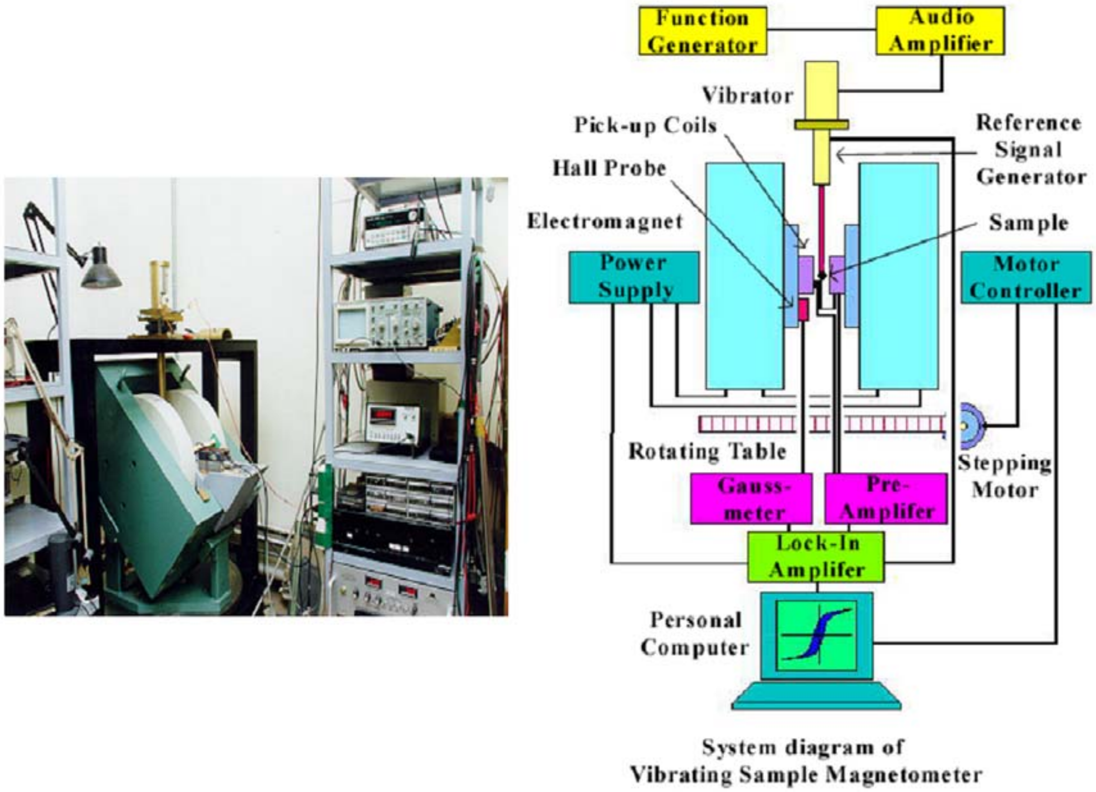

Figure 2.13. *The actual photograph of VSM instrument along with the pictorial representation [11b].*

Attached to the sample holder rod is a permanent magnet. A pair of stationary coils pick up the induced ac signal, which is proportional to the amplitude and frequency of the vibration and is used as a control signal for modulation of the transducer. The output of the sample coil is fed to the differential input of a lock-in amplifier. The reference input of the lock-in comes from the sine wave oscillator used to drive the sample holder. The output of the lock-in goes to the data acquisition computer as well as the magnitude of the applied magnetic field coming from a gaussmeter. The signal from the lock-in amplifier is directly proportional to the magnetic moment of the sample. The computer is now able to graph the magnetic moment of the sample against the applied magnetic field [11].

2.16. SUPERCONDUCTING QUANTUM INTERFERENCE DEVICE (SQUID):

In ordinary quantum mechanics it is well known that a particle can tunnel through a potential barrier. In 1962 Josephson showed that a similar process is also possible for a superconductor. Here the Cooper pairs as described by the BCS theory (pairs of electrons that can carry a current in a superconductor without resistance) can tunnel through a weak link or Josephson junction. This is a thin (< 30 Angstrom) layer of insulator between two superconducting layers [12]. The photograph of SQUID magnetometer and the pictorial representation of the configuration of the dc SQUID is schematically shown in *Figure 2.14A and B* respectively.

It consists of a superconducting ring biased with a current I. An external magnetic field $H=B/\mu_0$ is applied to the loop. A Josephson junction is incorporated into each of the two arms of the dc SQUID named as X and W in *Figure 2.14B*. The Josephson junctions limit the maximum supercurrent I_c that can flow across the ring to a maximum value given by the sum of the critical currents of the two junctions. The magnetic flux enclosed inside the SQUID ring modulates I_c periodically. This modulation, caused by an interference of the superconducting wave functions in the two SQUID arms, forms the basis of the working principle of the dc SQUID. The direct way to detect this modulation is to read out I_c directly, e.g. by increasing the bias current at fixed magnetic field until a nonzero dc voltage develops across the junctions. The external field also causes the critical currents of the two Josephson junctions to modulate. Since, however, the area of the SQUID loop is usually much larger than the area of the junctions this modulation occurs on a field scale much larger than the modulation period of Ic. It thus can be ignored in most practical cases.

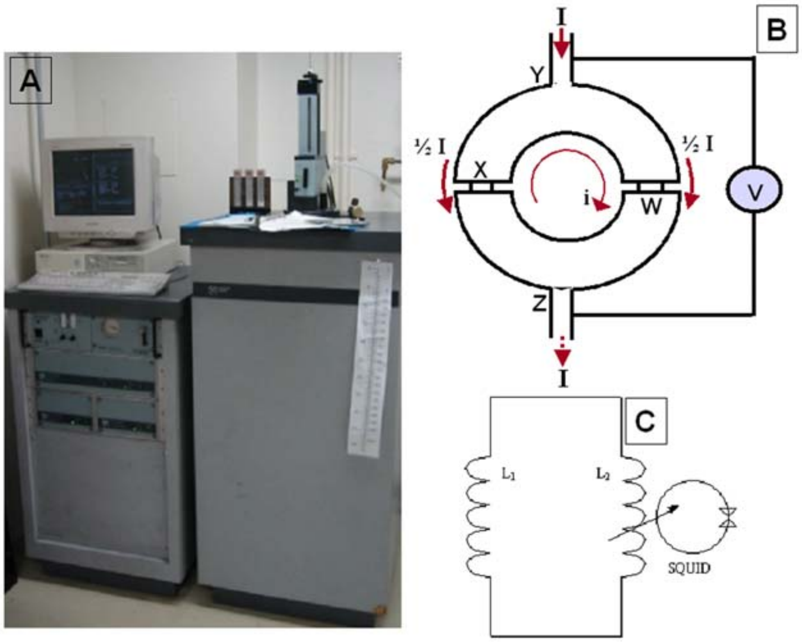

Figure 2.14. *(A) Photograph of SQUID magnetometer. (B) Construction of SQUID. (C) Construction of SQUID magnetometer.*

The system for magnetic measurement comprises of two main sections: the dewar, probe and SQUID assembly, and the electronic control system. The probe contains a high precision temperature control system, allowing measurements between 1.9 K and 400 K with an accuracy of 0.01 K and superconducting electromagnet, giving a field of up to 50 kG with an accuracy up to 0.1 G. The dewar consists of an inner liquid helium reservoir and outer liquid nitrogen jacket, to reduce excessive liquid helium boil off. The liquid helium is used both for maintaining the electromagnet in a superconducting state and for cooling the sample space. In practice measurements are obtained by linking the SQUID to a flux transformer. Such a circuit consists of some type of pick-up coil, configured approximately 3 cm in length, linked to a secondary coil, which in turn is closely connected to the SQUID loop. Samples are mounted within a plastic straw and connected to one end of a sample rod, which is inserted into the dewar/probe. The other end is attached to a stepper motor, which is used to position the sample within the center of the SQUID pickup coils. The close proximity of the sample with the SQUID leads to a very efficient and direct flux coupling. The pick-up coil is placed in the field to be measured, causing a field to be set up by the secondary coil, which in turn is detected by the SQUID [12].

2.17. ELECTRON SPIN RESONANCE SPECTROSCOPY (ESR):

Electrons generally occupy electronic shells in atoms as pairs. In such pairs the electrons have their spins anti parallel to each other, so the associated magnetic fields cancel. In some ions, free radicals or paramagnetic materials, however, a single electron may occupy an orbital. When the molecules of a solid exhibit paramagnetism as a result of unpaired electron transitions can be induced between spin states by applying a magnetic field and then supplying electromagnetic energy, usually in the microwave range of frequencies. The resulting absorption spectra are described as electron spin resonance (ESR) or electron paramagnetic resonance (EPR) [13, 4 a]. The interaction of an external magnetic field with an electron spin depends upon the magnetic moment associated with the spin, and the nature of an isolated electron spin is such that two and only two orientations are possible. The application of the magnetic field then provides a magnetic potential energy, which splits the spin states by an amount proportional to the magnetic field (Zeeman effect), and then radio frequency radiation ($3X10^6$ - $3X10^{10}$ Hz) can cause a transition from one spin state to the other. The energy associated is given by the formula

$$\Delta E = g\ \mu_B\ B$$

where B is the applied magnetic field, g is Lande splitting factor and μ_B is called the Bohr magneton.

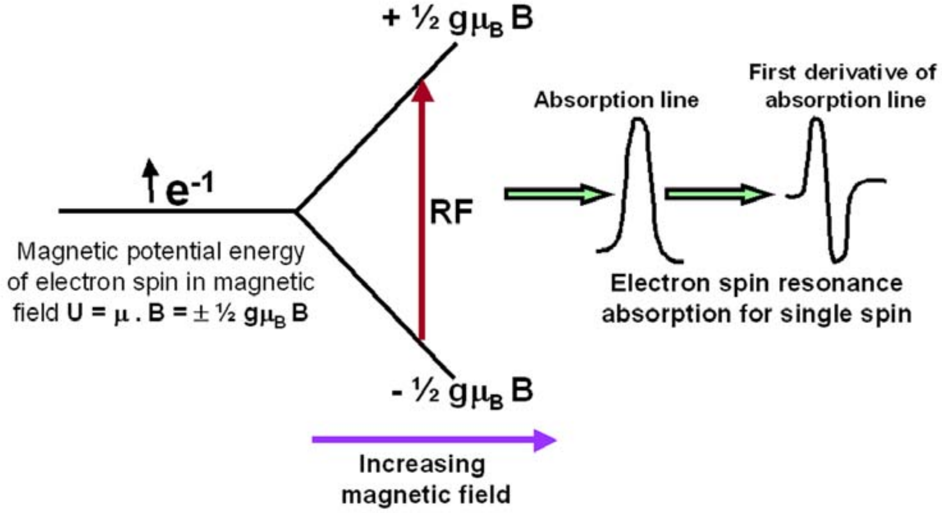

Figure 2.15. Pictorial representation of the principle of ESR.

If the radio frequency excitation was supplied by a klystron at 20 GHz, the magnetic field required for resonance would be 0.71 Tesla, a sizable magnetic field typically supplied by a large laboratory magnet. The principle is schematically shown in the *Figure 2.15.* If the system contains a single spin, then ESR would always consist of just one line and would have little value as an investigative tool, but several factors influence the effective value of g in different settings. Most of the information obtained from ESR comes from the splittings caused by interactions with nuclear spins in the vicinity of the unpaired spin, splittings called nuclear hyperfine structure.

Ferromagnetic resonance (FMR) i.e. resonant absorption of external electromagnetic radiation in ferromagnetic substances is one of the youngest brance of physics. In ferromagnetic substances due to the presence of internal field, we need certain effective field for the resonant frequency instead of simple externally applied field. This makes the measurement complicated as we may not know the effective field beforehand [14]. Valuable information can be gathered considering the line shape and width as explained in the subsequent chapters.

The samples were prepared in powder form for the measurements and the ferromagnetic resonance spectra of the samples were obtained using a conventional X-band ESR spectrometer (JEOL JES-TE20) at room temperature, where the magnetic field and microwave frequency were calibrated using a NMR gaussmeter and a frequency counter, respectively.

2.18. References

[1]. (a) Denney, R.C; Sinclair, R. *Visible and Ultraviolet Spectroscopy Analytical Chemistry by open learning series*, John Wiley and Sons, USA. (b) Wang, Z. L. Ed. *Characterization of nanophase materials*, Wiley-VCH, Weinheim, **2000**. (c) Willard, H. H.; Merritt, L. L.; dean, J. A. *Instrumental methods of analysis*, D van Nostrad Publications, Torranto, **1951.** (d) bouman.chem.georgetown.edu/.../spectrometer.htm

[2]. Cullity, B. D.; Stock, S. R. *Elements of X-Ray Diffraction* (Third Edition), **2001.**

[3]. http://www.matter.org.uk/tem/

[4]. (a) Banwell, C. N.; McCash, E. M. *Fundamentals of Molecular Spectroscopy* Fourth edition ed. Tata Mc-Graw-Hill Publishing Company limited, **1994**. (b) Silverstein, R.;

Bassler, G.; Morrill, T. *Spectrometric Identification of Organic Compounds*, Wiley, New York, **1981.**

[5]. Ulman, A. *An introduction to Ultrathin Organic Films: from Langmuir-Blodgett to Self-Assembly*, Academic Press, San Diego, CA, **1991**.

[6]. (a) http://en.wikipedia.org/wiki/Brewster's_angle

(b) http://www.gk689.uni-essen.de/stipendiaten/andreivassiliev/research.html

[7]. (a) Siegbahn, K.; Nordling, C.; Fahlman, A.; Hamrin, K. H. J.; Ndberg, R.; Johansson, C.; Bergmark, T.; Karlsson, S-E.; Lindgren, I.; Lindberg, B. *Nova Acta Regiae Soc. Sci. Upsal.. Ser. IV* **1967**, *20*, 1. (b) Wagner, C. D.; Riggs, W. M.; Davis, L. E.; Moulder, J. F.; Muilenberg, G. E. *Handbook of X-ray photoelectron spectroscopy, Perkin Elmer Corp. Publishers, Eden Prairie, MN*, **1979.** (c) Shirley, D. A. *Phys. Rev. B* **1972**, 5, 4709. (d) http://www.iopb.res.in/~dipakpk/IOP_XPS.html

[8]. Maissel, L. I.; Glang, R. *Handbook of thin film technology*, McGraw Hill Book Company, NewYork, **1970**.

[9]. (a) www.thebritishmuseum.ac.uk/.../sr-tech-aas.html (b) Notes written by Chasteen, T. G. Department of Chemistry, Sam Houston State University, Huntsville, Texas 77341. Copyright **2000**. (c) http://elchem.kaist.ac.kr/vt/chem-ed/spec/atomic/aa.htm

[10]. http://www.bolton.ac.uk/fire/Thermana.htm

[11]. (a) http://members.aol.com/RudyHeld/publications/unpublished/VSM/vsm.htm

(b) http://cnsm.kaist.ac.kr/vsm.html

[12]. (a) http://www.cmp.liv.ac.uk/frink/thesis/thesis/node3.html

(b) http://homepages.nildram.co.uk/~phekda/richdawe/squid/technical/part4.html

(c) Clarke, J.; Braginski, A. I. *SQUID Handbook*, Berlin: Wiley VCH, **2004**.

[13]. http://hyperphysics.phy-astr.gsu.edu/hbase/molecule/esr.html

[14]. Vonsovskii, S. V. *Ferromagnetic Resonance, Chapter I: Magnetic Resonance In ferromagnetics,* Pergamon press, Oxford, **1966**.

Chapter III

Interaction of different metal ions with the carboxylic acid group: verification of experimental observations by quantitative approach

---

It has been observed that there is considerable variation in the binding capacity of various metal cations when complexed with arachidic acid layers. The intake of cations when estimated conferred certain trend which was not really dependent on the charge to volume ratio of the cations chosen. The earlier experiments dealing with the competitive binding between Cd^{2+} and Pb^{2+} ions with –COOH group has shown that lead ions interact more strongly which seems to be exceptional considering the volume of the two cations. So the system needs detailed study to understand the real nature of interaction and the factors on which it depends. Again, ligands containing –COOH groups are also preferred as the capping agents for different nanomaterials like magnetic metallic nanoparticles (e.g. Co, Ni etc.) or magnetic oxides, ferrites or even for silver nanoparticles. Knowledge of this interaction can trigger a range of application in case of nanoparticle-based products. An effort was made here to understand the discrepancy by invoking theoretical models based on first principle density functional calculations. The results suggest that the trends in binding strength largely depend on the ground state geometries of the metal diacetates.

Part of the work presented in this chapter has been communicated:
(1) Bala, T.; Prasad, B. L. V.; Sastry, M.; Upadhyay Kahaly, M.; Waghmare, U. V. *J. Phys. Chem. B* **2006** (communicated)

3.1. INTRODUCTION:

The co-ordination properties of different organic molecules with different class of substrate have significant impact in many fields starting from biological systems, to many industrial products, to environmental processes. Among such interactions, complexation of different metal ions with a long chain organic molecule having a functional head group can be of enormous importance for biological and technological applications [1-16]. Cations are well known for their predilection to interact with various materials starting from lipid layers [1], polymers [2], surfactants [3], bolaamphiphiles [4] or even with certain enzymes of bacteria [5] through ionic, covalent or ion-dipole interactions and each of them can be explicitly used for a range of applications. For instance, the interaction of polycarboxylates with metal ions is utilized in waste-water treatment for the selective removal of toxic metal ions [6,7], which is a frontier area of research in environmental chemistry. The adsorption behavior of metal ions on functionalized activated charcoal is dependent on a similar kind of interaction and has great technological value [8], particularly again in the field of environmental science and catalysis. Transition metal and organic polymer complexes could be exploited for the preparation of smart catalysts that are highly reactive as well as possess long life with the advantage of easy separation [9]. The study of the carbohydrate-metal ion interaction plays a key role in many biochemical processes and remains one of the main objectives of carbohydrate co-ordination chemistry [10]. The negatively charged phosphate group of DNA binds with different metal ions with different strengths. Detailed studies of these interactions have revealed many important biological aspects [11].

Similarly, the -COOH group plays an important role in all biological systems as all proteins contain this group. There has been renewed interest in the study of metal ion -COOH interaction not only for their potential application but also for the detailed understanding of the basic physics and chemistry involved in it [12]. For example, the binding of Ca^{2+} ions with $–COO^-$ group of proteins can influence many biological processes like blood clotting [13], nerve cell transmission etc [14]. Dicarboxylic acid as chelating ligands controls the oxidation state of transition metal ions like Fe^{2+} and builds the skeleton of inorganic framework both as a part of the oxide sheet and pillars between layers [15]. Carboxylic acid binding to metal ions becomes imperative when nanoparticles are synthesized in a thermally evaporated fatty acid thin film by incorporating metal ions into the acid bilayers [16]. Basically the stability of the nanoparticles thus formed is vastly contributed from the interaction of the two [16]. In fact, thin films can also be exploited for the synthesis of bimetallic alloys and the strength of metal-carboxylic acid bond will play a crucial role in tailoring the amount of incorporated metal cations in the film, which in turn is the key to determine the composition of the alloy formed. It has already been witnessed that the insertion chemistry of cations into thin film is much more complex and considering simple electrostatic interaction between the two depending on their charge to size ratio fails to explain many of the observations made [17]. Hence the exact estimation of the cation-carboxylic acid bond strength is not just of theoretical interest but also very important for the commercialization of nanoparticle based products. Ordered supramolecular architectures that are generally achieved at the air/water interface through the combination of metal ions with polymers or polycarboxylate monolayer is the result of the metal ion-carboxylic acid interaction [18]. In this case also, if the subphase contains 1:1 mixture of various cations, the amount of different cations binding to the carboxylate monolayer never reflects the same composition that is present in the subphase. It has been observed from the earlier work of Sastry and co-workers that the competitive binding of different cations like Pb and Cd with arachidic acid monolayer using the Langmuir-Blodgett technique leads to higher binding of Pb^{2+} than Cd^{2+} [19] though the size of Pb^{2+} is bigger than Cd^{2+}. At that time, the result was, qualitatively, allied to the complex equilibrium in the immersed phase between the Pb^{2+}, Cd^{2+} and H^+ ions in the interlamellar regions and the solution phase [19] but a convincing explanation is still lacking. So in order to realize a desired composition of metal cations within the monolayer in such complicated systems we need to know the binding capacity of the cations with the –COOH group very precisely i.e. quantitatively.

Apart from these examples, the carboxylic acid group is in use as a stabilizing agent in the field of nanotechnology. Magnetic nanoparticles like Co [20a-c] or Ni are very prone to aerial oxidation, but addition of long chain carboxylic acids can alter the scenario altogether. It is discussed in details in Chapter IV. Such fatty acids can restrict the surface layer oxidation to a large extent and help in the generation of stable magnetic nanoparticles which can be stored for long time either in solution or as solid powder. The unique role played by the carboxylic head group of long chain organic molecules is detailed in Chapter IV. It is well known that the nanoparticles' surface is charged and thus it is also obvious that the ligand will interact with the charged surface of the particles which points towards the fact that in such cases also metal ion-COOH group interaction plays a major role. Not only for metallic nanoparticles, oleic acid (a long chain carboxylic acid) is used as capping agent for different ferrites and in our study we have utilized the same capping agent which is explained in Chapter V. Noble metal nanoparticles like Ag [20d, e] can also be capped and hence be stabilized by the –COOH moiety of long chain organic molecules. The phase transfer of these nanoparticles from one solvent to the other is often performed exploiting the strength of the interaction of acid group on various nanoparticle-surfaces. This issue is also addressed in this thesis in Chapter VI. Thus, it is pertinent that we understand this interaction thoroughly explaining various factors affecting it so as to exploit its usage in various applications. To have a precise idea, molecular modeling approach and charge density plot have been employed to probe the nature and the details of binding of carboxylic acid with different metal ions, as explained in this Chapter.

3.2. EXPERIMENTAL DETAILS:

The focus of our experiment is to develop a better understanding regarding the binding of different metal ions with ligands containing –COOH group as the prime interaction site and also to check the capability to form corresponding metal-carboxylates. We also wanted to investigate the details of preferential binding of metal ions with carboxylic group from a mixture. We designed our experiment accordingly. In one set of experiments, we allowed the mixture of cations to interact with the –COOH group to know the competitive binding ability and in another set, selected cations were reacted with the group one after another to check the replacement ability of the preferred cation over the weakly bonded one.

Various ions were selected for the experimental purpose e.g. Cd^{2+}, Pb^{2+}, Ca^{2+} and Co^{2+}. The choice has been made in such a way that all of them are divalent but possess different ionic size. Then five pairs of ions were made among the chosen cations namely (a) Cd^{2+}/Pb^{2+} (b) Cd^{2+}/Ca^{2+} (c) Cd^{2+}/Co^{2+} (d) Co^{2+}/Pb^{2+} and (e) Co^{2+}/Ca^{2+}.

For the experiment thin films of arachidic acid (Eicosanoic acid, $C_{20}H_{40}O_2$, Mol. Wt. 312.5) of 200 Å thickness were thermally deposited, in an Edwards E306 vacuum coating unit operated at a pressure of 2 X 10^{-7} Torr, onto gold-coated AT-cut quartz crystals (for monitoring film thickness), glass and Si (111) substrates for the metal ion binding experiments and their subsequent characterization like Atomic absorption spectroscopy (AAS), Fourier transform infrared (FTIR) spectroscopy and Energy dispersive analysis of X-ray (EDAX). The lipid (Arachidic acid, AA) was deposited by a process of sublimation in a vacuum at a temperature not exceeding 80°C for a period of 1 min. FTIR analysis, carried out on the thermally evaporated arachidic acid film showed no evidence of thermal degradation of the lipid molecules. The film thickness was monitored using a QCM fitted to the deposition chamber. The two sets of experiment are discussed in details in the following sections.

3.2.1. Experiment 1: To Check Competitive Binding:

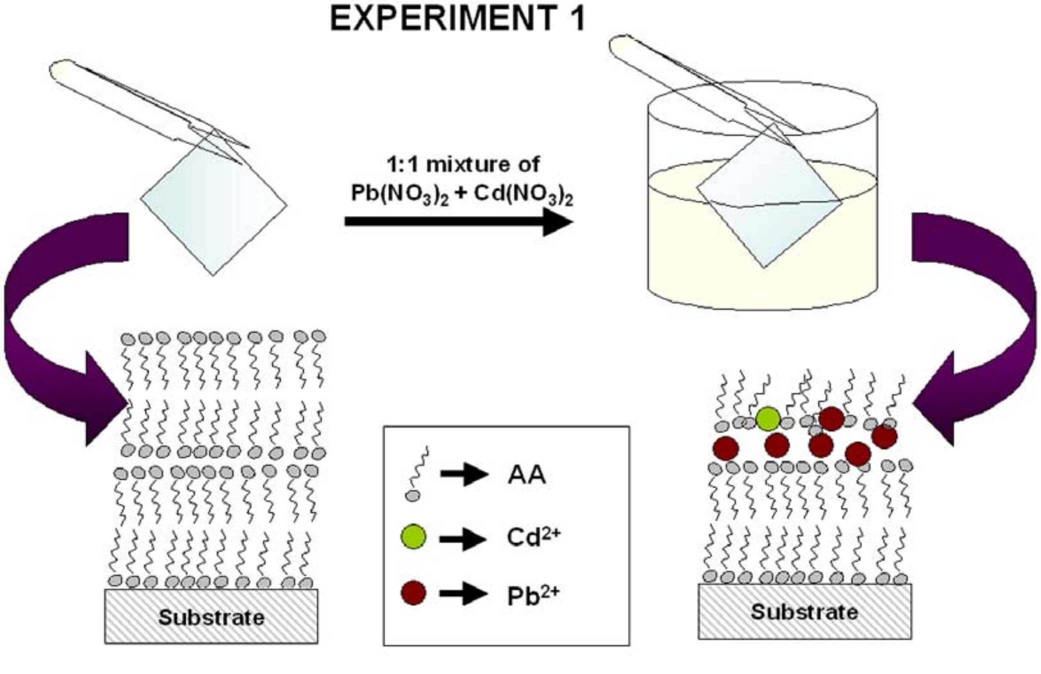

Figure 3.1. *Scheme showing the interaction between Arachidic acid layers and cations when the cations were taken together in a mixture in 1:1 concentration ratio. We have shown the scheme with respect to Pb^{2+} and Cd^{2+} cations, but the mechanism is equally true for other pairs.*

The Si (111) and glass substrates with the thin films of AA of 200 Å thickness were immersed in aqueous 50 ml solution of 1:1 mixture of both the metal ions of a particular pair *(Figure 3.1)*. The concentration was maintained as 1 X 10^{-2} M with respect to either of the ions with the pH of the solution above 5.5 to assure the presence of the carboxylate anionic form of AA (pKa of AA is ~ 4.82). The resulting di-carboxylate salt of different metal ions with arachidic acid films on Si (111) and glass substrates were washed with double distilled water to remove any physisorbed ions and ensure the presence of occluded cations only, then dried under nitrogen flow and subjected to FTIR and EDAX investigation. At this stage after analyzing the samples by FTIR and EDAX the glass substrates were kept in 10 ml of double distilled water with its pH adjusted to ~1.8-2 by drop wise addition of HCl. At this low pH the carboxylic acid groups are re-protonated leading to leaching out the metal ions entrapped inside the film of AA into water. 10 ml of these solutions were subjected to AAS measurements to estimate the amount of both the ions, which were actually trapped in the AA film and then dribbled out by the acid treatment as described above. The ratio of the concentration of the two ions from a particular pair can be related to the ratio of their bond strength. In principle, the concentration of the cations possessing higher binding capacity should be found in excess in AA film and thus when these entrapped cations are leached out in the acidic water solution to be examined by AAS technique, the solution is also expected to contain that particular cation in larger quantity.

The cations also bind to the carboxylate monolayer in a selective manner when mixture of metal ions is present in the subphase in a Langmuir trough having arachidic acid monolayer at the air/water interface. The surface pressure (π) – area (A) isotherms measurement shows the stability of the AA monolayer over the particular subphase of cations mixture. At an optimum pH the carboxylate group of the AA monolayer will interact more strongly with the cation having more affinity towards the head group of the amphiphiles (in this case $–COO^-$ of AA) and will remain in the form of metal-carboxylate composite. The film of metal-carboxylate can be lifted on substrates using the Langmuir-Blodgett technique at a particular surface pressure at which the monolayer is in its solid state ensuring the most compact arrangement (details have been discussed in Chapter II). The surface pressure (π) – area (A) isotherms were measured in a LB trough at 25 ^{o}C with the monolayer compression and expansion speed of 100 cm^2/min.

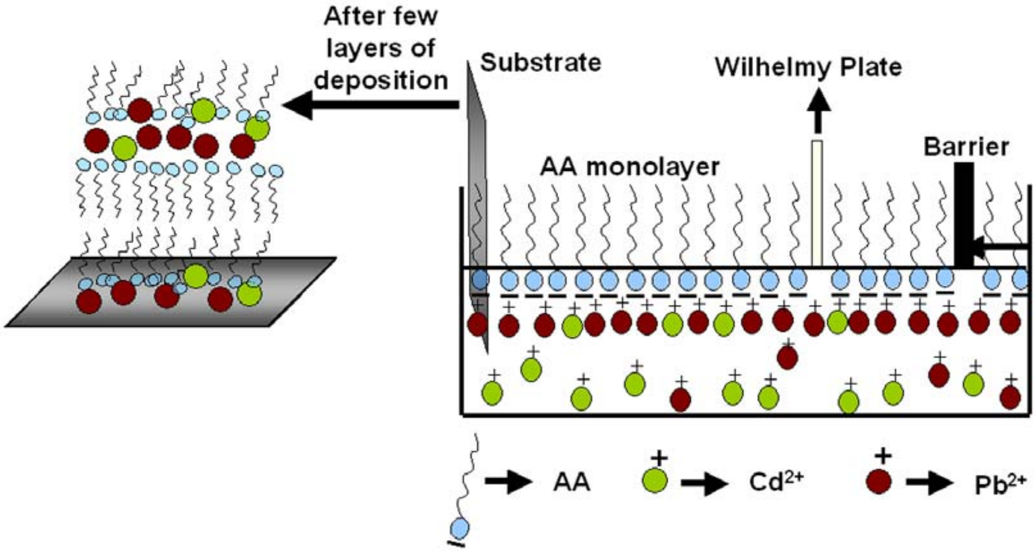

Figure 3.2. *Scheme showing the preferential bonding of strongly interacting cations (Pb^{2+}) with the AA monolayer spread at the air - water interface than the weaker cation (Cd^{2+}). It is true for other pairs of cations.*

In our experiment, AA (1 mg/ml) in chloroform was spread over 1:1 mixture of 5 X 10^{-3} M solution of the ion pair selected (subphase pH ~ 5.5). The compression started 10 min after spreading of the arachidic acid to allow complete evaporation of chloroform. Thirty monolayers were deposited on a Si (111) substrate and the film was subjected to X-ray photoelectron spectroscopy (XPS). It is clear from the schematic presented in *Figure 3.2* that strongly bonded cations are present in greater amount in the film lifted using this technique. After several layers of deposition of the film the substrate actually mimics the similar layer by layer arrangement of metal ions and lipid molecules as in the previous experiment. This experiment on LB thus acts as complimentary to the above mentioned one as in both the cases we have taken mixture of cations and have checked the competitive binding of a particular cation with –COOH group of AA.

3.2.2. Experiment 2: To Investigate Replacement Ability:

The preferential binding of a particular cation and its replacement ability was re-checked by designing a second set of experiments. Si (111) substrates and glass substrates having deposited AA layers of thickness 200 Å, were immersed in 50 ml of 1 X 10^{-2} M aqueous solution of a particular metal ion for 6-7 hrs, which is having lower binding capacity to the carboxylic acid group *(Figure 3.3)*, as implied from the result of the first set of experiments. In every case the pH of the solutions were maintained above 5.5 to assure complete ionization of AA. The resulting salt of metal ions with arachidic acid films on Si (111) and glass substrates were washed thoroughly, dried with N_2 jet, and subjected to FTIR and EDAX investigation. Then the same substrates were dipped in the second metal ion solution having a higher complexation tendency with the carboxylic head group for 6-7 hrs *(Figure 3.3)* and then cleaned in the similar way as in the first step of the experiment. At this stage after analyzing the samples for FTIR and EDAX, the Si substrates and the glass substrates were treated with 10 ml of water of pH ~2 to leach out the entrapped metal ions. This 10 ml solution was examined by AAS to determine the concentration of both the ions present.

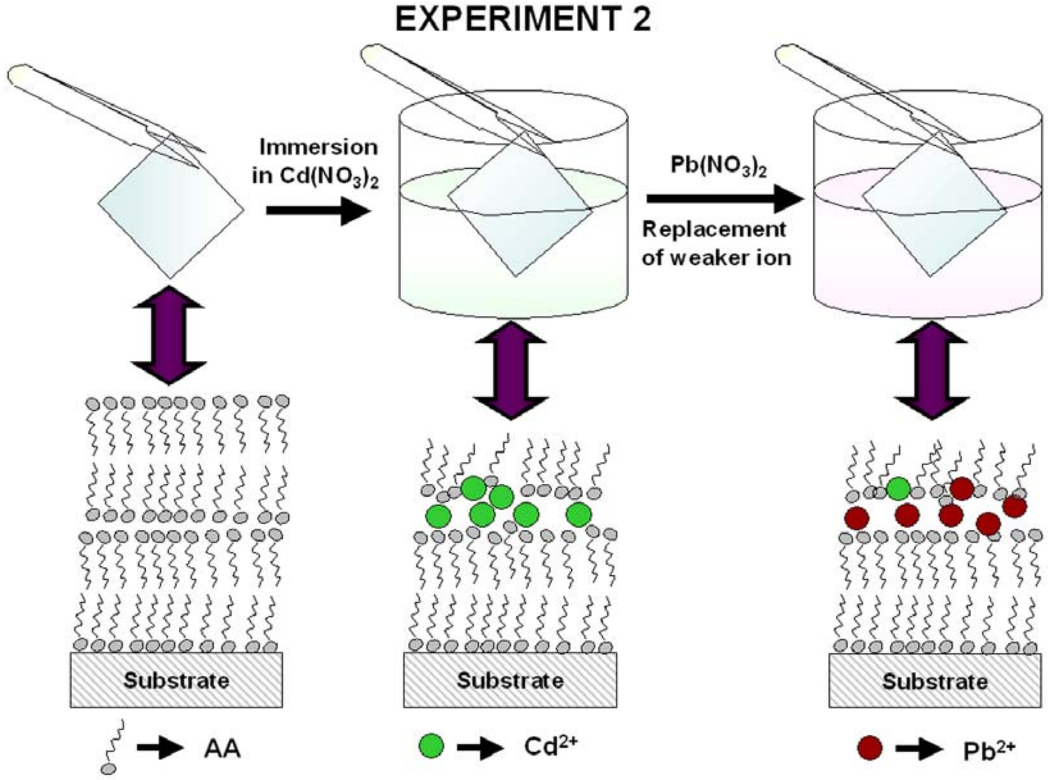

Figure 3.3. *Scheme showing the interaction between Arachidic acid layers and cations when the substrate, containing layers of AA deposited on it, was sequentially dipped in the solution of cation having lower binding capacity (e.g.* Cd^{2+}*), followed by the similar treatment with the strongly binding cation (e.g.* Pb^{2+}*). It is true for other pairs of cations.*

3.3. COMPUTATIONAL DETAILS:

In the theoretical model, the –COOH group containing ligand was assumed as acetic acid as it is the simplest carboxylic acid with minimum chain length and thus the steric interaction between the hydrocarbon tails of the adjacent ligands can be neglected which otherwise would make the calculations extremely complicated. Our calculations are based on first principles density functional theory (DFT) with a generalized gradient approximation (GGA) to the many electron exchange correlation energy as given by Perdew-Burke-Ernzerhof (PBE) functional [21]. We use PWSCF 2.0.1 [22] implementation of DFT [23, 24] which employs plane wave basis and ultra-soft pseudo-potentials [25] to represent interaction between ions and electrons. Energy cutoff of 25 Ry is used on the plane wave basis used in the representation of wave functions and that of 150 Ry for the representation of density. Periodic boundary conditions are used with a large super-cell such that periodic images of molecules are separated by a vacuum of at least 12 Å along its axis and at least 8 Å perpendicular to its axis. This ensures negligible interaction between the periodic images of metal diacetate (M diacetate) molecules. Resulting Brillouin zone is small and we use a single k-point (0,0,0) in its sampling.

Molecular structures are determined through total energy minimization using Broyden-Fletcher-Goldfarb-Shanno (BFGS) [26] algorithm and Hellman-Feynman forces on atoms. Structural optimization is carried out until the forces on all the atoms are less than 0.001 Ry/bohr. For acetic acid, calculated bond-lengths (shown in *Table 3.1*) agree within 2% with their experimental values.

Bond length	l_B **(C-H) Å**	l_B **(C-C) Å**	l_B **(C=O) Å**	l_B **(C-O) Å**	l_B **(O-H) Å**
Our results	1.10	1.51	1.22	1.38	0.98
Experiment	1.07	1.50	1.23	1.36	0.97

Table 3.1: *Comparison of different bond lengths in acetic acid*

These errors are typical of the density functional theory calculations with GGA. Calculated bond-length of H_2 molecule is 0.75 Å, which also compares well with the experimental bond-length of 0.74 Å. For determination of structures of metal diacetates, we used different initial structures: planar (a) cis, (b) trans structure of metal diacetate, (c) metal diacetate with one acetate group alligned in a plane perpendicular to the other. All the initial structures were generated using experimental bond-lengths, as available at www.gaussian.com.

Cohesive energy of each metal diacetate molecule (E_c^M) was estimated by subtracting total energies of its constituent atoms from the total energy of the molecule with optimized geometry. Energy as a measure of strength of metal-acetate bond, $E_{M\text{-}A}$ was calculated using:

$E_{M\text{-}A} = 0.5*(E_c^M + E_c^H - 2\times(E_c^{AA}))$,

where E_c^H is the cohesive energy for H_2 molecule and E_c^{AA} is the cohesive energy for acetic acid.

3.4. ATOMIC ABSORPTION SPECTROSCOPY:

The AAS measurements were accomplished on two kinds of samples obtained from two sets of experiments (the details of it is already discussed in section 3.2). The ratio of the concentration of different pair of ions as obtained from the AAS measurement is presented in the tabulated format in *Table 3.2.*

Selected ion pairs	**AAS analysis (Experiment 1)**	**AAS analysis (Experiment 2)**
Cd Pb	1:140	1:825
Cd Ca	1:10.7	1:10
Cd Co	1:6.29	1:13.4
Co Pb	1:2.67	1:3.78
Co Ca	1:0.67	1:0.79

Table 3.2. *AAS result illustrating the concentration ratio of the selected ion pairs where in Experiment 1, the AA film was immersed in the solution of ions of a particular pair taken together in equimolar proportion. The second column denotes the similar ratio of concentration of the ions when the AA film was dipped in solution of a particular cation having the weak bonding capacity with the –COOH group followed by the solution containing the strongly binding cation.*

The second column of the *Table 3.2,* demarcate the ratio of the concentration, of the pair of cations given in the first column, analyzed by AAS after leaching out the cations by acid treatment in *Experiment 1*. The strongly bonded cations are expected to be present in higher concentration compared to the other cation in the pair. On this basis the result indicated that Pb^{2+} binds very strong as compared to Cd^{2+}, an observation that is in agreement with the competitive binding trend as studied by Sastry et al. [19]. Cd^{2+} was paired up with other divalent cations too, as for example Ca^{2+} and Co^{2+}. In these cases also Cd^{2+} concentration was found to be low that clearly establish the fact that binding strength of Cd^{2+} is weakest among the chosen set of cations. On the contrary, Pb^{2+} can interact dominantly with AA films as compared to Cd^{2+} and Co^{2+}. The binding capacity of Co^{2+} and Ca^{2+} can be regarded as equivalent. Even the binding capability of Co^{2+} and Pb^{2+} are not markedly distinguishable. So a rough approximation of the binding strength of various cations with –COOH group follows the trend as $Pb^{2+} > Ca^{2+} \geq Co^{2+} > Cd^{2+}$.

Now, taking hints from the above analysis, *Experiment 2* was performed with pair of cations. In the following we analyze one such pair in detail. For example, AAS analysis *(Table 3.2 column 3)* should reveal that for Cd^{2+}/Pb^{2+} pair Pb^{2+} must possess a stronger binding than the other cation in duo. So in principle, when a AA-Cd^{2+} composite film is exposed to Pb^{2+} ions they should replace Cd^{2+} from the composite after sequential dipping. When the entrapped cations were dripped from the film in the solution, analysis should show an excess of Pb^{2+} ion concentration to Cd^{2+} ions and in fact the experimental analyses as substantiated in *Table 3.2* fully justified our hypothesis.

Similarly, for Cd^{2+}/Ca^{2+} pair, Ca^{2+} is found to be bound almost 10 times stronger than Cd^{2+} when the AA film was allowed to interact with the respective cations one by one. The results of the next three pairs were also in good agreement with the expected consequences.

3.5. ENERGY DISPERSIVE ANALYSIS OF X-RAYS:

EDAX analysis is another tool to judge the step by step process of incorporation of one cation into the AA film and their replacement by another as mentioned in *Experiment 2*. The EDAX spectra at every step as mentioned above are presented in *Figure 3.4A-C.* The spectra in *Figure 3.4A* is the original arachidic acid film just after deposition of the lipid layer. The film shows the presence of only C and O signal as expected. At the next step when AA film is dipped only in $CdCl_2$ solution and the corresponding EDAX (*Figure 3.4B)* analysis clearly demonstrated the presence of Cd peak along with the C and O signals with the atomic % of this cation as 1.76. Calculations from the atomic % of Cd and C (70.82 %) it showed that for every 2.01 -COOH group there is one Cd^{2+} ion. So basically it gave an idea towards the formation of dicarboxylate with the incorporated cations in the staked layers of carboxylic acid. The same film when investigated after the treatment with $Pb(NO_3)_2$ the atomic % of Cd is found to be below the detection limit of EDAX and we found a concomitant increase in atomic % of Pb^{2+} and here also for every Pb^{2+} there are 2.04 –COOH groups (*Figure 3.4C)*. Both the results in combination indicate that Cd^{2+} ions were almost fully replaced by Pb^{2+} plausibly because of the stronger bond formation with the carboxylic acid group.

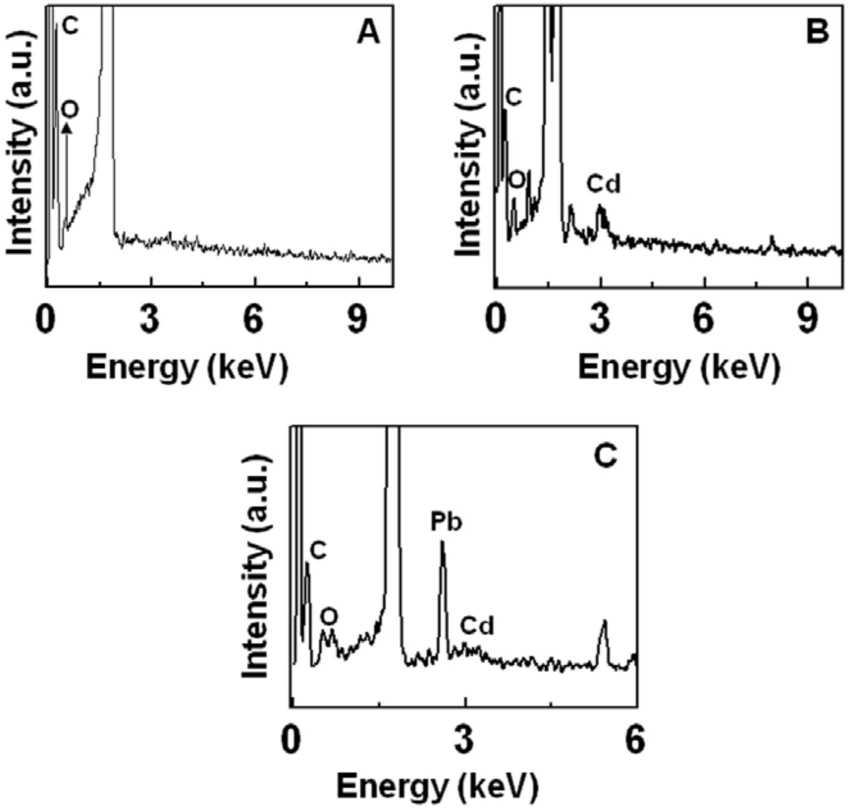

Figure 3.4. *(A) EDAX analysis of only arachidic acid layer just after deposition. (B) EDAX performed on the Si (111) substrate after dipping in* 10^{-2} *M solution of* Cd^{2+} *ions. (C) EDAX spectra after dipping the substrate containing AA-*Cd^{2+} *into* 10^{-2} *M solution of* Pb^{2+} *ions.*

Though in the above case of Cd^{2+} / Pb^{2+} pair after immersing the AA-Cd film in the $Pb(NO_3)_2$ the signal of Cd has totally diminished as observed in the EDAX analysis, in other cases the peak of the weaker ion was not fully wiped out after treatment of the film with the stronger binding cation solution. But in every case the atomic % of the preferred cations remain more as compared to the feebly interacting ion of the pair. The atomic % of the two cations of each pair after the sequential treatment are presented in the Tabular form below (*Table 3.3*):

Pair of cations	Atomic % of first ion	Atomic % of second ion
Cd Pb	0	1.78
Cd Ca	0.57	1.85
Cd Co	0.27	1.32
Co Pb	0.32	0.55
Co Ca	0.54	0.85

Table 3.3. *Atomic % of the cations of each of the five selected pair from the EDAX measurement after the sequential treatment of the AA film into solutions of the cations.*

3.6. FOURIER TRANSFORM INFRA-RED SPECTROSCOPY:

To follow the experimental binding trends of ions with AA we examined the films by different analytical techniques. The qualitative features of binding can be apprehended by a careful study of FTIR spectra recorded at every step of the reaction. In fact, when the substrates with 200 Å thick AA layer are dipped into the metal ion solution at a pH of 5.5 it is expected that the –COOH group are deprotonated and the cation will bind to the head group of the molecule. Consequently, the carbonyl stretching frequency of pure AA will shift to the lower wavenumber indicating a complexation between the head group with the cation. The extent of the shift recorded by FTIR is entirely dependent on the binding strength of the cation with –COOH group.

Figure 3.5 shows the FTIR spectra of pure AA *(curve 1)* and its interaction with Cd^{2+}/Ca^{2+} pair at different stages of the reaction *(curve 2 to curve 5)* in *Experiment 2*.

FTIR of pure AA film shows its carbonyl stretch at 1693 cm^{-1} *(curve 1)* [27] which is found to shift to 1531 cm^{-1} *(curve 2)* and 1578 cm^{-1} *(curve 3)* when two Si (111) substrates with AA film are immersed into the solution of 1 X 10^{-2} M $CdCl_2$ and 1 X 10^{-2} M $CaCl_2$ separately. As the interaction between O-Ca is strong the carbonyl lone pair will be attracted more towards the center and hence C=O stretch will require higher energy. As a consequence the AA-Ca^{2+} shows its carbonyl stretch at higher wavenumber (1578 cm^{-1}, *curve 3*) with respect to AA-Cd^{2+} film (1531 cm^{-1}, *curve 2*). When this AA-Cd^{2+} film is dipped in 1 X 10^{-2} M $CaCl_2$ solution followed by proper treatment of the film as mentioned in the experimental section a shift in carbonyl stretch to ~1578 cm^{-1} *(curve 4)* from 1531 cm^{-1} was evinced, suggesting a replacement of Cd^{2+} by the Ca^{2+} ions.

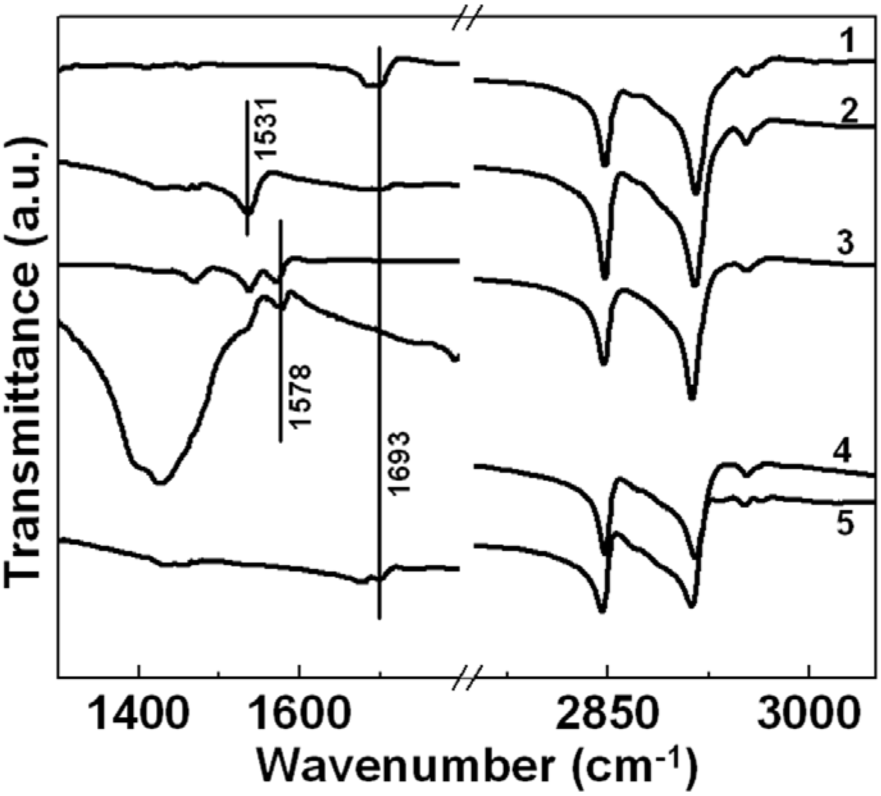

Figure 3.5. *FTIR spectra of pure AA (curve 1). Curve 2 displays the same after dipping the substrate containing AA film into $CdCl_2$ solution for 6-7 hrs. Curve 3 depicts the FTIR graph when AA film is treated with only $CaCl_2$ solution. The AA-Cd^{2+} film when plunged into the $CaCl_2$ solution the carbonyl peak shows a shift indicating the replacement of Cd^{2+} by Ca^{2+} (curve 4). The AA film with the cations when treated with an aqueous solution of pH 1.8, the FTIR curve shows the feature of pure AA. (Curve 5).*

The carbonyl stretch reappears at its original frequency of 1693 cm^{-1} *(curve 5)* after the cations are leached out by the acid treatment as mentioned in details in the experimental section. The re-generation of –COOH stretch authenticates that this is an easy protocol to ooze out the entrapped cations from the AA film very conveniently.

3.7. LANGMUIR-BLODGETT TECHNIQUE:

The specificity of binding capacity is also checked by spreading AA monolayer on equimolar mixture of the two ions (Cd^{2+} and Pb^{2+}) at air/water interface. The pH of the substrate was maintained at ~5.5 to ensure the de-protonation of the AA layer and the surface pressure-area isotherm was measured at 25 °C.

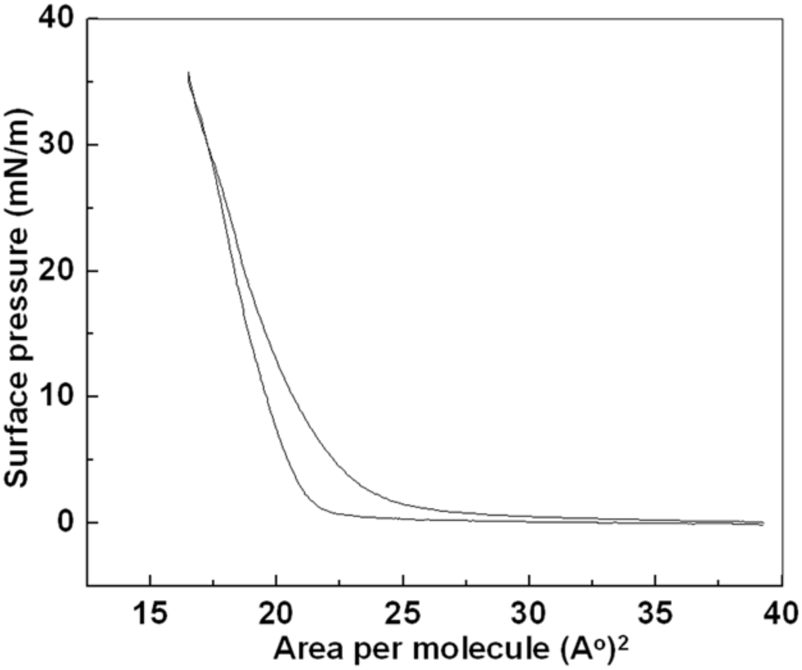

Figure 3.6. *The figure demonstrates the surface pressure-area isotherm of pure AA spread over the subphase of equimolar mixture of* Cd^{2+} *and* Pb^{2+}.

At the above-mentioned pH the carboxylic head group of the amphiphile will remain as $–COO^-$ and hence will interact with the cations present in the subphase. The arachidic acid $–COO^-$ group has equal accessibility towards both the cations, but only that cation will bind to the interface monolayer preferentially which has greater affinity for it, that means the cations with higher binding capacity. The presence of other cation at the monolayer cannot be ruled out completely, but apparently it should be in much lower concentration. The pressure-area isotherm in *Figure 3.6* shows a steady increase in the surface pressure with the inward movement of the barrier indicating the stability of the AA monolayer on ions mixture. The film was stable up to a surface pressure of 35 mN/m, after that the monolayer breaks as revealed by the sudden change in the slope of the curve. So the surface pressure was kept constant at 30 mN/m when the film of AA complexed with the preferred cations was lifted onto Si (111) substrate. The film on the substrate when investigated by XPS shows a prominent Pb 4f core level signal which can be fit into the binding energies of 138.9 eV ($4f_{7/2}$) and 144.0 eV ($4f_{5/2}$) and matches well [28] with the values reported for Pb^{2+}. But no such peak is observed for Cd 3d core level. As the AA molecules, in its de-protonated form, will bind to the subphase cations and depending on the strength of binding the preferred cations will be present in higher concentration in the film lifted from the trough using Langmuir-Blodgett technique. Photoelectron spectroscopic study of Cd^{2+} (*Figure 3.7A)* and Pb^{2+} (*Figure 3.7B*) corroborate the facts as discussed.

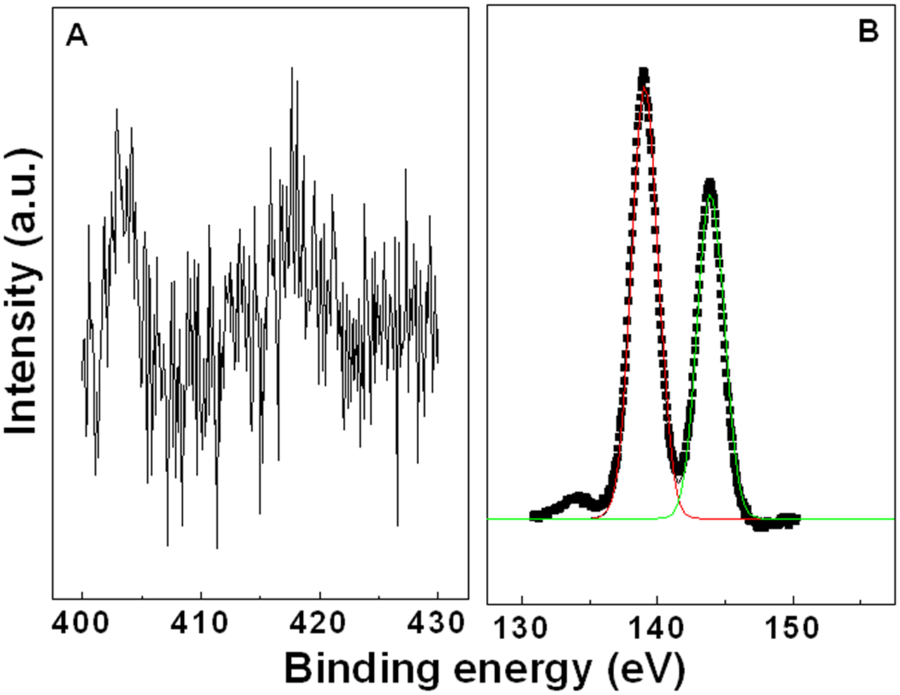

Figure 3.7. *X-ray photoelectron spectra of* Cd^{2+} *(A) and* Pb^{2+} *(B). Measurement was performed on a film lifted from the LB trough at a surface pressure 30 mN/m at 25 °C.*

Similarly when the other pairs of ions were taken in the subphase and the AA monolayer was spread on it, the film obtained was found to contain one cation in excess than the other. The curves are not shown to avoid mere repetition of similar set of data. In fact, all the results were found to follow the same trend as envisaged from *Experiments 1*. However, all these experimental results are in contradiction to expectation based on simple assumptions that the metal ion with smaller charge to size ratio will have weaker binding strength. Thus Pb^{2+} ions should have weaker binding competence than Cd^{2+} ions with –COOH groups which is not true in the actual case. Hence our experimental results as well as earlier studies [19] clearly indicate the complexity of this interaction and the necessity to study them in more detail.

3.8. DENSITY FUNCTIONAL CALCULATION AND DISCUSSION WITH RESPECT TO VARIOUS IONS-COOH GROUP INTERACTION:

The quantitative modeling approach based on DFT studies shows that E_{M-A} for most of the acetates is between 150 and 250 kJ/mol, with a notable exception of Cd-acetate bond, which has energy more than 10 times smaller than the rest *(Table 3.4)*.

M-diacetate($M-(CH_3COO)_2$)	E_{ch}^{M} (kJ/mol)	E_{M-A} (kJ/mol)
$Ca(CH_3COO)_2$	8449.145	249.063
$Ni(CH_3COO)_2$	8376.872	212.926
$Pb(CH_3COO)_2$	8287.706	168.343
$Co(CH_3COO)_2$	8311.319	180.150
$Fe(CH_3COO)_2$	8261.010	154.995
$Cd(CH_3COO)_2$	7984.286	16.633

Table 3.4. *M-diacetate cohesive energies and respective M-A bond energy for 6 types of metal diacetates, where M = Ca, Pb, Ni, Cd, Fe, Co.*

Each of the calculated energy is also smaller than that of a covalent *C-C* bond or standard ionic bonds. This is possibly because the *M*-acetate bonding is of mixed ionic and covalent type. Secondly, negatively charged acetate groups on the two sides of *M* ion would repel each other, destabilizing the *M-O* bond partially and resulting in smaller energies E_{M-A}. The binding strength *(Table 3.4)* of the cations trails the following order:

$$Ca^{2+} > Ni^{2+} > Co^{2+} > Pb^{2+} > Fe^{2+} > Cd^{2+}$$

The order is in good agreement with the experimental observations. The only inconsistency is observed in case of the fifth selected pair i.e. Co^{2+}/Pb^{2+}. In this case Co^{2+} showed weaker binding than Pb^{2+} but considering their strength of binding with –COOH group from the calculated figures the result can be considered to be within the experimental slip-up, though we have tried to address this issue in the later part of the chapter. The ratio of bond strength of Co^{2+} and Ca^{2+} predicts presence of both the cations in almost equal amount in the solution prepared for AAS. In reality the AAS results followed the trend very closely *(Table 3.2).*

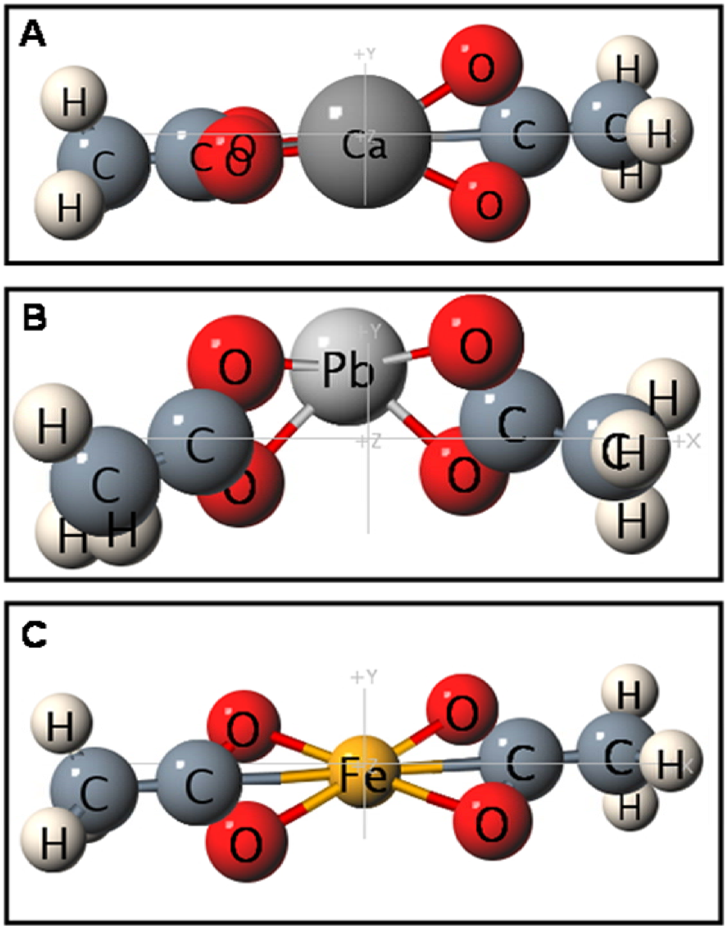

Figure 3.8. *The representative relaxed energy minimum model of different metal-diacetate e.g. tetragonal structures of Ca-diaectate (A), square pyramidal orientation of Pb-diaectate (B) and square planar geometry of Fe-diaectate(C).*

In fact, among the six different metal diacetates studied here, the structures are found to fall into three groups: (1) tetrahedral like geometry, for M = Ca, Cd (2) square planar geometry, for M = Ni, Co, Fe and (3) square pyramidal geometry for M = Pb. In *Figure 3.8A-C* we have demonstrated the relaxed minimum energy structures of three different M-diacetate, where M = Ca, Pb, Fe respectively, i.e. one from each structural group. The reasons for this grouping are the following: Ca^{2+} ion in calcium diacetate has outermost electronic structure as [Ar] $3d^0$, whereas Cd^{2+} in Cd diacetate has [Kr] $4d^{10}$. For these two metal ions with completely empty or completely filled d-orbital, very weak crystal field splitting is expected and the electrostatic interactions arising from their strongly ionic nature result in tetrahedral-like structure *(Figure. 3.8A)*. The conclusion of their ionicity is based on partial density of electronic states analysis, which revealed that lowest unoccupied molecular orbital (LUMO) exhibits a strong component of outermost *s*-electronic state of Ca and Cd and the highest occupied molecular orbital (HOMO) is made of *2p* states of oxygen. Calculated HOMO-LUMO energy gaps in Ca and Cd diacetates are 4.95 eV and 4.15 eV respectively, indicating stronger ionic nature of the Ca-acetate bond. Though Pb diacetate has ionic Pb^{2+} (electronic configuration of Pb^{2+} is [Xe] $4f^{14}$ $5d^{10}$ $6s^2$ $6p^0$), exhibits a rather different structure. Partial density of states of Pb diacetate bears two important facts: (a) the LUMO has primarily the character of *6p* states of Pb and (b) while the HOMO is dominantly oxygen *p*-like; the state immediately below the HOMO has a strong character of the *6s* state of Pb. It is also observed that the contribution of *6s* orbital of Pb to states about 4 eV lower in energy than the HOMO. The lone pair of electrons (*6s* state) of Pb is known to be stereochemically active and result in off-centering of Pb atom and lower symmetric structure of oxides and chalcogenides [29]. We find it has the same effect here, leading to pyramidal structure *(Figure 3.8B)*, where four oxygens remain in a plane and Pb^{2+} is off-centered in the perpendicular direction along the line passing through the center. Our estimate of the HOMO-LUMO gap of Pb diacetate is 4.46 eV. Ni^{2+}, Co^{2+}, Fe^{2+} (3d transition metals) in their respective diacetate form have outermost valence electronic configuration as [Ar] $3d^8$, [Ar] $3d^7$ and [Ar] $3d^6$ respectively, i.e. they all have valence d orbitals more than half-filled (but < 10 d-electrons) and are expected to undergo a strong crystal field splitting. For argument, we start from a tetrahedral coordination of the *M* ion in this case also, as in Ca and Cd diacetates. In this case, higher energy t_{2g} orbital is partially occupied (with 4, 3 and 2 electrons in case of Ni, Co and Fe respectively) and the system is unstable according to

Jahn-Teller theorem [30]. Since these orbitals are planar, these transition metal diacetates seem to favor planar geometry *(Figure 3.8C)*. Ni diacetate is more symmetric with a completely filled doubly degenerate HOMO and has a zero magnetic moment, with a HOMO-LUMO gap of 1.29 eV. On the other hand, Co and Fe diacetates possess geometries with further broken symmetry resulting in closely spaced singly degenerate states near HOMO and LUMO, with HOMO-LUMO gaps of 0.58 and 0.84 eV respectively. Strong exchange and crystal field splitting result in magnetic moment of about 3 and 4 μ_B of Co and Fe diacetates respectively. This is also reflected in the *M-O* bond-lengths: average bond-length of Ni-O is 1.91 Å, whereas that of Co-O and Fe-O bonds are 2.03 and 2.06 Å respectively. We note that the average Ca-O, Cd-O and Pb-O bond-lengths are 2.29, 2.25 and 2.41 Å respectively. Pb-O bond length is expected to be larger due to stereochemical activity of its lone pair (which provides an additional coordination).

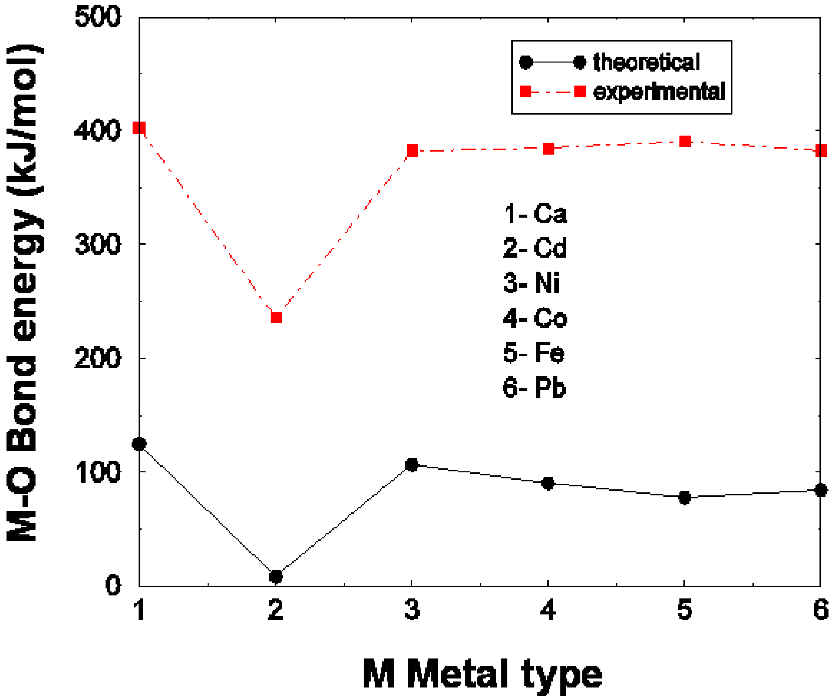

Figure 3.9. *Comparison of calculated M-O bond energy with those from literature: for different metal diacetates. 6 points along x axis denote 6 metal diacetates. Points joined by solid line are obtained from our calculation (for metal diacetates) while points joined by dot-dashed line are from literature (M-O from metal oxide).*

Since we relaxed structures starting from different initial structures, we now assess relative stability of different structures for a given *M* diacetate, which gives a quantitative idea of different mechanisms leading to its stability. Energy of Ca diacetate in the tetrahedrally coordinated structure is 0.238 eV lower than its planar (Co diacetate like) structure. Energy of the planar structure of Co diacetate is 1.261 eV lower than its tetrahedrally coordinated structure. Energy of Pb diacetate in square pyramidal geometry is 1.099 eV lower than its energy in the tetrahedrally coordinated structure, whereas the energy of Cd diacetate in the tetrahedral geometry is 1.062 eV lower than the energy of its square pyramidal structure. The trend in the calculated *M-A* bond energies is rather similar to that in the energies of respective oxides *(Figure 3.9)* available in literature (www.webelements.com, www.psigate.ac.uk/newsite/reference/plambeck/chem2/p01083.htm). Calculated cohesive energies and consequent *M-A* bond energies are found to be underestimated in comparison to the experimental data (obtained by summing up individual bond energies as approximated from www.psigate.ac.uk).

From *Table 3.4*, we see that Pb diacetate is found to have *M-O* bond energy almost 10 times of that from Cd diacetate. We try to understand this by examining the nature of bonding through electron densities and partial density of states. Pb diacetate is observed to have a special pyramidal structure (bouquet kind).

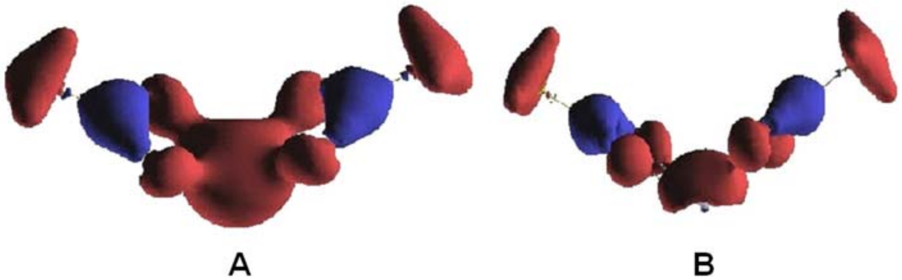

Figure 3.10. *Isosurface of charge densities of the Pb ion in Pb diacetate: (A) at isovalue 0.002 e/bohr*^{3} *showing a clear mixing of oxygen 2p and Pb 6s orbitals, (B) at isovalue 0.004 e/bohr*^{3}.

Electronic charge density of Pb diacetate *(Figure 3.10)* reveals that there is a mixing of oxygen 2*p* and Pb 6*s* orbitals in Pb diacetate indicating partially covalent character of Pb-O bond (evident in *Figure 3.10A)*, whereas the asymmetric nature of the isosurface at a higher value of density indicates that *6s* state of Pb is locally polarized (*Figure 3.10B)*, similar to its role in off-centering of Pb in ferroelectric materials [29].

On the other hand, isosurfaces of electron density of Cd diacetate *(Figure 3.11A)* and Ca diacetate *(Figure 3.11B)* are consistent with ionic bonding between the metals and acetate groups. We observe an important feature particular to Cd diacetate: there is an isosurface centered at Cd site at a high value of density, which becomes more extended at lower densities.

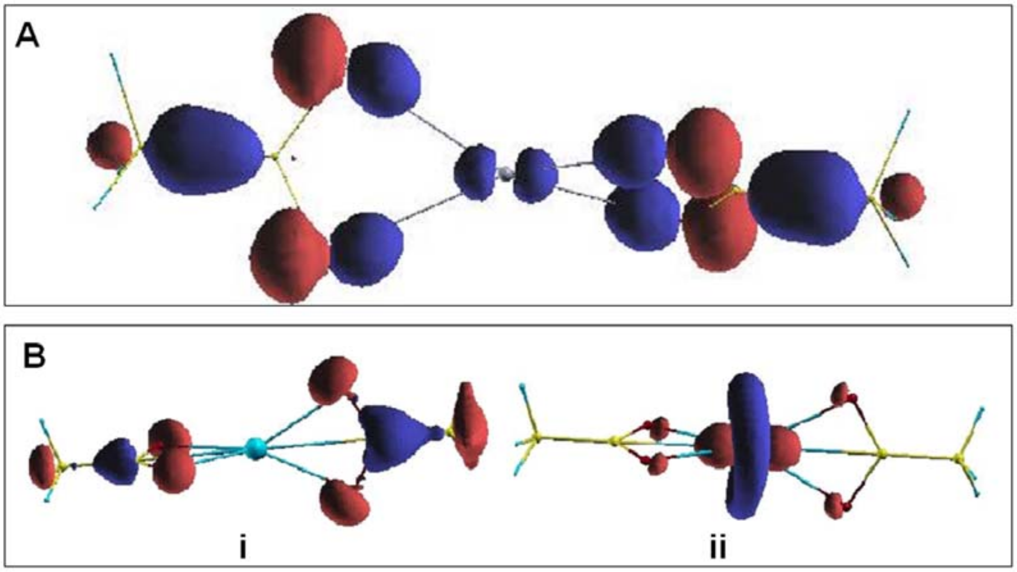

Figure 3.11. (A). *Isosurface of charge densities of Cd diacetate with isovalue = 0.006 e/bohr^3.* ***(B).*** *Isosurface of charge densities of the Ca ion in Ca diacetate: (i) at isovalue 0.007 e/bohr^3 showing no mixing of oxygen 2p and Ca 4s orbitals (ii) at isovalue 0.003 e/bohr^3 for the first unoccupied band above the Fermi level.*

From the partial density of states, we find that (a) Cd is *not* completely ionic and (b) the fully occupied *d* states of Cd mix strongly with oxygen *p* states. The strength of this mixing estimated from the width of energy of d-states is about 0.8 eV. This is similar to the *p-d* mixing in ZnO and GaN, where the energies of *d* and *p* states are comparable resulting in their mixing [31]. Binding of Cd with acetates is weaker than that of Ca due to its weaker ionic character, whereas binding of Pb is stronger than that of Cd due to additional gain in energy from off centering. Due to *p-d* coupling, we expect Cd displacements (along *y* and *z*) to exhibit a shallow (less stiff) potential energy well and couple well with strain.

In contrast to group II metals, the transition metals clearly show mixed ionic and covalent bonding with acetates. From the partial density of states, as mentioned earlier, Ni, Co and Fe are in the *2+* ionic states. However, their *d*-states are at the HOMO and LUMO, giving rise to (a) covalent interactions with oxygens and (b) possibility of non-zero magnetic moment. As discussed earlier, Ni diacetate has a doubly degenerate HOMO that is fully occupied with a vanishing magnetic moment, whereas Co and Fe diacetates have fewer *d* electrons and result in lower symmetry structure with magnetic moments of 3 and 4 μ_B respectively. Thus, smaller bond-length of Ni-O bond yields a stronger covalency while binding in Ni diacetate *(Figure 3.12A*, the O-C-O complex binds strongly with Ni). Co diacetate *(Figure 3.12B)* exhibits relatively weaker *M-O* covalent bonds, resulting in decreasing strength of *M-O* bond as one goes from Ni to Fe along the row of the periodic table.

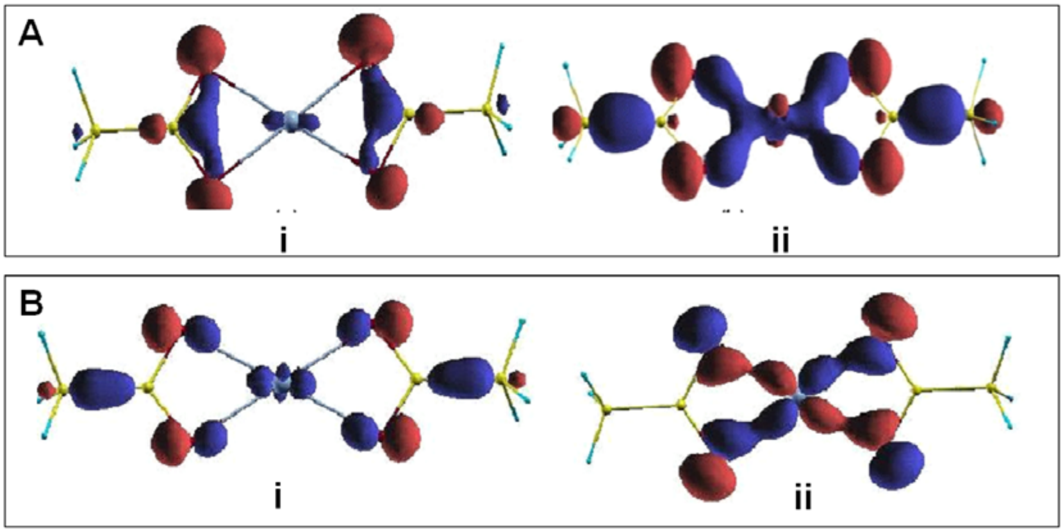

Figure 3.12. (A). *Isosurface of charge densities of Ni diacetate: (i) at isovalue = 0.011 e/bohr^3. Ni 4s state does not mix with O 2p states. (ii) at isovalue = 0.006 e/bohr^3 , Ni 3d states mix with O 2p states to produce partial covalent bonding.* ***(B).*** *Isosurface of charge densities of Co diacetate: (i) at isovalue = 0.011 e/bohr^3, (ii) at isovalue = 0.006 e/bohr^3.*

In order to understand the stiffness of binding of a metal ion *M* with acetate groups, we determined self force constant matrix (whose eigenvalues are proportional to square of frequencies given in *Table 3.5*) of each *M*, which gives a harmonic description of the potential energy well faced by the motion of the *M* ion from its equilibrium position. We note that, one can show using the acoustic sum rule (or the translational invariance) that this stiffness is also a measure of the overall stiffness of bonding of the *M* ion with the rest of the molecule. Eigenvectors of the self-force constant matrix are the principal directions of the stiffness of local potential energy well of *M*. For Ca and Cd diacetates, potential energy well is stiffest (k_1 in *Table 3.5*) along the axis of the molecule pointing towards carbon, and relatively isotropic (expected from the tetrahedral symmetry) and more than two times softer in the transverse plane (k_2, k_3).

***M* type**	**ω_1 (cm^{-1})**	**k_1(eV/Å^2)**	**ω_2 (cm^{-1})**	**k_2(eV/Å^2)**	**ω_3 (cm^{-1})**	**k_3(eV/Å^2)**
Ca	2203	18.154	978	3.570	942	3.270
Cd	1513	23.961	497	2.616	446	2.055
Pb	797	11.537	764	11.179	356	3.199
Ni	2626	37.720	2107	24.276	1099	6.607
Co	2141	25.233	1966	21.295	1482	11.891
Fe	1394	18.004	1360	12.021	696	2.676

Table 3.5. *Self spring constants k_1, k_2 and k_3 and local vibrational frequencies ω_1, ω_2 and ω_3 (cm^{-1}) associated with motion of an M ion in M diacetate, as determined from its self-force constant matrix.*

If one accounts for the difference in masses of Ca and Cd, it is clear that stiffness of energy well for axial displacements of Cd is greater than that of Ca and that for displacements perpendicular to the axis is smaller, consistent with partial covalency of Cd-acetate bond arising from *p-d* interactions. Energy well associated with motion of Pb^{2+} ion in its diacetate is relatively soft in comparison with Ca, and its anisotropy is quite different. Its stiffness along the axis of the molecule (797 cm^{-1}) and along the off-centering (pyramidal axis) direction (764 cm^{-1}) is comparable, while it is much softer along the direction perpendicular to these two. We note that the energy well of Cd displacements in the transverse plane is the softest of all. Structure of the transition metal

(TM: Ni, Co, Fe) diacetates is planar and the potential energy well is softest (shallowest) for a displacement of a TM is softest (shallowest) along the direction perpendicular to the molecular plane (k_3). While the in-plane stiffness (k_1, k_2) of the potential energy well is higher and it decreases monotonically from Ni to Fe, there is an interesting feature: the principal axis corresponding to the highest stiffness is along the TM-C bond (molecular axis) in Ni and Fe diacetates, whereas it is along the Co-O bond in Co diacetate. This correlates with the stiffest potential well of Co for out-of plane displacements. In electronic structure too, Co diacetate is different from others in that its HOMO and LUMO have majority and minority spins respectively. Overall, Ni-O bonds are the stiffest, which can be traced down to the shortest bond-length of Ni-O. The trend in overall stiffness of TM-A bonds is very similar to that in their binding energies.

3.9. CONCLUSION:

In summary, this work shows that the carboxylic acid group interacts with different cations with different strength of bonding. The trend obtained from the experiments is verified by theoretical calculations. We have analyzed binding of various inorganic metal ions with acetate groups through determination of the energy of binding and its quadratic curvatures with respect to motion of the metal ions. Geometries of these metal acetates fall in three categories: (a) tetrahedrally co-ordinated strongly ionic Ca and Cd, (b) off-centered Pb ion due to its lone pair of electrons and (c) planar structures of the TM diacetates, with role of Jahn-Teller mechanisms. Cd^{2+} is most weakly bound to acetates and energy well associated with Cd displacements exhibits exceptional softness along the direction perpendicular to the molecular axis. We find that bonding of Cd^{2+} with acetates is affected by the interaction between *p* states of oxygen with fully occupied *d* states of Cd, which are close in energy. Though the amount of cations interacting with the –COOH group of arachidic acid is not following the exact values as obtained from the mathematical derivation, it can be rationalized as a difference between the ideal model preferred for calculation purpose and the non-ideality which is always associated with the real systems. But the experimental results along with the mathematical values can provide a guideline to select the right combination and can be very helpful in many of the technological applications. The strong bonding with Pb^{2+} with ligands as compared to Cd^{2+} at air-water interface could not be explained so-far. In this chapter we have addressed this issue successfully but the presence of Pb^{2+} ions about ~800 times more than that of Cd^{2+} in AA film can't be accounted at this moment with this model. It could be taken up for further studies considering other effects like hydration, orientation of the acid in solution etc. that may offer more intimate details of a real system.

3.10. REFERENCES:

[1]. (a) Shankar, S. S.; Rautaray, D.; Pasricha, R.; Pavaskar, N. R.; Mandale, A. B.; Sastry, M. *J. Mater. Chem.* **2003**, *13*, 1108 (b) Shankar, S. S.; Joshi, H.; Pasricha, R.; Pavaskar, N. R.; Mandale, A. B.; Sastry, M. *J. Colloid Interface Sci.* **2004**, *269*, 126. (c) Mandal, S.; Sainkar, S. R.; Sastry, M. *Nanotechnology***,** **2001**, *12*, 358. (d) Mandal, S.; Phadtare, S., Selvakannan, PR.; Pasricha, R.; Sastry, M. *Nanotechnology,* **2003**, *14*, 878. (e) Shankar, S. S.; Ahmad, A.; Pasricha, R.; Khan, M. I.; Kumar, R.; Sastry, M. *J. Colloid Interface Sci.* **2004**, *274*, 69. (f) Shankar, S. S.; Chatterjee, S.; Sastry, M. *PhysChemComm,* **2003**, *6*, 36.

[2]. Moreno-Villoslada, I.; Rivas, B. L. *J. Phys. Chem. B* **2002,** *106,* 9708.

[3]. (a) Custers, J. P. A.; Kelemen, P.; Van-den Broeke, L. J. P.; Stuart, M. A. C.; Keurentjes, J. T. F. *J. Am. Chem. Soc.* **2005**, *127*, 1594. (b) Shivshankar, S.; Patil, U.; Prasad, B. L. V.; Sastry, M. *Langmuir* **2004,** *20,* 8853.

[4]. (a) Lu, Q.; Luo, Y.; Li, L.; Liu, M. *Langmuir* **2003,** *19,* 285. (b) Buller, R.; Cohen, H.; Jensen, T. R.; Kjaer, K.; Lahav, M.; Leiserowitz, L. *J. Phys. Chem. B* **2001,** *105,* 11447.

[5]. Larrabee, J. A.; Leung, C. H.; Moore, R. L.; Thamrong-nawasawat, T.; Wessler, B. S. H. *J. Am. Chem. Soc.* **2004**, *126*, 12316.

[6]. Rivas, B. L.; Pereira, E. D.; Moreno Villoslada, I. *Prog. Polym. Sci.* **2002,** *28*, 173.

[7]. (a) Boerlage, S. F. E.; Kennedy, M. D.; Bremere, I.; Witkamp, G. J.; Vander-Hoek, J. P.; Schippers, J. C. *J. Membr. Sci.* **2002**, *197*, 251. (b) Bonne, P. A. C.; Hofman, J. A. M. H.; Vander Hoek, J. P. *Desalination* **2000**, *132*, 109.

[8]. Xiao, B.; Thomas, K. M. *Langmuir* **2004,** *20,* 4566.

[9]. (a) Ku´znik, N.; Krompiec, S. *Coordination Chemistry Reviews* **2006**, doi:10.1016/j.ccr.2006.07.006 (b) Bergbreiter, D. E. *Catal. Today* **1998,** *42*, 389. (c) Bergbreiter, D. E.; Case, B. L.; Liu, Y. S.; Careway, J. W. *Macromolecule*, **1998**, *31*, 6053.

[10]. Yang, L.; Su, Y.; Xu, Y.; Wang, Z.; Guo, Z.; Weng, S.; Yan, C.; Zhang, S.; Wu, *J. Inorg. Chem.* **2003**, *42*, 58444.

[11]. Catte, A.; Cesare-Marincola, F.; vander Maarel, J. R. C.; Saba, G.; Lai, A.; *Biomacromolecules* **2004,** *5*, 1552.

[12]. (a) Glusker, J. P.; Katz, A. K.; Bock, C. W. *The Rigaku Journal,* **1999,** *16,* 8. (b) Felix, C. C.; Hyde, J. S.; Sarna, T.; Sealy, R. C. *J. Am. Chem. Soc.* **1978,** *100,* 3922.

[13]. Prigent-Dachary, J.; Faucon, J. -F.; Boisseau, M. R. And Du Fourcq, J. *Eur. J. Biochem.* **1986**, *155*,133.

[14]. (a) Tasaki, I.; Byrne, P. M. *Biopolymers*, **1994**, *34*, 209. (b) Iwasa, K.; Tasaki, I.; Gibbons, R. C. *Science,* **1980**, *210*, 338.

[15]. Kim, Y. J.; Jung, D.Y. *Bull. Korean Chem. Soc.* **1999**, *20*, 827.

[16]. (a) Mandal, S.; Sastry, M. *Mater. Res. Bull.* **2002**, *37*, 1613. (b) Mandal, S.; Damle, C.; Sainkar, S.R.; Sastry, M. *J. Nanosci. Nanotech,* **2001**, *1*, 281. (c) Damle, C.; Kumar, A.; Sastry, M. *J. Mater. Chem.* **2002**, *12*, 1860. (d) Rautaray, D.; Kumar, A.; Reddy, S.; Sainkar, S. R.; Sastry, M. *Crystal Growth & Design* **2002**, *2*, 197. (e) Rautaray, D.; Sainkar, S. R.; Sastry, M. *CrystEngComm* **2003**, *5*, 400. (f) Rautaray, D.; Sainkar, S. R.; Sastry, M. *Langmuir* **2003**, *19*, 888. (g) Rautaray, D.; Sainkar, S. R.; Sastry, M. *Chem. Mater.* **2003**, *15*, 2809. (h) Rautaray, D.; Sinha, K.; Sainkar, S. R.; Pasricha, R.; Pavaskar, N. R.; Sastry, M. *J. Am. Ceram. Soc.* **2004**, (*In Press*).

[17]. Nanoparticles Building Blocks for Nanotechnology, Edited by Vincent Rotello, Kluwer Academic/Plenum Publishers, New York, **2004**, pp 225-250.

[18]. (a) Sastry, M.; Patil, V.; Mayya, K. S. *J. Phys. Chem. B* **1997**, *101,* 1167. (b) S.; Mann, *Nature* **1988**, *332*, 119.

[19]. Ganguly, P.; Paranjape, D. V.; Pal, S.; Sastry, M.; *Langmuir* **1994**, *10*, 1670.

[20]. (a) Fu, L.; Liu, X.; Zhang, Y.; Dravid,V. P.; Mirkin, C. A. *Nano lett.* **2003,** *3*, 757. (b) Murray, C. B.; Sun, S.; Doyle, H.; Betley, T. A. *MRS Bull.,* **2001**, 985. (c) Puntes, V. F.; Krishnan, K. M.; Alivisatos, A. P. *Appl. Phys. Lett.* **2001**, *78,* 2187. (d) Wang, W.; Efrima, S.; Regev, O.; *Langmuir* **1998**, *14*, 602. (e) Wang, W.; Chen, X.; Efrima, S. *J. Phys. Chem. B* **1999**, *103*, 7238.

[21]. Perdew, J. P.; Burke, K.; Ernzerhof, M. *Phys. Rev. Lett.* **1998**, *80*, 891.

[22]. Baroni, S.; Corso, A. D.; Gironcoli, S.; Giannozzi, P. http://www.pwscf.org.

[23]. Hohenberg, P.; Kohn, W. *Phys. Rev.* **1964**, *136*, 863B.

[24]. Kohn, W.; Sham, L. J. *Phys. Rev.* **1965**, *140*, 1133A.

[25]. Vanderbilt, D. *Phys. Rev. B* **1990**, *41*, 7892.

[26]. http://www.library.cornell.edu/nr/bookcpdf/c10-7.pdf

[27]. Pouchart , C. J. *The Aldrich Library of Infrared Spectra edition III,* Aldrich Chemical Company, Wisconsin, Pages 283 and 286.

[28]. Wagner, C. D.; Riggs, W. M.; Davis, L. E.; Moulder, J. F.; Muilanberg, G. E. *Handbook of X-ray Photoelectron Spectroscopy*, **1979,** pp160-161

[29]. Waghmare, U. V.; Hill, N. A.; Kandpal, H.; Seshadri, R. *Phys. Rev. B* **2003**, *67*, 125111.

[30]. Huhyee, J. E. *Inorganic Chemistry* (Third Edition)

[31]. Waghmare, U. V.; Rabe, K. M.; in Materials Fundamentals of gate Dielectrics, ed. A. A. Demkov and A. Navrotsky (Springer, The Netherlands, **2005**), pp. 215.

Chapter IV

Synthesis of magnetic metallic nanoparticles using liquid foams as template followed by their conversion to magnetic-core noble metal-shell systems via transmetallation reaction

---

This chapter demonstrates the use of foam lamellae as a dynamic template for the synthesis of magnetic nanoparticles. A combination of extremely large interfacial area provided by the foam lamellae comprising of surfactants and electrostatically complexed metal ions with the surfactants, have been used successfully for the synthesis of magnetic metal nanoparticles such as Co and Ni. This was accomplished by first making a dry foam with Co^{2+} / Ni^{2+} ions, SDS (surfactant) and oleic acid (capping agent) molecules followed by reduction with $NaBH_4$ solution. These metallic magnetic nanoparticles were further utilized for the formation of magnetic-core noble metal-shell type nanocomposites by performing transmetallation reaction with silver ions, which not only increased the functionality of the samples but also the stability of the core from aerial oxidation. Detailed magnetic characterization based on the variation of magnetization with temperature and applied field are presented. The utility of ESR spectroscopic study in characterizing the magnetic metal nanoparticles and their core-shell analogues is also described.

Part of this work has been published in:
(1) Bala, T.; Arumugam, S. K.; Pasricha, R.; Prasad, B. L. V.; Sastry, M. *J. Mater. Chem.* **2004**, *14*, 1057. (2) Bala, T.; Bhame, S. D.; Joy, P. A.; Prasad, B. L. V.; Sastry, M. *J. Mater. Chem,* **2004**, *14,* 2941. (3) Bala, T.; Enoki, T.; Prasad, B. L. V. *Chem. Phys. Lett.* **2006** (communicated)

4.1. INTRODUCTION:

Magnetism has fascinated human beings from time immemorial because of their brilliant attraction-repulsion capability and amazing pole-seeking properties. The presence of these extraordinary capacities of the magnetic materials inspired inventors to use them in a range of complex devices, though for this purpose the naturally occurring magnets have been replaced by laboratory based ferromagnets. Even in the present era magnetism is an equally fascinating and interesting branch of science, which can be easily realized from the number of contemporary research activities going on worldwide on this topic. But due to the invention of more and more sophisticated appliances, the requirement of highly functional magnetic materials has become a pre-requisite for many technological applications. In this context, nanomagnetic materials have turned out to be the key component of various technologies of the present time owing to the vast scope of application in diverse fields [1]. Ferrofluid is another material of interest and has found its application in mainly mechanical (e.g. seals, bearing and dampers) and electromechemical (e.g. loudspeakers, stepper motor and sensors) fields [2]. Magnetic metallic nanoparticles like Co, Ni and Fe are imperative for advanced technologies because of their striking superparamagnetic character and improved catalytic activities. In particular Ni nanoparticles are used extensively as catalyst in number of chemical reactions like decomposition of ammonia [3], oxidative dehydrogenation [4], steam reforming [5], hydrogenation [6] etc., as well as for the formation of carbon nanotubes [7]. Co has also been employed as catalyst [8], particularly in intramolecular Pauson Khand reaction to prepare cyclopentenone compounds [8a] or in reaction like cyclotrimerisation of bis-alkynes and cyanamides to obtain multisubstituted 2-aminopyridines, including macrocyclic products [8b]. All these magnetic materials, having unusual properties that cannot be achieved by their bulk counterparts, are also useful for biological applications [9] and of course in recent electronics [10]. But the main quandary in the employment of these magnetic metallic nanoparticles for industrial applications is the unstable nature of the particles. They are inherently prone towards aerial oxidation producing thick layers of oxides surrounding the nanostructures. Hence there is renewed endeavor to overcome this by changing the route of preparation [11], by using different capping agents [12] or even sometimes by depositing a few layers of noble metal as shell on the magnetic core [13]. Magnetic core-noble metal shell systems have attracted considerable attention not only for increasing the stability of the magnetic core but also due to the fact that it can provide enhanced functionality to the system.

Several synthetic routes are available for the preparation of Co and Ni nanoparticles. The general synthetic procedures reported for the synthesis of cobalt nanoparticles could be categorized as: (i) reverse micelle-based methods and (ii) purely organic solution-based methods. Reverse micelles are water droplets in oil stabilized by a monolayer of surfactant. Preparation of cobalt nanoparticles by this method involves multiple steps with the preparation of $Co(AOT)_2$ [AOT = bis(2-ethylhexyl) sulfosuccinate] being the first step [14]. Subsequently, micellar solutions of $Co(AOT)_2$ and sodium borohydride in water with Na(AOT) are mixed to carry out the reduction of Co^{2+} ions. They are then extracted under anaerobic conditions, covered with trioctylphosphine and redispersed in pyridine [14]. Purely organic-based methods also involve complex synthetic procedures and high temperatures where $[Co_2(CO)_8]$ is reduced with hot trioctylphosphaneoxide (TOPO) reagent [15]. The resulting Co nanoparticles are stabilized by the TOPO itself or in several cases by organic carboxylic acids like oleic acid and lauric acid, etc., which are taken together with TOPO. High temperature polyol processes in which a high boiling point alcohol is used both as solvent and as reductant have also been successful in synthesizing cobalt nanoparticles [16]. Here, the typical synthetic procedure involves the addition of 1,2-dodecanediol to hydrated cobalt acetate in diphenyl ether, in the presence of oleic acid and trioctylphosphene at 250 ^{o}C, where particle size control is achieved by changing the relative concentrations of cobalt acetate and oleic acid [16]. There are different methods available for the synthesis of Ni-containing nanoparticles also [17,18] but the frequently used routes for the synthesis of pure Ni nanoparticles involve high temperature decomposition of nickel carbonyl compounds in organic solvents [19], microemulsion based preparatory method [20], reduction of Ni^{2+} with hydrazine in ethylene glycol [21], reduction in water-alcohol medium [22], synthesis by physical method like laser ablation technique in vacuum [23] etc. Most of the above mentioned reports emphasize on the preparation of these particles in the organic medium, utilizing several toxic chemicals and high temperatures. Hence the processes are cumbersome for scaling up and as they are prepared in organic medium, the nanoparticles are incompatible with biological applications.

As an alternative to the above mentioned procedures we present in this chapter liquid foam as a template for the synthesis of different magnetic metal-nanomaterials. Study of liquid foam has so far been restricted to the domain of physicists and only recently Davey et. al. have used foams as templates for the nucleation of calcium carbonate crystals [24]. That concept opened up vast possibility of carrying out a range of chemical reactions in foams for synthesis of nanomaterials. The typical foam-based synthesis of metal nanoparticles involves the following steps: 1) generation of a liquid foam from a mixture of metal salts and a suitable surfactant (if the metal is in cationic form then the surfactant taken is anionic and vice versa); 2) removal of excess liquid by drainage to get a dry foam, and 3) reducing the metal ions in situ by exposure of the foam to suitable reducing agents [24b, c]. While this general procedure works for most of the noble metal nanoparticles, for magnetic metal nanoparticles a slight modification of the procedure was required in the sense that we needed to take oleic acid along with the surfactant inside the foam matrix. We have observed that this leads to the immediate capping and stabilization of the metal nanoparticles with oleic acid as soon as they are formed in the foam. The magnetic characterization revealed that both the Co and Ni nanoparticles are superparamagnetic in nature. Though the magnetic nanoparticles capped by oleic acid are quite stable in nature and can be stored for long time without much deterioration, both Co and Ni nanoparticles were subjected to transmetallation reaction with Ag^+ to form the shell of Ag on top of the magnetic core that gave rise to additional functionality to the system. The details of the enhanced functionality and the ensuing utility of this feature for phase transfer process are delineated in Chapter VI. The composite system of magnetic metal core-Ag shell was thoroughly characterized with different techniques to ensure their composition and also characterized for magnetic properties, which showed that they retain their superparamagnetic nature even after the shell formation.

4.2. SUPERPARAMAGNETIC PROPERTIES:

Cobalt and nickel both are ferromagnetic in their bulk form and are expected to be superparamagnetic in the nano-size regime. As already discussed in Chapter I, the property of superparamagnetism is observed in the single domain particles of a particular size where the anisotropy energy (given by $\Delta E = KV$) can be readily overcome by the thermal fluctuation of the environment. As a result the magnetization of the particle is reversed from the direction of one easy axis to the other. For superparamagnetic particles, the net magnetic moment in zero field and at $T > 0K$, will average to zero. In an applied field, there will be a net statistical alignment of magnetic moments. This is analogous to paramagnetism, except now the magnetic moment is not that of a single atom, but is of a single domain particle containing $\sim 10^5$ atoms on average. Hence, the term superparamagnetism, which denotes a much higher susceptibility value than that for simple paramagnetic substances [25].

To have a rough idea regarding the size limit of Co/Ni nanoparticle to be essentially superparamagnetic, we can employ the equation described in Chapter I (the equation is $f_0\, e^{-KV/kT} = 1/\tau$.) and show that a spherical nanoparticle of Co of diameter 6.8 nm has a relaxation time of 10^{-1} sec. An assembly of such particle can reach thermal equilibrium ($M_r = 0$) almost instantaneously, so M_r will appear zero at any normal measurement and the assembly will appear superparamagnetic. But slight change in the size of the magnetic single domain to say 9-10 nm in diameter leads to a relaxation time of the order $\sim 10^9$ sec, so extremely stable particles results [25a].

Measurement of magnetization with respect to temperature and applied magnetic field not only probes the nature of the magnetic particles but also can conclusively prove the presence of any oxide layers on the top of the magnetic core nanoparticles. The interface between two types of magnetic materials namely ferromagnetic and anti ferromagnetic substance generates exchange anisotropy effect. As CoO and NiO both are anti- ferromagnetic in nature, the possession of few layers of oxide on Co and Ni nanoparticles exemplifies the ideal situation of exchange anisotropy. There are three characteristic features of this interaction: shifted hysteresis loop, sinθ torque curve and rotational hysteresis in magnetic field greater than $2K/M_s$. The cause of shift of the hysteresis curve is delineated below [25b].

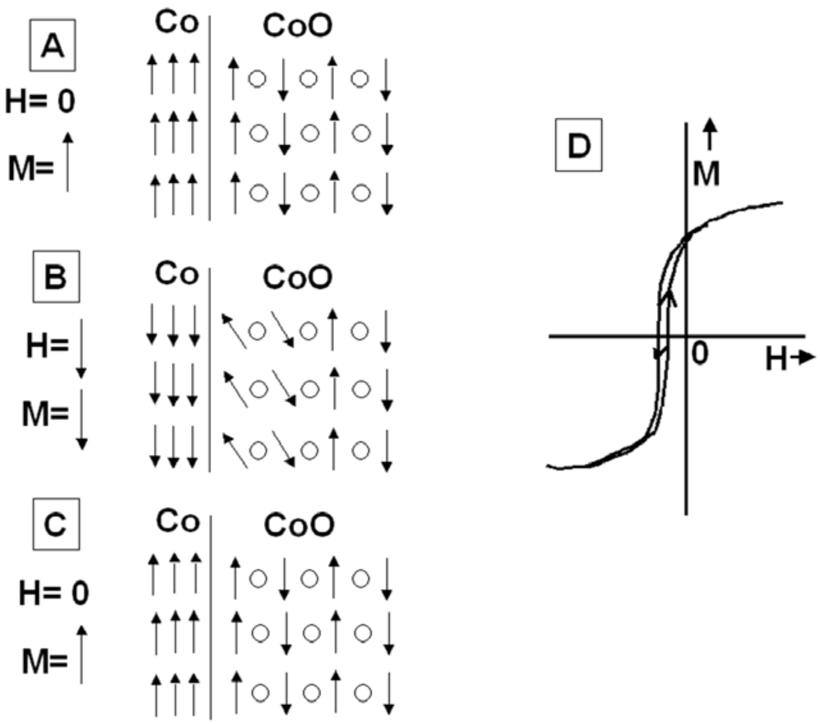

Figure 4.1. *(A-C)****:*** *Orientation of spin of Co and CoO in a Co-core CoO-shell composite system under different conditions. (D) The shifted hysteresis due to the exchange interaction at Co-CoO interface [25a].*

As described in *Figure 4.1* the ferromagnetic Co of Co-CoO system will force the first layer of CoO to align its spin parallel to itself. When the sample is cooled under field below the Neel temperature of pure CoO (~20 ^{o}C), an antiferromagnetic ordering will be achieved by the sample, which can be retained even in the absence of the field *(Figure 4.1A).* Now a strong negative field will reverse the spin of ferromagnetic Co and the exchange coupling at the interface will try to reverse the orientation of spins of the oxide too *(Figure 4.1B)*. But the strong crystal anisotropy in antiferromagnets will definitely resist such change resulting only in the partial rotation in the vicinity of the interface. When this downward field is removed, the up-spins of oxide layer will compel the spins of Co to regain its initial configuration *(Figure 4.1C)*, with a positive retentivity. Thus the hysteresis loop is shifted *(Figure 4.1D)*. So apart from other analytical characterizations the observation of such features in magnetic measurement can clearly indicate the presence of CoO on the surface.

4.3. FOAM AS TEMPLATE:

Liquid foam can be defined as the dispersion of gas bubbles in micronic or submicronic level in a liquid medium. The foam lamellae owe its existence to the presence of surfactant molecules at the liquid-gas interface. The surfactants are basically amphiphilic species containing a hydrophilic (water-loving part of the molecule) head group and a hydrophobic tail (water repelling segment). In particular, the surfactant molecules accumulate at an air-water interface pointing their hydrophilic head towards the liquid phase. A surfactant's activity depends on the sizes of these groups and their relative solubilities. Because of the differing solubilities, surfactants are surface active, that is, they accumulate at surfaces.

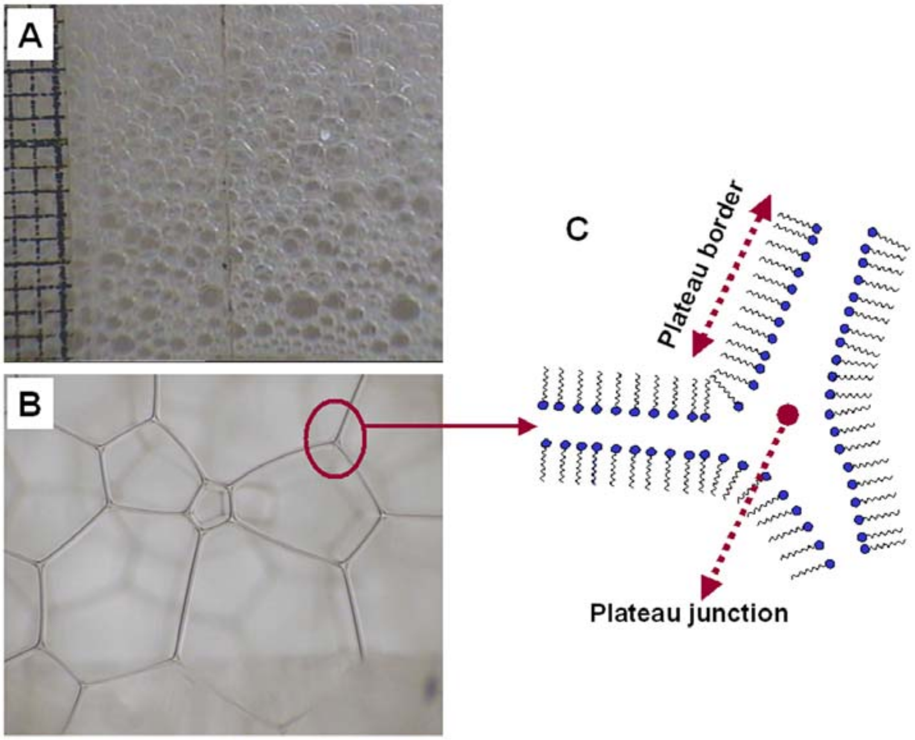

Figure 4.2. *(A) The photograph of wet foams generated with only surfactants without adding any metal ions in the precursor solution. (B) Photograph of the same foam after draining the excess liquid for 20 min. (C) The arrangement of surfactant molecules at the air-liquid interface. The picture is basically demonstrating the internal structure of the highlighted area in (B).*

Initially just after generation of foam, it contains large fraction of liquid in it and the bubbles assume more spherical shape (*Figure 4.2A*). We can achieve dry foam condition by allowing the drainage of excess liquid from wet foam [26]. At the dry foam limit the liquid fraction is at minimum generating polyhedral morphology of the bubbles and providing very thin junctions between the gas bubbles *(Figure 4.2B)*. Here, the ‘liquid lamellae’ are very similar to Langmuir monolayers juxtaposed one on top of the other with the thickness corresponding to a few nanometers *(Figure 4.2.C)*. The second location is the junction of four air bubbles, commonly known as Plateau junction, which contains a slightly larger liquid pool generally of micron dimensions [26]. In foam based synthesis method when cations are allowed to bind to the anionic surfactants they get entrapped in the thin Plateau border and Plateau junction region *(Figure 4.3)* where the chemical reaction can be carried out as desired [24].

4.4. SYNTHESIS OF Co AND Ni NANOPARTICLES USING LIQUID FOAM AS TEMPLATE:

In a typical experiment, a rectangular column of 50 cm height and a square base of 10 X 10 cm^2 with sintered ceramic discs embedded in it were used for generation of the foam. An aqueous mixture of 50 ml of 1 X 10^{-3} M cobalt chloride solution, 10 ml of 1 X 10^{-3} M oleic acid in methanol and 40 ml of 1 X 10^{-1} M SDS was taken in the rectangular column and the foam was built up by injecting nitrogen at a pressure of 1-5 psi through the porous ceramic disc fixed to the bottom of the foam column. Stable foams of upto 50 cm height could be routinely obtained. The foam column was kept as it was for 15 min so that the excess liquid was drained out from the foam lamellae and very dry foam was generated. After carefully draining out the excess aqueous SDS/oleic acid + $CoCl_2$ solution from the foam with the help of an outlet attached at the bottom of the column, the cobalt ions in the foam were subjected to reduction by spraying 0.5% sodium borohydride solution into the foam. The cations bound to the surfactants in the Plateau border and Plateau junctions, were reduced by the strong reducing agent $NaBH_4$ immediately after spraying. As the cobalt ions were reduced and nanoparticle formation progressed, the foam changed to a gray color and gradually collapsed. The collapsed foam solution containing the cobalt nanoparticles was collected through the outlet at the bottom of the column. The details of the steps are clearly depicted in *Figure 4.3.* This solution was then subjected to centrifugation at 5000 rpm for 30 minutes following which the pellet and supernatant were separated. The pellet was washed several times with ethanol before further characterizations were carried out. This pellet could be easily redispersed either in water or organic solvents like toluene.

In a control experiment, the foam was formed without prior addition of oleic acid and the reduction was carried out. Although the experiment progressed exactly the same way as in the presence of oleic acid, the final cobalt nanoparticle solution was extremely unstable and except TEM no further characterization could be carried out. The color of the solution changed from grayish black to dirty green within half an hour of the formation of the particles.

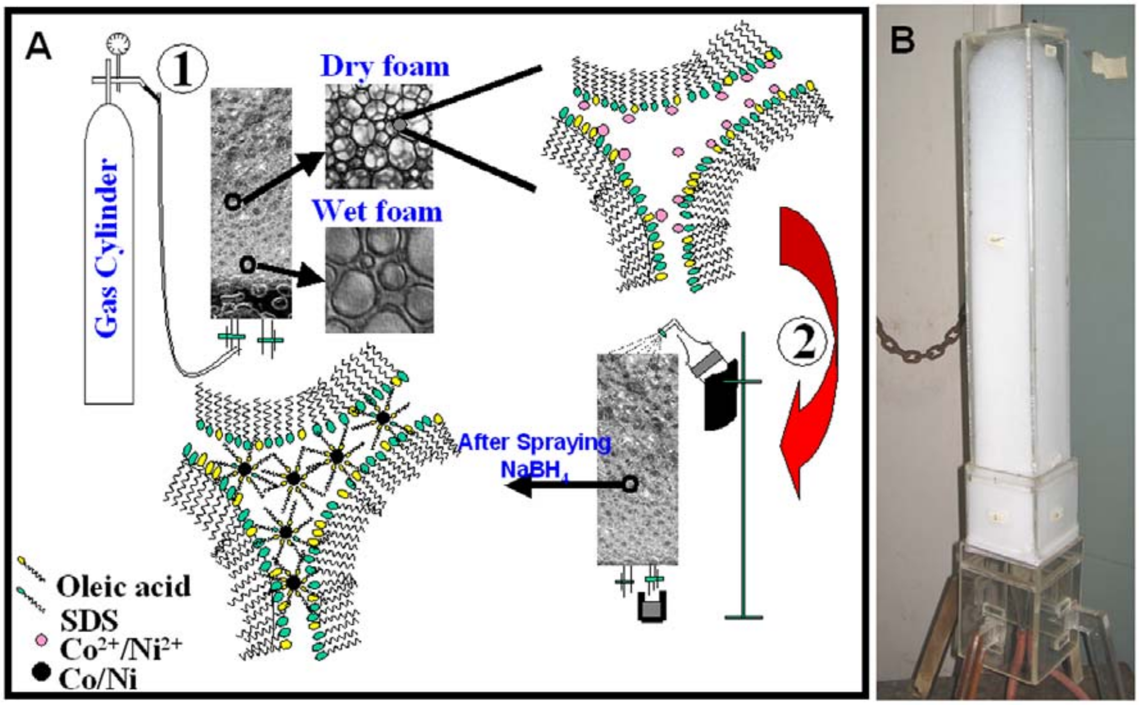

Figure 4.3. *(A) Scheme showing the different steps involved in the foam-based synthesis of stable cobalt/nickel nanoparticles. Steps 1 and 2 are described in the text in detail. (B) The actual photograph of the foam column that is used for carrying out all the experiments.*

Ni nanoparticles were also prepared by following the same foam-based protocol. In this case, an aqueous mixture of 50 ml of 1 X 10^{-3} M nickel nitrate solution, 10 ml of 1 X 10^{-3} M oleic acid in methanol and 40 ml of 1 X 10^{-1} M SDS was placed in the base and the foam was built up by injecting nitrogen. After drainage, the nickel ions in the foam lamellae were subjected to reduction by spraying sodium borohydride solution. As the nickel ions were reduced to nanoparticles the foam changed to gray-black and gradually collapsed. The collapsed foam solution containing the oleic acid capped Ni nanoparticles was collected and was then subjected to centrifugation at 5000 rpm for 30 minutes following which the pellet and supernatant were separated. The pellet was washed several times and dissolved in water before further characterizations were carried out. Unlike the previously prepared Co nanoparticles, the Ni nanoparticles could not be dispersed in organic solvent like toluene.

All chemicals and solvents required for the experimental purpose were purchased from Aldrich Chemicals and were used as received.

4.5. CONVERSION OF Co AND Ni NANOPARTICLES INTO CORE SHELL SYSTEM:

We have utilized the redox potentials of Ag and Co/Ni to our advantage to prepare the nano-composites. From the reported redox potentials [27], the reduction of silver ions by cobalt and nickel metal can easily progress according to the simple galvanic exchange reaction which is an energetically favorable reaction. This forms the basis of core-shell structure formation in our scheme. The transmetallation reactions in both the cases are spontaneous and should occur according to the equations mentioned below.

$Ag^+ + e^- \rightarrow Ag^0$ +0.80 V ------------ (1)
$Co^{2+} + 2e^- \rightarrow Co^0$ -0.28 V ------------- (2)
$Ni^{2+} + 2e^- \rightarrow Co^0$ -0.23 V ------------- (3)

Therefore,

$Co^0 + 2Ag^+ \rightarrow Co^{2+} + 2Ag^0$ + 1.08 V ----------- (4),
$Ni^0 + 2Ag^+ \rightarrow Ni^{2+} + 2Ag^0$ + 1.03 V ----------- (5),

For the preparation of core-shell nanoparticles, the pellet of oleic acid-stabilized Co/Ni nanoparticles (5 ml) was collected after centrifugation, washed several times with ethanol and dissolved in water. To this, 1ml of 5 X 10^{-5} M Ag_2SO_4 solution was added. The color of the solution changed to brownish yellow indicating formation of the Ag shell. There are reports of using similar methodology for the formation of core-shell structures in the literature [28]. However, in many cases, those reactions are carried out at elevated temperatures and with slightly complex reaction conditions.

4.6. UV-VIS SPECTROSCOPY:

The optical properties of the oleic acid-stabilized Co nanoparticle and the $Co_{core}Ag_{shell}$ solutions were probed by UV-vis spectroscopy (*Figure 4.4 A curves 1 and 2,* respectively). The Co nanoparticles solution was obtained after the re-dispersion of the centrifuged pellet in water. The spectrum of oleic acid capped Co nanoparticles (*curve 1, Figure 4.4A)* does not reveal any peak in the studied wavelength region. The graph showed a monotonic increase in the absorbance towards the lower wavelength region. The trend is in good agreement with the reported spectra for Co nanoparticles [29]. After reaction of the Co nanoparticle solution with Ag_2SO_4, a clear peak around 410 nm is observed (*curve 2, Figure 4.4A)* and is attributed to the formation of metallic silver in the nanoscale regime. This absorption band arises due to excitation of surface plasmon vibrations in the Ag shell [29].

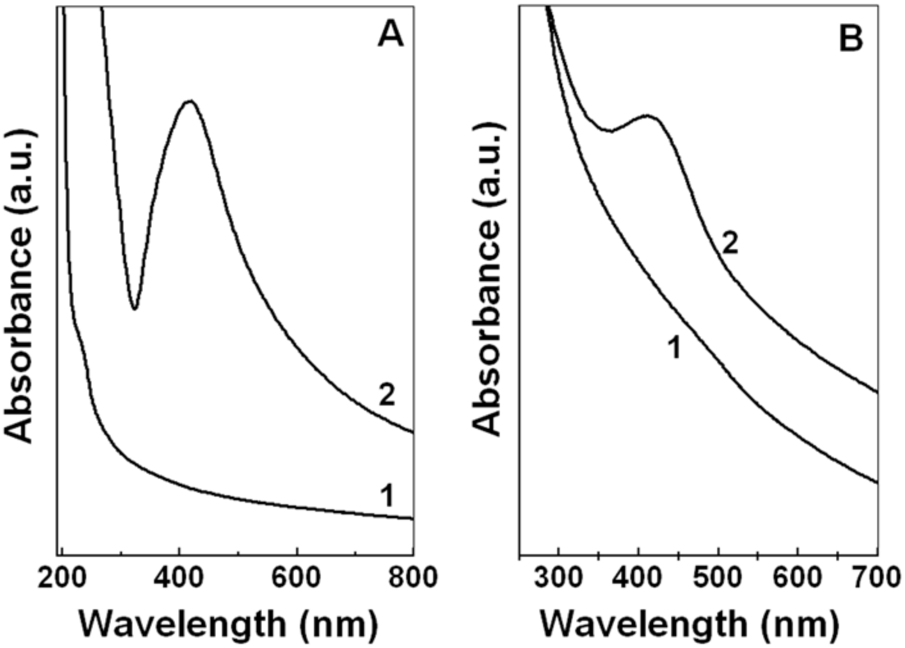

Figure 4.4. *(A) UV-Vis spectra of the cobalt nanoparticle (curve 1) solution and that of the* $Co_{core}Ag_{shell}$ *nanoparticle solution (curve 2). (B) UV-Vis spectra of Ni nanoparticles formed by foam based synthetic method (curve 1). Curve 2 revealed the growth of Ag plasmon peak when the spectrum was recorded after the transmetallation reaction carried out with* Ag^+.

The UV-Vis spectrum of the pristine oleic acid capped Ni nanoparticles *(Figure 4.4B, curve 1)* is also featureless and agrees well with those reported for Ni nanoparticles

[29]. The development of a surface plasmon resonance peak around 415 nm attributed to silver in the nanoscale regime is observed once the transmetallation reaction is carried out *(Figure 4.4B, curve 2)*.

4.7. X-RAY DIFFRACTION ANALYSIS:

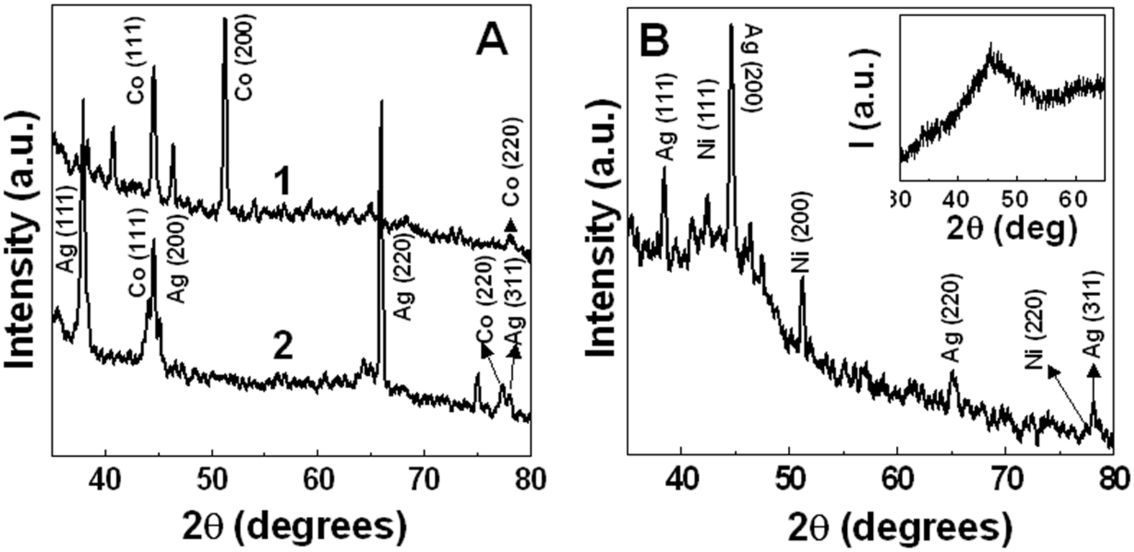

Figure 4.5. *(A) X-Ray diffractogram recorded from films of Co-core (curve 1) and Co-core Ag-shell nanoparticles (curve 2) solutions drop coated onto glass substrates. (B) Similar XRD pattern obtained from the Ni-core Ag-shell nanoparticles when the solution was drop coated on a glass plate. The inset is the XRD evidence of pristine oleic acid capped Ni nanoparticles.*

X-ray diffraction analysis of oleic acid-stabilized Co nanoparticle and the $\mathrm{Co_{core}Ag_{shell}}$ nanoparticles were performed on the film made by drop coating with the respective solutions on glass substrates. A number of Bragg reflection planes corresponding to the *fcc* Co [30] could be identified and indexed accordingly as shown in *curve 1, Figure 4.5A.* This is in agreement with earlier reports wherein it was observed that while bulk cobalt assumes an hcp phase, smaller particles, especially in the nanoscale regime, crystallize in the *fcc* phase [30]. The diffraction pattern changes after the formation of Ag-shell on the Co core *(curve 2, Figure 4.5A)* when the Bragg reflections of *fcc* Ag (a= b= c= 4.067, space group= fm3m, PCPDF # 030931) appeared along with the peaks for *fcc* Co. As both Co and Ag have diffraction planes at $2\theta \sim 44^{o}$, the peak could be seen to broaden in this region as compared to the peak of pristine oleic acid capped Co nanoparticles. The appearance of separate Ag peaks at the position of *fcc* Ag along with the peaks for Co nanoparticles also confirmed the fact that transmetallation led to only core shell structures and not to the alloy formation of the two metals.

Similar XRD analysis was also performed on the Ni and $Ni_{core}Ag_{shell}$ nanoparticles after forming drop-cast film on glass substrates and the diffractograms are demonstrated in the *Figure 4.5B*. Because of the poor crystalline nature of the sample, oleic acid capped Ni nanoparticles revealed only one broad peak *(inset Figure 4.5B)* at 2θ ~ 44° which corresponds to the (111) plane of the *fcc* Ni nanoparticles (a= b= c= 3.523, space group= Fm3m, PCPDF # 040850). But the crystallinity definitely improved after the transformation of Ni nanoparticles to Ni-core Ag-shell nanocomposites as is very much evident from main graph in *Figure 4.5B,* but the fact is not very well understood at this moment. In this case along with the *fcc* Ag peaks, a number of Bragg refections for Ni could also be recognized from the graph.

4.8. ENERGY DISPERSIVE ANALYSIS OF X-RAYS:

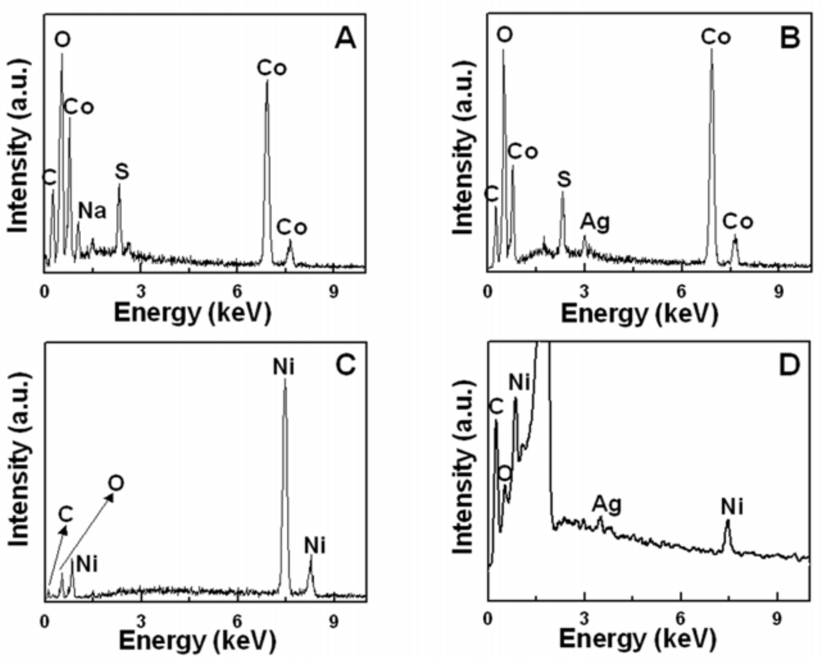

Figure 4.6. *Spot profile EDAX spectra recorded from the Co (graph A) and Ni (graph C) nanoparticles synthesized by foam based method. EDAX analysis was also performed on the* $Co_{core}Ag_{shell}$ *(graph B) and* $Ni_{core}Ag_{shell}$ *(graph D) system obtained after the transmetallation reaction.*

Additional proof for the formation of Co-Ag nanocomposite came from the EDAX analyses of the powdered samples. *Figure 4.6A and B* illustrates the EDAX signals obtained from powdered Co and $Co_{core}Ag_{shell}$. In addition to the expected Co signal there are strong signatures of the elements C, O and weak peaks from Na and S (*Figure 4.6A)*. The presence of C and O can be rationalized due to the presence of capping agent oleic acid on the surface of the nanoparticles, whereas Na and S sources are possibly the precursors used in the synthesis like $NaBH_4$ and SDS. The presence of adsorbed SDS on the nanoparticle surface cannot be ruled out completely even after repeated centrifugation. The appearance of Ag peak in *Figure 4.6B* after transmetallation reaction confirmed the presence of silver in the nanocomposites.

Similar data for Ni and $Ni_{core}Ag_{shell}$ are presented in *Figure 4.6C and D*. Here also, no Ag peak was observed in *Figure 4.6C* indicating the reduction of Ag^+ only after the transmetallation reaction. The existence of Ni peak along with Ag in *Figure 4.6D* signified the formation of composite system.

4.9. TRANSMISSION ELECTRON MICROSCOPY:

4.9.1. TEM Study for Co and Co-core Ag-shell System:

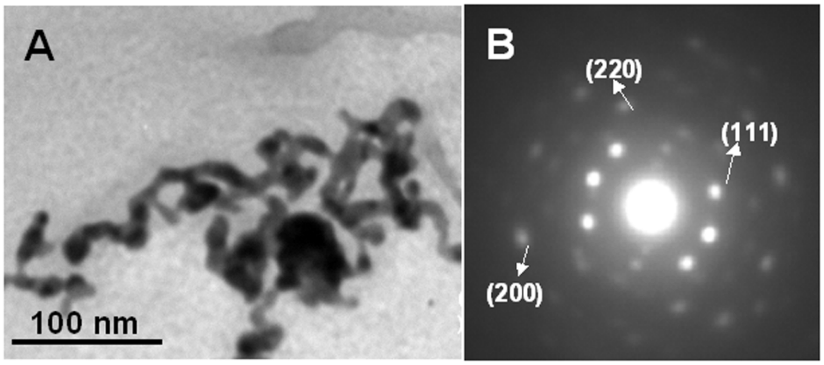

Figure 4.7. *(A) TEM pictures of cobalt nanoparticles. These were obtained when the foam was formed from the aqueous mixture of* Co^{2+} *ions and SDS. (B) Selected area electron diffraction from the same particles. The diffraction pattern could be indexed to the fcc phase of cobalt.*

Figure 4.7A shows the TEM image of cobalt nanoparticles prepared with just SDS and cobalt ions as the foam constituents. Particles with typically tape-like morphology are observed along with very small percentage of spherical particles. The

Selected Area Electron Diffraction (SAED) pattern from these particles *(Figure 4.7B)* clearly supports the formation of crystalline cobalt nanoparticles. It is important to note here that this particular sample was imaged immediately (within minutes) after the sample preparation. The cobalt nanoparticle solution prepared with only SDS as the foaming agent was grayish-black in color immediately after preparation. However, within few minutes this solution was observed to turn green. Powder X-ray diffraction analysis of a film prepared from this green solution revealed the formation of cobalt oxide. Hence this procedure was abandoned and we have used an alternative strategy for obtaining stable cobalt nanoparticles using oleic acid for capping the nanoparticles along with SDS in experimental technique. The transmission electron micrographs of the nanoparticles obtained by the alternative strategy are displayed in *Figure 4.8A and B*.

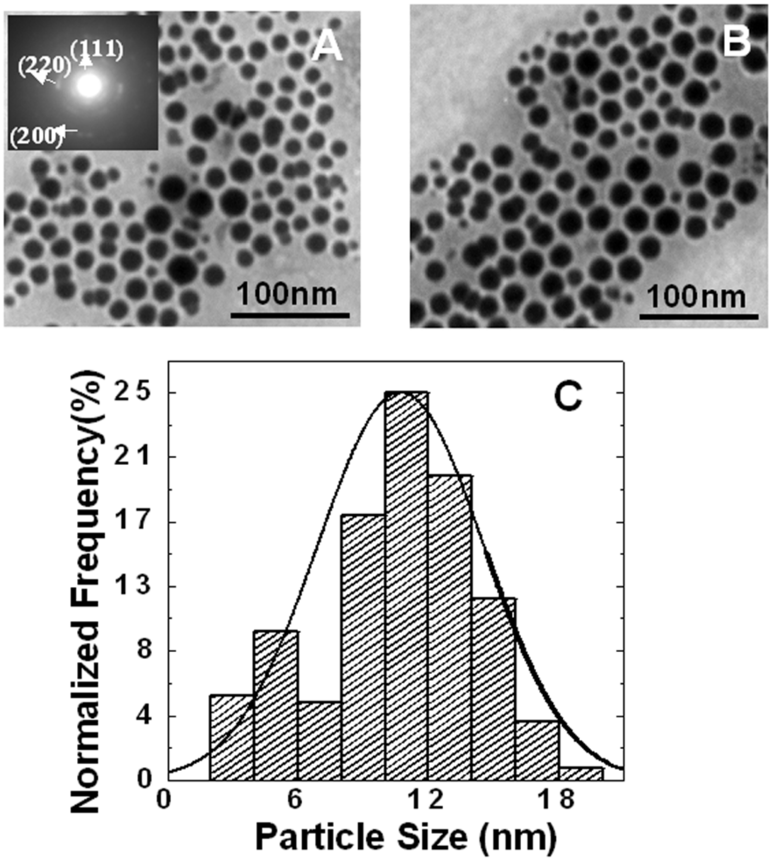

Figure 4.8. *(A), (B) TEM pictures, from different areas on the grid, of cobalt nanoparticles obtained when oleic acid was added to the* Co^{2+} *and SDS aqueous mixture prior to the formation of foam. The SAED pattern indexed to fcc cobalt is included as the inset in (A). (C) A particle size histogram of Co nanoparticles.*

A perceptible change in the morphology and arrangement of the nanoparticles is clearly visible. This suggests an important change in the environment around the cobalt ions when the reduction is taking place inside the foam in presence of mixed surfactant like oleic acid and SDS. The particles are predominantly spherical and of uniform size. Analysis of the particle size histogram obtained from measurement of the diameters of over 250 particles revealed the average size to be 11 ± 3 nm *(Figure 4.8C).* These particles are also crystalline as can be clearly seen from the electron diffraction which has been indexed to *fcc* phase of cobalt *(inset Figure 4.8A).* The SAED pattern clearly verifies the result obtained from the XRD analysis. The striking difference in the contrast of the TEM pictures recorded from the Co nanoparticle solution after addition of silver salt *(Figure 4.9A–C)* clearly reveals the Co core and Ag shell.

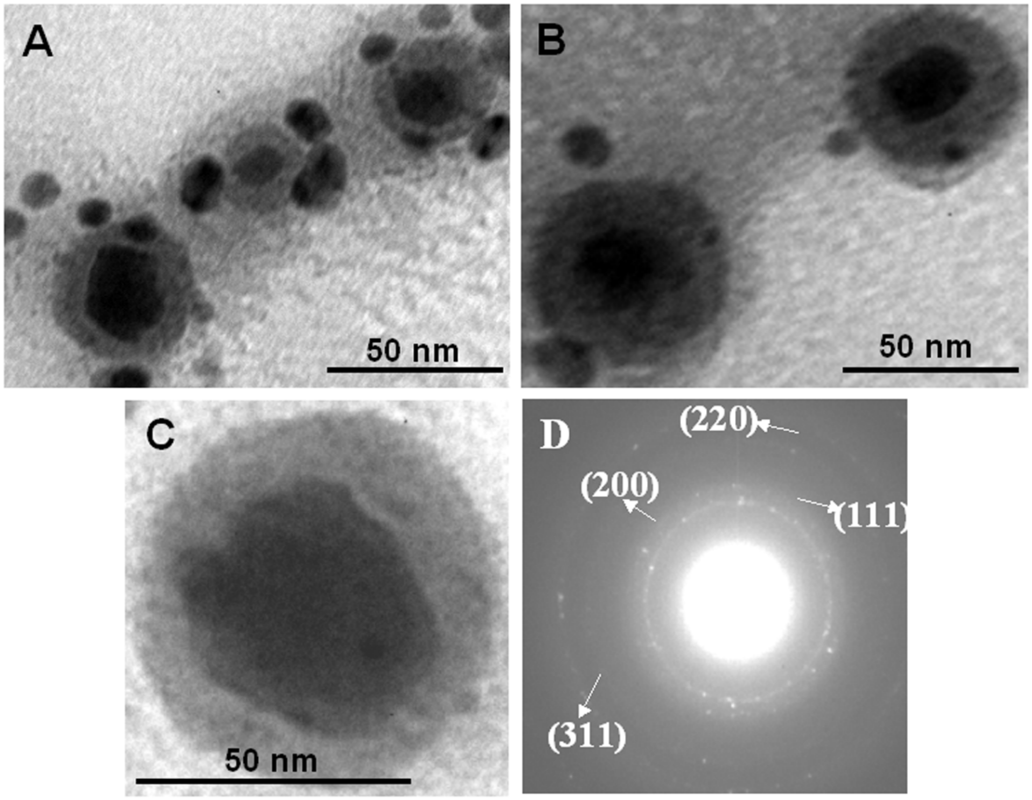

Figure 4.9. *(A), (B) TEM pictures of $Co_{core}Ag_{shell}$ nanoparticles from different areas of the TEM grid. (C) Represents a higher magnification image from the region shown in (A). (D) Selected area electron diffraction pattern from these particles.*

The electron diffraction from the core–shell structures *(Figure 4.9D)* could be indexed based on the *fcc* structure of silver. The SAED pattern did not show any reflections that could be associated with the core cobalt nanoparticles. While this is not fully understood at this stage, a possible explanation could be that the presence of a thick Ag shell (ca. 3–5 nm thick) prevents efficient electron scattering from the cobalt core.

4.9.2. TEM Analysis of Ni Nanoparticles and Its Core-Shell Nano Composite:

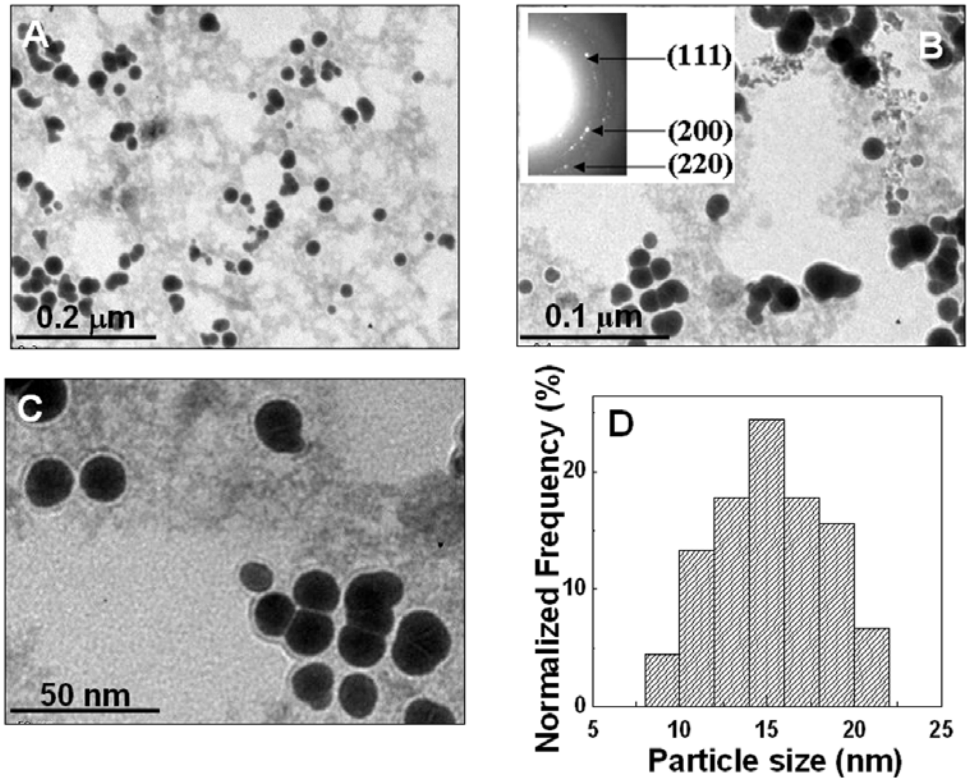

Figure 4.10. *(A–C): Representative TEM images of Ni nanoparticles from several areas of the grid. The selected area diffraction and the indexing of the rings to the fcc phase of nickel are provided in the inset of B. Note the diffuse spot pattern obtained (see text for more details). The particle size distribution (D) reveals the average size to be around 12–15 nm.*

The TEM images of the nickel nanoparticles at different magnification, prepared by the foam based technique are displayed in *Figure 4.10A–C.* It is clear from the TEM images that the Ni nanoparticles prepared by the above procedure are polydisperse in nature with an average size of 12–15 nm *(Figure 4.10D)*. The selected area electron diffraction pattern (SAED) from these nanoparticles revealed a diffuse ring structure with spots superimposed *(inset of Figure 4.10B)*. This suggests that the nanoparticles formed are quite polycrystalline in nature. The ‘d’ values calculated from the positions of the electron diffraction rings agreed well with the ‘d’ values reported for *fcc* Ni. It is worth noting here that no diffraction patterns corresponding to nickel oxides were observed. The nickel nanoparticles are capped by oleic acid as they are being formed in the foam matrix and this could be the reason for extra stability of Ni nanoparticles against oxidation in the aqueous dispersion form as well as in the powder form.

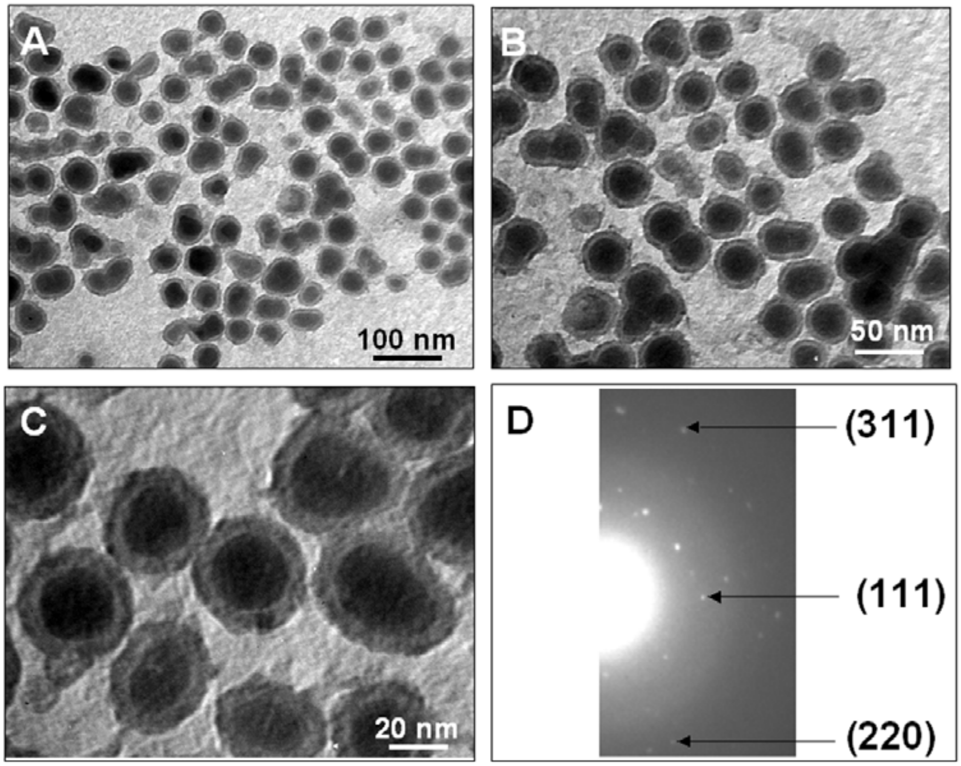

Figure 4.11. *(A–C) Representative TEM images of the* $Ni_{core}Ag_{shell}$ *system. (D) SAED diffraction pattern from the* $Ni_{core}Ag_{shell}$ *nanoparticles with rings indexed with respect to fcc silver.*

The TEM images of the $\mathrm{Ni}_{\mathrm{core}}\mathrm{Ag}_{\mathrm{shell}}$ system are presented in *Figure 4.11A–C*. The particles clearly show a core capped with a shell indicating the formation of a $\mathrm{Ni}_{\mathrm{core}}\mathrm{Ag}_{\mathrm{shell}}$ structure. The core–shell structure is more clearly seen in the higher magnification image *(Figure 4.11C)*. The size of core–shell particles range from 15–30 nm. The SAED pattern recorded from the $\mathrm{Ni}_{\mathrm{core}}\mathrm{Ag}_{\mathrm{shell}}$ nanoparticles is shown in *Figure 4.11D*. The pattern is characteristic of polycrystalline particles and the rings could be indexed with reference to the *fcc* silver structure. This indicates that the shell is reasonably thick (as inferred from the TEM images) and prevents penetration of the electron beam to the Ni core just like in the previous case of cobalt.

4.10. FOURIER TRANSFORM INFRA-RED SPECTROSCOPY:

It is expected that after following the purification process as described in the section 4.2.1, the excess surfactant SDS and the uncoordinated oleic acid were removed and the surface bound organic molecules were only present in the purified Co/Ni nanoparticle solution. This solution was drop coated on Si (111) substrate for the FTIR analysis to check the presence of capping agent on the surface of the Co/Ni nanoparticles. Similarly FTIR was performed on $Co_{core}Ag_{shell}$ and $Ni_{core}Ag_{shell}$ nanoparticles also and are displayed in *Figure 4.12 and Figure 4.13* respectively. The spectrum of pure oleic acid was recorded for comparison *(Figure 4.12, curve 1).*

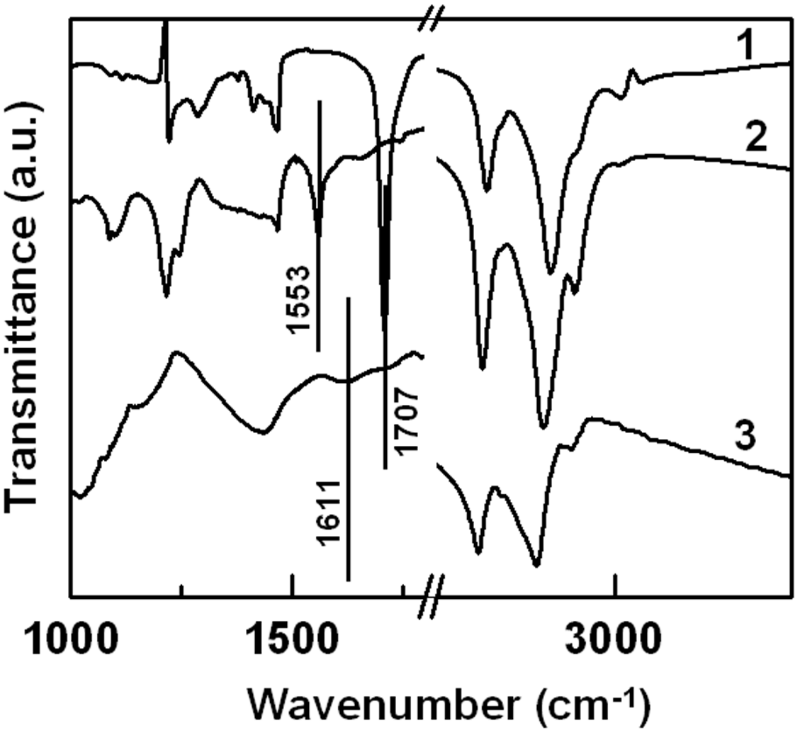

Figure 4.12. *FTIR spectra of pure oleic acid (trace 1), Co nanoparticles capped with oleic acid (trace 2), and Co-core Ag-shell nanoparticles capped with oleic acid (trace 3).*

The carboxylic acid band around 1707 cm^{-1} in pure oleic acid [31] is shifted to 1553 cm^{-1} in the presence of Co nanoparticles *(Figure 4.12, curve 2)* and to the lower wavenumber of 1611 cm^{-1} after the Ag shell is formed *(Figure 4.12, curve 3)*. In the case of Ni nanoparticles also, the –COOH peak of oleic acid moiety was shifted from 1707 cm^{-1} to 1657 cm^{-1} for pristine oleic acid capped Ni nanoparticles *(curve 1 Figure 4.13)* and to relatively lower wavenumber (1537 cm^{-1}) for NiAg core shell which is shown in *Figure 4.13, curve 2.*

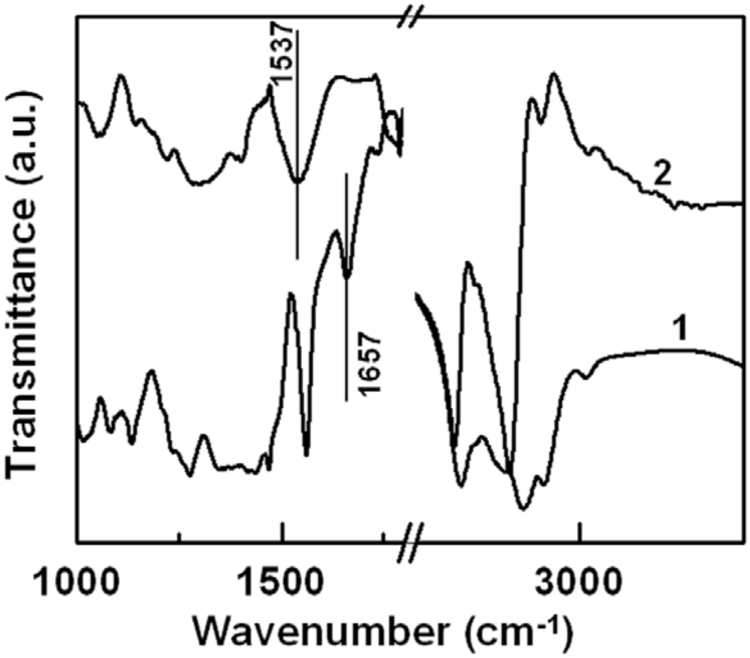

Figure 4.13. *FTIR spectra of Ni nanoparticles formed by foam based synthesis (curve 1) and Ni-core Ag-shell composite in curve 2 after carrying out the transmetallation reaction between Ni nanoparticles and Ag^+ ions in solution.*

These shifts clearly indicate that the chemical environment in which the carboxylate ion present is different in each step of our synthesis: in the first step it is on the surface of the Co nanoparticles and then in the $Co_{core}Ag_{shell}$ case it is bound to the Ag surface. In fact oleic acid is already well known for its ability to stabilize Co nanoparticles [32] and in our study also, we verified its efficiency as capping agent. The capped nanoparticles are more stable and not very prone towards aerial oxidation which prevents the formation of CoO layers on Co nanoparticles. This on the other hand assists the transmetallation reaction facilitating the Ag^+ ion to come in contact with the Co^0 surface. It is already well known that oleic acid binds quite strongly with the Ag surface [32c], so even after the core shell formation the molecules were not detached from the surface of the core-shell. The fact that oleic acid really acts as capping agent for both types of system is substantiated from the FTIR studies. The spectral study of Ni and $Ni_{core}Ag_{shell}$ (*Figure 4.13)* also proves the capping efficiency of oleic acid for Ni nanoparticles. It is worth mentioning here that the double bond of oleic acid molecule is also electron rich and can have significant interaction with the surface of nanoparticles. But the signature of the =C-H in FTIR in the region of ~3000 is very weak and it is difficult to address this issue at this point. So here we have mainly concentrated on the 1500-1700 cm^{-1} region, which is specific for carbonyl functional group of oleic acid. The topic related to the interaction of double bond of the capping agents with the nanoparticles is elaborated in Chapter VI.

4.11. THEROGRAVIMETRIC ANALYSIS:

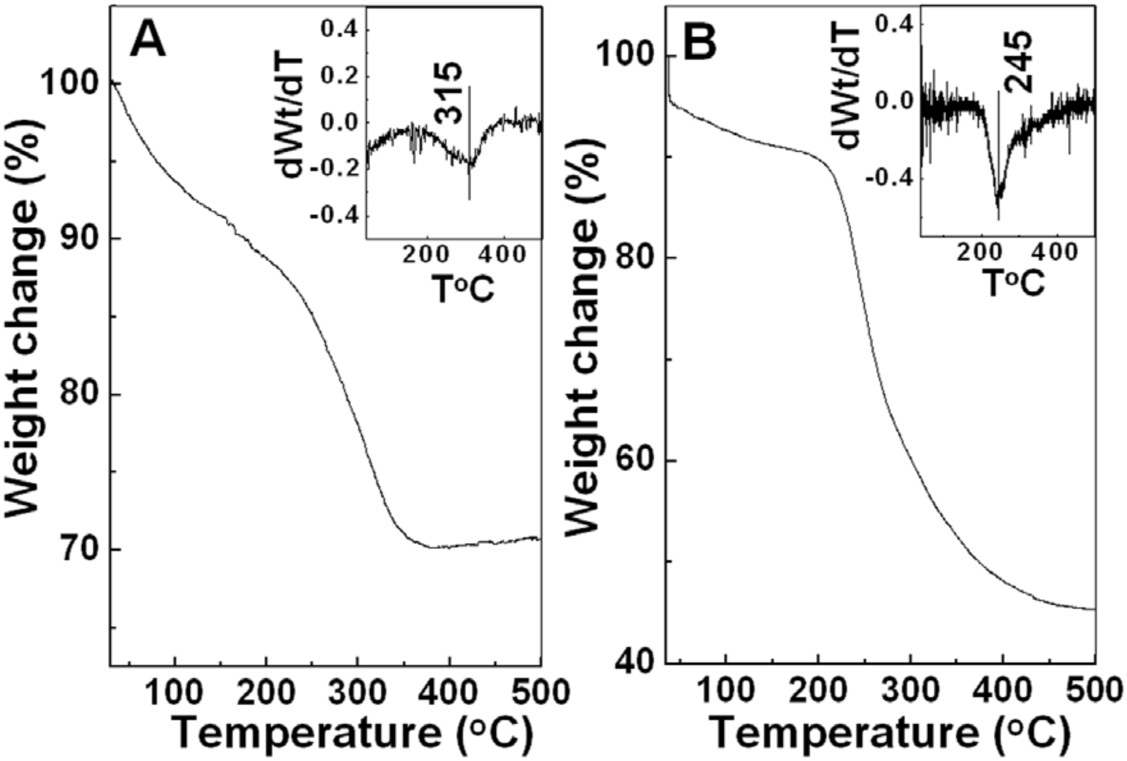

Figure 4.14. *(A) TGA curve of the oleic acid capped nickel nanoparticles. The inset is the first derivative of the weight loss curve indicating that the maximum of weight loss occurs at 315 °C. (B) Similar thermogram of $Ni_{core}Ag_{shell}$ is displayed in this figure, shows a greater weight loss as compared to the core Ni nanoparticles. The major weight loss took place at ~245 °C as observed from the first derivative plot in the inset.*

Thermogravimetric analysis was carried out to determine the amount of capping agent (oleic acid) present per gram of the sample. As shown in *Figure 4.14A* the pristine oleic acid capped Ni nanoparticles show a small weight loss at around 100 °C (probably due to loss of water) that is followed by a more significant weight loss of about 18% around 315 °C. This weight loss is attributed to the desorption/decomposition of oleic acid present on the surface of the Ni nanoparticles. Assuming that the oleic acid forms a close packed monolayer on the surface of the Ni nanoparticle and an area per carboxylic unit of roughly 21.4 $Å^2$ [33], each nanoparticle would be covered by 2000–3250 molecules of oleic acid for the 12–15 nm particles. This translates into roughly 10–12 weight % of oleic acid. Our TGA analysis shows that there is a slight excess of oleic acid on the surface compared with what was expected. A number of factors such as a large variance in the nanoparticle surface area due to polydispersity could contribute to this discrepancy. Such results have been observed earlier for ligands capping nanoparticle surfaces and have been explained on the basis of either smaller area occupied by the ligand on the nanoparticle surface or due to the presence of excess ligand at interstitial sites of nanoparticle aggregates [34].

4.12. ELECTRON SPIN RESONANCE SPECTROSCOPY:

The comparison of the room temperature ferromagnetic resonance spectra of Ni *(curve 1)* and $Ni_{core}Ag_{shell}$ *(curve 2)* nanoparticles is shown in *Figure 4.15A*. Both the samples show broad resonance line at room temperature. The ΔH value in this case is found be 127 mT for Ni nanoparticles of size ~12-15 nm. In order to convert these Ni nanoparticles into core-shell structure we carried out transmetallation reaction as a result of which some Ni atoms from the surface of the nanoparticles are sacrificed for the reduction of Ag^+ to Ag^0. Consequently the size of the magnetic core is reduced. The FMR line width of the core-shell nanoparticles is found to be 90 mT, a value less than found for the pristine Ni nanoparticles itself. It is generally reported that the line width decreases as the size of the magnetic particles decreases [35a]. Thus our results are in concurrence with the expected trends.

Similar electron spin resonance spectra of Co and $Co_{core}Ag_{shell}$ systems are given in *Figure 4.15B*. The spectra of pristine oleic acid capped Co nanoparticles exhibit a width of 70 mT compared to the $Co_{core}Ag_{shell}$ system, which has a line width of 32 mT. So here also the reduction in the line width can be attributed to the reduction of the core size due to transmetallation reaction.

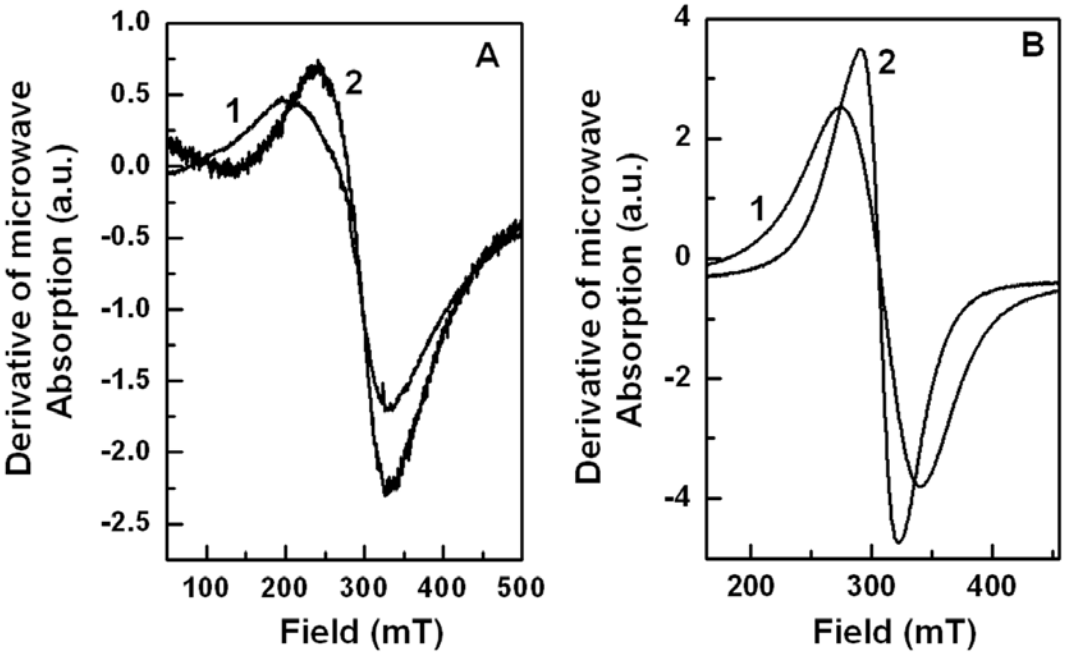

Figure 4.15. *(A) The field dependent FMR spectra of pure Ni (Curve 1) and the core shell system (Curve 2) measured at room temperature. (B) Similar measurement for Co nanoparticles (curve 1) and CoAg coreshell nanocomposite (curve 2).*

The main observations that could be made here are i) the lines of the samples are quite broad for pristine Co/Ni nanoparticles and ii) the line width decreases on the formation of Ag shell by transmetallation reaction on the magnetic Ni/Co nanoparticles. The plausible reasons for the above observations are delineated below. Basically there are several factors upon which the line width depends like the polycrystallinity, state of sample's surface, magnetic anisotropy etc [35]. All the nanoparticles investigated in this study display polycrystalline nature as suggested by SAED patterns and contain oleic acid as capping agent on the surface. So the resonance line obtained by FMR measurement is expected to be broad as compared to single crystalline samples. The decrease in the line widths upon Ag-shell formation could be ascribed to the reduction in size of the Co and Ni nanoparticles due to the reaction with Ag^+ ions. Thus we could show that ESR could be used as a signature to obtain information on the size of the particles as well as core-shell systems.

4.13. MAGNETIC MEASUREMENTS:

The temperature dependence of the magnetization for the Ni and $Ni_{core}Ag_{shell}$ nanoparticles are shown in *Figure 4.16 and 4.19*, respectively. In all the cases, the applied magnetic field was 50 Oe and the temperature was varied between room temperature and 12 K. *Curve 1 in Figure 4.16* corresponds to the magnetization vs. temperature plot for the pristine Ni system in the zero-field-cooled (ZFC) mode while *curve 2* is the measurement carried out in the field-cooled (FC) mode. As can be clearly seen, the curves of temperature dependent ZFC and FC magnetizations are typical of magnetic nanoparticles.

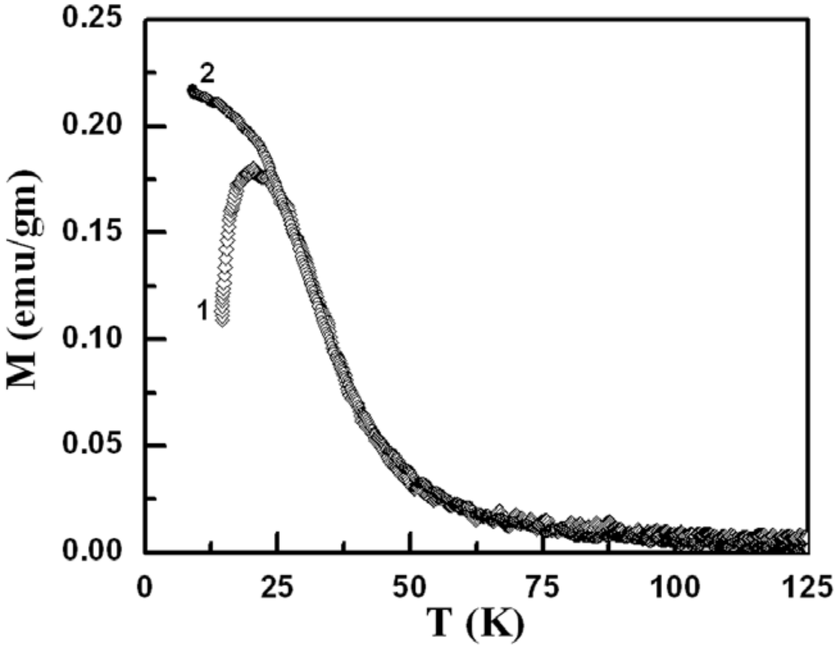

Figure 4.16. *Temperature dependent magnetization of nickel nanoparticles in the zero field cooled (ZFC, curve 1) and field cooled (FC, curve 2) modes. The divergence between the two curves at 20 K is related to the blocking temperature. The applied magnetic field was 50 Oe.*

As already mentioned in the introductory remarks, magnetic particles below a certain size regime behave as superparamagnetic particles. The features characteristic of superparamagnetic particles are: i) the maximum in the zero-field-cooled DC magnetization at a certain temperature, measured using very low magnetic fields, called the blocking temperature, T_B; ii) a divergence in the ZFC and FC magnetization curves below the blocking temperature and iii) magnetic hysteresis loop and remnant magnetization below T_B and the disappearance of magnetic hysteresis above T_B. For the pristine oleic acid capped nickel nanoparticles, the ZFC curve shows a maximum at 20 K and the ZFC and FC curves show a divergence below this temperature revealing that the blocking temperature is ~20 K. The blocking temperature is actually related to the size of the magnetic particles and the magnetocrystalline anisotropy constant (K) by the equation

$$K = (25k_BT_B) / V$$

where k_B and V are the Boltzmann constant and the volume of a single particle, respectively and T_B is the blocking temperature. By substituting the values for a 12 nm particle we deduce K to be 0.76 X 10^5 erg cm^{-3}, which is comparable to that of bulk nickel (0.5 X 10^5 erg cm^{-3}) [25a]. The small difference between the values is expected as we calculated K using the average particle size and not the individual crystallite size which actually controls the individual magnetic directions of the grains and hence the blocking temperature. Apart from this, several other phenomena related to the nanoscale regime such as the structural disorder, surface anisotropy, non-magnetic or weak magnetic interfaces, the lack of surface coordination for the surface magnetic atoms and the electron exchange between the capping agent and surface atoms are also known to influence the magnetic properties. One or several of these phenomena could also have led to the smaller values of the magnetic characteristics in our systems.

The field dependent magnetic behavior data, measured at 12 K (below the blocking temperature, curve 1) and at 60 K (well above the blocking temperature, curve 2) are displayed in *Figure 4.17*. Again, the features observed in the M–H curves are in accordance with those expected for superparamagnetic particles, i.e. i) no saturation was observed in the magnetization even at very high fields (actually up to our instrument limit); ii) magnetic hysteresis with a coercivity of 160 Oe and remnant magnetization below the blocking temperature and iii) disappearance of magnetic hysteresis above the blocking temperature. All these features suggest again that the oleic acid capped nickel nanoparticles prepared by the foam technique indeed behave as superparamagnetic particles. The shape and the position of the hysteresis loop also ruled out the possibility of existence of thick NiO layers at the surface of the particles.

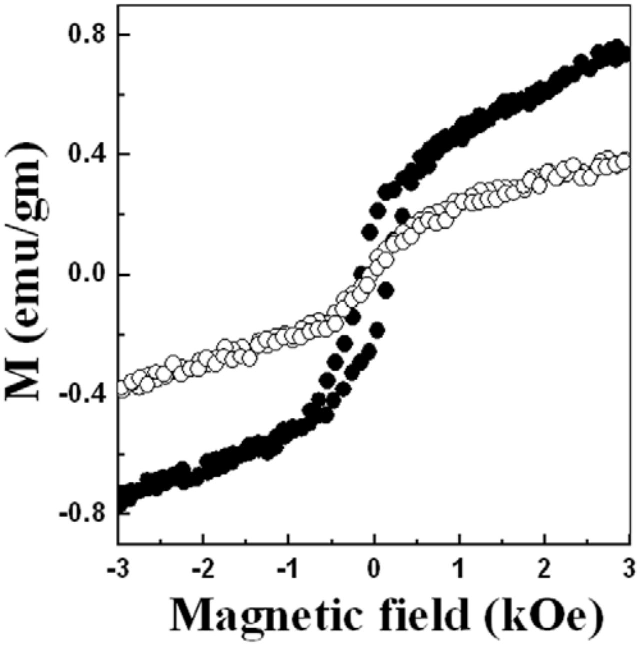

Figure 4.17. *Field dependent magnetization of Ni nanoparticles below (•, 12 K) and above (o, 60 K) the blocking temperature.*

Figure 4.18 symbolizes the magnetic response from Co nanoparticles formed by the above-mentioned method with respect to temperature (*Figure 4.18A)* and applied external field *(Figure 4.18B).*

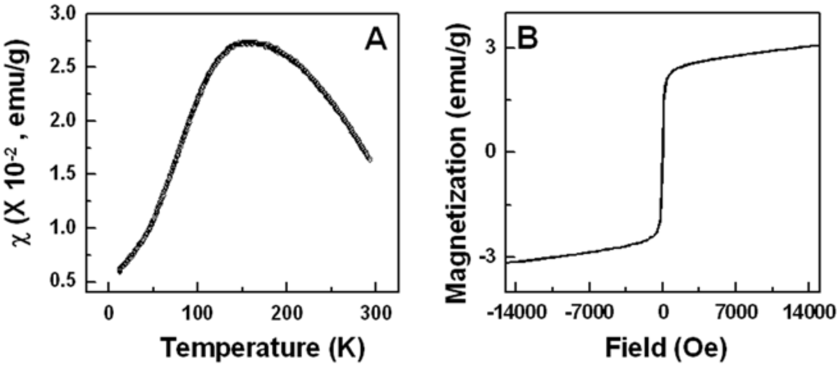

Figure 4.18. *(A) Zero field cooled curve of powdered Co nanoparticles formed by the foam-based method. (B) The field dependent magnetization signature of Co nanoparticles at room temperature.*

The ZFC curve in *Figure 4.18A* detects the blocking temperature as ~150K which matches well with the reported value of Co nanoparticles within this size range. *Figure*

4.18B is the room temperature hysteresis curve of the same Co nanoparticles. The zero M_r and H_c in the hysteresis curve clearly points out to the superparamagnetic behavior of the Co nanoparticles as in the case of Ni nanoparticles.

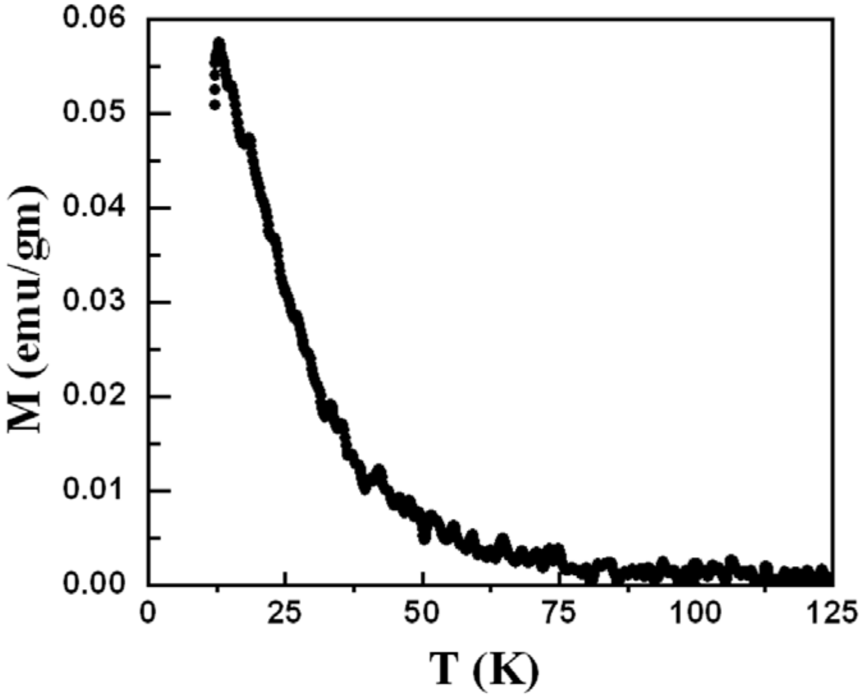

Figure 4.19. *The temperature dependent magnetization of the Ni- core Ag-shell nanoparticles under the same external field.*

The curve in *Figure 4.19* is the temperature dependence of ZFC magnetization observed for the $Ni_{core}Ag_{shell}$ nanoparticle sample. The silver shell around the Ni nanoparticles is formed by a transmetallation reaction wherein a few layers of the surface nickel atoms are oxidized to Ni^{2+} in the process of reducing silver ions. This reduces the average particle size of nickel. Since the as-prepared nickel nanoparticles are polydisperse in nature we observe a polydispersity in the core–shell structures also with the size of the $Ni_{core}Ag_{shell}$ particle in the range of 15–30 nm comprising a core of 10–20 nm size. In general the blocking temperature is expected to shift to lower temperatures as the magnetic particle size is reduced. Accordingly, no maximum in the ZFC susceptibility or no divergence between the ZFC and FC susceptibilities was observed down to 12 K (compared to T_B ~ 20 K for the 12 nm Ni particles) indicating that the blocking temperature is now shifted to below 12 K (the lower limit of our cryostat) which could be attributed to the reduced Ni core size. In fact, the blocking temperature of the 10 nm sized Ni nanoparticles is calculated as ~11 K from the relation $T_B = KV/25k_B$, by using the deduced value of $K = 0.76 \times 10^5$ erg cm^{-3} for the 12 nm Ni particles.

4.14. CONCLUSION:

The Co and Ni nanoparticle solutions prepared by the novel foam-based method were highly stable in aqueous medium against oxidation and sedimentation and could be stored as solutions for long periods of time. An aqueous/organic dispersion of Co nanoparticles could be readily obtained by separating the nanoparticles from water by centrifugation and re-dispersing the resulting paste-like pellet in water/organic solvents such as toluene. Thus, this simple foam-based synthetic procedure yields stable dispersions of magnetic nanoparticles. Although it is difficult to unequivocally ascertain the formation of core–shell structures from UV-vis, EDAX and FTIR studies alone, these results in conjunction with the TEM pictures and XRD results, and the fact that the reduction of Ag^+ ions can take place only on the surface of Co/Ni nanoparticles, clearly provide evidence for the formation $Co/Ni_{core}Ag_{shell}$ structures. The stability of Co/Ni nanoparticles by oleic acid capping may be rationalized in terms of electrostatic complexation of carboxylic acid groups or interaction with the electron rich double bond in oleic acid with Co/Ni ions bound to the surface of the magnetic nanoparticles. This is also supported by the FTIR study. The binding of oleic acid to the nascent Co and Ni nanoparticles could also be responsible for inhibiting anisotropic growth of these nanoparticles, which otherwise is expected for the reaction at air-liquid junction of foam lamellae. The magnetic characterization showed that the particles are superparamagnetic in nature and also provides us very useful information regarding the absence of oxide layer on the surface of the nanoparticles. So we can conclusively affirm the formation of Ni and Co nanoparticles by foam-based technique and as the synthesis of the nanoparticles exploit the dynamic nature of the foam bubbles so the method can be easily upgraded for industrial application. The method is very flexible and can be utilized for the preparation of a range of metallic nanomaterials. As only the desired cations are bound to the surfactants, the probability of the effect of unwanted ions while carrying out the chemical reaction is minimum. In fact anions influence the quality and the crystallinity of the end product in case of many oxide formation processes. As the system can even be employed for more complex systems like simple oxides, sulphides, ferrites etc., the potential of the system to generate superior quality ferrite nanoparticles is explained in the next chapter.

4.15. REFERENCES:

[1]. (a) Nelson, J. A.; Bennett, L. H., Wagner, M. J.; *J. Am. Chem. Soc.* **2002**, *124*, 2979. (b) Bukhtiyarov, V. I.; Slinko, M. G. *Russian Chemical Reviews* **2001**, *70,* 147. (c) Kim, D. K.; Mikhaylova, M.; Wang, F. H.; Kehr, J.; Bjelke, B.; Zhang, Y.; Tsakalakos, T.; Muhammed, M. *Chem. Mater.* **2003,** *15,* 4343. (d) Bertorelle, F.; Wilhelm, C.; Roger, J.; Gazeau, F.; Menager, C.; Cabuil, V. *Langmuir*, **2006**, *22,* 5385. (e) Zhou, J.; Leuschner, C.; Kumar, C.; Hormes, J.; Soboyejo, W.O. *Materials Science and Engineering C* **2006,** *26*, 1451. (f) Stoeva, S. I.; Huo, F.; Lee, J-S.; Mirkin, C. A. *J. Am. Chem. Soc.* **2005**, *127*, 15362.

[2]. Buscher, K.; Helm, C. A.; Gross, C.; Glockl, G.; Romanus, E.; Weitschie,W. *Langmuir* **2004,** *20,* 2435.

[3]. Li, X. K.; Ji, W. J.; Zhao, J.; Wang S. J.; Au, C. T. *J. Catal.* **2005**, *236*, 181.

[4]. Heracleous, E.; Lee, A. F.; Wilson, K.; Lemonidou, A. A. *J. Catal.* **2005**, *231*, 159.

[5]. Fatsikostas, A. N.; Verykios, X. E. *J. Catal.* **2004,** *225*, 439.

[6]. Molina, A. I.; Robles, J. M.; Garcia, P. B.; Castellan, E. R.; Finoechio, E.; Busca, G.; Torres, P. M.; Lopez, A. J. *J. Catal.* **2004**, *225*, 479.

[7]. (a) Li, Y.; Zhang, B.; Xie, X.; Liu, J.; Xu, Y.; Shen, W. *J. Catal***.** **2006,** *238*, 412. (b) Chen, D.; Christensen, K. O.; Fernandaz, E. O.; Yu, Z.; Totdal, B.; Latorre, N.; Monzon, A.; Holmen, A. *J. Catal.* **2005,** *229*, 82.

[8]. (a) Son, S. U.; Lee, S. I.; Chung,Y. K.; Kim, S-W.; Hyeon, T. *Org. Lett*. **2002**, *4*, 277. (b) Bonaga, L. V. R.; Zhang, H. C.; Maryanoff, B. E. *Chem. Commun.,* **2004**, 2394.

[9]. Wildt, B.; Mali, P.; Searson, P. C. *Langmuir,* **2006**, DOI no. 10.1021/la061184j

[10]. (a) Menendez, J. L.; Bescos, B.; Armelles, G.; Serna, R.; Gonzalo, J.; Doole, R.; Petford-Long, A. K.; Alonso, M. I. *Phys. Rev. B*, **2002**, *65*, 205413. (b) Yakushiji, K.; Mitani, S.; Takanashi, K.; Takahashi, S.; Maekawa, S.; Imamura, H.; Fujimori, H. *Appl. Phys. Lett*., **2001,** *78*, 515. (c) Fiete, G. A.; Zarand, G.; Halperin, B. I.; Oreg, Y.; *Phys.*

Rev. B **2002**, *66*, 024431 (d) Aktsipetrov, O. A. *Coll. Surf. A* **2002**, *202*, 165. (e) Graf, H.; Vancea, J.; Hoffmann, H. **2002**, *80*, 1264.

[11]. Hyeon, T. *Chem. Commun*. **2003**, 927.

[12]. (a) Wu, S. H.; Chen, D. –H. *Chem. Lett.* **2004**, *33*, 406. (b) Song, Y.; Modrow, H.; Henry, L. L.; Saw, C. K.; Doomes, E. E.; Palshin, V.; Hormes, J.; Kumar, C. S. S. R. *Chem. Mater.* **2006,** *18,* 2817.

[13]. (a) Kim, H.; Achermann, M.; Balet, L. P.; Hollingsworth, J. A.; Klimov, V. I. *J. Am. Chem. Soc.* **2005**, *127*, 544. (b) Park, J.-I.; Cheon, J. W. *J. Am. Chem. Soc.,* **2001**, *123*, 5743.

[14]. Petit, C.; Taleb, A.; Pileni, M. P. *J. Phys. Chem. B*, **1999**, *103*, 1805.

[15]. Sun, S.; Murray, C. B. *J. Appl. Phys*., **1999**, *85*, 4325.

[16]. (a) Murray, C. B.; Sun, S.; Gaschler, W.; Doyle, H.; Betley, T. A.; Kagan, C. R. *IBM J. Res. Dev.,* **2001**, *45*, 47. (b) Murray, C. B.; Sun, S.; Doyle, H.; Betley, T. A. *MRS Bull.,* **2001**, 985. (c) Puntes, V. F.; Krishnan, K. M.; Alivisatos, A. P. *Appl. Phys. Lett.* **2001**, *78,* 2187. (d) Dinega, D. P.; Bawendi, M. G. *Angew. Chem. Int. Ed.***1999,** *38,* 1788.

[17]. Khomutov, G. B., Byko, I. V.; Gainutdinov, R. V.; Polyakov, S. N.; Sergeyev-Cherenkov, A. N.; Tolstikhina, A. L. *Colloids and Surfaces A: Physicochemical and Engineering Aspects* **2002**, *198–200*, 559.

[18]. Leng, Y. G.; Shao, H. Y.; Wang, Y. T.; Sizuki, M.; Li, X. G. *J. Nanosci. Nanotechnol.* **2006**, *6*, 221.

[19]. Koltypin, Y.; Katabi, G.; Prozorov, R.; Gedanken, A. *J. Non-Cryst. Solids* **1996**, *201*, 159.

[20]. (a) Chen, J. P.; Sorensen, C. M.; Klabunde, K. J.; Hadjipanayis, G. C. *J. Appl. Phys.* **1994**, *76*, 6316. (b) Petit, C.; Taleb, A.; Pileni, M. P. *J. Phys. Chem. B* **1999,** *103*, 1805. (c) Petit, C.; Taleb, A.; Pileni, M. P. *Adv. Mater.* **1998**, *10*, 259. (d) Chen D. H.; Hsieh, C. H. *J. Mater. Chem.* **2002**, *12*, 2412. (e) Chen D. H.; Wu, S. H. *Chem. Mater.* **2000**, *12*, 1354.

[21]. Wu, S.-H.; Chen, D.-H. *J. Colloid and Int. Sci.* **2003**, *259*, 282.

[22]. Duan, Y.; Li, J. *Materials Chemistry and Physics* **2004**, *87,* 452.

[23]. Amoruso, S.; Ausanio, G.; Lisio, C. de.; Iannotti, V.; Vitiello, M.; Wang, X.; Lanotte, L. *Appl. Surf. Sci.* **2005**, *247,* 71.

[24]. (a) Chen, B.-D.; Cilliers, J. J.; Davey, R. J.; Garside J.; Woodburn, E. T. *J. Am. Chem. Soc.,* **1998**, *120*, 1625. (b) Mandal, S.; Arumugam, S. K.; Adyanthaya, S. D.; Sastry, M. *J. Mater. Chem.* **2004**, *14*, 43. (c) Mandal, S.; Arumugam, S. K.; Pasricha, R.; Sastry, M. *Bull. Mater. Sci.* **2005,** *28*, 503. (d) Rautaray, D.; Sinha, K.; Shiv Shankar, S.; Adyanthaya, S. D.; Sastry, M. *Chem. Mater.* **2004**, *16*, 1356. (e) Shankar, S. S.; Patil, U. S.; Prasad, B. L. V.; Sastry, M. *Langmuir* **2004**, *20*, 8853.

[25]. (a) Cullity, B. D.; *Introduction to Magnetic Materials,* Addison-Wesley Publishing, Reading, **1972.** (b) Meiklejohn, W.H. *J. Appl. Phys.* **1962**, *33*, 1328.

[26]. (a) Weaire, D.; Hutzler, S. *The Physics of Foams*, Oxford University Press, Oxford, **1999**. (b) Pashley, R. M.; Karaman, M. E.; *Applied Colloid and Surface Chemistry,* John Wiley & Sons, Ltd., **2004** (c) Hedreul, C.; Frens, G. *Coll. Surf. A,* **2001,** *186*, 73**.**

[27]. Atkins, P.; Paula, J-de. *Atkins' Physical Chemistry,* Seventh Edition, Oxford University Press, **2002**.

[28]. (a) Lee, W.; Kim, M. G.; Choi, J.; Park, J-II.; Ko, S. J.; Oh, S. J.; Cheon, J. *J. Am. Chem. Soc.,* **2005**, *127*, 16090. (b) Sun, Y.; Xia, Y. *J. Am. Chem. Soc.,* **2004**, *126*, 3892.

[29]. (a) Creighton, J. A.; Eadon, D. G. *J. Chem. Soc., Faraday Trans.* 1, **1991**, *87*, 3881. (b) Ershov, B. G.; Sukhov, N. L.; Janata, E. *J. Phys. Chem. B,* **2000**, *104,* 6138.

[30]. Kitakami, O.; Sato, H.; Shimada, Y.; Sato, F.; Tanaka, M. *Phys. Rev. B,* **1997**, *56*, 13849.

[31]. http://www.fdmspectra.com/fdm_ftir_surf_index.htm

[32]. (a) Samia, C. S. A.; Hyzer, K.; Schlueter, J. A.; Qin, C. J.; Jiang, J. S.; Bader, S. D.; Lin, X. M. *J. Am. Chem. Soc.* **2005**, *127*, 4126. (b) Wu, N.; Fu, L.; Su, M.; Aslam, M.; Wong, K. C.; Dravid, V. P. *Nano lett*. **2004**, *4*, 383. (c) Wang, W.; Efrima, S.; Regev, O. *Langmuir,* **1998,** *14*, 602.

[33]. Ulmann, A. *An Introduction to Ultra Thin Organic Films: From Langmuir–Blodgett to Self Assembly*, Academic Press, San Diego, **1991**.

[34]. Badia, A.; Singh, S.; Demers, L. M.; Cuccia, L. A.; Brown, G. R.; Lennox, G. R. R. B. *Chem. Eur. J.,* **1996,** *2*, 205.

[35]. (a) Yager, W. A.; Merritt, F. R.; Guillaud, C. *Phys. Rev.* **1951**, *81*, 477. (b) Turov, E. A. *Ferromagnetic Resonance*, S.V. Vonskovskii (ed.), Chapter IV. (c) McGuire, T. R.; Aboaf, J. A.; Klokholm, E. J. *Appl. Phys.* **1981**, *52*, 2205.

Chapter V

Aqueous foam as a template for the synthesis of different ferrite nanoparticles

---

This chapter describes the formation of cobalt ferrite and magnesium ferrite nanoparticles at room temperature using liquid foams as template. The desired cations were entrapped in the foams by electrostatic interactions with the anionic surfactants and hydrolysis was carried out by spraying NaOH in the final step. However, in the formation of ferrites with the formula MFe_2O_4 where the metal ion and iron possess oxidation states of +2 and +3, respectively, if a foam is formed from a 1:2 mixture of the desired ionic solutions, a foam composition at variance with the original solution mixture results due to greater electrostatic binding of ions possessing higher charge with the surfactant. In our procedure we circumvent this problem by preparing the foam from a 1:2 mixture of M^{2+} and Fe^{2+} ions and then utilizing the in-situ conversion of Fe^{2+} to Fe^{3+} under basic conditions inside the foam matrix to get the desired composition of the metal ions with the required oxidation states. The ferrite nanoparticles so obtained were capped with oleic acid, found to exhibit good crystallinity and were superparamagnetic in nature. The fact that we could prepare both $CoFe_2O_4$ and $MgFe_2O_4$ particles showed the vast scope of this method for making even multi component oxides.

Part of this work has been published in:
(1) Bala, T.; Sankar, C. R.; Baidakova, M.; Osipov, V.; Enoki, T.; Joy, P. A.; Prasad, B. L. V.; Sastry, M. *Langmuir* **2005**, *21*, 10638.

5.1. INTRODUCTION:

The term ferrite, the Latin word for iron, connotes slightly different meaning to different group of scientists. To metallurgists ferrite means pure iron whereas geologists will consider the term as minerals based on iron oxides [1]. Chemists consider ferrites as a group of multi-component oxides, generally magnetic in nature, of the general formula AB_2O_4 where 'A' can be a divalent cation (e.g. Co^{2+}, Ni^{2+}, Cu^{2+}, Mn^{2+}, Zn^{2+}, Mg^{2+} etc) and 'B' is Fe(III) [2]. The importance of this group of compounds has cropped up in recent time due to their potential application in diverse fields. In fact there is a renewed interest in the synthesis of ferrites in nanometer size regime owing to their enhanced magnetic character. Magnetic particles in the single domain size range, which is generally attained in nanoparticulate materials, often exhibit superparamagnetic character and high field saturation [3]. A better understanding of magnetism at the nanoscale is required not only for basic physics [4] but also for the technological use of these substances in data storage [5], color imaging [6], ferrofluids [7] and in biomedical applications such as magnetic labeling in immunoassays [8], drug delivery [9] and hyperthermia of cancer cells [10].

There are several methods reported for the synthesis of ferrite nanoparticles. Normal micelle [11], reverse micelle [12] based synthesis methods and co-precipitation by hydrolysis of the suitable precursors [13] are old techniques for this purpose whereas the solvo-thermal synthetic procedure [14], sonochemical approach [15], mechanical milling [16], growth in form of films by spin-coating [17] or development of epitaxial films by molecular beam epitaxy at lower temperature [18] are few examples of relatively new routes for the fabrication of various ferrites nanoparticles. Even the use of microbes has been reported for ferrite synthesis, with the process involving the oxidization of Fe(II) to Fe(III) present in the spent sulfuric acid pickling solution by the microbes and the extraction of the product with organic solvent followed by hydrolysis in the presence of another carboxylate (e.g. Ni(II) carboxylate). The process is industrially important as the organic solvent and sulfuric acid free from Fe(III) can be reused [19]. In fact it is a big challenge for scientists to channelize laboratory based synthetic procedure into large-scale production. Large volume applications really need the product in hefty amount and we believe foam based synthetic process can help realize the issue in near future as foam lamellae (as already described in the previous chapter) [20] provide extremely high concentration of gas bubbles dispersed in a liquid yielding large interfacial areas which is used for the growth of the nanomaterials. Again as these regions are populated by the surfactant, this not only leads to generation of nanoparticles stabilized by the surfactants present but also endow with some size and shape modulation in the products. This has made this template more attractive for the utilization.

In this chapter we describe the synthesis of magnetic spinel cobalt ferrite ($CoFe_2O_4$) and magnesium ferrite ($MgFe_2O_4$) nanoparticles using liquid foam as template. The choice of the two different ferrites is guided by the fact that though both of them acquire a similar spinel structure, their magnetic properties exhibit disparity. This is due to the possibility of strong magnetic interaction in $CoFe_2O_4$ from the L-S coupling at the Co^{2+} lattice sites, which on the other hand is absent in magnesium ferrites [21]. The foam is formed from an aqueous mixture of an anionic surfactant and the desired metal ions, where the metal ions are electrostatically entrapped by the surfactant at the thin borders between the air bubbles and their junctions. The hydrolysis is carried out using alkali resulting in the formation of desired nanoparticles with the foam playing the role of a template. However, if the formation of foam is carried out from a 1:2 mixture of the desired ionic solutions (Co^{2+} and Fe^{3+} in case of $CoFe_2O_4$) a foam composition with preferential loading of Fe^{3+} ions is resulted, most likely due to greater electrostatic binding of ions possessing higher charge with the surfactant. In fact, earlier endeavor in our laboratory to generate Fe_3O_4 nanoparticles in foam from an initial solution of Fe^{2+} and Fe^{3+} in 1:2 ratio was not successful and ended with the formation of phase-pure Fe_2O_3 only. The preferential binding with cations of higher oxidation state may have contributed considerably to the consequence [22]. Thereafter we devised a new strategy where we circumvent this problem by preparing the foam from a 1:2 mixture of M^{2+} and Fe^{2+} ions and then utilizing the *in-situ* conversion of Fe^{2+} to Fe^{3+} under basic conditions inside the foam matrix to get the desired composition of the metal ions with the required oxidation states. Indeed our results substantiated our hypothesis by the formation of $CoFe_2O_4$ and $MgFe_2O_4$ nanoparticles as detailed in this chapter. With this it becomes very apparent that liquid foam based method can open up new opportunity for synthesis of different types of nanomaterials starting from metallic nanoparticles to simple oxides or minerals or ferrites or even multi-component oxides. .

5.2. FERRITES: STRUCTURE AND PROPERTIES

5.2.1. Structure of the Spinel Ferrite:

The structure of the spinel ferrites is quite simple from crystallographic point of view and their structures have been investigated for nearly a century. The structure possesses a large unit cell containing eight formula units, or a total of 8 X 7= 56 ions per unit cell. Spinel ferrites generally enjoy face-centered cubic close packed structure of oxygen along with M^{2+} (M^{2+} can be various divalent cations) and Fe^{3+} ions in two different crystallographic locations. These positions have tetrahedral (T-sites) and octahedral (O-sites) co-ordination of oxygen, so the local resultant symmetries of both the sites are different [3, 21].

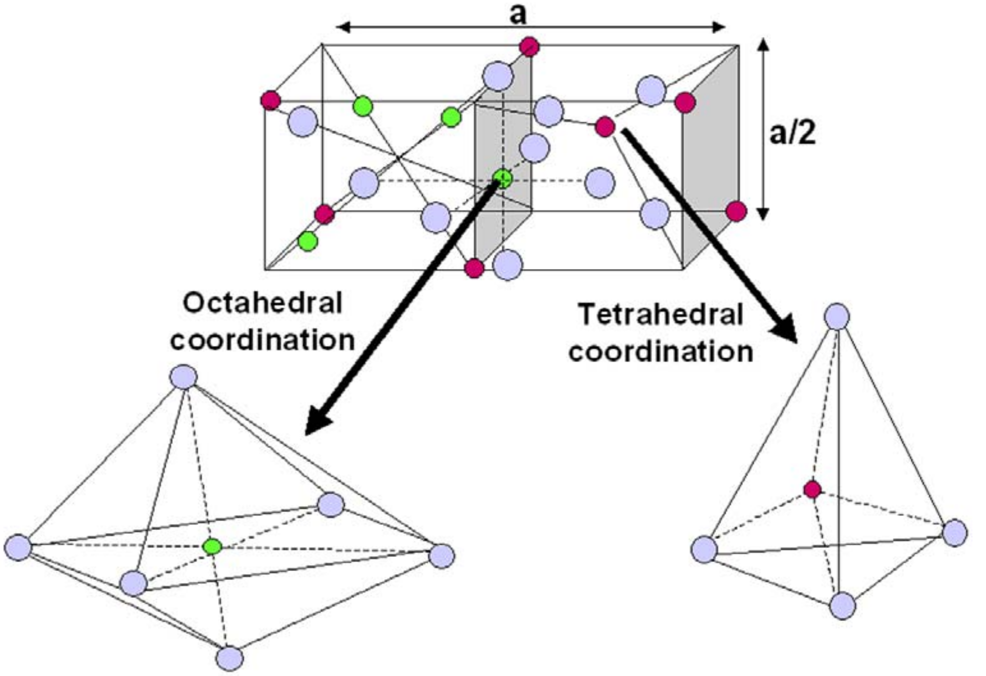

Figure 5.1. *Structure of spinel ferrite where in the model the red spheres are the representative divalent metal ions, green are the Fe(III) cations and violet balls are oxygen. Instead of the whole unit cell of edge length a, it is imagined to be divided in 8 octants of edge length a/2, two of which are shown in the above [3].*

Spinel ferrites can be divided into two groups e.g. normal spinel and inverse spinel depending on the distribution of M^{2+} and Fe^{3+} ions in T-sites and O-sites. The ionic distribution for normal spinel ferrites is simple, with all the divalent cations present in the tetrahedral sites and the Fe^{3+} cations in the octahedral sites. But it is worth mentioning here that the inverse spinel structures have half of the Fe^{3+} cations in tetrahedral sites and half in octahedral sites along with the divalent cations exclusively present in the octahedral sites. The general ionic distribution for spinel ferrites can be represented as $[M_{\delta}\ Fe_{\delta-1}]^T\ [M_{1-\delta}\ Fe_{1+\delta}]^O$ where δ is the inversion parameter (defined by the fraction of T-sites occupied by Fe^{3+} ions) and δ=1 for normal spinel and 0 for inverse spinel structure. [16a, 23]

The general spinel structure can be better understood when viewed along the four-fold symmetry axis i.e. perpendicular to a face of the cubic unit cell (*Figure 5.2*).

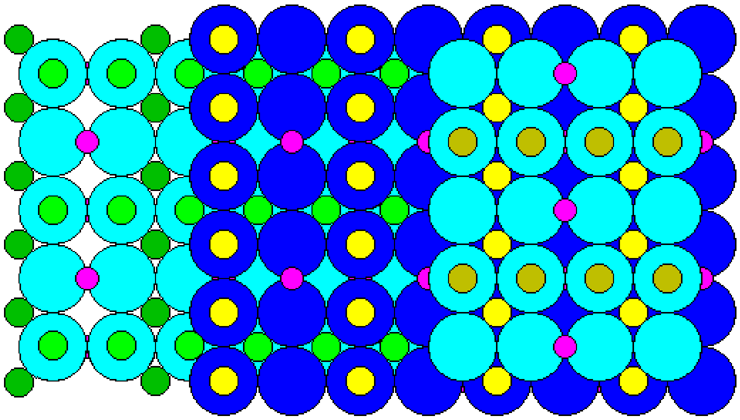

Figure 5.2. *Structure of spinel ferrite. Three layers of oxygen atoms are shown in alternating shades of blue. Atoms in octahedral sites are shown in shades of green and yellow. Atoms in tetrahedral sites are shown in purple [24].*

5.2.2. Magnetic Nature of Spinel Ferrite:

The cubic ferrites are ionic compounds and their magnetic properties arise due to the magnetic cations they contain. In fact ferrites are well-known magnetic materials but till date the understanding of their magnetic properties is not sufficient. Particularly in nanoscale regime when particles tend to assume single domain status several factors come into play. Magnetocrystalline anisotropy, mainly coming into play due to spin orbit coupling, is one such aspect which is largely responsible for the change in magnetization of materials. In ferrites as the two types of cations reside in two different crystallographic sites namely A (tetrahedral site) and B (octahedral site), there are three different magnetic interactions possible in the lattice. Actually, the AB, AA and BB exchange interactions all tend to be negative, like antiferromagnets, as per the assumption made by Neel [3]. In most of the spinel ferrites A-B interaction is usually the strongest forcing the spins on A and B sites to be antiparallel. However the magnitude of magnetic moments on A-sites and B-sites are not equal, hence a net magnetic moment results. All ferrites are thus ferrimagnets though they exhibit most of the properties associated with ferromagnets such as spontaneous magnetization below Curie temperature, magnetic saturation and hysteresis. We must mention here that very commonly, the divalent cation and Fe^{3+} ions are distributed in both the lattice sites and while the Fe^{3+}(A)- Fe^{3+}(B) interaction leads to complete cancellation of magnetic moment, the M^{2+}(A)-Fe^{3+}(B) interaction does not. Thus the flexibility of the structures of spinel ferrite i.e. variation of cation distribution in tetrahedral and octahedral sites gives rise to different magnetic properties in these kind of spinel ferrites. Then at the nanoscale, due to different coordination and bond breaking at the surface of the nanoparticles, there is different distribution of exchange fields as well as spin canting or perturbations in crystal field that generates surface anisotropy [16a, 21]. As expected this phenomenon becomes very prominent in nano regime because of the increase in the surface to volume ratio. The exchange interaction is also obstructed if one of the cations is nonmagnetic in nature like Mg^{2+} in $MgFe_2O_4$ and hence its overall magnetization is diminished. Therefore the nanoparticles of these ferrites offer us a rich repertoire of properties attracting many researchers to study them. However, it is also important that the synthetic methodology used should give reproducible and reliable results and we feel the foam-based methodology fills in that gap. This chapter deals with the preparation of $CoFe_2O_4$ and $MgFe_2O_4$ nanoparticles and reports their characterizations with different analytical techniques. The temperature and field dependent magnetization measurement enable us to get useful information regarding their magnetic nature and several other factors like saturation magnetization, anisotropy etc.

5.3. SYNTHESIS OF FERRITES IN FOAM LAMELLAE:

The foam-based protocol is explained in detail in the previous chapter and only a brief description pertinent to the current requirement is given here. As explained in the previous chapter, a rectangular column of 50 cm height and a square base of 10 X 10 cm^2

with sintered ceramic disc embedded in it was made using Pyrex and was used for the generation of foam. An aqueous mixture of 25 ml of 5 X 10^{-3} M ferrous sulfate solution, 25 ml of 2.5 X 10^{-3} cobalt chloride/magnesium sulfate solution and 50 ml of 1 X 10^{-1} M SDS were taken in the base and the foam was built up by injecting air at a pressure of 1-5 psi through the porous ceramic disc fixed to the bottom of the foam column. Stable foams of upto 50 cm height could be routinely obtained. After carefully draining out the excess aqueous solution from the foam, 0.5% sodium hydroxide solution was sprayed into the foam. At this stage, the color of foam changed to dark brown color and the foam slowly collapsed, as the nanoparticle formation was complete. The collapsed foam solution containing the nanoparticles was collected and then subjected to repeated centrifugation at 8000 rpm for 30 minutes following which the pellet and supernatant were separated. The pellet was washed several times with water and ethanol. This pellet could be readily dispersed in water. After washing, excess oleic acid (1 X 10^{-2} M) in methanol was added to the precipitate and stirred overnight. The excess oleic acid was then removed by precipitating out the ferrite from the solution and then by repeated washing with ethanol. The air-dried powder obtained with this simple oleic acid treatment could be easily redispersed in hexane or other non-polar organic solvents by sonication. These purified powders were then subjected to different analyses.

The hydrolysis of the cations takes place on addition of alkali according to the equation:

$$M^{2+} + 2FeSO_4 + 6NaOH + \frac{1}{2} O_2 \rightarrow MFe_2O_4 + 3H_2O + 2Na^+ + 2Na_2SO_4$$

(M=Co or Mg)

Since this reaction occurs in the restricted spaces of the juxtaposed liquid lamellae between the bubbles, the resulting particles are in the nanometer size regime. The success of the synthesis invariably involves the binding of two different divalent cations Co^{2+} or Mg^{2+} and Fe^{2+} to an anionic surfactant with equal probability and the in-situ conversion of Fe^{2+} to Fe^{3+} in the foam matrix. Different characterizations carried out, clearly demonstrate the nanoparticle composition to be $CoFe_2O_4$ and $MgFe_2O_4$ exemplifying the successful performance of our strategy.

5.4. UV-VIS SPECTROSCOPY:

The UV-vis absorption spectra recorded from the aqueous cobalt and magnesium ferrite nanoparticles *(Figure 5.3)* significantly revealed a 'shoulder' in the range 300-350 nm [25].

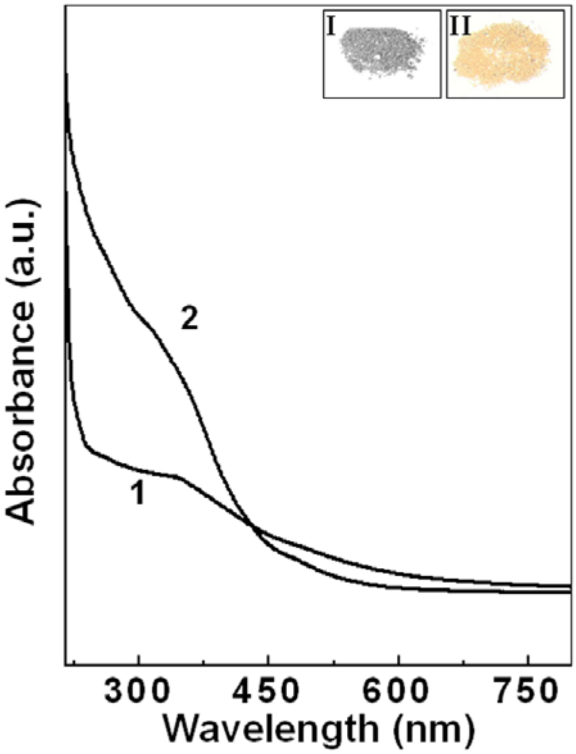

Figure 5.3. *UV-Vis absorption spectra recorded from $CoFe_2O_4$ (curve 1) and $MgFe_2O_4$ (curve 2) nanoparticles formed in the foam and capped with oleic acid. The insets I and II represent the photographs of the dry powder of cobalt and magnesium ferrites respectively.*

In general the ferrites show this hump in the UV-Vis region because of the presence of the Fe^{3+} ions [25] in the octahedral sites of the crystal and is considered as a characteristic of the ferrite nanoparticles. The inset of the figure gives further details about the color of the samples. Inset I and II correspond to the photographs of $CoFe_2O_4$ and $MgFe_2O_4$ powdered samples respectively. The $CoFe_2O_4$ nanoparticles are dark brown in color whereas the other ferrite has dim brownish shade.

5.5. X-RAY DIFFRACTION ANALYSIS:

The X-ray diffraction pattern of cobalt ferrite and magnesium ferrite samples was recorded from the powdered materials obtained by drying the colloidal solution at room temperature. The XRD patterns of cobalt and magnesium ferrite nanoparticles along with their simulated curves are shown in the *Figure 5.4A and B* respectively.

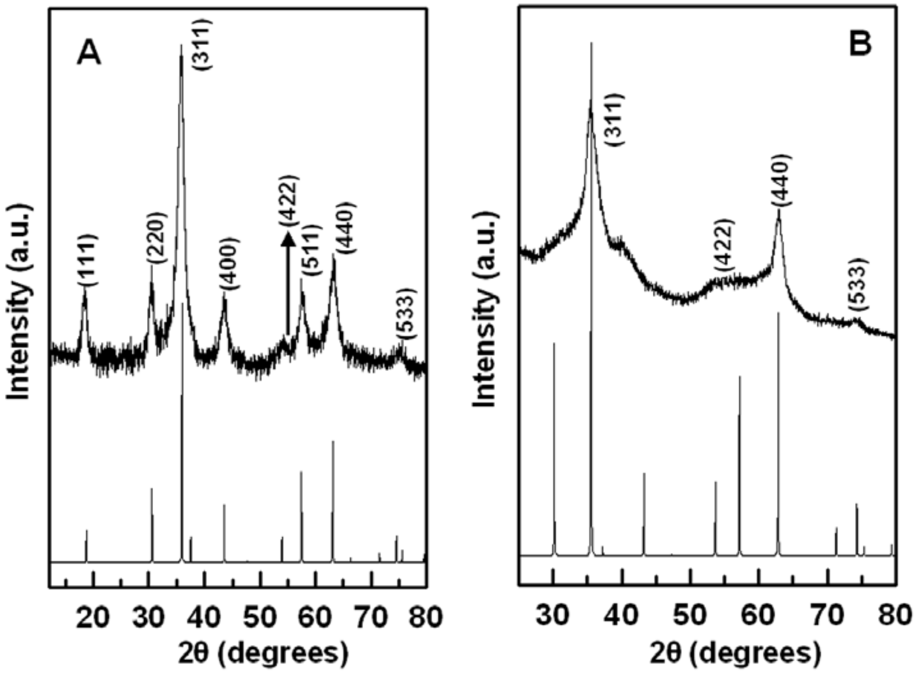

Figure 5.4. *Powder X-ray diffractograms of (A)* $CoFe_2O_4$ *and (B)* $MgFe_2O_4$ *nanoparticles along with their simulated pattern. The peaks are indexed to the fcc lattices of the respective ferrites.*

A number of Bragg reflections can be identified for both of the materials. Cobalt ferrite nanoparticles are found to possess face-centered cubic crystal structure (a= b= c= 8.391, space group= Fd3m, PCPDF # 221086) and so is the magnesium ferrite (a= b= c= 8.387, space group= Fd3m, PCPDF # 360398). The experimentally observed diffractograms match very well with the reported diffractograms of $CoFe_2O_4$ and $MgFe_2O_4$ underlining the good quality of both the ferrites with no trace of any impurity phase to the detectable limit of the instrument. The peaks, characteristic of very fine nanocrystals, are quite broad. From the broadening of the Bragg reflections, the size of the particles is evaluated to be ~7-8 nm using the Scherrer formula [26]. The average crystallite size as calculated from X-ray diffraction analysis are in reasonably good agreement with the average particle size values obtained from TEM images as described below.

5.6. TRANSMISSION ELECTRON MICROSCOPY:

Representative TEM images of the ferrite nanoparticles synthesized in the foam are shown in *Figure 5.5A-D* which correspond to the $CoFe_2O_4$ nanoparticles capped with oleic acid while *Figure 5.6A-D* depict those from $MgFe_2O_4$ having similar capping on the surface. The samples were made by putting a drop of ferrite nanoparticles from its dispersion in organic solvent on a carbon coated Cu-grid. The grid was ensured to be dried entirely before performing the transmission electron microscopic imaging.

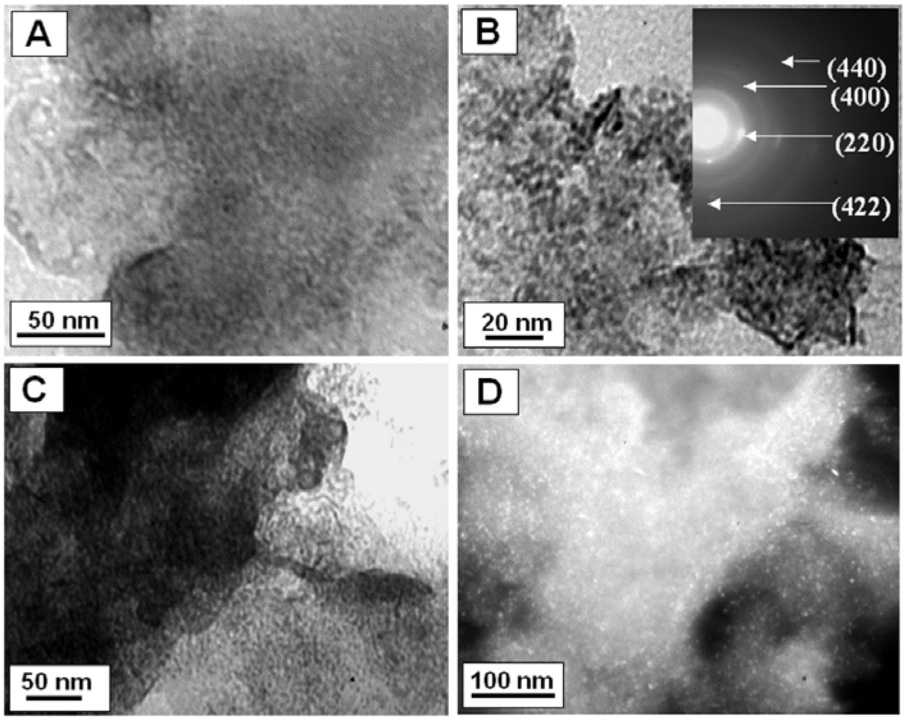

Figure 5.5. *(A-C) show the Transmission Electron Micrographs of $CoFe_2O_4$ nanoparticles at different magnifications whereas (D) shows the dark field image of the previous image corresponding to the (220) plane of the sample. The SAED pattern indexed as cubic cobalt ferrite given in the inset of B.*

The particle size distribution analysis reveals that the average particle size in both cases is around ~3-5 nm in diameter, though the presence of some big aggregates cannot be ruled out. The treatment on the particles after their formation (e.g. centrifugation etc) can lead to clustering of the samples. Aggregation can also be initiated because of their inter-particle magnetic interaction. The nanoparticles, in our synthetic procedure, are formed in the limited space offered at the Plateau Border and Plateau junction of the foam lamellae. In a dry foam, when the liquid fraction remains at its minimum, the

Plateau border and Plateau junction are only few nanometers in thickness [20f]. So the particles synthesized using this dry foam as template are expected to be very small in size and the fact can actually be visualized in TEM images.

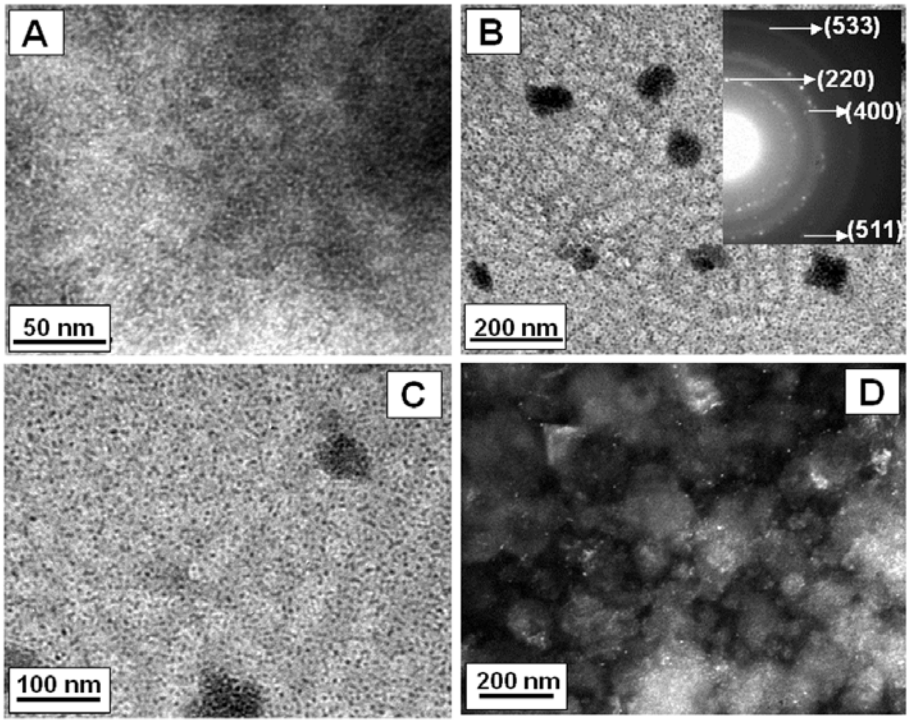

Figure 5.6. *(A-C) TEM pictures of $MgFe_2O_4$ nanoparticles at different magnifications whereas (D) shows its dark field image of the previous image corresponding to the (220) plane of the sample. The SAED pattern indexed as cubic magnesium ferrite is given in the inset of B.*

The insets of *Figure 5.5B* and *Figure 5.6B* represent the selected area electron diffraction (SAED) patterns for $CoFe_2O_4$ and $MgFe_2O_4$ nanoparticles respectively. The ring patterns are the characteristic of small crystallites of the ferrites that could be indexed to *fcc* structures validating the formation of fine crystalline ferrite nanostructures. It is worth noting here that no diffraction spots or XRD peaks corresponding to the cobalt and magnesium oxides were observed. *Figure 5.5D* and *Figure 5.6D* show dark field images of the $CoFe_2O_4$ and $MgFe_2O_4$ particles respectively corresponding to the (220) diffraction plane of the image presented in *Figure 5.5C* and *Figure 5.6C* and thus clearly highlighting the diffracting nature of the ferrite nanocrystals.

5.7. DETERMINATION OF COMPOSITION:

5.7.1. Eenergy Dispersive Analysis of X-rays:

The chemical composition of the ferrite was roughly estimated by performing spot-profile EDAX analysis on the powdered sample of $CoFe_2O_4$ and $MgFe_2O_4$ and the spectra are shown in the *Figure 5.7A and B* for the respective nanoparticles.

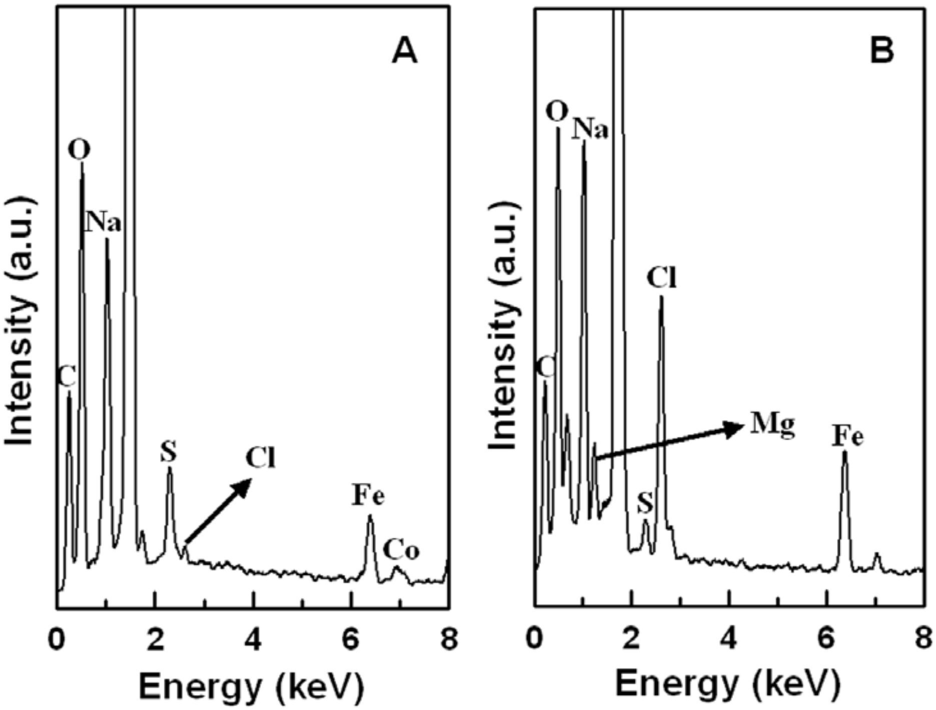

Figure 5.7. *Spot profile EDAX for $CoFe_2O_4$ (graph A) and $MgFe_2O_4$ (graph B) performed on the powdered samples of the respective nanoparticles obtained after oleic acid capping.*

In addition to the expected Fe, Co and O signal, moderately strong signals of C, Na, Cl and S can also be observed. The C signal arises from the surface capping of oleic acid and the use of NaOH as the hydrolyzing agent probably gives rise to the Na peak (*Figure 5.7A)*. Weak signals of Cl and S can be attributed to the precursors and SDS used for the generation of foam. Similarly in the $MgFe_2O_4$ case also beside the predictable Fe, Mg and O peak, the signals for C and Na are also present (*Figure 5.7B).* The Co : Fe and Mg : Fe atomic ratios in the capped cobalt and magnesium ferrite nanoparticles as determined by EDAX were 1 : 2.3 and 1 : 2.4 respectively. The ratio is slightly higher than the actual atomic ratio as anticipated from the chemical formula of ferrites but can be considered within the experimental or instrumental error.

5.7.2. Atomic Absorption Spectroscopy:

The samples of $CoFe_2O_4$ and $MgFe_2O_4$ were subjected to AAS analysis to have better chemical analysis of the sample. The ratios of Co:Fe and Mg:Fe from AAS measurements were found to be ~1:1.9 in both the cases. Hence the analyses are in close agreement with what is expected from the chemical formula.

5.7.3. X-Ray Photoelectron Spectroscopy:

The chemical state of the cations present in the compound near surface region is best characterized by XPS analysis performed on the drop coated sample on clean Si (111) substrate. *Figure 5.8A-F* show various core level spectra recorded from $CoFe_2O_4$ (core levels O 1s, Co 2p, Fe 2p) and $MgFe_2O_4$ (core levels O 1s, Mg 2p, Fe 2p) nanoparticles by this technique [27]. The O 1s core level spectra in both cobalt and magnesium ferrite nanoparticles (*Figure 5.8A and D* respectively) can be fit to a single component at 532 eV binding energy (BE). The absence of additional components in the O 1s level attests to the absence of impurity phases such as single component oxides of the corresponding metals. The Co 2p core level from the cobalt ferrite nanoparticles (*Figure 5.8B*) may be fit to a single peak centered at 781.7 and 797.5 eV BE for $2p_{3/2}$ and $2p_{1/2}$ transition respectively with a characteristic weak satellite peak at 786.8 eV. The position of the peak i.e. towards the higher BE as compared to pure Co nanoparticles conclusively establishes the valency of the cation. Though the BE articulates the valency of the cation, unfortunately the absolute BE of $2p_{3/2}$ cannot be used to recognize the chemical environment of the Co^{2+} in its crystal lattice. The splitting factor (separation between $2p_{3/2}$ and $2p_{1/2}$), as it is dependent on the L-S coupling, can provide some information for the purpose [28, 29]. In ferrites, cations are distributed in two different lattice sites. When the same cation is distributed in two different lattice sites namely tetrahedral and octahedral sites (true for inverse spinel structure) a difference in binding energy is observed due to the variation in the stabilization between two sites that arises from varying co-ordination of the particular ion with oxygen. Very strong satellite peak is characteristic of Co in octahedral site [28, 29]. In our case cobalt ferrite evidenced a weak satellite peak. But the occurrence of less intense and broad satellite peak does not essentially point towards the tetrahedral occupancy of Co^{2+} expected for cobalt in normal spinel cobalt ferrite [28, 29]. In fact, normal and inverse spinel are to be regarded as extreme case as many times the analysis reveals that intermediate structure can exist and XPS alone is insufficient to conclusively prove the occupancy of the cations in tetrahedral or octahedral sites in spinel ferrites. The Fe 2p core level spectra (*Figure 5.8C*) with binding energies of 711.6 ($2p_{3/2}$) and 724.9 ($2p_{1/2}$) eV match well with the values reported for Fe^{3+}. Similarly, the observation of the Mg 2p core level at 49.84 eV BE and Fe 2p at 711.5 ($2p_{3/2}$) and 724.9 ($2p_{1/2}$) (*Figure 5.8E and F* respectively) again proves the formation of phase pure magnesium ferrite in our foam-based experiments. The spin orbit pair of Mg 2p was difficult to resolve here as the splitting factor is only 0.4 eV [30].

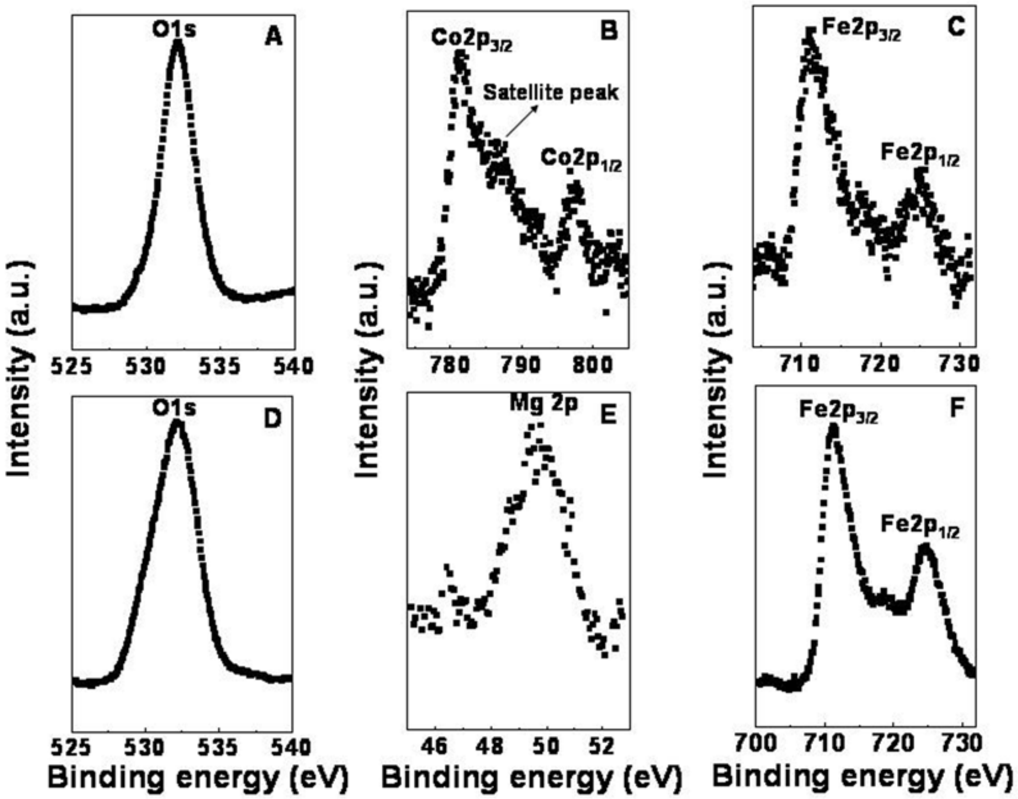

***Figure 5.8**. XPS core level spectra recorded from cobalt ferrite nanoparticles on Si (111) substrate - (A) O1s, (B) Co 2p and (C) Fe 2p levels. XPS core level spectra recorded from magnesium ferrite nanoparticles on Si (111) substrate – (D) O 1s, (E) Mg 2p and (F) Fe 2p levels.*

5.8. FOURIER TRANSFORM INFRA-RED SPECTROSCOPY:

It is already established that oleic acid can act as the capping agents for numbers of oxides including ferrites [31]. The ferrite nanoparticles synthesized by the foam-based technique were found to be clustered and almost inseparable even after prolonged sonication when oleic acid treatment was not accomplished.

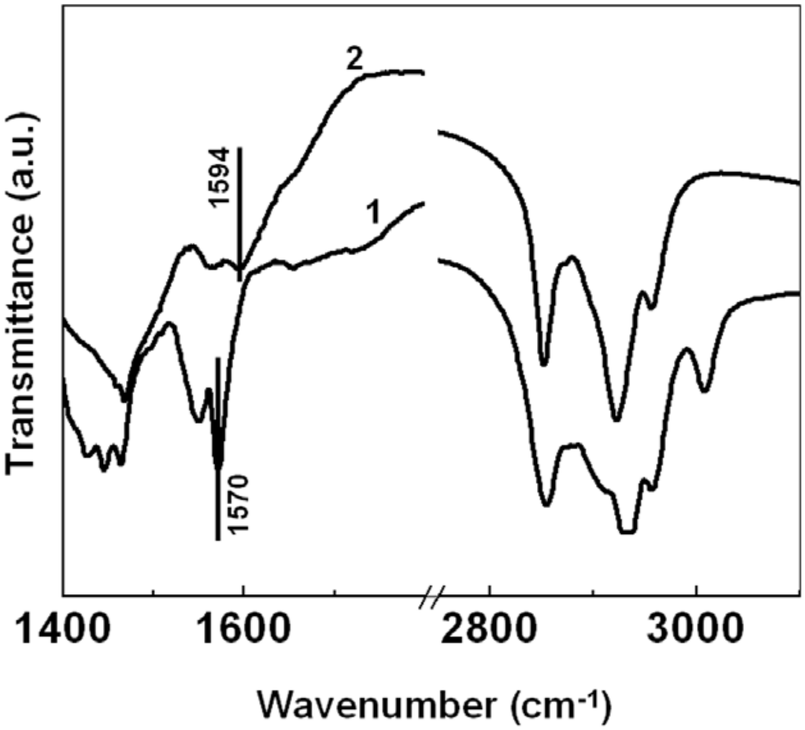

Figure 5.9. *FTIR spectra of drop-coated films of nanoparticles of cobalt ferrite (curve 1) and magnesium ferrite (curve 2) capped with oleic acid on Si (111) substrates.*

Therefore in our experiment after the formation of ferrite nanoparticles, the sample was stirred with oleic acid to ensure capping of the particles and it was found to bring about the stability of the magnetic ferrite nanoparticles by preventing clustering. The presence of the surface-bound oleic acid on the nanoparticles can be verified from the shift of FTIR peaks for the –COOH functional group of oleic acid. The –COO$^-$ bond stretching frequency is shifted from 1707 cm^{-1} (pure oleic acid) [32] to 1570 cm^{-1} *(Figure 5.9, curve 1)* and 1594 cm^{-1} *(Figure 5.9, curve 2)* for cobalt ferrite and magnesium ferrite respectively. There is no shift in the =C-H bond stretching (~3007 cm^{-1}) showing that the capping is basically through the carboxylic groups of oleic acid. The FTIR spectra of pure oleic acid was recorded which has been already reported in the previous chapter and hence omitted here.

5.9. THERMOGRAVIMETRIC ANALYSIS:

Though the presence of capping molecules on the surface of the ferrite nanoparticles was ensured from the previous FTIR study, thermogravimetric analysis (TGA) was carried out to estimate the amount of capping agent (oleic acid) present per gm of the sample of ferrite.

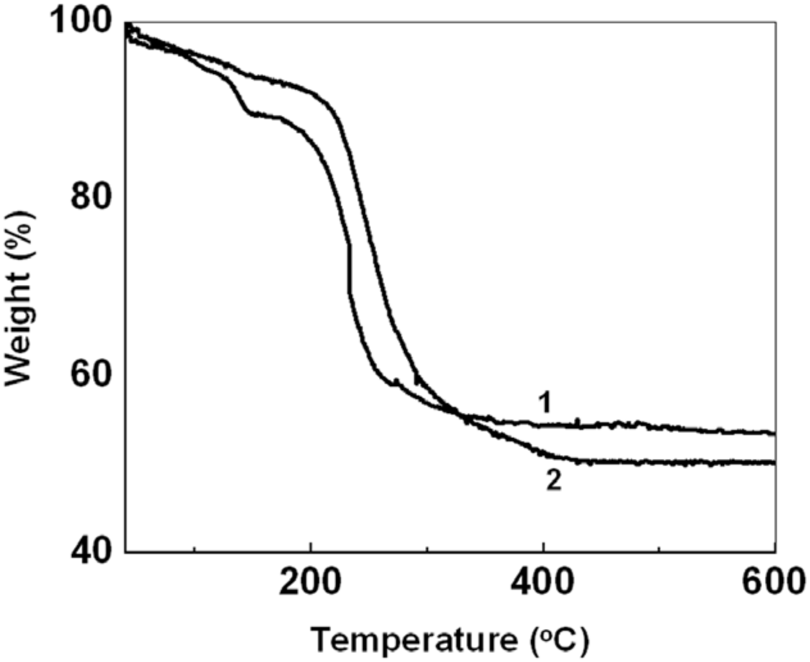

Figure 5.10. *TGA data obtained from of oleic acid-capped* $CoFe_2O_4$ *(curve 1) and* $MgFe_2O_4$ *(curve 2) nanoparticles.*

As shown in *Figure 5.10 (curve 1)*, the pristine oleic acid-capped cobalt ferrite nanoparticles show a small weight loss around 100 ^oC probably due to loss of water and a more significant weight loss of ca. 35% at ~234 ^oC whereas magnesium ferrite nanoparticles show a weight loss of ca. 37% at ~254^oC *(Figure 5.10, curve 2).* The major weight loss in both the cases is attributed to desorption of the oleic acid from the surface of the particles. The process of desorption continued upto a temperature of ~325^oC and the weight loss remained constant after that temperature when monitored till 600^oC.

5.10. MAGNETIC MEASUREMENTS:

Typical temperature and field dependence of the magnetization of the ferrites is shown in *Figure 5.11, Figure 5.12 and 5.14* respectively. Magnetic particles below a certain size display superparamagnetic characteristics as already discussed in Chapter I and Chapter IV. The different magnetization features of our samples, as summarized in *Table 5.1*, are well in accordance with this behavior. In what follows, we give a concise description of the different magnetic characteristics of $CoFe_2O_4$ system first and extend it and compare them to the $MgFe_2O_4$.

Samples	Coercivity H_C at 5K (kOe)	Blocking temperature T_B (K)	Anisotropy constant K_{eff} (erg cm^{-1})	K_{eff} of the bulk* (erg cm^{-1})
$CoFe_2O_4$	11.1	~75	23 X 10^6	2 X 10^6
$MgFe_2O_4$	1.2	~25	0.61 X 10^5	0.25 X 10^5

* Values taken from Ref. 3.

***Table 5.1**. Comparison of magnetic features of cobalt and magnesium ferrite nanoparticles.*

5.10.1. Temperature Dependent Magnetization:

The temperature dependent zero field cooled (ZFC) and field cooled (FC) magnetization curves for $CoFe_2O_4$ and $MgFe_2O_4$ are displayed in *Figure 5.11A and B.* In all the cases the magnetization was measured as a function of temperature at an applied field of 100 Oe. The blocking temperature, T_B, is observed as the maximum in the ZFC curve which is also the point of divergence between ZFC and FC curves. The estimated blocking temperature for $CoFe_2O_4$ nanoparticles is ~75 K *(curve 1and 2, Figure 5.11A)* and ~25 K for $MgFe_2O_4$ nanoparticles *(Figure 5.11B, curve 1 and 2).*

The anisotropic constant K_{eff} values deduced from the equation mentioned in Chapter I (the equation is given as $K_{eff} V = 25 k T_B$) for a 3 nm $CoFe_2O_4$ and similar sized $MgFe_2O_4$ particle are already presented in *Table 5.1.*

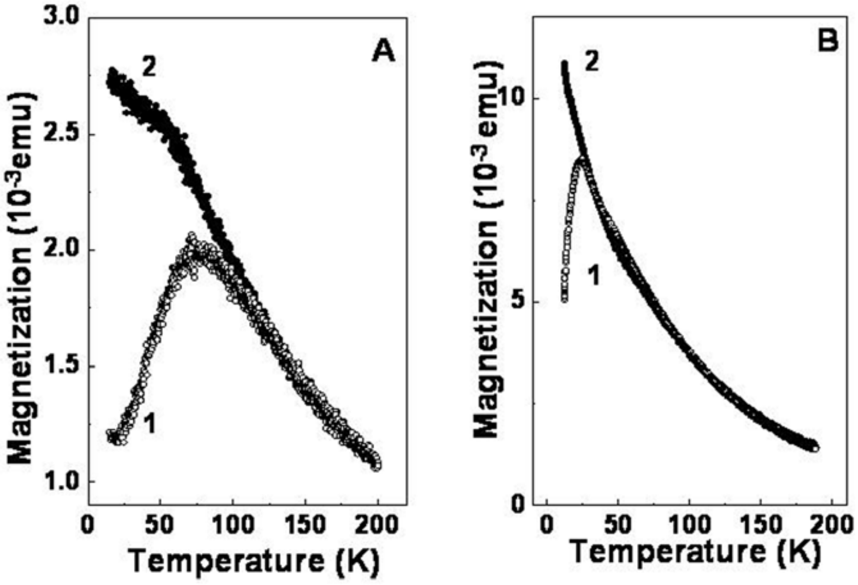

Figure 5.11. *(A) Temperature dependent magnetization of cobalt ferrite nanoparticles in the zero field cooled (ZFC, curve 1) and field cooled (FC, curve 2) modes. The superparamagnetic blocking temperature is ~75K. The applied magnetic field was 100 Oe. (B) Temperature dependent magnetization of magnesium ferrite nanoparticles in the zero field cooled (ZFC, curve 1) and field cooled (FC, curve 2) modes. The blocking temperature of these nanoparticles is ~25K.*

As can be seen the values obtained are in agreement with reported values for similar sized crystallites [21] and are larger than the values reported for bulk. Larger values of the anisotropy constant are expected for nano-sized materials because of the additional contribution from surface anisotropy and other size related contributions. But it is observed that though the magnetocrystalline anisotropy is considered as intrinsic to the materials, the results obtained by different investigators are in poor agreement. Plausible reasons could be the various crystal imperfections like residual strain, lattice vacancies, inclusions, porosity and even the accuracy of measurement leading to the discrete results [3]. It is evident from the above results that $CoFe_2O_4$ particle possesses very high K_{eff} value as compared to $MgFe_2O_4$. The anisotropy energy E_A is related to volume (V) of the nanoparticles and also on the K_{eff} values according to the equation:

$$E_A = K_{eff}V \sin^2 \theta$$

where θ is the angle between the magnetization direction and the easy axis of the particles. In our case, both the ferrites have similar particle size and hence similar volume. So the difference in the anisotropy energy is due to the variation in the anisotropic constant values. The quantum origin of magnetocrystalline anisotropy energy is the L-S coupling at crystal lattice and K_{eff} points towards the strength of such coupling. In $CoFe_2O_4$ and $MgFe_2O_4$ the distribution of divalent and trivalent cations are very similar and so the contribution of L-S coupling at Fe^{3+} cation sites towards the E_A can be considered to be equal. Thus the main difference arises from the contribution of divalent cations. In $MgFe_2O_4$ the Mg^{2+} has no unpaired electrons, hence possesses total electron spin as zero. But in $CoFe_2O_4$, Co^{2+} have high spin ligand field with 7 d-electrons, among which 3 electrons are unpaired. So the strong L-S coupling at Co^{2+} cation sites produce higher magnetocrystalline anisotropy energy as compared to the case of $MgFe_2O_4$ which is well reflected in the high value of K_{eff}. Further due to this high E_A value in $CoFe_2O_4$, more thermal energy is required to rotate the spins, hence $CoFe_2O_4$ has a blocking temperature which is ~50 K higher than the similar sized $MgFe_2O_4$.

5.10.2. Field Dependent Magnetization:

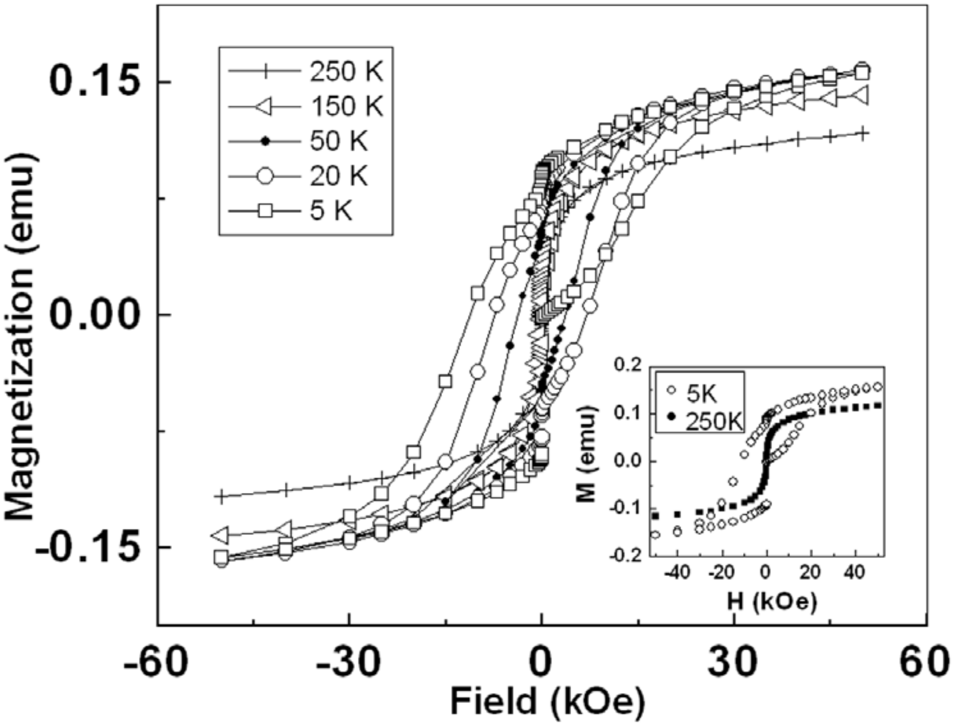

Figure 5.12. *Field dependent magnetization curves of cobalt ferrite nanoparticles below (5K, 20K and 50K) and above (150 and 250K) the blocking temperature (75K). The inset clarifies the opening of the hysteresis loop at temperature (5K) lower than the T_B as compared to the curve above the blocking temperature (250K, inset).*

The isothermal magnetizations obtained at different temperatures spanning the regions below (5K, 20K, 50K) and above the T_B (150K, 250K) are shown in *Figure 5.12*. As expected opening of the magnetic hysteresis loops is observed only below the blocking temperature. The coercivity observed for $CoFe_2O_4$ at 5K is slightly greater than 11 kOe which is similar to the value observed by others for very well characterized ferrite particles of size smaller than 4 nm synthesized by the reverse micellar microemulsion method [31b].

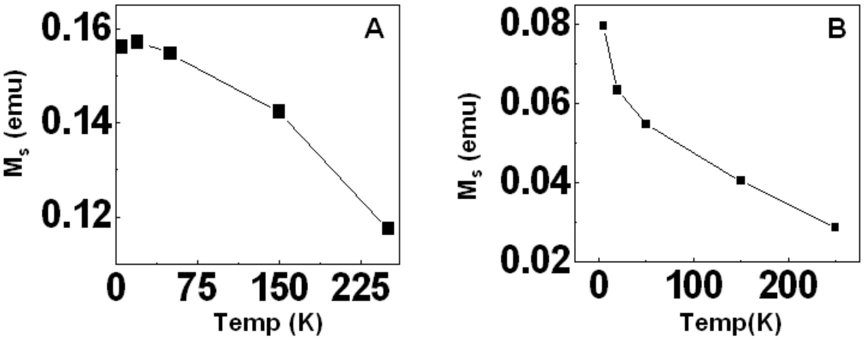

Figure 5.13. *The saturation magnetization Vs temperature plot for superparamagnetic cobalt (A) and magnesium (B) ferrite nanoparticles at different temperatures.*

Interestingly, the saturation magnetization (M_s) values observed *(Figure 5.13A)* for $CoFe_2O_4$ display a broad maximum with a smaller value of M_s at the lowest temperature 5K compared to that observed at 20 K. The M_s values are calculated by extrapolating M Vs 1/H curve to zero. The high anisotropy in $CoFe_2O_4$ probably prevents the easy magnetization direction from aligning with the applied magnetic field, resulting in larger coercive fields and lower M_s value at low temperatures as observed.

Magnetic characteristics of $MgFe_2O_4$ present a different picture altogether. First the blocking temperature observed for this system is only ~25K *(Figure 5.11B)* and consequently the deduced K_{eff} value is 0.61 X 10^5 erg cm^{-1}, very close to the bulk value. The field dependent hysteresis curves for $MgFe_2O_4$ nanoparticles are displayed in *Figure 5.14* measured below the blocking temperature (5K, 20K) and also above the T_B (50K, 150K and 250K). Though there recorded no hysteresis above the blocking temperature a clear hysteresis loop is observed at 5K *(Figure 5.14, inset)*. Other notable differences between these two systems are the coercivity and the temperature variation of the saturation magnetization (M_S) value. The coercivity at 5 K for $MgFe_2O_4$ is found to be

1.2 kOe *(Figure 5.14, inset)*, which is extremely low when compared to that of $CoFe_2O_4$ at the same temperature. Similarly the M_s values of $MgFe_2O_4$ continue to increase with decreasing temperatures *(Figure 5.13B),* quite in contrast to the behavior of $CoFe_2O_4$ nanoparticles.

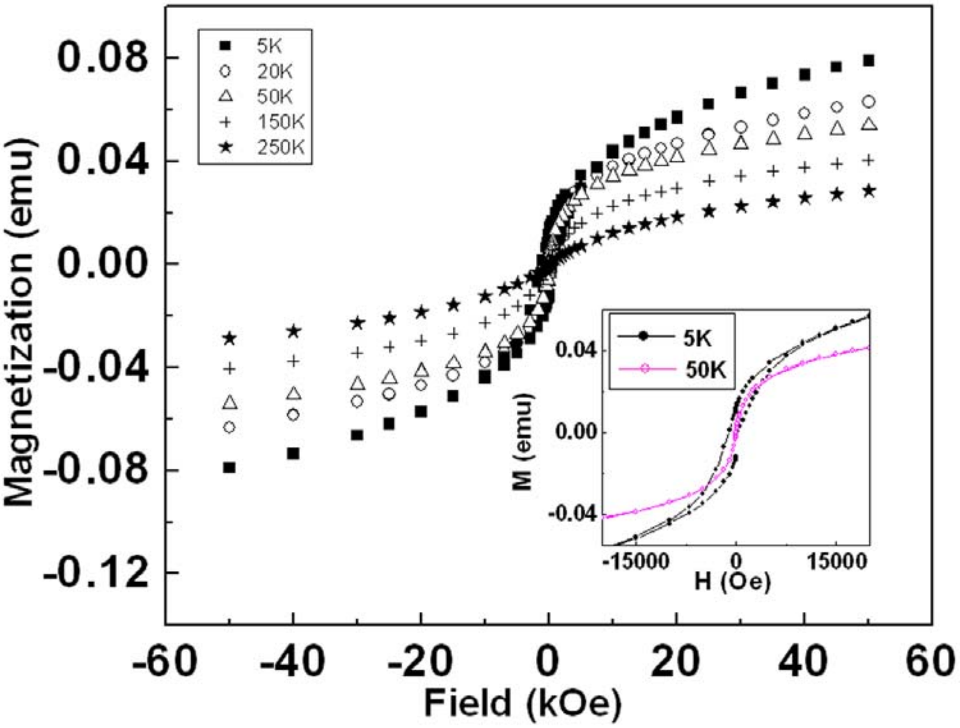

Figure 5.14. *Field dependent magnetization of magnesium ferrite nanoparticles below (5K, 20K) and above (50K, 150K and 250K) the blocking temperature (25K). The hysteresis loop at 5K and 50K are displayed as inset to show the presence of opening of the magnetic hysteresis loops below the blocking temperature.*

All these magnetic features reported for the $CoFe_2O_4$ and $MgFe_2O_4$ nanoparticles formed by foam based method are in good agreement with the trends reported [21] and conclusively proved both of them to be superparamagnetic in nature.

5.11. FERROMAGNETIC RESONANCE SPECTRA:

The ferromagnetic resonance curves of the ferrites, measured at room temperature, are represented in *Figure 5.15.* The striking difference between the two curves is the broadness of the spectra in case of $CoFe_2O_4$ *(graph A)* as compared to that of $MgFe_2O_4$ *(graph B, Figure 5.15).* The data corroborates well with the reported nature of the curves [33a, 33b]. Line width is sometimes connected with the inherent randomness in the sample like inhomogeneity of the sample, non-uniformity of the internal magnetic field, particularly in case of polycrystalline ferrites and porosity. It is also almost impossible to obtain polycrystalline ferrites with porosity lower than 1%, so there is always line broadening of ΔH ≥ $10\text{-}10^2$ oersted. The state of the sample's surface is another conduit through which the line-broadening effect can creep in. It is reported that line width can be reduced by a factor of 20 on polishing the surface of a bulk material. Nanoparticles are expected to possess large surface area with almost ~40-50% of the molecules present on the surface of 3-4 nm particles [34]. Thus the surface roughness is likely to be maximum in them contributing to the broad line width. Magnetic anisotropy is another obvious reason for the broadening of resonance line in polycrystalline ferrites [33].

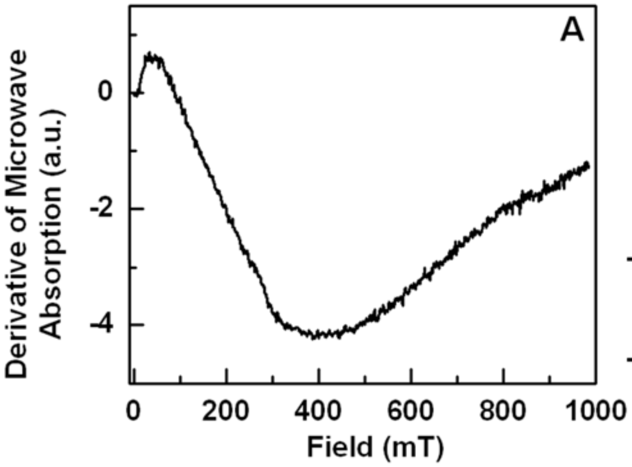

Figure 5.15. *The ferromagnetic resonance spectra of* $CoFe_2O_4$ *(A) and* $MgFe_2O_4$ *(B) synthesized by foam based the technique.*

In our case as both the ferrites are synthesized by same procedure their porosity and surface chemistry can be considered to be comparable. So the basic difference between the line widths probably resulted from the magnetic anisotropy effect. The difference in the strength and direction of the internal anisotropy field of the crystallites is expected to modify the externally applied magnetizing field resulting in the resonance to occur at different values for the two ferrites nanoparticles.

Indeed the g-value calculated for magnesium ferrite nanoparticles is found to be 2.05, which matches well with the reported value of these ferrite nanoparticles of equivalent size [33a]. The calculation of g-value is almost impossible for cobalt ferrite for extremely broad nature of the curve. Between the two ferrite nanoparticles prepared here

$CoFe_2O_4$ is a hard magnetic material. Thus it possesses a larger internal field opposing the external field and results in a broad FMR line at very small magnetic field. $MgFe_2O_4$ has a very low magnetic moment and thus results in a FMR line shape similar to the paramagnetic substance at higher field strength.

5.12. CONCLUSION:

The excellent templating potential of aqueous foam for the formation of nanoparticles like multi component oxides has been demonstrated. The inherent difficulty of this method in preparing ferrites of formula MFe_2O_4 with the 'M' metal ions and iron possessing different oxidation states has been overcome by utilizing the in-situ conversion of Fe^{2+} to the Fe^{3+} state thus circumventing the differential binding of ions to the surfactant while preparing the foam. Reaction of NaOH with Fe^{3+} and Co^{2+}/Mg^{2+} ions electrostatically entrapped in the foam results in the formation of very fine superparamagnetic crystals of spinel ferrites in the Plateau border regions of the foam. The presence of oleic acid as the capping agent is found to be essential in order to avert coagulation of the nanoparticles. The big advantage of our method is the convenience with which we could get good quality ferrite nanoparticles in the less than 5 nm regime. It is well documented that the nature and concentration of anions such as phosphate, sulfate and chloride present in solution greatly influence several characteristics of the resulting nanoparticles in solution-based synthesis methods [35]. However, when we carry out the reaction in a foam, the presence of the counter-ions is reduced significantly because the foam matrix is expected to be composed of only the metal ions and surfactant through electrostatic complexation, averting the problems associated with the presence of counter-ions. A combination of extremely large interfacial templating area provided by the liquid lamellae in foams stabilized by ionizable surfactants and the dynamic nature of the foam bubbles makes this method potentially exciting for the large scale synthesis of important materials.

5.13. REFERENCES:

[1]. http://scienceworld.wolfram.com/chemistry/SpinelStructure.html

[2]. Huhyee, J. E. *Inorganic Chemistry* (Third Edition)

[3]. Cullity, B. D. *Introduction to Magnetic Materials*, Addison-Wesley Publishing, Reading, **1972.**

[4]. Pileni, M. P. *J. Phys. Chem. B* **2001,** *105,* 3358.

[5]. Speliotis, D. E. *J. Magn. Magn. Mater.* **1999**, *193*, 29.

[6]. (a) Semelka, R.; Helmberger, T. *Radiology.,* **2001**, *218*, 27. (b) Coroiu, I. *J. Magn. Magn. Mater*. **1999**, *201*, 449. (c) Jung, C.; Jacobs, P. *Magn. Reson. Imag.* **1995**, *13*, 661. (d) Wu, E. D.; Tang,H.; Jensen, J. H. *NMR Biomed.* **2004**, *17*, 478.

[7]. Rosenweig, R. E.; *Ferrohydrodynamics*, Cambridge University Press, Cambridge **1985.**

[8]. (a) Weitschies, W.; Kötitz, R.; Bunte,T.; Trahms, L. *Pharm. Pharmacol. Lett.* **1997**, *7*, 5. (b) Kotitz, R.; Weitschies, W.; Trahms, L.; Brewer, W.; Semmler, W. *J. Magn. Magn. Mater.* **1999**, *194*, 62.

[9]. Goodwin, S.; Peterson, C.; Hoh, C.; Bittner, C. *J. Magn. Magn. Mater*. **1999**, 194, 132.

[10]. Hiergeist, R.; Andra, W.; Buske, N.; Hergt, R.; Hilger, I.; Richter, U.; Kaiser, W. *J. Magn. Magn. Mater.* **1999**, *201*, 420.

[11]. (a) Hochepied, J. F.; Bonville, P.; Pileni, M. P. *J. Phys. Chem. B* **2000**, *104,* 905. (b) Liu, C.; Rondinone, A. J.; Zhang, Z. J. *Pure Appl. Chem.,* **2000,** *72*, 37.

[12]. (a) Kale, S.; Gubbala, R. D. K.; Misra, J. *J. Magn. Magn. Mater.* **2004**, *277*, 350. (b) Liu, C.; Zou, B.; Rondinone, A. J.; Zhang, Z. J. *J. Phys. Chem. B,* **2000***, 104,* 1141.

[13]. (a) Ghosh, M.; Lawes, G.; Gayen, A.; Subbanną,G. N.; Reiff, W. M.; Subramanian, M. A.; Ramirez, A. P.; Zhang, J. P.; Seshadri, R. *Chem. Mater.* **2004,** *16,* 118. (b) Ammar, S.; Helfen, A.; Jouini, N.; Fievet, F.; Rosenman, I.; Villain, F.; Molinie, P.; Danot, M. *J. Mater. Chem.* **2001**, *11*, 186.

[14]. (a) Sun, S.; Zeng, H.; Robinson, D. B.; Raoux, S.; Rice, P. M.; Wang, S. X.; Li, G. *J. Am. Chem. Soc.* **2004**, *126*, 273. (b) Thimmaiah, S.; Rajamathi, M.; Singh, N.; Bera, P.; Meldrum, F.; Chandrasekhard, N.; Seshadri, R.; *J. Mater. Chem.,* **2001**, *11*, 3215. (c) Kang, E.; Park, J.; Hwang, Y.; Kang, M.; Park, J-G.; Hyeon, T. *J. Phys. Chem. B* **2004,** *108,* 13932.

[15]. Shafi, K.V. P. M.; Gedanken, A. *Chem. Mater.* **1998,** *10,* 3445.

[16]. (a) Manova, E.; Kunev, B.; Paneva, D.; Mitov, I.; Petrov, L.; Estournes, C.; D'Orle´ans, C.; Rehspringer, J. L.; Kurmoo, M. *Chem. Mater.* **2004,** *16,* 5689. (b)

Sÿepelak, V.; Menzel, M.; Becker, K. D.; Krumeich, F. *J. Phys. Chem. B* **2002,** *106,* 6672.

[17]. Sathaye, S. D.; Patil, K. R.; Kulkarni, S. D.; Bakre, P. P.; Pradhan, S. D.; Sarwade, B. D.; Shintre, S. N. *J. Material Science* **2002,** *37,* 1.

[18]. Hornga, L.; Chernb, G.; Chenb, M.C.; Kanga, P.C.; Lee, D.S. J. Magn. Magn. Mater. **2004**, *270*, 389.

[19]. Konishi, Y.; Nomura, T.; Mizoe, K. *Hydrometallurgy* **2004**, *74*, 57.

[20]. (a) Mandal, S.; Arumugam, S. K.; Adyanthaya, S. D.; Sastry, M. *J. Mater. Chem.* **2004***, 14,* 43. (b) Mandal, S.; Arumugam, S. K.; Pasricha, R.; Sastry, M. *Bull. Mater. Sci.* **2005,** *28*, 503. (c) Rautaray, D.; Sinha, K.; Shankar, S. S.; Adyanthaya, S. D.; Sastry, M. *Chem. Mater.* **2004**, *16*, 1356. (d) Shankar, S. S.; Patil, U. S.; Prasad, B. L. V.; Sastry, M. *Langmuir* **2004**, *20*, 8853. (e) Weaire, D.; Hutzler, S. *The Physics of Foams*, Oxford University Press, Oxford, **1999**.

[21]. Liu, C.; Zou, B.; Rondinone, A. J.; Zhang Z. J. *J. Am. Chem. Soc.* **2000,** *122,* 6263.

[22]. Shivshankar, S.; Patil, U.; Prasad, B. L. V.; Sastry, M. *Langmuir*, **2004,** *20,* 8853.

[23]. http://macbeth.if.usp.br/~goya/ferrites.htm

[24]. http://www.uwgb.edu/dutchs/PETROLGY/Spinel%20Structure.HTM

[25]. Bonini, M.; Wiedenmann, A.; Baglioni, P. *Physica A* **2004**, *339*, 86.

[26]. Cullity, B. D.; Stock, S. R. *Elements of X-Ray Diffraction* (Third Edition) **2001,** pp 170-173

[27]. Wagner, C. D.; Riggs, W. M.; Davis, L. E.; Moulder, J. F.; Muilenberg, G. E.; *Handbook of X-ray photoelectron spectroscopy, Perkin Elmer Corp. Publishers, Eden Prairie, MN*, **1979.**

[28]. (a) Chu, Y. Q.; Fu, Z. W.; Qin, Q. Z.; *Electrochimica Acta.* **2004**, *49*, 4915. (b) Mittal, V. K.; Bera, S.; Nithya, R.; Srinivasan, M. P.; Velmurugan, S.; Narasimhan,S. V. *Journal of Nuclear Materials* **2004**, *335*, 302. (c) Fu, L.; Liu, X.; Zhang, Y.; Dravid,V. P.; Mirkin, C. A. *Nano lett.* **2003,** *3*, 757. (d) Yang, X.; Wang, X.; Zhang, Z. *J. Cryst. Growth* **2005**, *277*, 467. (e) Ji, G. B.; Tang, S. L.; Ren, S. K.; Zhang, F. M.; B. Gu, X.; Du, Y. W. *J. Cryst. Growth* **2004,** *270*, 156.

[29]. Kim, J. G.; Pugmire, D. L.; Battaglia, D.; Langell, M. A. Applied Surface Science, **2000,** *165*, 70.

[30]. Shen, C.; Kahn, A.; Schwartz, J. *J. Appl. Phys.,* **2001,** *89,* 449.

[31]. (a) Song, Q.; Zhang, Z. J. *J. Am. Chem. Soc.* **2004**, *126*, 6164. (b) Hyeon, T.; Chung, Y.; Park, J.; Lee, S. S.; Kim, Y.-W.; Park, B. H. *J. Phys. Chem. B* **2002,** *106,* 6831.

[32]. Wu, N.; Fu, L.; Su, M.; Aslam, M.; Wong, K. C.; Dravid, V. P. *Nano Lett.* **2004,** *4*, 383.

[33]. (a) Yager, W. A.; Merritt, F. R.; Guillaud, C. *Phys. Rev.* **1951**, *81*, 477. (b) Zysler, R.D., Tejada, J.; Molins E. *J. Magn. Magn. Mater.,* **2004,** *272-276*, e1191. (c) Koseoglu, Y. *J. Magn. Magn. Mater.,* **2006,** *300*, e327. (d) Turov, E. A.; *Froomagnetic Resonance, Chapter VI*, pp 184-230.

[34]. Klabunde, K. J. Nanoscale Materials In Chemistry, A John Wiley & Sons Inc. Publication, **2001**.

[35]. (a) Matijevic, E. *Chem. Mater*. **1993**, *5*, 412. (b) Domingo, C.; Rodriguez-Clemente, R.; Blesa, M. *J. Colloid Interface Sci*. **1994**, *165*, 244.

Chapter VI

Phase transfer of different nanoparticles to organic media, their assembly and transmetallation reaction in organic phase

---

This chapter illustrates the phase transfer of various nanomaterials from aqueous to organic phase synthesized by different experimental conditions followed by the assembly of the phase transferred particles to form long organized linear structure and also describes the utilization of phase transferred nanoparticles for transmetallation reaction to produce core-shell structures. Ag and Ni-core Ag-shell nanoparticles when capped with oleic acid could be readily phase transferred to organic phase like cyclohexane in presence of ortho-phosphoric acid due to orientational flexibility of oleic acid on the surface of Ag. Same protocol also worked for AOT surfactant capped silver nanoparticles, which can be transported to number of organic solvents like chloroform, toluene, cyclohexane etc. Interestingly pristine oleic acid capped Ni nanoparticles cannot be phase transferred following the earlier method. A thin layer of Ag on Ni can circumvent the difficulty or the presence of stearic acid is essential in the organic medium to achieve the goal, due to space exchange between oleic acid and stearic acid. These hydrophobized nanoparticles can be assembled in linear fashion at air-water interface using Langmuir-Blodgett technique. On the other hand Co nanoparticles synthesized in the aqueous phase and coated with surfactant SDS and oleic acid can be directly re-dispersed into toluene. These Co nanoparticles were then utilized to accomplish transmetallation reaction in toluene with hydrophobized chloroauric acid.

Part of this work has been published in:
(1) Bala, T.; Swami, A.; Prasad, B. L. V.; Sastry, M. *J. Colloid and Interf. Sci.* **2005**, *283*, 422. (2) Prasad, B. L. V.; Arumugam, S. K.; Bala, T.; Sastry, M. *Langmuir* **2005**, *21*, 822. (3) Bala, T.; Joshi, B.; Iyer, N.; Sastry, M.; Prasad, B. L. V. *J. Nanosci. Nanotechnol.* **2006**, *6*, 1. (4) Bala. T.; Katsuyama, C.; Enoki, T.; Sastry, M.; Prasad, B. L. V. (manuscript under preparation)

6.1. INTRODUCTION:

Water as a solvent has unique physicochemical properties like relatively high thermal stability and low evaporation rate, hence its use circumvents many of the environmental and safety problems, which result from the traditional volatile organic compounds. As a result, it is regarded as potential “green solvents” [1]. Likewise it continues to attract an increasing amount of interest as a medium for the synthesis of nanomaterials. But there are several disadvantages associated with the nanoparticles synthesized in aqueous solvents, particularly from application point of view. The nanoparticles synthesized in water are not easily separated from solution in the form of a powder that would be readily re-dispersible in water after storage. Moreover to generate spontaneous close-packed, hexagonal monolayer assembly of nanoparticles upon solvent evaporation is exigent when the nanoparticles are synthesized in water. Such kind of self-assembly is crucial to generate well organized layers of magnetic materials in electronic industries and the solvent evaporation rate can be easily accelerated when it is a low boiling non-polar organic solvent. The collective properties of the nanoparticle assembly may be controlled by varying the inter-particle separation via capping with different chain length organic molecules which can be accomplished more conveniently in the organic phase [2]. Nanoparticles also have enormous application in the field of catalysis and to catalyze an organic reaction we need to synthesize the nanoparticles in nonionic organic solvents. So a large component of contemporary research involves the synthesis of various nanomaterials in organic phase and the assembly of organically dispersible nanoparticles covering large surface area.

In most of the synthetic processes, the nanoparticles after synthesis remain dispersed in the medium in which they are prepared, either aqueous or organic solvents, but not both. There are number of advantages/disadvantages associated with the synthesis of nanoparticles in aqueous and non-polar organic environments and the process of phase transfer of nanoparticles synthesized in one medium to another highly different environment enables marrying the advantages of the two media. Nevertheless, the ability to direct nanoparticles into various physicochemical environments i.e. different liquid phases is often needed for various applications, particularly in the field of catalysis and sensors [3]. Thus, growing research efforts have been directed toward the study of the phase transfer of nanoparticles from an aqueous phase into an organic phase or vice versa, where the latter is generally termed as reverse phase transfer. In regard to transference from the aqueous phase into the organic phase, nanoparticles must be rendered hydrophobic by complexation with organic molecules by covalent or electrostatic interactions and in the first part of this chapter we have mainly focused our discussion towards the phase transfer of various nanoparticles after their synthesis in aqueous medium. The phase transfer is achieved in presence of different capping agents, which being present on the surface of nanomaterials, make them dispersible in both aqueous and organic media. Apart from the issues of phase transfer the later part of the chapter deals with the utilization of the phase transferred materials. These phase-transferred nanoparticles were exploited for long range assembly using Langmuir-Blodgett technique and also for the synthesis of core shell composites in the organic phase. Hence we shall restrict our discussion to different phase transfer procedures reported so far by different research groups in the following section.

Several experimental procedures have been reported for the phase transfer of nanoparticles dispersed in an aqueous medium to various non-polar organic media. The water-organic medium phase transfer of nanoparticles is generally achieved by hydrophobization of the nanoparticle surface by exchanging the surface capping agent of the nanoparticles in water with a ligand having a surface sensitive head group and a long alkyl chain making it easily dispersible in non-polar organic solvents. Here, the surface sensitive head group attaches itself firmly to the nanoparticle surface while the hydrophobic hydrocarbon groups are directed towards the solvent environment making the nanoparticles non-polar organic solvent friendly [4-15]. While alkanethiols have been shown to be effective ligands for the phase transfer of aqueous gold, silver, platinum and palladium nanoparticles [4-10], it has been shown by Sastry et al. that alkylamines are equally effective in promoting the phase transfer of aqueous gold [12] and silver [14] nanoparticles into non-polar organic environments. In some instances, the water-organic solution nanoparticle phase transfer has been assisted by addition of inorganic acids such as HCl or $H_3PO_4/HClO_4$ [4-11]. One of the procedures for the phase transfer of aqueous gold, silver and palladium nanoparticles assisted by hydrochloric acid involves the capping of these metal nanoparticle surfaces by alkanethiol molecules present in the organic medium during the phase transfer [4-9]. In an interesting different approach, Efrima and co-workers have reported that aqueous silver nanoparticles capped with oleic acid molecules undergo phase transfer assisted by phosphoric acid or perchloric acid without ligand exchange [10, 11]. Addition of these acids is purported to render the surface-bound oleic acid molecules orientationally flexible and thus make the surface hydrophobic and amenable for the phase transfer from aqueous to organic medium. A similar phenomenon appears to be operating in the precipitation of aqueous oleic acid-capped metal nanoparticles induced by sodium salts that may subsequently be dispersed in non-polar organic solvents [16, 17].

Investigations on nanoparticle phase transfer in the other direction - organic to aqueous medium - are relatively rare. The few reports that deal with this reverse phase transfer process, are based on the place exchange mechanism where the uni-functional surface capping agents are replaced by bi-functional surface active agents, with one group attached to the nanoparticle surface and the hydrophilic group at the other end rendering the nanoparticle water dispersible. Examples of such protocols include those reported by Rotello and co-workers where alkanethiol molecules on the gold nanoparticle surface were replaced with 11-thioundecanoic acid [18]. In this case, the thiol group is attached to the gold nanoparticle surface and the free carboxylic group at the other end makes the nanoparticles water dispersible. Other examples involve the usage of short chain length stabilizers [19] or forming cyclodextrin [20] or polymer [21] bi-layers on the nanoparticle surface thereby rendering them hydrophilic. Earlier work from this laboratory has focused on the reverse phase transfer of nanoparticles through the formation of interdigitated bilayers on the nanoparticle surface [22]. These approaches involved the formation of interdigitated bilayers between the hydrocarbon chain of the capping agent on the nanoparticle surface and the hydrocarbon chains of an anionic or cationic surfactant present in the aqueous phase. Thus, formation of interdigitated bilayers imparts significant charge to the nanoparticle surface rendering them hydrophilic [22]. In a very recent report by Zubarev et al. it has been shown that the same Au nanoparticles can be dispersed in solvents like water as well as any organic solvent including hexane. They achieved the goal by making a hybrid structure of Au and a V-shaped amphiphilic organic molecule that has one hydrophobic and one hydrophilic arm, which are distributed along the surface in alternating fashion [23]. All the reported methods are summarized in the *Figure 6.1*.

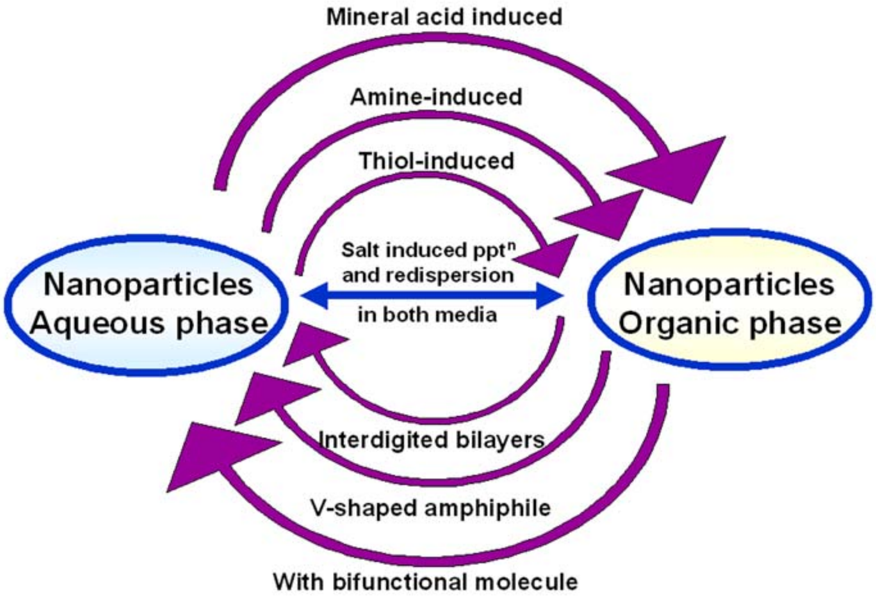

Figure 6.1. *Preview of different methods reported for phase transfer of nanoparticles.*

Majority of experimental protocols for the phase transfer of the nanoparticles involve the modification of nanoparticle surface permanently, the exceptions to this rule being the methods developed by Efrima and co-workers [10,11], Hirai et al. (salt induced precipitation and redispersion) [16,17] and our bi-layer formation strategies [22,23]. While detailed investigations have been carried out to understand the acid-facilitated phase transfer of oleic acid-caped silver nanoparticles [10,11], a clear understanding of the mechanism is yet to emerge. We address this issue herein and investigate the role of acids in modulating the surface hydrophobicity/hydrophilicity of oleic acid-capped silver nanoparticles. Our experiments also reveal that the time of reaction with acid plays an important role in determining the percentage of silver nanoparticles phase transferred. We also seek to understand the organic solvent redispersibility of oleic acid-capped silver nanoparticles precipitated using a salt and how this process is connected to acid-facilitated changes in the organization of the oleic acid monolayer on the silver nanoparticles. During the course of this work, we have observed that salt induced precipitation leads to the isolation of oleate capped silver nanoparticles, which could then be re-dispersed both in organic and aqueous media. Another interesting finding that emerged from our experiments is that the orientational flexibility of oleic acid seems to be unique to certain metal surfaces. Our experiments clearly show that both acid- and salt-facilitated phase transfers fail when we attempt to transfer oleic acid capped Ni nanoparticles from aqueous to an organic medium. Recognizing the versatility of oleic acid-capped silver nanoparticles in such a phase transfer, we got around this problem by coating a thin shell of silver on the Ni nanoparticle surface. The presence of a layer of silver on Ni provided the necessary flexibility for the oleic acid molecules enabling the phase transfer process. This method can be generalized to other metal cores having few layers of silver coating on the surface. We also tried to look for other molecules, which can show similar orientational change and render the nanoparticles dispersible in both aqueous and organic media. Sodium bis (2-ethyl hexyl) sulpho succinate, commonly known as AOT, a double tailed surfactant having sulphonate group as its functional head part, has found to have similar orientational flexibility as shown by oleic acid. The AOT capped Ag particles are stable in aqueous medium and can also be phase transferred to make stable organic dispersions.

6.2. PHASE TRANSFER OF OLEIC ACID CAPPED NANOPARTICLES:

6.2.1. EXPERIMENTAL DETAILS:

(A) Silver hydrosol. In a typical experiment, 1 X 10^{-3} M Ag_2SO_4 was reduced with 0.1% $NaBH_4$ in the presence of 1 X 10^{-4} M oleic acid. A brownish yellow colloidal solution of silver was obtained immediately. This solution was kept for 2 h for complete decomposition of $NaBH_4$.

(B) Silver organosol. To a biphasic mixture of 25 ml each of the silver hydrosol and cyclohexane, 0.2 ml of 0.1 M H_3PO_4 was added under the condition of vigorous stirring. The color of the organic phase changes to bright yellow immediately indicating phase transfer of Ag nanoparticles to organic phase when H_3PO_4 is added to the silver nanoparticle hydrosol. Occurrence of phase transfer of Ag nanoparticles was also confirmed by UV-Vis spectra of respective solutions. The time-dependent phase transfer of the silver nanoparticles was also studied by measuring the UV-Vis spectra of the organic and aqueous phases at t =10 min and t = 1 h after the addition of acid.

(C) Precipitation of silver nanoparticles. In a different strategy to achieve phase transfer, the Ag nanoparticles capped by oleic acid were precipitated by the addition of 0.8 M

NaCl solution to 20 ml of the silver hydrosol. The precipitate obtained could be readily redispersed in both water and cyclohexane without additional treatment.

(D) Preparation of $Ni_{core}Ag_{shell}$ nanoparticles. Synthesis of oleic acid capped Ni and $Ni_{core}Ag_{shell}$ systems was accomplished following the same foam based method as reported in Chapter IV. We do not describe the details of the synthesis here in order to avoid repetition.

It is to be noted that all the chemicals required for the experiments were purchased from Aldrich and used as received.

6.2.2. PHASE TRANSFER OF SILVER NANOPARTICLES CAPPED BY OLEIC ACID FROM AQUEOUS TO ORGANIC MEDIUM:

6.2.2-1. UV-VIS SPECTROSCOPY:

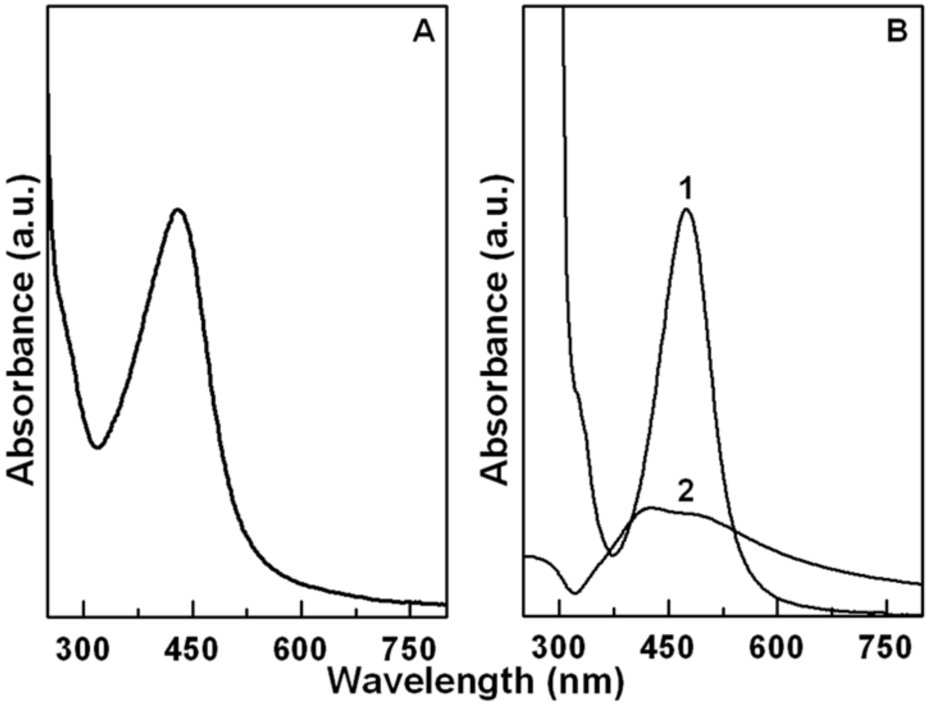

Figure 6.2. *(A) UV-Vis spectrum of as prepared Ag hydrosol. (B) UV-Vis spectra of Ag nanoparticles after phosphoric acid induced phase transfer to cyclohexane (curve 1) whereas Curve 2 depicts the aqueous layer after phase transfer of Ag nanoparticles.*

The UV-Vis spectrum of Ag nanoparticles in the aqueous layer shows a distinctive surface plasmon resonance [24] peak at ~429 nm *(Figure 6.2A)* indicating the formation of the desired nanoparticles. After the acid induced phase transfer into the cyclohexane layer, the organic layer showed the presence of a peak at ~470 nm *(Figure*

6.2B, curve 1) whereas the aqueous layer after phase transfer showed minimum absorbance *(Figure 6.2B, curve 2)* indicating a complete phase transfer from aqueous to organic layer has occurred. The UV-Vis spectra of the water and cyclohexane re-dispersed phases after the salt induced precipitation of hydrosol are provided in *Figure 6.3*. The accompanying picture in this figure shows the precipitate as well as the sample bottles containing aqueous and organic dispersed samples. This is in contrast to the acid induced phase transfer as described above where the phase transfer is irreversible. Indeed once the silver nanoparticles are dispersed in organic media by the acid induced method, any attempts to achieve the reverse phase transfer by adding salts and/or bases and shaking with water for several hours to days proved futile in directing the carboxylic acid capped silver nanoparticles from organic to aqueous media.

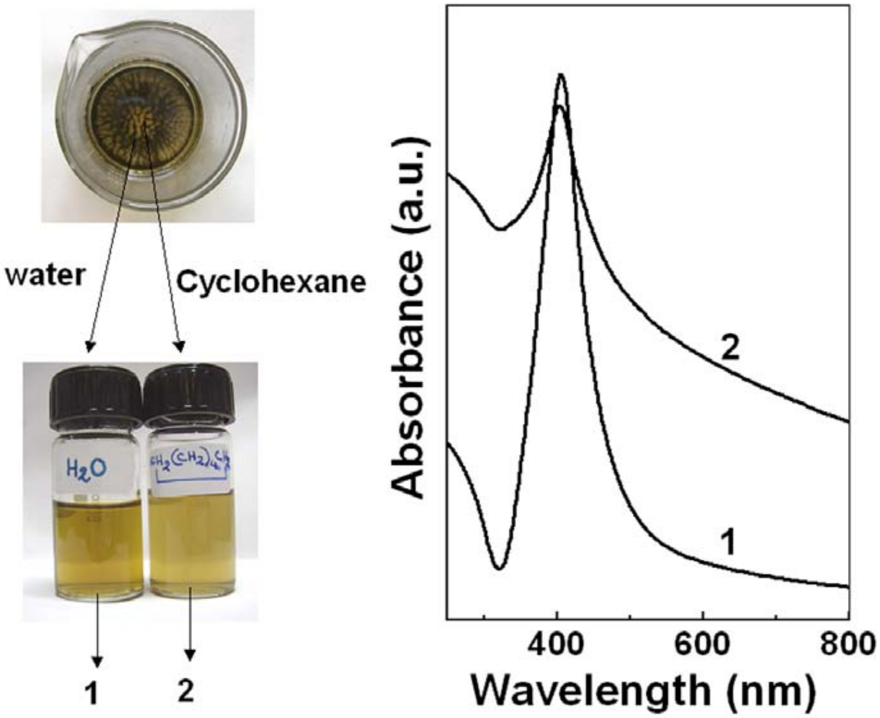

Figure 6.3. *UV–vis spectra of oleic acid-capped silver nanoparticles precipitated out by the addition of salt to the as-prepared hydrosol and redispersed in water (curve 1) and cyclohexane (curve 2). The photograph to the left displays the precipitate after the salt addition and the redispersion in water and cyclohexane.*

6.2.2-2. TRANSMISSION ELECTRON MICROSCOPY:

The formation of silver nanoparticles was confirmed from the TEM images of the oleic acid capped silver nanoparticles in the aqueous medium *(Figure 6.4A, B)*. The selected area diffraction pattern in the inset of *Figure 6.4A* proved the crystals to have fcc lattice arrangement. The phase transferred nanoparticles in organic medium are depicted in *Figure 6.4C, D* along with the indexed diffraction pattern in the inset of *Figure 6.4D* showing the fcc structure of the silver nanoparticles.

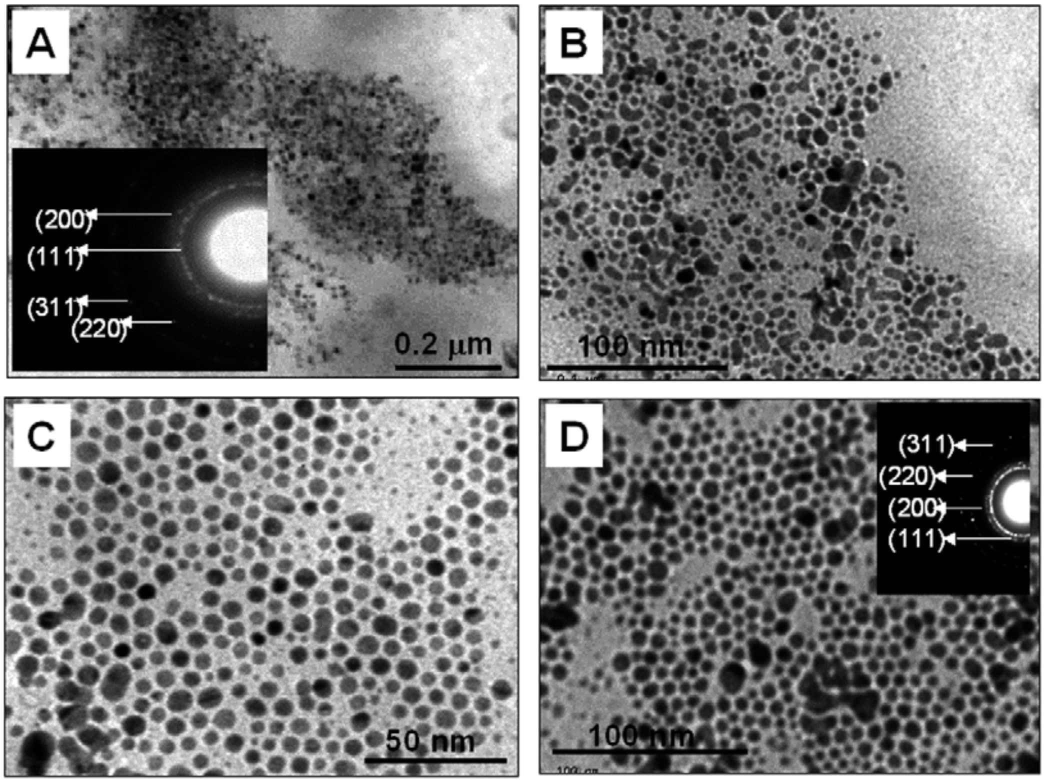

Figure 6.4. *TEM images of the Ag hydrosol (A and B) and those of the organosol (C and D) after phase transfer. The phase transfer is brought about by the addition of phosphoric acid to silver hydrosol and shaking with an organic solvent (cyclohexane). The selected area diffraction patterns in the insets of A and D can be indexed to fcc Ag.*

The images clearly revealed that in organic medium the particles are well separated and assembled into a quasi-hexagonal arrangement. In fact, for all practical purposes our findings are very similar to the findings of Efrima and co-workers [10, 11].

Figure 6.5A represents the TEM images of Ag nanoparticles after re-dispersing the Ag nanoparticle powder obtained by salt induced precipitation in water and *Figure 6.5B* is that of the organic phase. The silver nanoparticles phase transferred by this method behave in the same way as the acid induced one in all the respects except that the particles are more sintered in this case, probably due to the induced coagulation procedure (*Figure 6.5A-B)*. The particles are quite irregular in size hindering us to calculate the particle size distribution in this case. The fcc crystal structure of the re-dispersed Ag nanoparticles after salt-induced precipitation is confirmed from the SAED pattern in the inset of *Figure 6.5B*.

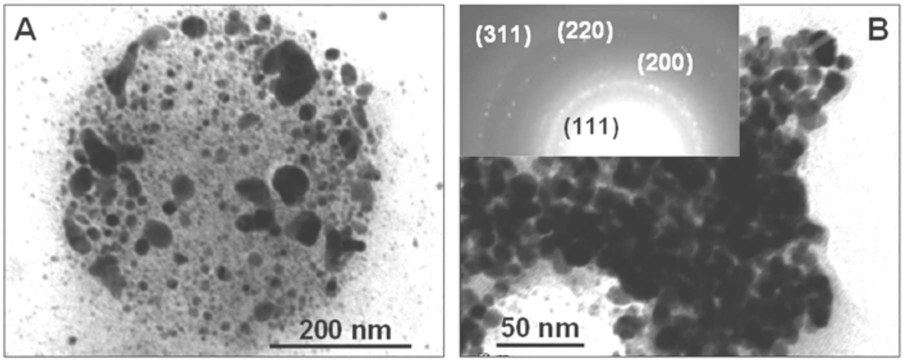

Figure 6.5. *TEM pictures of Ag hydrosol (A) and organosol (B) obtained after re-dispersing the Ag nanoparticles precipitated by addition of excess NaCl in the aqueous phase.*

6.2.2-3. FOURIER TRANSFORM INFRARED SPECTROSCOPY:

FTIR studies provide many useful hints to understand the mechanism of phase transfer. *Figure 6.6* provides the FTIR spectra of the silver nanoparticles in the aqueous as well as organic environments where the phase transfer was achieved by both means. *Curve 1* in *Figure 6.6* is that of pure oleic acid. *Curve 2* depicts the FTIR spectra taken from the hydrosol while *Curve 3* is the spectra recorded from the organosol where the phase transfer was induced by the addition of phosphoric acid. In *Curves 4 and 5,* we provide the FTIR spectra of the hydrosol and organosol respectively where the phase transfer was achieved by the salt induced precipitation and re-dispersion in cyclohexane. From the FTIR studies and from previous literature the stabilization of silver nanoparticles in aqueous medium can be summarized as follows. First, silver nanoparticles are stabilized better by long alkyl chain carboxylic acid molecules bearing one double bond in the *cis* form (presence of more double bonds or the *trans* form actually make the colloids destabilized) [10]. Accordingly the =C-H stretching is found to be generally shifted to 3013 cm^{-1} from 3004 cm^{-1} as observed in pure oleic acid or sodium oleate [10, 11]. In our procedure we use $NaBH_4$ as the reducing agent and that acts as the source of sodium ions, while in some of the earlier reported procedures sodium oleate was taken as the stabilizing agent [25]. We would like to caution, however, that the intensity of the peak and the shifts observed in the =C-H stretch are rather weak and ambiguous many times, hence we will build up our discussion based on the –COO$^-$ stretch, which shows more convincing shifts. We also provide ^{1}H NMR spectra in the next section, which support our arguments.

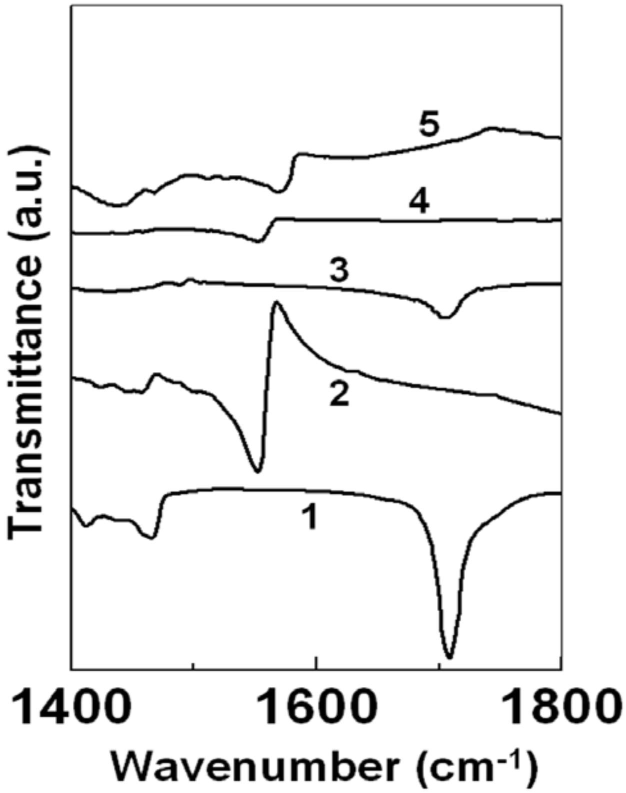

Figure 6.6. *FTIR spectra of the pure oleic acid (curve 1) and the oleic acid-capped silver nanoparticles in the aqueous and organic media. Curve 2 is that of the as-prepared hydrosol, curve 3 is from the organosol obtained by the addition of phosphoric acid and shaking with cyclohexane, and curve 4 is recorded from the hydrosol prepared through the salt-induced precipitation method. Curve 5 is of the organosol (in cyclohexane) prepared through the salt-induced precipitation method.*

Thus since the carboxylic acid is bound to the silver surface through the double bond in the hydrosol, the carboxylic acid moiety is exposed to the aqueous medium with the FTIR studies clearly showing that the carboxylic acid actually exists as a carboxylate stabilized by the sodium ions [25]. This is confirmed by the fact that in the hydrosol the -COO^- stretch band of the oleate appears at 1559 cm^{-1} which is similar to that observed for sodium oleate whereas silver oleate band is observed at 1517 cm^{-1}. The scenario changes drastically once phosphoric acid is added with the oleic acid undergoing a major orientational change. First, the carboxylate group is converted to the acid form and then the double bond attached to the silver surface is released. The oleic acid molecule then re-orients itself and now the carboxylic acid is attached to the silver surface exposing the hydrophobic tail towards the solvent allowing the phase transfer. These steps are clearly delineated by the FTIR measurements where the spectra from organosol show features corresponding to free carboxylic acid *(Figure 6.6, curve 3)* as observed in pure oleic acid at 1707 cm^{-1}. Our observations are clearly in agreement with earlier reports where it was suggested that in organosol obtained via the acid assisted protocol the adsorption on silver particles is through the carboxylic acid group rather than by dissociated carboxylate [11]. The salt induced precipitation and re-dispersion in water does not seem to bring about any major changes in the orientation or structure of oleic acid on the silver surface. *(Figure 6.6, curve 4)* and the FTIR spectrum is similar to the as-prepared hydrosol for all practical purposes.

There is a small deviation in the mechanism involved in the salt induced precipitation and re-dispersion into organic solvents. Here, the organosol still shows features at 1559 cm^{-1} clearly revealing that the acid is still in carboxylate form stabilizing the silver particles *(Figure 6.6, curve 5)*. This can only be rationalized by considering that the sodium ions are now probably adsorbed on the silver surface providing some anchoring sites to the carboxylate groups. This again directs the hydrophobic tail to the organic solvent allowing the silver particles to be dispersible in organic solvents. However, in terms of oleic acid undergoing an orientational change both the mechanisms are very similar. What is actually remarkable about the salt induced precipitation method is that the precipitate can actually be re-dispersed in both aqueous as well as organic solvents.

6.2.2-4. NUCLEAR MAGNETIC RESONANCE SPECTROSCOPY AND CONTACT ANGLE MEASUREMENT:

To further understand the mechanism involved in the redispersibility of salt induced precipitate in both organic and aqueous media we have carried out the ^{1}H NMR and contact angle measurements. In *Figure 6.7* we provide the ^{1}H NMR of pure oleic acid *(Curve 1)*, Ag-oleic acid in $CDCl_3$ phase transferred by H_3PO_4 *(Curve 2)* and Ag-oleic acid in $CDCl_3$ obtained by dispersing the salt induced precipitate *(Curve 3)* and Ag-oleic acid in D_2O again obtained by dispersing the salt induced precipitate *(Curve 4)*. The main regions of concern for the discussion here are situated at 5.3 ppm (olefenic proton) and at 11.0 ppm (carboxylic proton). It becomes immediately clear that the ^{1}H NMR spectra of Ag-oleic acid dispersed in $CDCl_3$ by both the methods are *similar* for all practical purposes with the absence of any features at 11.0 ppm and a diminished peak around 5.3 ppm.

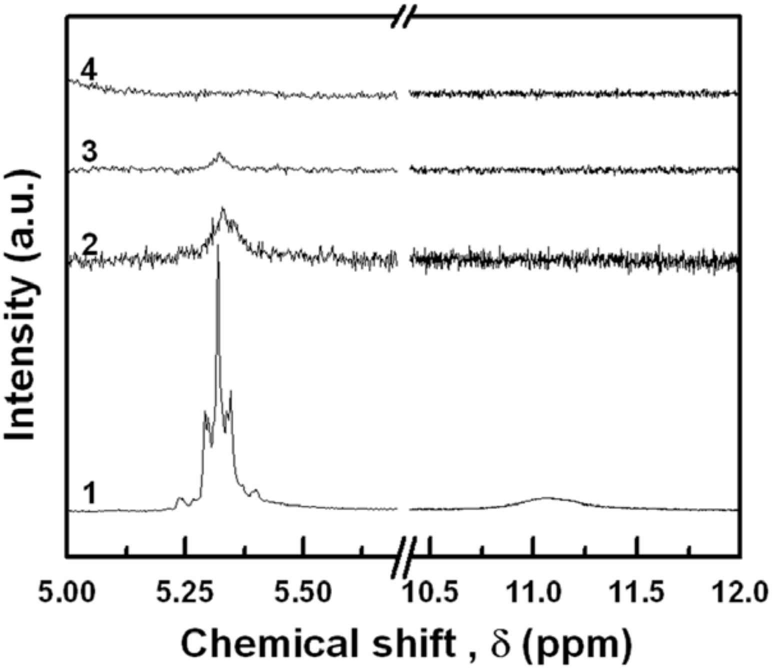

Figure 6.7. *^{1}H NMR spectra of oleic acid (curve 1), oleic acid-capped silver nanoparticles in cyclohexane obtained by H_3PO_4 route (curve 2), the same obtained via the salt-induced precipitation (curve 3), and oleic acid-capped silver nanoparticles in water obtained from the salt-induced precipitation (curve 4).*

This suggests that in these two cases the carboxylic acid is in a bound state while the double bond is free and away from the silver surface. In contrast the FTIR experiments show that the salt induced product in cyclohexane exhibits the $–COO^-$ stretch at 1559 cm^{-1} while the same obtained via the H_3PO_4 assisted protocol comes at 1707 cm^{-1} indicating a sodium oleate formation in the former case and a free carboxylic acid in the latter case. This discrepancy can be resolved by the conjecture that during the salt induced precipitation the oleic acid is present as sodium oleate and then probably the sodium ions are adsorbed/anchored on the silver surface during shaking with cyclohexane exposing the hydrophobic moiety to the solvent environment and hence rendering them organic solvent dispersible. On the other hand in the H_3PO_4 assisted situation the acidic pH conditions convert the sodium oleate to the oleic acid and then the carboxylic acid is anchored to the silver surface. This explains the presence of 1707 cm^{-1} peak in the FTIR spectrum. In NMR spectra, however, due to the demagnetization fields of the metal surface, proton signal from the carboxylic acid group in the proximity to the surface could be inhomegeneously broadened leading to the apparent disappearance of the peaks. Similar observations were made and are well documented in the alkanethiol capped gold nanoparticles [26]. So in both the above scenarios either the carboxylic acid or the carboxylate is facing the silver surface exposing the hydrophobic tail to the solvent environment.

While this explains the dispersibility of the salt induced precipitate in organic media the dispersibility of the same in aqueous medium is still intriguing and the events leading to this interesting phenomenon can be summarized as follows. Initially in the precipitate the sodium ions are anchored/adsorbed on the silver surface. When the precipitate is exposed to aqueous environments some water molecules diffuse onto the nanoparticle surface. These diffused water molecules solvate the sodium ions on/around the silver surface and bring them out to the bulk of the solvent. The resulting local diminishing of sodium ion concentration makes the oleate molecules to slowly reorient so that the carboxylates are now arranged towards the bulk solvent (water) making the surface and hence the nanoparticles hydrophilic. Thus in the water dispersed case the oleate is solvated by water and is away from the silver surface and the double bond appears to be bound to the silver surface. Indeed no peaks could be observed either near the olefinic proton region or near the carboxylic proton region in the NMR spectra of the oleate capped nanoparticles where the dispersion in D_2O was obtained by the salt induced method supporting this conjecture. Further support to our hypothesis comes from the contact angle measurements. First the contact angles measured for the films prepared from aqueous suspensions of the salt induced precipitate were almost zero indicating the hydrophilicity of the surface. The contact angle from the organic solvent dispersed films, on the other hand, were about 20°. The interesting phenomenon, however, was that as the time progressed, the water droplet slowly spread over the surface completely wetting the surface within few minutes. This indicates that the initially hydrophobic surface slowly became completely hydrophilic in accordance with the above hypothesis. Thus our results clearly point out that in the salt induced precipitation method the solvation of sodium ions and the related orientational change in the oleic acid plays big role in the redispersibility of this system in water.

6.2.2-5. PRESSURE-AREA ISOTHERM MEASUREMENT:

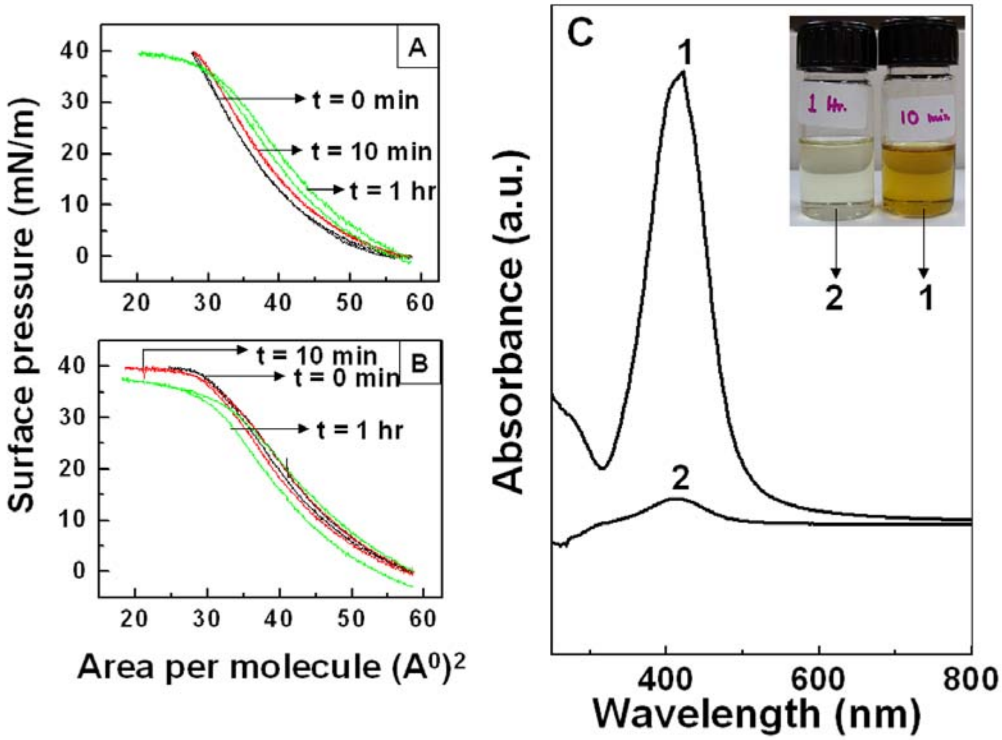

Figure 6.8. π-A isotherms of oleic acid at different time intervals spread on (A) H_3PO_4 and (B) HCl subphases. Curves 1 and 2 in C are the UV–Vis spectra of oleic acid silver nanoparticles in cyclohexane obtained by the addition of H_3PO_4 and affecting the phase transfer after waiting for 10 min and 1 h, respectively. A picture of the bottles containing the samples phase transferred after 10 min and 1 h of phosphoric acid addition is provided in the inset of C.

Another interesting observation is that the phase transfer is feasible with only acids like phosphoric or perchloric acid. Common acids like HCl and H_2SO_4 fail to induce any phase transfer. It is also observed that time plays an important and crucial role when the phase transfer is effected by the addition of acid. In *Figure 6.8A and B* we provide the time dependent π-A curves of oleic acid monolayer on H_3PO_4 and HCl subphases having pH of 1.8 and 2.1 respectively. Here, it is observed that the oleic acid molecules assume a very fluid like nature on HCl subphase almost immediately after the addition of the acid, while it takes almost an hour to get into that stage with H_3PO_4. At the same time there is also a direct correlation between the phase transfer and the oleic acid fluidity where the oleic acid in this very-fluid like state impedes phase transfer. As a proof for this statement we provide the optical absorption of silver nanoparticles phase transferred with H_3PO_4 immediately after the addition and 1 h. after the addition *(Figure 6.8C)*. The photograph of the sample vials corresponding to the *Curves 1 and 2* is provided in the inset of *Figure 6.8C*. The UV-Vis spectra clearly reveal a drastic decrease in absorbance when the phase transfer is attempted after waiting for 1 h following the addition of phosphoric acid. In the case of HCl since oleic acid gets into the phase transfer hampering fluid like state almost immediately after the addition, no phase transfer is observed. The exact mechanism of what is causing these effects is not clear at this moment. Plausible explanations include better solvation of oleates with phosphoric acid owing to the possibility of hydrogen bond formation and that oleate may interact better with bigger and softer ions such as $H_2PO_4^-$ etc [10]. Nevertheless, this effect needs to probed very thoroughly with the aid of probably some simulation studies and our investigations clearly provide additional information which could be very important to study this interesting phenomenon of time dependence on the phase transfer of silver-oleic acid system.

6.2.2-6. THERMOGRAVIMETRIC ANALYSIS:

The thermogravimetric analysis on the pristine oleic acid capped Ag nanoparticles hydrosol shows a continuous weight loss up to a temperature of 550 ^{o}C as observed in *Figure 6.9*. This points towards our postulate that oleic acid renders a flexible attachment to the surface of Ag nanoparticles and they can be easily desorbed from the surface.

Hence the TGA graph is devoid of any sharp weight loss signature. The total weight loss is calculated to ~13 % of the initial sample weight.

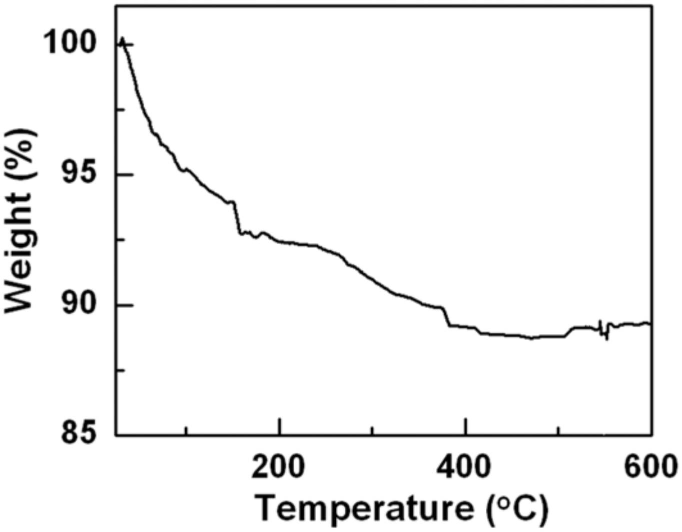

Figure 6.9. *Thermogravimetric analysis of Ag-hydrosol.*

Hence all the above characterizations confirmed the fact that oleic acid molecules really do not possess firm attachment with the Ag surface, which can be exploited for the facile phase transfer of the nanoparticles. The attachment of oleic acid may have different rigidity on different surface, which make the phase transfer issue more complicated for other nanoparticles like Ni. The issue is discussed in the following section and we tried to overcome the limitation by putting Ni nanoparticles in the envelop of thin layer of Ag.

6.2.3. PHASE TRANSFER OF $\mathrm{Ni_{CORE}Ag_{SHELL}}$ NANOPARTICLES CAPPED BY OLEIC ACID FROM AQUEOUS TO ORGANIC MEDIUM:

The utilization of the oleic acid flexibility on silver surfaces to phase transfer Ni based nanoparticuate systems is discussed henceforth. In our lab we could prepare stable aqueous dispersions of oleic acid capped Co and Ni nanoparticles using a novel foam based protocol, which has already been discussed in Chapter IV. Although the synthetic procedures involved in obtaining these two metal nanoparticle dispersions is exactly similar they behave differently especially in terms of their dispersibility in organic media. For example, when the oleic acid capped Co nanoparticles are separated from the aqueous phase by centrifuging and drying, they could be easily dispersed in an organic medium like toluene by simple dissolution of this dried product. However, the same is not true for the Ni nanoparticle system and the oleic acid capped Ni nanoparticles could not be dispersed in organic solvents following the similar procedure adapted for Co-oleic acid system or by any phase transfer protocol as described above.

After the above mentioned series of experiment we had a premonition that if the Ni nanoparticle surface could be coated by a thin shell of any other metal (silver for example) on whose surface oleic acid is flexible we should be able to achieve the phase transfer. Accordingly we prepared $Ni_{core}Ag_{shell}$ nanoparticles by a simple transmetallation reaction [27]. We have used similar reaction earlier to prepare $Co_{core}Ag_{shell}$ nanoparticles [28]. In this reaction the Ni atoms on the surface of Ni nanoparticles are used as sacrificial localized reducing agents. Since the redox potentials of Ni^o oxidation and Ag+ reduction are such that the reaction $Ni^o + 2Ag^+ \rightarrow Ni^{2+} + 2Ag^o$ is a spontaneous one and a simple mixing of Ni nanoparticle and Ag+ ions is expected to result in $Ni_{core}Ag_{shell}$.

The pristine oleic acid capped Ni nanoparticles formed by foam based method and the Ni-Ag core-shell nanocomposites were well characterized by different techniques like UV-Vis spectroscopy, XRD and TEM. The results are already presented in the Chapter IV and hence omitted here. But we include the discussion of TEM, FTIR and TGA, which have the relevance in order to explain the phase transfer process and to give useful information to support the orientational change of oleic acid on Ag surface.

6.2.3-1. TRANSMISSION ELECTRON MICROSCOPY:

The TEM pictures of the Ni_{core} and $Ni_{core}Ag_{shell}$ systems prepared by the above procedures are provided in *Figure 6.10.*.

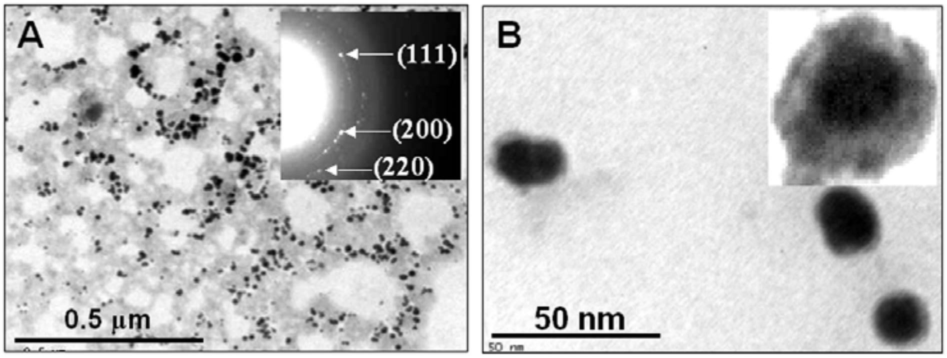

Figure 6.10. *TEM pictures of the Ni nanoparticles in aqueous medium (A and B) and those of the* $Ni_{core}Ag_{shell}$ *system (C and D). A high magnification image showing the contrast difference is presented in the inset of D. Selected area electron diffraction (inset of A) can be indexed to fcc Ni.*

The Ni nanoparticles in the aqueous media are quite spherical and are in the size range 15-20 nm *(Figure 6.10A)*. Selected area electron diffraction clearly points out that the Ni nanoparticles are polycrystalline assuming an fcc phase *(inset, Figure 6.10A)*. A clear difference in contrast surrounding each particle can be clearly seen on the Ni nanoparticle surface after the transmetallation reaction *(Figure 6.10B)*. These contrast differences prove that a $Ni_{core}Ag_{shell}$ system is formed after the transmetallation reaction

6.2.3-2. FOURIER TRANSFORM INFRARED SPECTROSCOPY:

As expected the formation of $Ni_{core}Ag_{shell}$ composites immediately render them phase transferable to the organic medium either by acid assisted method or by the salt induced method. The different orientations of oleic acid on core-shell surface are delineated by FTIR spectroscopy (*Figure 6.11)* and the findings from FTIR are summarized as follows.

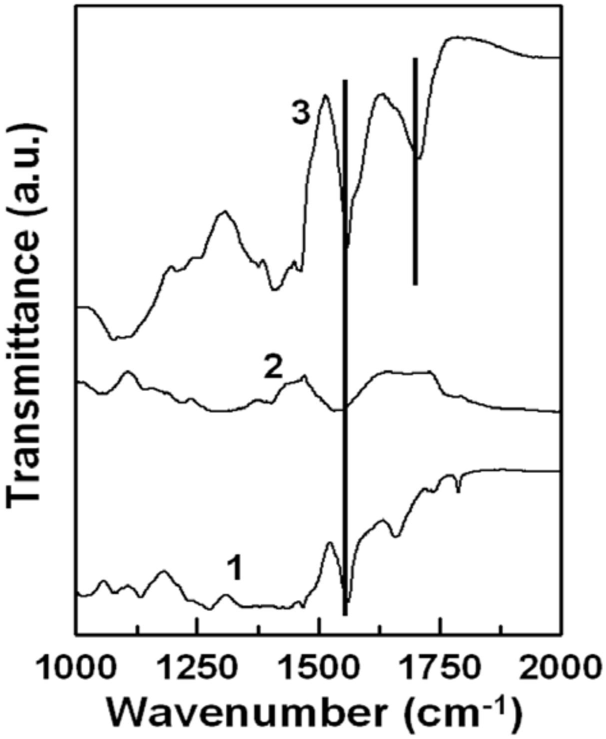

Figure 6.11. *FTIR spectra of the Ni and $Ni_{core}Ag_{shell}$ nanoparticles in different environments. Curve 1 is obtained from the nascent oleic acid capped in Ni nanoparticles in the aqueous medium, curve 2 is that of the $Ni_{core}Ag_{shell}$ in aqueous medium, and curve 3 is from the $Ni_{core}Ag_{shell}$ nanoparticles in organic medium obtained by the phosphoric acid-induced phase transfer protocol.*

In the hydrosol the oleic acid is attached to the Ni nanoparticle surface through the double bond, and the carboxylic acid is exposed to the water being stabilized as sodium carboxylate, which is confirmed by the 1559 cm^{-1} $–COO^-$ stretching frequency *(Figure 6.11, curve 1).* Addition of phosphoric acid or the salt induced precipitation and re-dispersion failed to induce phase transfer of this nascent oleic acid capped nickel nanoparticle system. This could be due to the strong attachment of oleic acid on Ni surface as described in detail. The FTIR spectra from the $Ni_{core}Ag_{shell}$-oleic acid system in water is similar to the pure Ni-oleic acid or the Ag-oleic acid aqueous system indicating that there is no major change in the oleic acid orientation on the silver surface when compared to the nickel surface *(Figure 6.11, curve 2).* This orientation again undergoes a major change on the addition of phosphoric acid, which facilitates the phase transfer of $Ni_{core}Ag_{shell}$-oleic acid system to organic solvents like cyclohexane or toluene. Here, again the phosphoric acid converts the carboxylate to the carboxylic acid group and the double bond is detached from the silver surface. Then, the oleic acid re-orients itself with the carboxylic acid group anchoring to the silver surface exposing the hydrophobic tail to the solvent environment facilitating the phase transfer. This proposition is confirmed by the FTIR spectra where the phosphoric acid addition re-generates the 1707 cm^{-1} –C=O stretching frequency apart from the 1559 cm^{-1} peak *(Figure 6.11, curve 3).*

Different modes of binding of oleic acid on Ni and silver in different environments and its orientational flexibility are schematically depicted in the scheme of *Figure 6.12* and can be summarized as follows. On silver, oleic acid is attached to the surface through the double bond and the carboxylate stabilized by sodium ions is exposed to the solvent. Upon H_3PO_4 addition the carboxylate is converted to carboxylic acid and undergoes a flipping when exposed to the organic non-polar environments. Here, carboxylic acid groups cap the silver surface and the hydrophobic tail is directed towards the solvent media. Likewise, similar stabilization modes and flipping mechanism are possibly taking place in the salt induced precipitation and re-dispersion procedure also, though the situation is little complicated here, where even in organic solvents the oleic acid is present as carboxylate. This might be explained by considering that the silver nanoparticle surface is now covered by Na^+ ions. This is possible because we add excess amounts of salt to induce precipitation. However, further studies are needed to completely understand this particular phenomenon. Interestingly, this surface flipping of oleic acid seems to be specific to certain metal surfaces only, which as mentioned earlier could be due to the relative strengths of binding on different metal surfaces of this molecule.

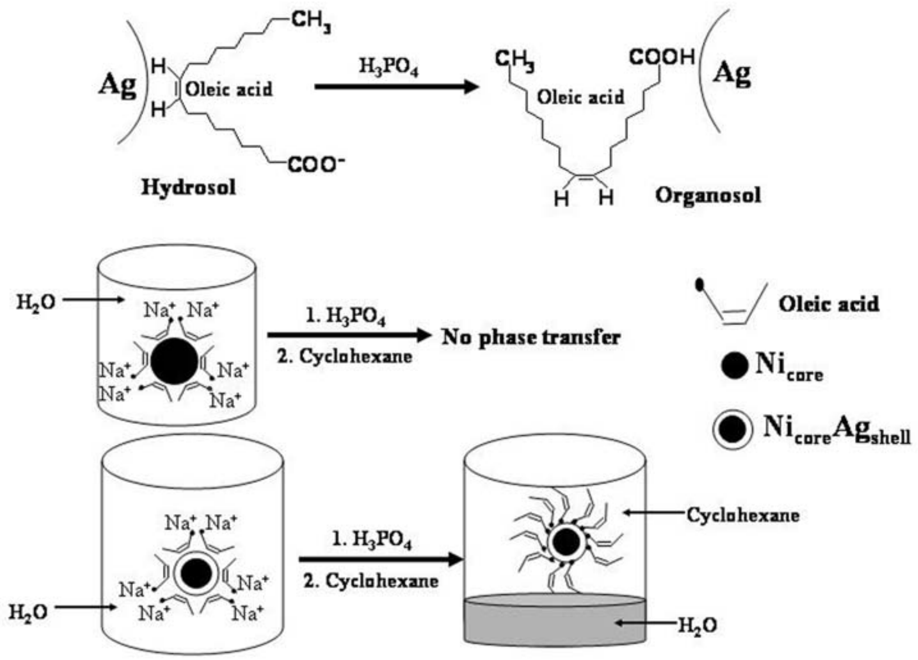

Figure 6.12. *Different modes of binding of oleic acid on silver surface in different environments. A schematic model of the phase transfer of Ni-core Ag-shell nanoparticles is also given.*

6.2.3-3. THERMOGRAVIMETRIC ANALYSIS:

To investigate the relative strengths of oleic acid on silver as well as nickel surfaces we carried out TGA experiments on the Ni-oleic acid and $\mathrm{Ni_{core}Ag_{shell}}$-oleic acid systems. Both undergo weight loses of 20% to 45%, respectively *(Figure 6.13)*. Assuming an average size of 20 nm for Ni nanoparticles a monolayer coverage of oleic acid molecules on their surface would amount to ~19% of the total weight, which is in good agreement with the observed weight loss. Here, it is assumed that the area per molecule for oleic acid on silver surface is 21.3 Å^2 taken from the reported values [29]. The extra weight loss for the $\mathrm{Ni_{core}Ag_{shell}}$-oleic acid could be attributed to several reasons including slightly larger size of these particles and the ability to form more compact oleic acid monolayers on the silver surface when compared to the nickel surface [30].

Nevertheless, the important point is that the major weight loss in the Ni system occurs at 315 °C *(Curve 1)* while it occurs at 245 °C in the $Ni_{core}Ag_{shell}$ *(Curve 2)* system.

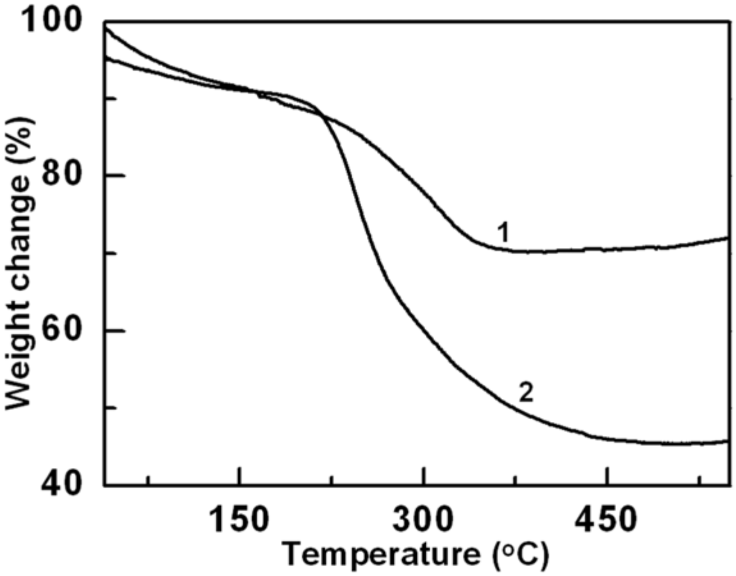

Figure 6.13. *The TGA curves of oleic acid-capped Ni (curve 1) and* $Ni_{core}Ag_{shell}$ *(curve 2) nanoparticles.*

Though it is very difficult to directly correlate these temperatures to the strengths of oleic acid-surface bonds in the Ni-oleic and silver-oleic systems, we can qualitatively conclude that the Ni surface-oleic acid interaction is probably stronger and hence less flexible when compared to the corresponding Ag surface-oleic acid interaction. In this context it is worth noting that carboxylic acids are known to form highly ordered self assembled monolayers on silver metal surfaces while they are not known to adsorb on nickel surfaces very well. The possible explanations include the presence of a highly basic AgO layer on the surface of silver when compared to nickel surface and the possible binding of carboxylic acid with this layer [38]. However, this phenomenon is still under focus of continued research. Thus, the extra flexibility of oleic acid on silver surface can be exploited profitably to affect the phase transfer of any system, which is otherwise difficult to phase transfer.

6.2.4. SUMMARY:

The two major protocols in practice for phase transfer of oleic acid capped silver nanoparticle system are examined carefully. It is established that in both the procedures the orientational change of oleic acid on silver surface plays a crucial role. The salt induced precipitation and re-dispersion is found to be more versatile in that the precipitate can be dispersed in both aqueous and organic media with equal ease. The orientational flexibility of oleic acid on silver surface is exploited profitably to induce phase transfer of oleic acid-Ni nanoparticulate system by a simple coating of a thin shell of Ag on the nickel surface. This method of coating a thin shell of Ag and then affecting the phase transfer could be generalized to other systems where they are other wise non-phase transferable.

6.3. PHASE TRANSFER OF AOT CAPPED Ag NANOPARTICLES:

6.3.1. EXPERIMENTAL DETAILS:

(A) Silver hydrosol preparation: In a typical experiment, 1 X 10^{-4}M of Ag_2SO_4 in water was reduced with 0.1% $NaBH_4$ in the presence of AOT at different concentrations (1 X 10^{-4} M, 5 X 10^{-3} M and 1 X 10^{-2} M). A yellowish brown colloidal solution of silver was obtained almost immediately. However, the reaction was continued for 2 h to ensure completion. To remove excess AOT used during the preparation the samples were subjected to dialysis in a dialysis bag (12 kDa) for 24 hrs. with regular change of water after every 6 hrs.

(B) Silver organosol: To a biphasic mixture of 25 ml each of the silver hydrosol and cyclohexane, 0.2 ml of 0.1 M H_3PO_4 was added under vigorous stirring. The color of the organic phase changes to bright yellow immediately when H_3PO_4 was added to the silver nanoparticle solution.

(C) Re-dispersion of silver nanoparticles: The silver organosol thus prepared was extremely stable. The silver solution was evaporated in vacuum, and the silver nanoparticle powder remaining could be readily redispersed in both water and in different nonpolar organic solvents.

6.3.2. UV-VIS SPECTROSCOPY:

The phase transfer of the aqueous silver nanoparticles prepared with various concentrations of AOT into the organic phase is illustrated in *Figure 6.14A.* It shows pictures of test tubes before (test tube 1 on the left) and after phase transfer of the colloidal Ag particles into cyclohexane when the AOT concentration was maintained at 5 X 10^{-3}, 1 X 10^{-2}, and 1 X 10^{-4} M for test tubes 2, 3 and 4 respectively. The UV-Vis spectra reveal only small shifts in the absorbance maximum from the aqueous to the organic phase, where the phase transfer is attempted after waiting for 1 h of addition of phosphoric acid. *Curve 1* corresponds to the UV-Vis spectrum recorded from the aqueous phase and shows a sharp resonance at ca. 406 nm. This band arises due to excitation of surface plasmon vibrations in the silver nanoparticles and is responsible for the striking yellow colour of silver nanoparticle solutions. After the phase transfer, the peak is marginally red shifted to around 410 nm. The fact that very little shifts are observed in the peak positions clearly reveals that the particles are practically phase transferred as-is without undergoing any agglomeration.

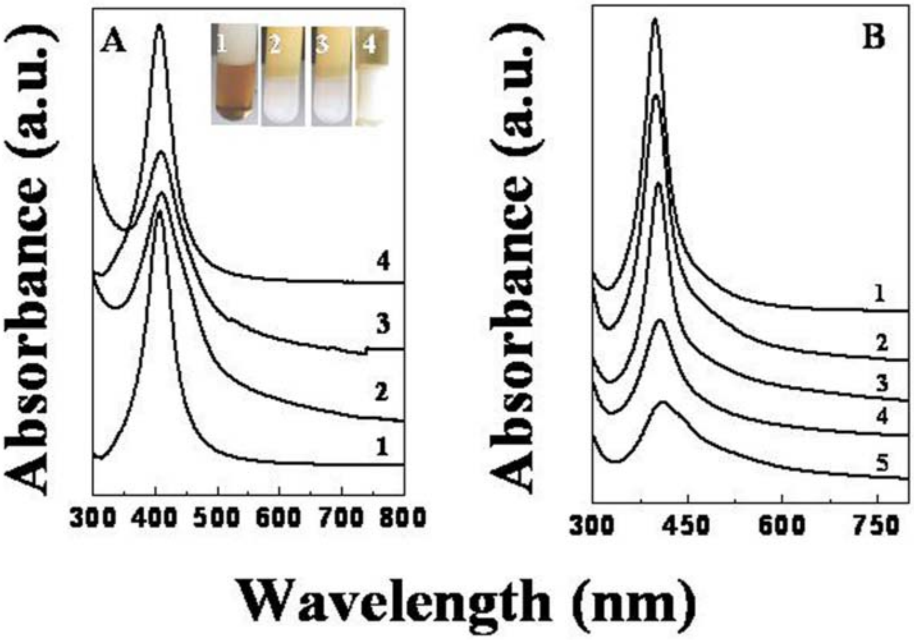

Figure 6.14. *(A) UV-vis spectra recorded from the as-prepared silver hydrosol (with AOT concentration of 5 X 10^{-3} M; curve 1) and silver organosols after phase transfer into cyclohexane (curves 2-4); curves 2-4 correspond to the spectra recorded from silver nanoparticles capped with 5 X 10^{-3}, 1 X 10^{-2}, and 1 X 10^{-4} M AOT, respectively. The curves have been displaced vertically for clarity. The inset shows pictures of test tubes of silver nanoparticle solutions of the samples in curves 1-4, respectively. (B) UV-vis spectra recorded from the silver nanoparticle powder after redispersion in aqueous (curve 1) and nonpolar organic solvents (curves 2-5). Silver nanoparticles in water (curve 1), chloroform (curve 2), toluene (curve 3), cyclohexane (curve 4), and benzene (curve 5). These spectra have also been displaced vertically for clarity.*

The resulting organosol was then rotary evaporated and resulted in a brownish solid powder that could be readily redispersed in water and different solvents such as toluene, benzene, chloroform and cyclohexane. Here, we would like to emphasize that we did not see any perceptible time dependence in the re-dispersibility of this powder in water or cyclohexane, two solvents differing vastly in their polarities indicating that there is no particular preference that these AOT-capped silver nanoparticles display. An important point to note here that there does not seem to be any particular size separation upon phase transferring into different solvents apart from the general size selection that is observed in other reports [31]. Apart from the visual observation to check the phase transferability, we have recorded the UV-Vis spectra of the solutions obtained after the brownish powder was re-dispersed in water and different solvents such as toluene, benzene, chloroform and cyclohexane. *Figure 6.14B, curve 1* shows the spectrum of the AOT-capped silver nanoparticle powder re-dispersed in water. *Curves 2-5* correspond to the spectra recorded from the brownish silver nanoparticle powder after re-dispersion in chloroform, toluene, cyclohexane and benzene, respectively. The small shifts observed in the peak positions approximately follow a trend as expected from the refractive index changes in the solvent. This exercise clearly proves that our simple method is very effective in getting silver nanoparticles dispersed in a variety of solvents including re-dispersibility in water.

6.3.3. X-RAY DIFFRACTION ANALYSIS:

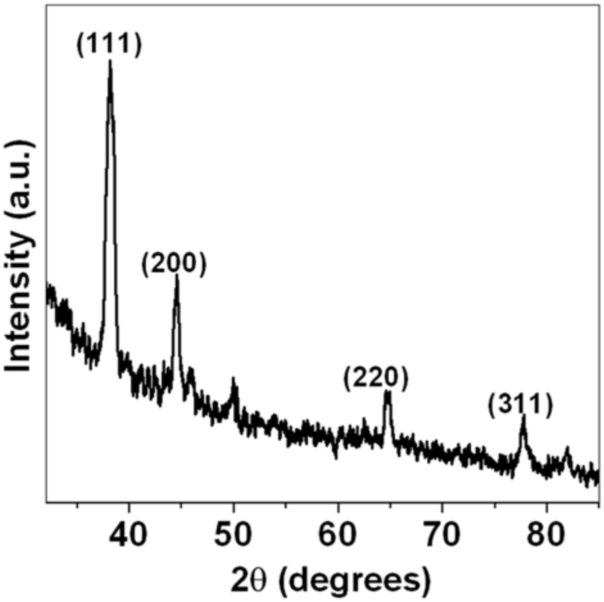

Figure 6.15. *Powder XRD pattern of a film of silver nanoparticles prepared on a glass substrate, corresponds to the fcc crystal structure of Ag.*

The XRD pattern recorded from a drop-cast film of the silver hydrosol prepared in the presence of 5 X 10^{-3} M of AOT shows strong Bragg reflections corresponding to the (111), (200), (220), (311) reflections of fcc silver *(Figure 6.15)*. The XRD results thus show that the as-prepared silver nanoparticles are crystalline [32].

6.3.4. TRANSMISSION ELECTRON MICROSCOPY:

Figure 6.16A shows a representative TEM image of the as prepared AOT-capped silver nanoparticles (AOT concentration = 5 X 10^{-3} M) in water. The inset of the *Figure 6.16A* shows the selected area electron diffraction (SAED) pattern recorded from the AOT-capped silver hydrosol. In the figure the diffraction rings have been indexed and showed that crystallinity of the particles is consistent with the fcc structure of silver. The particle size distribution analysis *(Figure 6.16B)* reveals that the particles are polydisperse with an average size of 12 ± 3 nm.

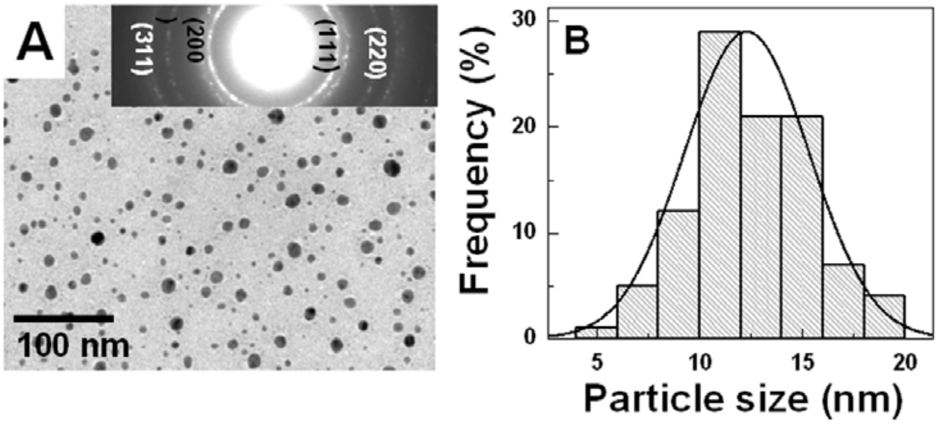

Figure 6.16. *(A) Representative TEM micrograph from a drop-cast film of the as-prepared silver hydrosol. The inset shows the SAED pattern of the particles indexed to fcc silver. (B) Particle size distribution histogram of the silver nanoparticles. The solid line is a Gaussian fit to the data. The AOT concentration for the preparation of the sample used in this image is 5 X 10^{-3} M.*

Different concentrations of AOT were used to probe its effect on the resulting nanoparticle sizes. These changes are reflected better in the TEM images obtained from the organosols and are given in *Figure 6.17.* When the initial concentration of AOT in water was varied systematically the average particle sizes varied as 6.1±0.9, 12.3±3 and 10.6±1.8 nm for the AOT concentrations 1 X 10^{-2}, 5x10^{-3} and 1 X 10^{-4} M, respectively *(Figure 6.17A-C)*. The critical micelle concentration (CMC) of AOT is reported to be 2.5

X 10^{-3} M. Around the CMC or below the CMC the particles tend to be bigger. Micelles are considered equilibrium structures where the surfactant molecules are always coming out and joining the micellar moiety. This could explain the larger sizes of particles observed when we have lower concentrations of the surfactant where the micelles may not possess very compact structures. However, when we take really excess quantity of the surfactant compared to the CMC the micelles are packed probably in a more compact manner leading to the smaller sizes of particles observed as in the case of 1 X 10^{-2} M concentration.

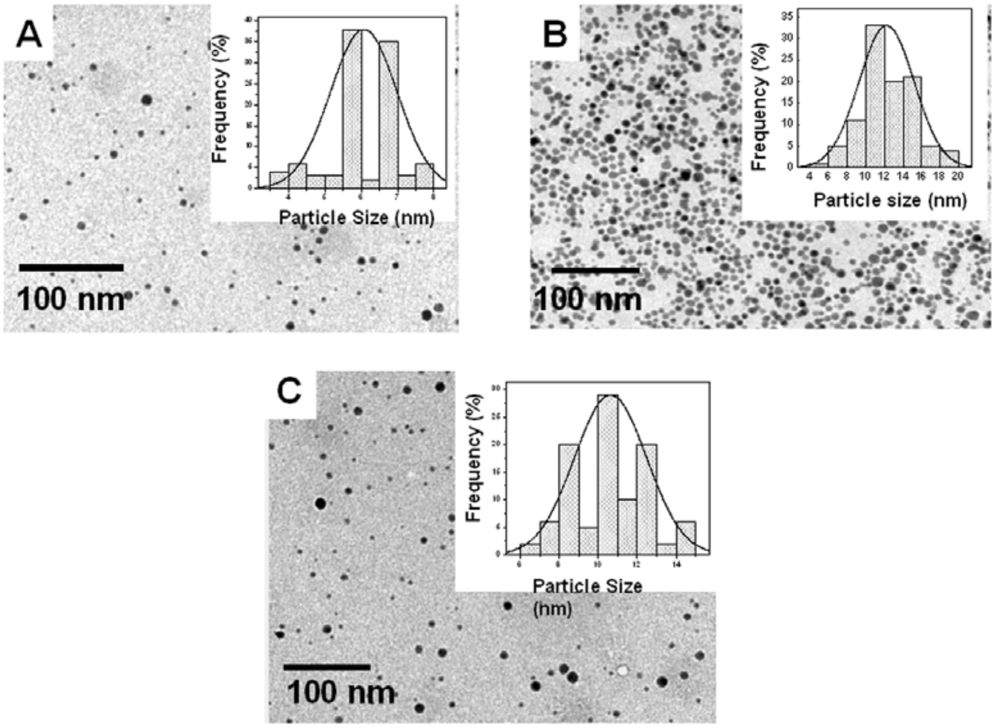

Figure 6.17. (A-C) Representative TEM micrographs recorded from drop-cast films of silver organosol in cyclohexane obtained from the hydrosol prepared with different concentrations of AOT: A, 1 X 10^{-2} M; B, 5 X 10^{-3} M; and C, 1 X 10^{-4} M. The respective particle size distributions are plotted in the insets.

6.3.5. FOURIER TRANSFORM INFRARED SPECTROSCOPY:

A systematic FTIR investigation of the as-prepared, organic dispersed and aqueous re-dispersed samples was carried out in order to understand the mechanism of phase transfer. *Figure 6.18* provides the FTIR spectra of the silver nanoparticles in the aqueous as well as in organic environments (*Curve 1* - spectrum of pure AOT; *Curve 2* – spectrum of the as-prepared hydrosol in the presence of $5\text{x}10^{-3}$ M of AOT; *Curve 3* - spectrum recorded from the dialyzed silver hydrosol; *Curve 4* - spectrum of the AOT-capped silver nanoparticle powder after re-dispersion in water and *Curve 5* - spectrum of the AOT-capped silver nanoparticle powder after the re-dispersion in chloroform).

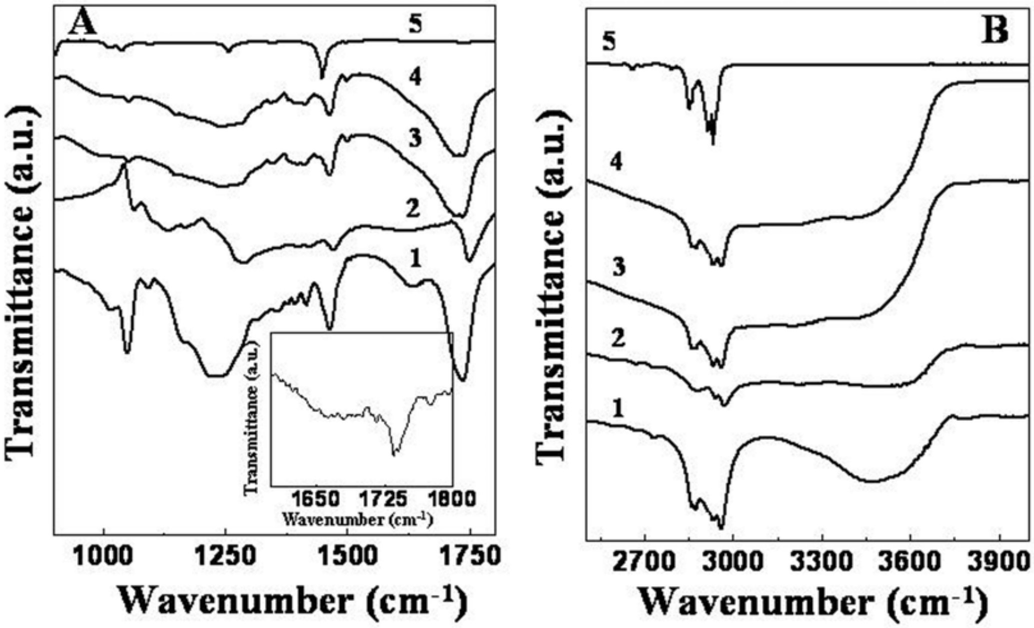

Figure 6.18. *FTIR spectra in the spectral range 1000-3100 cm^{-1} recorded from the drop-coated film on the Si(111) substrate. For clarity the spectra are split in the regions 950-1800 cm^{-1} (A) and 2600-4000 cm^{-1} (B). The details of the spectra are as follows: pure AOT (curve 1); as-prepared AOT-capped silver hydrosol (curve 2); the silver hydrosol after removal of excess AOT by dialysis (curve 3); the AOT-capped silver nanoparticle powder after redispersion in water (curve 4); and the AOT capped silver nanoparticle powder after redispersion in chloroform (curve 5). The peaks from the carbonyl stretches almost disappear after transfer to the organic solvent, and the weak transmittance in this region is shown in the inset of part A after a magnification of 100 times.*

For this discussion the major interest is in the regions 950-1800 cm^{-1} and 2500-4000 cm^{-1} and are plotted separately in *Figure 6.18A and B,* respectively. The C-H symmetric and antisymmetric stretching vibration frequencies of the $-CH_2$ groups occur at 2877 and 2934 cm^{-1} for pure AOT and those in as-prepared hydrosol are at approximately the same frequencies of 2882 and 2944 cm^{-1} *(curve 1 and 2 in Figure 6.18B*). This might be due to the large excess of AOT present in the as-prepared hydrosol. After dialysis the excess AOT is removed and only the molecules bound to the silver nanoparticle surface remain. In *Curve 3* the FTIR spectrum from the hydrosol after dialysis and removal of excess

AOT is displayed. The stretching frequencies now occur at 2866 and 2945 cm^{-1} for the dialyzed silver hydrosol indicating that the hydrocarbon chain now acquires some kind of order because it is adsorbed to the silver surface. However, in the hydrosol the functional (ester and sulfonate) groups of the AOT molecule are directed towards the solvent and the molecule is only weakly adsorbed to the silver surface due to some weak van der Waals interactions *(Figure 6.19)*.

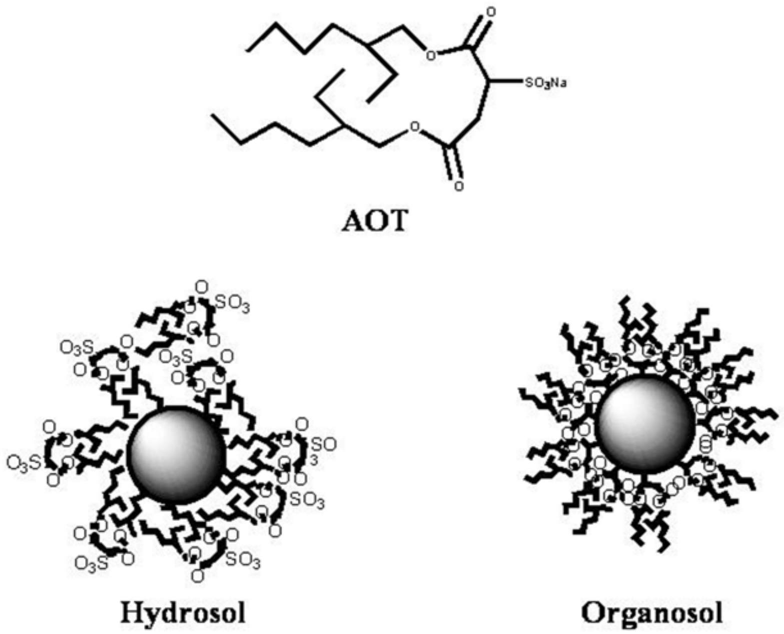

***Figure 6.19**. Schematic representation of the orientations of AOT on the silver nanoparticle surface in different environments and the molecular structure of AOT.*

In the re-dispersed organosol, on the other hand, the functional groups are now directed towards the silver surface and the molecules are arranged like a self-assembled monolayer with a very good packing arrangement *(Figure 6.19)*. However, we would like to mention here that the packing of AOT on the surface may be different for particles of different sizes because of vast differences in their curvature and at present till date we cannot make any specific comments on this effect and hence it is difficult to assess its effect on the phase transferability. Here, the better packing of AOT molecules on the silver surface in the organic media is known to result in stronger shifts of the –C-H symmetric and antisymmetric stretches towards lower frequencies and indeed we observe peaks at 2852 and 2933 cm^{-1} *(Curve 5)*. The IR spectrum of hydrosol obtained from the re-dispersion of organic solvent evaporated powder is an exact replica of the dialyzed hydrosol. This clearly indicates that once the powder is re-dispersed in water it is undergoing an orientational change where the functional groups are again directed towards the solvent environment and that the hydrocarbon chains are attached to the silver surface leading to poor packing order.

The absorption band at 1466 cm^{-1} in *Figure 6.18A* is ascribed to the methylene (CH_2) scissoring mode in pure AOT *(Curve 1)*. In the as-prepared case this undergoes almost no difference and occurs at 1471 cm^{-1} *(Curve 2)*. For the dialyzed and re-dispersed hydrosols where we probe only the AOT adsorbed on the silver surface the band is shifted to a lower frequency at 1460 cm^{-1} as expected for a poorly ordered molecule on the surface *(Curves 3 and 4)*. Finally in the silver organosol *(Curve 5)* this peak is shifted to a lower frequency and appears at 1448 cm^{-1} as expected for a packed and ordered monolayer of hydrocarbons on the silver surface [31].

Coming to the peaks from functional groups we first consider the sulfonate group in *Figure 6.18A*. The peaks at 1059 and 1160 cm^{-1} in the case of pure AOT *(Curve 1)* are assigned to the symmetric and asymmetric S=O stretching vibration of the sulfonate group present in the AOT molecules and are shifted to 1049 and 1154 cm^{-1} in as-prepared silver hydrosol *(Curve 2)*. In *Curves 3 and 4* (dialyzed hydrosol and re-dispersed hydrosol respectively) these occur at exactly same frequencies at 1049 and 1154 cm^{-1} but in *Curve 5* i.e. silver organosol, they are shifted to lower frequencies and appear at 1033 and 1100 cm^{-1}. This is because in the organosol the SO_3^- group is bound to the silver surface where as in the hydrosol they are free and are directed towards the solvent medium.

The most dramatic changes are depicted in the carbonyl stretches in *Figure 6.18A*. First, the band at 1736 cm^{-1} due to carbonyl stretch vibrations in the AOT molecules *(Curve 1)* is shifted to 1749 cm^{-1} in silver hydrosol *(Curve 2)*. At this moment it is not clear why a small upward shift in this peak position of the as-prepared hydrosol was observed. However, once the excess AOT is removed by dialysis the peak appears at 1729 cm^{-1} *(curve 3, Figure 6.18A)*, a small shift probably arising due to the poor ordered state of the molecules on the silver surface. The scenario changes drastically once the phosphoric acid is added to the silver hydrosol when the AOT molecule undergoes a major orientational change where the functional groups are strongly attached to the silver surface forming a self assembled monolayer. Accordingly, in the silver organosol the peaks due to –C=O almost disappear and occur at 1736 cm^{-1} and as a broad peak at 1667 cm^{-1} *(Curve 5).* These peaks are very weak and are displayed in the inset of *Figure 6.18A* after a magnification of 100 times. If the disappearance of these peaks in organic medium is due to the binding and close proximity of these functional groups to the silver nanoparticle surface, re-dispersion of the powder in water should regenerate these peaks. Indeed, as displayed in *Curve 4,* redispersion of the organic solvent evaporated powder in water regenerates the peak at 1729 cm^{-1} and is in very good agreement to our hypothesis of orientational change in AOT molecules brought about by the solvent environment.

In order to get a more distinct picture of what is the role of phosphoric acid in the phase transfer process we tried other acids also to effect the phase transfer from aqueous to the organic phase of AOT capped silver nanoparticles. Our results indicated that the extent of phase transferability varies as $HClO_4 \geq H_3PO_4 > H_2SO_4$ while addition of HCl destabilizes the Ag colloid in the aqueous phase itself. While it is very difficult to give a clear explanation for the role of the phase transferring agents, the trends are exactly same as those observed by Efrima and co-workers for the oleic acid capped silver nanoparticle phase transfer procedures [10, 11]. Hence, tentatively we assume that the hydrogen bonding mechanism they proposed is operational in our case also.

6.3.6. SUMMARY:

A simple and efficient way where the same molecule AOT is used for the synthesis, stabilization and phase transfer of silver nanoparticles is described. The silver nanoparticles are initially prepared in water in the presence of aerosol OT (sodium bis (2-ethylhexyl) sulfosuccinate, AOT). Thereafter, transfer of the AOT-capped silver nanoparticles to an organic phase is induced by the addition of small amount of orthophosphoric acid during shaking of the biphasic mixture. The AOT-stabilized silver nanoparticles could be separated out from the organic phase in the form of a powder. The phase transfer is actually the most versatile of the reported methods so far in that the powder obtained after the organic solvent is evaporated can be re-dispersed in a variety of solvents including water. Thus a simple and efficient way of obtaining silver nanoparticles that are dispersible both in organic and aqueous solvents using a single capping agent is described. The amphiphilic nature of the silver surface is brought about by a small orientational change in the AOT monolayer on the silver surface in response to the polarity of the solvent.

6.4. PHASE TRANSFER AND ASSEMBLY OF Ni NANOPARTICLES:

6.4.1. EXPERIMENTAL DETAILS:

In a typical experiment, 100 ml aqueous solution containing 1 X 10^{-3} M $Ni(NO_3)_2$ and 5 X 10^{-4} M oleic acid in methanol was added with 0.045 gm of $NaBH_4$ and stirred for ~10 min. The colour of the solution immediately turned black. 25 ml of this aqueous Ni nanoparticle solution was then taken in a conical flask along with 25 ml of 1 X 10^{-3} M stearic acid (STA) in toluene. While the biphasic mixture was stirred, 0.25 gm of NaCl was directly added to the mixture and the stirring was continued for ~10-12h. At the end of the process, the organic phase turned black. The organic layer was separated from the colorless aqueous layer using a separating funnel. The organic layer was again stirred with 25 ml of aqueous Ni nanoparticles solution and the process was repeated many times to make the organic layer saturated with Ni nanoparticles. This saturated organic layer was then dried by evaporating the solvent using rota-vapour. The dried mass was washed with ethanol thrice to remove any uncoordinated STA. The exchange of oleic acid with STA as confirmed by FTIR studies leads to the phase transfer of pristine oleic acid capped Ni nanoparticles. These particles were subjected to the following treatment before assembling them at air-water interface using Langmuir-Blodgett technique (the Langmuir-Blodgett technique is illustrated in *Figure 6.20*).

The dried mass was weighed and dissolved in chloroform keeping the overall concentration at 1 mg/ml. A known quantity of hydrophobized Ni nanoparticles was then assembled at air-water interface using Langmuir-Blodgett technique by spreading them on water at pH 6.5 in a Model 611 Nima LB trough. Surface pressure(π) - area(A) isotherms were measured at 25^{o}C as a function of time from spreading the monolayer with the compression and expansion speed for monolayer being 100 cm^2/min. Similar measurements were also made with respect to the different volume of Ni nanoparticles spread at the air-water interface. A standard Wilhelmy plate was used for surface pressure sensing. Multilayers of the Ni nanoparticles were formed on substrates by LB technique at surface pressure 15 mN/m and a deposition rate of 50 mm/min with a waiting time of 120 sec between the consecutive dips *(Figure 6.20).*

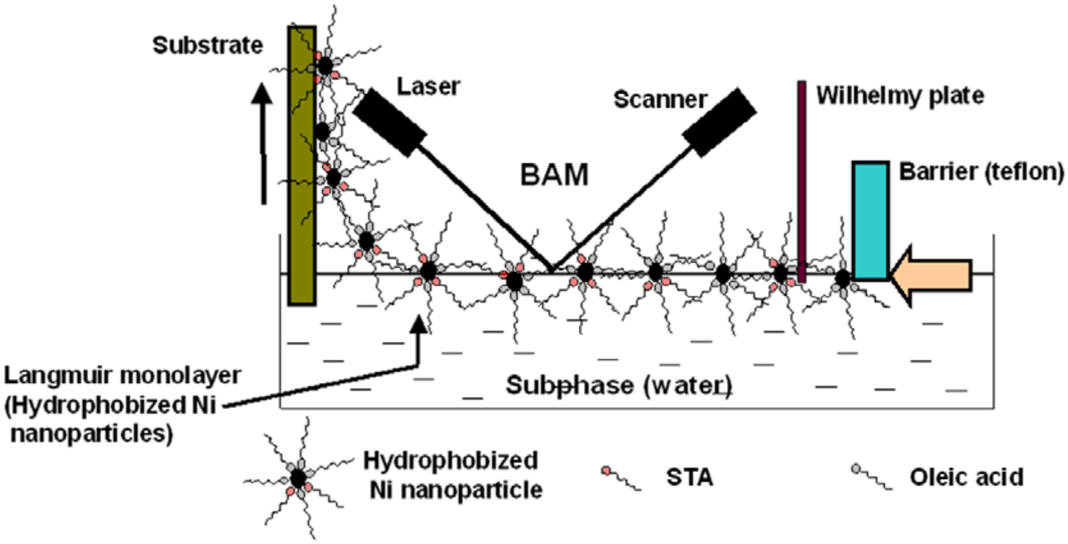

Figure 6.20. *Schematic of Ni nanoparticles spread at the air–water interface after phase transferring the oleic acid capped Ni nanoparticles into toluene containing STA. Brewster Angle Microscopy (BAM) arrangement employed to view the assembly process in-situ is also shown.*

Brewster Angle Microscopy was used to probe the in-situ domain structure i.e. the morphology of the hydrophobized Ni assembled at the air water interface in form of Langmuir monolayer. The set-up consists of a laser diode of 25mW power at 650 nm. The emitted beam passes through a polarizer and then illuminates a spot of about 2 mm^2 on the surface. The reflected light passes through specially designed objective and then is captured by a CCD camera (Kocom model 310). The image sensor of the CCD camera is 1/3 rd inch. The lateral resolution of the microscope is ~ 1μm CCD camera is coupled to Frame Grabber card for real time capturing of the compressed monolayer. The developed software has a facility to record the video while monolayer is being compressed by the barrier. The BAM images were recorded for different initial concentrations of hydrophobized Ni nanoparticles: 2.5 mg/ml and 5 mg/ml. It was found that any effort to increase the concentration beyond 5 mg/ml lead to only partial dispersion of the Ni powder in toluene.

6.4.2. UV-VIS SPECTROSCOPY:

Figure 6.21A shows the UV-Vis spectra recorded from the oleic acid capped Ni nanoparticles in aqueous solution *(Curve 1)* and Ni nanoparticles after phase transfer by STA in toluene *(Curve 2).* Both the spectra depict a typical monotonous increase in absorbance [24], which matches well with the reported UV-Vis spectra of Ni nanoparticles [24]. *Curve 3 in Figure 6.21* evidences the UV-Vis spectra recorded from the aqueous part after the completion of phase transfer. The absence of any absorbance clearly indicates the complete phase transfer of Ni nanoparticles to toluene in presence of STA.

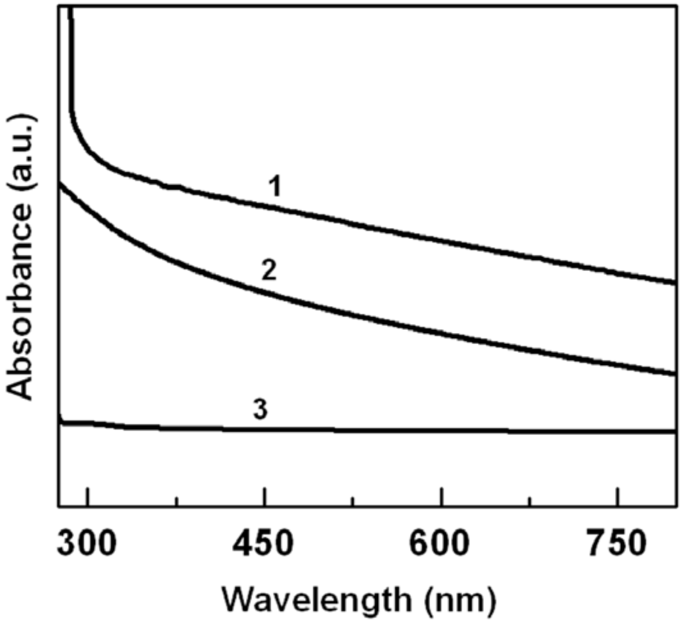

Figure 6.21. *UV-Vis spectra of Ni nanoparticles in aqueous (curve 1) and organic phase (curve 2).The UV-Vis spectrum of the aqueous phase after complete phase transfer is depicted in curve 3 which indicates a complete phase transfer of Ni nanoparticles from aqueous to organic medium.*

6.4.3. ENERGY DISPERSIVE ANALYSIS OF X-RAY:

The EDAX analysis was performed on the film of hydrophobized Ni monolayer deposited on Si(111) substrate by Langmuir-Blodgett technique. The spectrum ensures the presence of Ni *(Figure 6.22)*. Intense peaks of C, Ni and weak signals for O and Na can be seen which indicates the phase transfer of Ni nanoparticles into the organic layer and the formation of Langmuir monolayer of the hydrophobized Ni nanoparticles on water subphase at air-water interface. The presence of Na can be attributed to the addition of excess NaCl in the aqueous Ni nanoparticles solution during phase transfer while the oxygen signal can be due to the –COOH group of both oleic acid and STA.

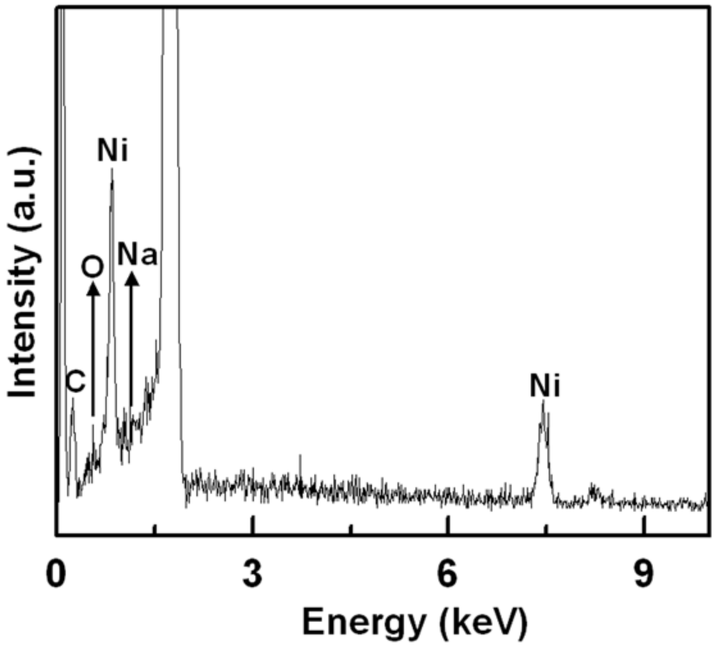

Figure 6.22. *The energy dispersive analysis of X-ray (EDAX) showing the presence of Ni along with C, O, and Na.*

6.4.4. X-RAY PHOTOELECTRON SPECTROSCOPY:

The presence of Ni in the organic phase is substantiated from XPS analysis of the film *(Figure 6.23)*. *Figure 6.23A, B and C* represent the core level photoelectron spectra of C 1s, O 1s and Ni 2p respectively. All the peaks are corrected for the static charge accumulation on the sample and then aligned considering C 1s binding energy as 285 eV. The core level spectra were background corrected using the Shirley algorithm [33] and the chemically distinct species were resolved using a nonlinear least-square fitting procedure. There is a small peak at 288.4 eV apart from the main peak at 285 eV for C 1s *(Figure 6.23A)*. This may be due to the carboxylic carbon, which is bound to more electronegative oxygen atom and thus leads to a peak at higher binding energy.

The O 1s peak *(Figure 6.23C)* is resolved into two distinct peaks, the main peak at 532.0 eV and a small hump at 530.6 eV. The Ni 2p *(Figure 6.23C)* spectra can be resolved into two sets of spin – orbit pairs (spin orbit splitting ~ 17.4 eV) with a $2p_{3/2}$ binding energy of 855.3 eV [34-35]. The deconvolution of the fitted Gaussian curve showed the presence of another hump at 861.45 eV, which is generally observed due to the presence of binding of Ni to oxygen. This may occur either due to presence of few layers of NiO on the surface of the nanoparticles or due to the binding of –COOH head group of oleic acid and/or STA to the surface of Ni nanoparticles.

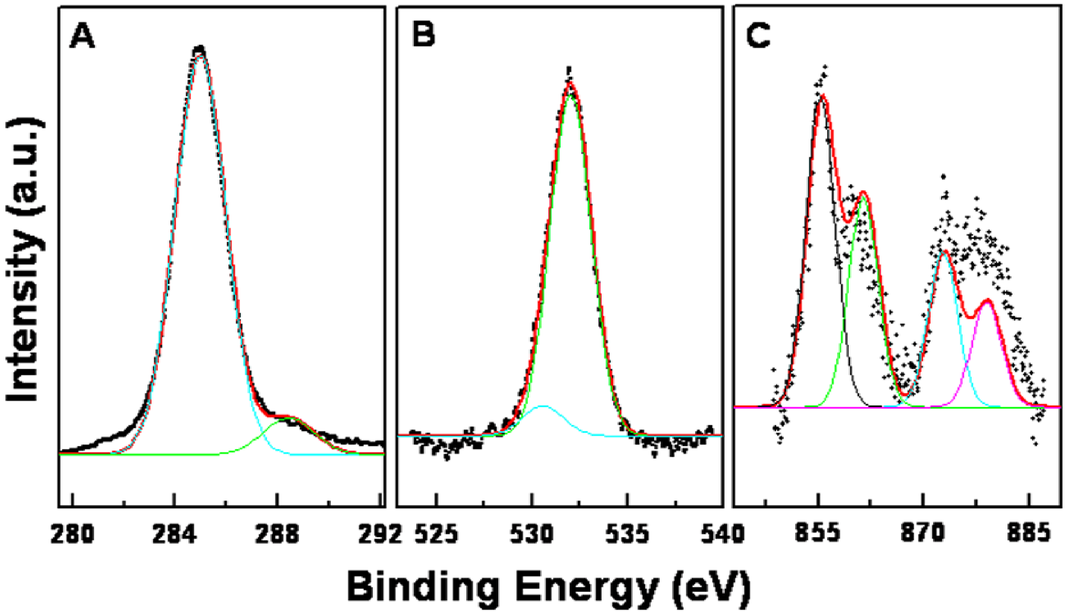

Figure 6.23. *XPS core level spectra recorded from Ni nanoparticles after phase transfer to toluene on Si(111) substrate—(A) C1s, (B) O1s, and (C) Ni2p levels.*

6.4.5. FOURIER TRANSFORM INFRARED SPECTROSCOPY:

The stability imparted to the Ni nanoparticles in aqueous medium originates from the capping of oleic acid on the surface of the Ni nanoparticles and the interaction of Ni nanoparticles with the organic molecules adsorbed on the surface can be proved from a careful FTIR study *(Figure 6.24)*. *Curve 1* in *Figure 6.24* denotes the FTIR spectra for pure oleic acid which shows its –COOH stretch at 1707 cm^{-1} and the C=C-H stretching vibration at 3004 cm^{-1} [36]. The carboxylic stretch shifts to 1561 cm^{-1} in aqueous Ni nanoparticles capped only with oleic acid *(Curve 2)* and there is a complete disappearance of 3004 cm^{-1} peak. This observation leads to the hypothesis that probably the oleic acid molecules are randomly oriented on the surface and the electron rich double bond interacts significantly with the nanoparticles but the carboxylic groups are also bound to the surface thereby showing a large shift in the value of its vibrational modes. The –COOH groups, which are exposed towards the solvent are also bound to the Na$^+$, hence no free –COOH peak is observed. This oleic acid capped nanoparticles when phase transferred to toluene using STA display the retention of the peak at 1561 cm^{-1} along with the appearance of a peak at 1682 cm^{-1} *(Curve 4)*. The pure STA shows the –COOH band at 1701 cm^{-1} *(Curve 3)* and a shift to 1682 cm^{-1} *(Curve 4)* indicates its binding to the nanoparticle surface.

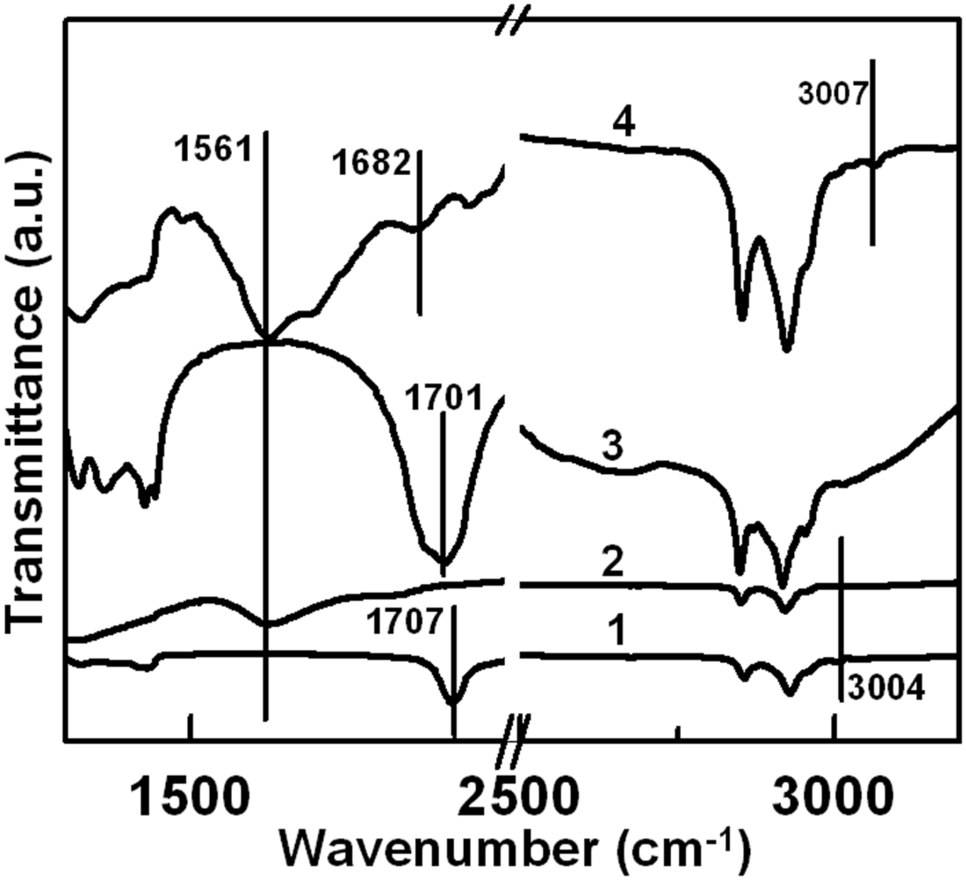

Figure 6.24. *FTIR spectra of pure oleic acid (curve 1) and pristine oleic acid capped Ni nanoparticles in aqueous phase (curve 2). The vertical lines delineate a shift in the –COOH group stretching due to the interaction of this functional group with Ni nanoparticles. The pure stearic acid spectra (curve 3) and Ni nanoparticles after phase transfer (curve 4) are also presented to show that –COOH group frequency of STA is also shifted again indicating an interaction with the nanoparticle surface. Curve 4 also depicts the regeneration of methylene stretch at 3007 cm^{-1}.*

A very careful observation reveals that there is a small hump at 3007 cm^{-1} *(Curve 4)* which can arise due to the detachment of the double bond of oleic acid from the surface of the Ni nanoparticles. This suggests that some of the bound oleic acid molecules are probably exchanged with STA molecules imparting a hydrophobic nature to the surface of nanoparticles. The hydrocarbon chain is thus exposed to the solvent environment, bringing about the phase transfer. The pristine oleic acid capped Ni nanoparticles when stirred with only an organic solvent like toluene or cyclohexane in absence of STA, formed aggregates at the interface without any phase transfer to the organic medium. Oleic acid capped Ni nanoparticles could not be phase-transferred using methods like adding orthophoshoric acid as is done for Ag nanoparticles, which is already discussed in the section 6.2 of this chapter. This is probably due to the fact that on silver surface, addition of orthophoshoric acid brings an orientational change in the oleic acid molecule while on Ni nanoparticles surface no such phenomenon occurs which is essential for phase transferring them. On the other hand in this case, STA could either be interacting with the –COOH group of oleic acid through hydrogen bonding or place exchanging some of the oleic acid molecules on the Ni surface and both the phenomena lead to exposure of the hydrophobic aliphatic chain of ligand acids to the organic solvent environment facilitating the phase transfer.

6.4.6. ASSEMBLY OF HYDROPHOBIZED Ni NANOPARTICLES BY LANGMUIR-BLODGETT TECHNIQUE:

The hydrophobized Ni nanoparticles capped with oleic acid and STA were weighed and dissolved in chloroform keeping the concentration as 1mg/ml. A known volume of this solution was spread on the surface of double distilled water at pH 6.5. *Figure 6.25A* exemplifies the π-A isotherm recorded from the Langmuir monolayer as a function of volume added to the air/water interface. It is monitored that the pressure can be augmented to 21 mN/m when the volume added is increased from 50 microlitre *(Curve 1)* to 125 microlitre *(Curve 2).* When the volume is further increased to 250 microlitre *(Curve 3)* the monolayer could again be compressed upto a pressure of 25 mN/m beyond which the monolayer does not seem to be very stable as indicated by a change in slope of the curve. Notably, the take-off area is diminished with the increase in volume of the hydrophobized Ni nanoparticles added to the monolayer. So an optimum surface pressure of 15 mN/m was selected as the pressure for deposition of the film onto various substrates for characterizations. This result combined with the fact that TEM images (vide infra) obtained from these assemblies do not show any multiple layer formation point to the presence of more compact monolayer.

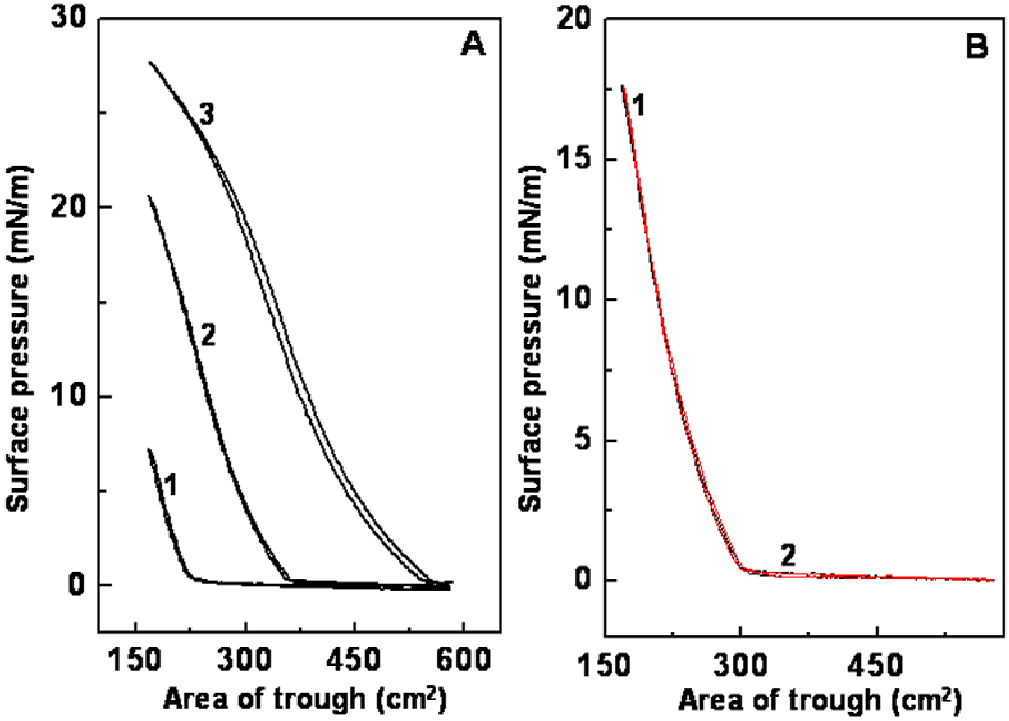

Figure 6.25. *(A) Surface pressure-area (π-A) isotherms recorded during compression and expansion cycle of hydrophobized Ni nanoparticles when spread on the subphase of distilled water after addition of different volumes of the nanoparticles like 50 microlitre (curve 1), 125 microlitre (curve 2), 250 microlitre (curve 3). (B) The similar isotherms were also recorded 10 min (curve 1, black) and 30 min (curve 2, red) after spreading the monolayer which evinced the stability of the monolayer over the water subphase.*

However it is a point of concern that here the Langmuir layer could have many components viz. the hydrophobized Ni nanoparticles plus the uncoordinated oleic acid and STA molecules. These uncoordinated molecules could be playing a crucial role in determining the nature of the Langmuir layer at different amounts of spread and therefore it is difficult to relate the changes in take-off area with the area per nanoparticle etc. Nevertheless it is observed that the monolayers formed are quite stable as documented by the π-A isotherm with time and presented in *Figure 6.25B*. The isotherms show no shift and no significant hysteresis is observed in the curve at t=10 min *(Curve 1)* and t=30 min cases *(Curve 2).*

6.4.7. BREWSTER ANGLE MICROSCOPY:

The long range assembly is a phenomenon that took place at the air water interface and it can be visualized in-situ using Brewster Angle Microscopy. A real time measurement of the domain structure formed at the air-water interface and the effect of pressure or concentration of the Ni nanoparticles on the assembly pattern can also be studied using the same set-up.

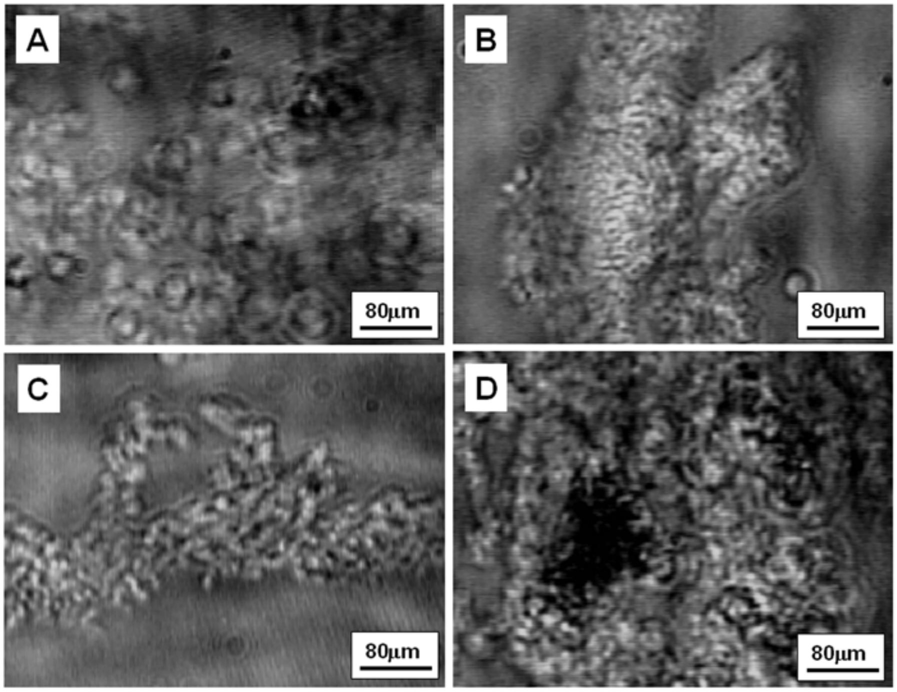

Figure 6.26. *Brewster Angle Micrograph of hydrophobized Ni nanoparticles assembled at air water interface.The images were recorded at different surface pressure like 0 mN/m (A), 15 mN/m (B, C). (D) represents the image when the initial concentration was taken as 5mg/ml and the pressure was maintained at 15 mN/m.*

Figure 6.26A-D show Brewster angle micrographs which correspond to the morphology of the assembled Ni nanoparticles at the air water interface at different surface pressure. *Figure 6.26A* illustrates that the particles with a concentration of 1mg/ml and at 0 mN/m pressure are not arranged into any patterns, but with the increase of surface pressure to 15 mN/m, the particles show interesting linear arrangements *(Figure 6.26B and C)* at several regions. These linear arrangements themselves seem to consist of compact assembly of several smaller regions with linear assemblies though there does not seem to be any registry among these smaller regions. The concentration of the initial solution was then increased to 5 mg/ml and the hydrophobized nanoparticles were spread at the air water interface in a similar way and the surface pressure was increased to 15 mN/m, but it did not produce any linear assembly and at similar pressure the whole surface appeared to be filled with the nanoparticles *(Figure 6.26D)*. This observation can be explained on the basis that due to the higher concentration of the nanoparticles in chloroform the particles turn into clusters. The second reason can be the presence of a large number of nanoparticles at the air-water interface bringing linear structures close to each other, thus destroying the distinct linear type arrangement.

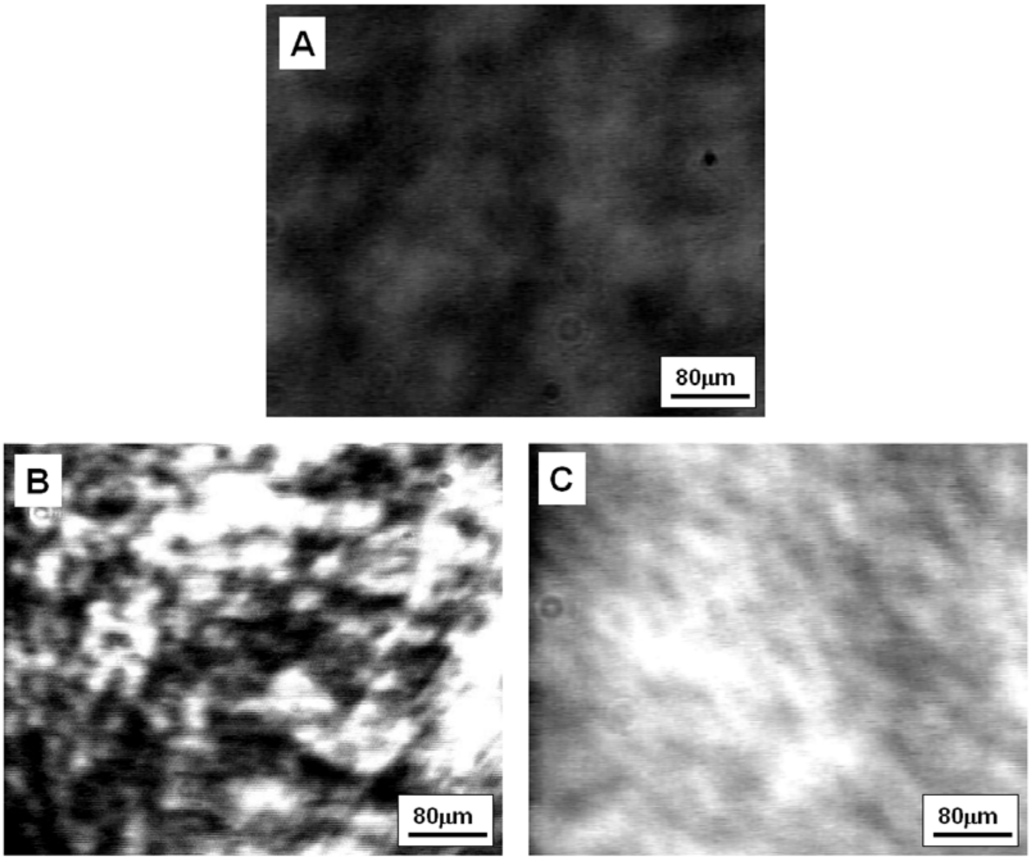

Figure 6.27. *(A) BAM image of pure water. (B) BAM image of stearic acid, and (C) BAM image of pure oleic acid on a subphase of pure water at pH 6.5 at a surface pressure of 15 mN/m.*

For comparison, the BAM images of pure water, STA and pure oleic acid on pure water subphase are shown in *Figure 6.27A, B and C respectively*. The STA [37] and oleic acid [38] monolayer does not show any definite structure whereas linear structures are observed only with hydrophobized Ni nanoparticle spread at the air-water interface (*Figure 6.26)*.

6.4.8. TRANSMISSION ELECTRON MICROSCOPY:

Figure 6.28A and B display the transmission electron micrographs of Ni nanoparticles from the aqueous solution. The images clearly indicate bimodal distribution nature. The selected area diffraction pattern in the inset of *Figure 6.28B* can be indexed to *fcc* Ni nanoparticles [39]. The diffraction pattern displays very diffuse and broad ring like pattern pointing to the poor crystalline nature of the particles. The aqueous Ni nanoparticles when phase transferred to toluene containing STA, retain the bimodal distribution which is demonstrated in *Figure 6.28C and D* respectively.

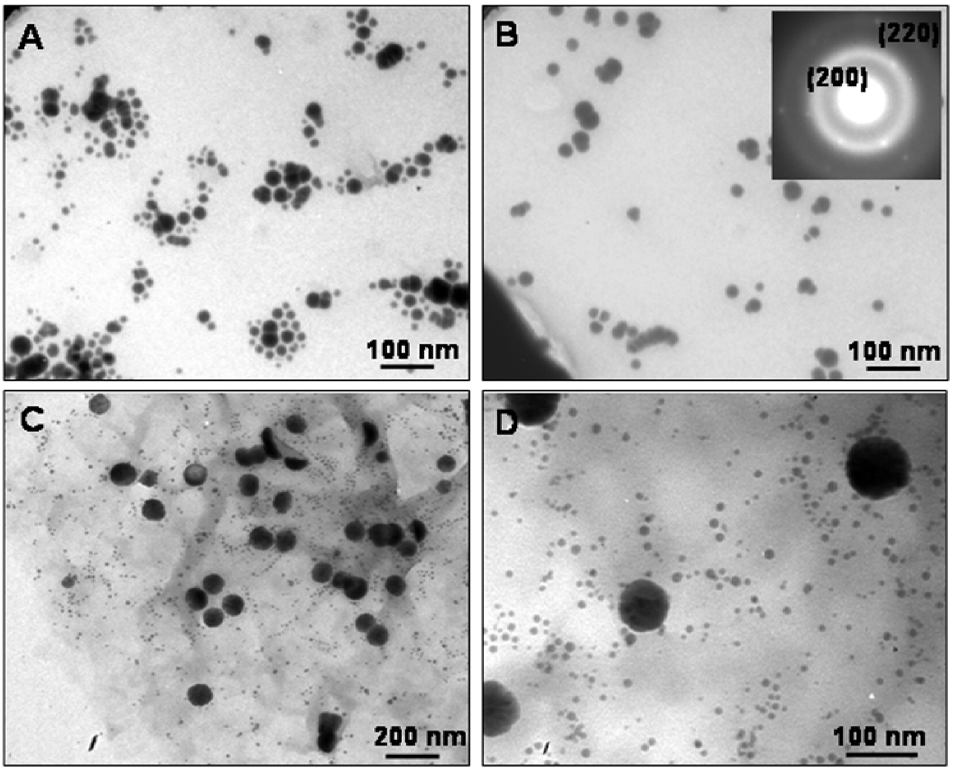

Figure 6.28. *(A) and (B) represent the TEM of oleic acid capped Ni nanoparticles in aqueous phase where the inset in (B) shows the SAED pattern of fcc Ni. The organic phase TEM images are presented in (C) and (D), respectively. All the micrographs were recorded from the drop cast film from the respective aqueous and organic phase.*

Figure 6.29A–H depict the TEM pictures when a monolayer formed with 150 microlitre of hydrophobized Ni solution, was compressed at 15 mN/m surface pressure and was transferred to the TEM grid by dipping it vertically. The images show long range compact linear ensemble of the Ni nanoparticles at the air water interface, which was predicted from the BAM pictures in *Figure 6.26B , C.*

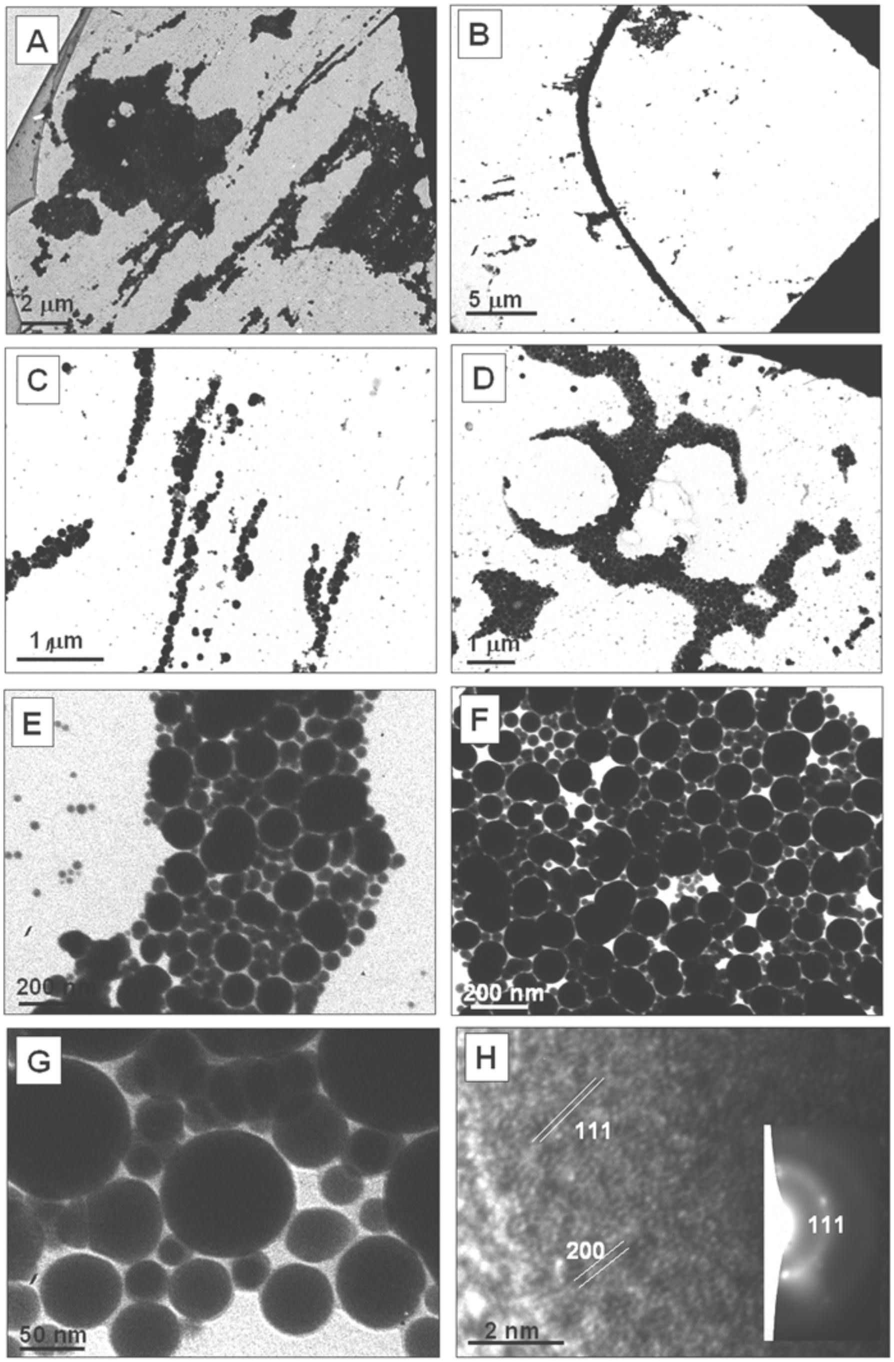

Figure 6.29. *Representative TEM images obtained when the Ni nanoparticles monolayer was transferred on to a TEM grid after compressing the monolayer at 15 mN/m surface pressure. The linear arrangement of the particles can be visible at lower magnification (A–D) whereas the internal arrangement of the bigger and smaller particles is evidenced in (E-G). The high resolution TEM image in (H) showed the Ni nanoparticles to be polycrystalline. The SAED pattern in the inset of (H) reveals diffused ring pattern of fcc Ni.*

The difference in the scale of BAM as compared to the TEM is basically due to the difference in the resolution of the two imaging techniques. The closely spaced area of the Langmuir film of Ni nanoparticles as observed on transmission electron microscope (*Figure 6.29A*) cannot be resolved by BAM and thus appeared as thicker assembly. As mentioned previously the BAM images look like a compact arrangement of several linear structures. In transmission electron microscopy, we have highlighted the smaller linear ensemble of Ni nanoparticles and the internal arrangement of the small and relatively bigger particles (*Figure 6.29B-G*). It is reported that for purely monodisperse particles regular hexagonal close-packed monolayer films are formed on LB. But particles having well-defined bimodal size distributions can organize themselves into complex, ordered two-dimensional arrays. The magnified images *(Figure 6.29B-G)* clearly show the arrangement of the two kinds of particles in the assembly. The bigger particles (avg size ~110 nm) are surrounded by the smaller ones (avg size ~52 nm) making the assembly more compact. From the particle size measurement and the theoretical calculation the radius ratio of the smaller to bigger particle is evaluated to be $R_B/R_A = \sim 0.47$ ($R_A > R_B$) which predicts a AB_2 type distribution when ensembled on LB. the TEM images reveal the expected structure showing a clear parallelism between the bimodal structures formed and those predicted either for atomic scale intermetallic alloys or for colloidal crystals based on the geometrical packing of hard spheres [40-41]. The high resolution TEM image presented in the *Figure 6.29H* clearly showed the presence of (111) and (200) planes of fcc Ni very near to the surface of the particle. This indicates that the Ni prepared by our synthetic method is polycrystalline and also proves the absence of any crystalline NiO layers at the surface. The SAED pattern *(inset of Figure 6.29H)* obtained from the same particle points towards the similar polycrystalline nature as indicated by the diffused ring pattern of the diffraction. The most intense ring in the SAED pattern can be matched with the (111) plane of fcc Ni (a= b= c= 3.523, space group= Fm3m, PCPDF # 040850).

However, when the monolayer was compressed beyond a pressure of 22 mN/m the particles at the interface are found to coalesce into each other (the TEM image is shown in *Figure 6.30*). The change of slope in the π-A isotherm in *Curve 3* of *Figure 6.25A* can be due to the above phenomenon or multilayer formation. But the TEM images of *Figure 6.29* prove that at a pressure of 15 mN/m there is only a monolayer of the nanoparticles ruling out the possibility of any multilayer formation.

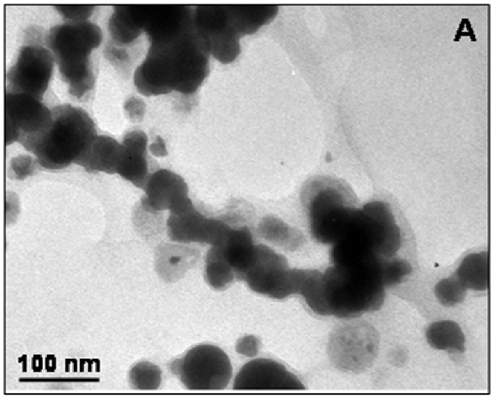

Figure 6.30. *The TEM picture of hydrophobized Ni nanoparticles monolayer at surface pressure 22 mN/m clearly reveals the fusion of adjacent particles of the linear ensemble and also the assembly of one particle on top of other.*

The TEM grid when lifted vertically from the Langmuir film obtained by spreading Ni nanoparticles with the initial concentration of 5 mg/ml, is found to have no linear assembly, but disordered polydisperse particles all over the grid *(Figure 6.31A and B)* and can be linked comprehensibly to the BAM image observed for this case *(Figure 6.26D)*. The particles appeared to be more aggregated and linear structures were very scarce.

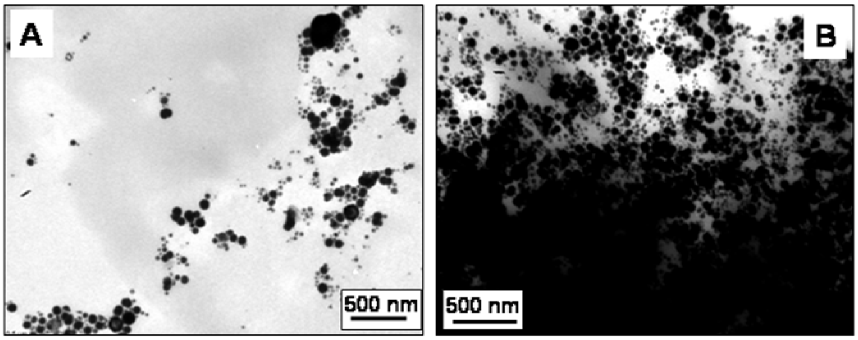

Figure 6.31. *TEM images of the monolayer of hydrophobized Ni nanoparticles formed with the solution of initial concentration 5 mg/ml when the monolayer was compressed at surface pressure 15 mN/m.*

There is a possibility that such linear structures and assembly of nanoparticles are formed due to the hydrodynamic flow that is present during the lifting process of the substrate and can also be caused by evaporation of the solvent. However, we have now conclusively shown with the help of BAM and TEM studies that the linear assembly is truly occurring at the air-water interface at the surface pressure of 15 mN/m and the Langmuir film formed with the hydrophobized Ni nanoparticles can be effectively transferred to any substrate. We mention here that there is still lot of optimization needed to get the much desired purely linear assembly of few nanoparticles for elecronic and magnetic application and our BAM studies could prove to be very valuable to obtain very important information about the conditions under which interesting assemblies of nanoparticles at the air-water interface could be achieved. There are also reports where the linear assemblies of nanoparticles are exploited to form nanowires by sintering of nanoparticles on the substrate by heat treatment or electron beam bombardment [42]. Similar experiment in this case could be utilized to obtain Ni nanorods, which can lead to some unusual magnetic properties and these issues could be taken up for further studies.

6.4.9. SUMMARY:

Development of simple and efficient protocol for the synthesis of Ni nanoparticles in aqueous media and their subsequent phase transfer to organic media is reported. The phase transfer was effective probably due to the space exchange between the oleic acid moiety and stearic acid molecules. The hydrophobized Ni thus obtained was organized at the air–water interface and it was observed that by controlling the pressure and concentration of hydrophobized Ni nanoparticles at air–water interface, linear ribbon like assemblies could be obtained. Availability of more data like these can give us a great control in assembling the nanoparticles in desired shape and can address many fundamental issues related to the assembly of nanoparticles at the air–water interface. As the Ni nanoparticles are synthesized in aqueous medium and phase transferred afterwards, they can be utilized for biological application as well as for different catalytic organic reaction. The linear close packed assembly of Ni can also be exploited in modulating the magnetic behavior.

6.5. SYNTHESIS OF Co-CORE Au-SHELL NANOPARTICLES IN ORGANIC PHASE:

6.5.1. EXPERIMENTAL DETAILS:

(A) Preparation of Co nanoparticles: In a typical experiment, 100 ml solution was taken containing 1 X 10^{-3} M $CoCl_2$, 1 X 10^{-2} M SDS and 1 X 10^{-4} M oleic acid. Then 0.05% $NaBH_4$ was added slowly with constant stirring when the colour of the solution changed to dark blackish from colorless. The solution was kept for an hour to ensure the complete decomposition of the borohydride which is followed by centrifugation of the solution at a speed of 8000 rpm for 20 min. The pellet and the supernatant were separated; the pellet was diluted in water and again kept for centrifugation under the same set of conditions. The pellet was dried thoroughly under normal atmospheric temperature and pressure. The dried mass can be redispersed in toluene easily. The Co nanoparticles thus dispersed in organic medium was used for the transmetallation reaction.

(B) Preparation of hydrophobized $HAuCl_4$: 25 ml of 1 X 10^{-3} M aqueous $HAuCl_4$ was stirred with 25 ml of toluene containing 1 X 10^{-3} M benzyl di stearyl ammonium chloride (BDSAC) in it. The yellow colour of the aqueous chloroauric acid turned colourless within 15 min of stirring. The organic layer was separated from the aqueous layer using a separating funnel. The organic layer was again stirred with $HAuCl_4$ to saturate the organic layer with chloroaurate ions followed by the separation of the organic layer. These hydrophobized chloroaurate ions were used for the transmetallation reaction.

(C) Preparation of Co_{core} Au_{shell} with variable shell thickness: The hydrophobized $HAuCl_4$ solution was added to Co nanoparticles solution in toluene in three different proportion of their volume like 1:10, 1:15 and 1:50 respectively. The black colour of Co nanoparticle solution exhibited pink-red shade in all three cases in different extent. The solutions were kept for ~1 hr to complete the transmetallation reaction between Co nanoparticles and chloroaurate ions depending on their redox potential. The detail investigations of the samples containing Co and $HAuCl_4$ in 15:1 and 50:1 ratio are discussed here and the samples are referred as sample A and sample B respectively.

6.5.2. UV-VIS SPECTROSCOPY:

The solution of Co nanoparticles in toluene was added with hydrophobized chloroaurate ions in two different proportions like (a) 15:1 and (b) 50:1. In every case the toluene solution changed its color and a surface plasmon resonance band corresponding to Au^0 state appeared at ~540 nm. The UV-Vis spectra of pure Co do not show any absorpbance in UV-Vis region, hence the signs of SPR clearly indicate the occurrence of transmetallation reaction in organic phase. The UV-Vis spectra are shown in *Figure 6.32* where curve 1 corresponds to the absorption spectra of pure Co and curve 2 and curve 3 illustrate the UV-Vis spectra for core shell nanoparticles for sample A and B respectively, prepared with different proportion of Co to Au as mentioned above.

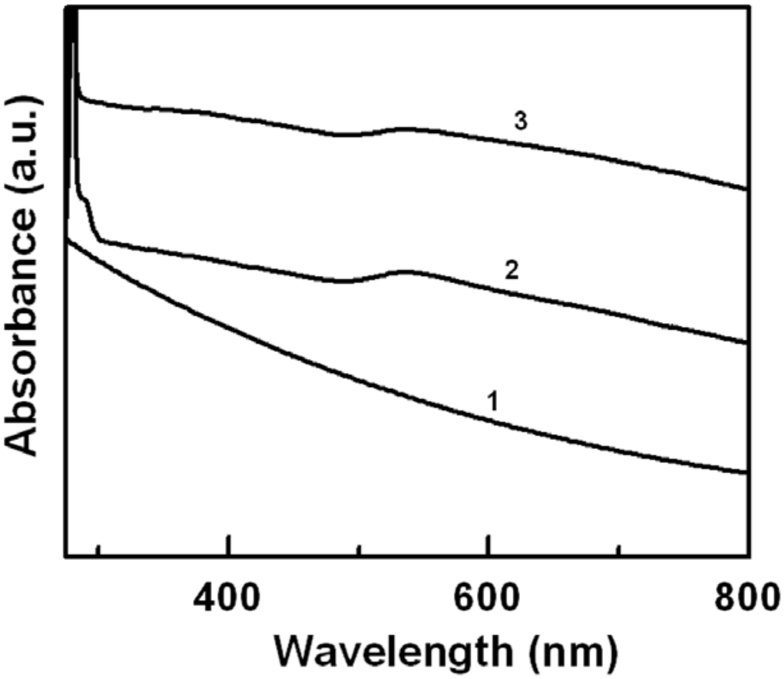

Figure 6.32. *UV-Vis spectra of only Co nanoparticles showing a monotonic increase in the absorbance with decrease in wavelength (curve1). Curves 2-3 represent the UV-Vis spectra of* $Co_{core}Au_{shell}$ *nanoparticles synthesized with different proportion of Co to hydrophobized chloroaurate ions namely 15:1 (curve 2), and 50:1 (curve 3).*

6.5.3. TRANSMISSION ELECTRON MICROSCOPY:

Figure 6.33A represents the TEM image of Co nanoparticles formed in the aqueous phase with surfactant SDS and oleic acid as the capping agent. The black solution of the Co nanoparticles was centrifuged to separate excess surfactants prior to the TEM analysis. The nanoparticles are found to be fairly dispersed and the SAED from these particles shown in *Figure 6.33B*, clearly supports the formation of face centered crystals of cobalt nanoparticles [43]. These nanoparticles are capped with oleic acid. The phase transferability can be explained based on the orientational change of oleic acid when the dried powder comes in contact with the organic solvents as explained in the case of silver earlier. The Co nanoparticles, dispersed in toluene are shown in *Figure 6.33C*. The particles retained their crystallinity after the re-dispersion in organic solvents as illustrated by the SAED pattern given in *Figure 6.33D*.

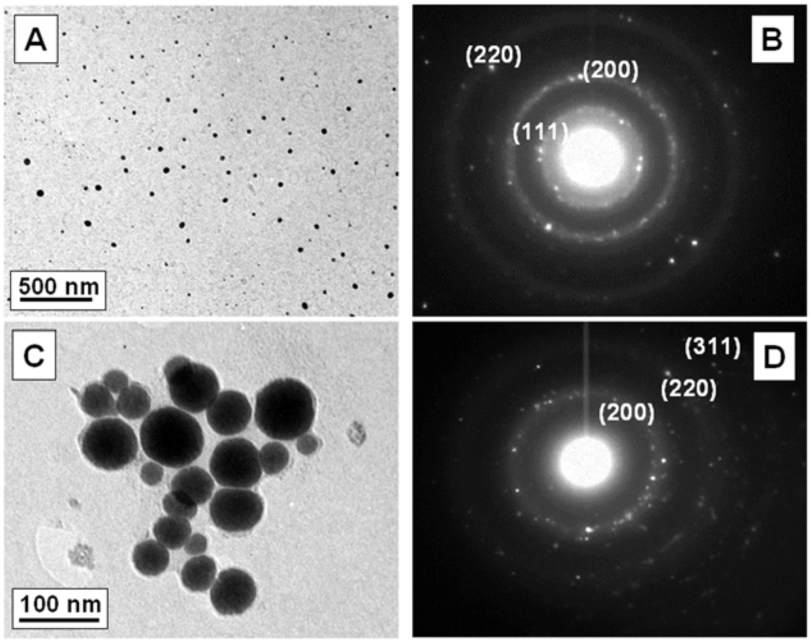

Figure 6.33. *(A) Representative TEM images oleic acid capped Co nanoparticles prepared in aqueous medium. (B) Selected area electron diffraction (SAED) pattern from the Co nanoparticles with rings indexed with respect to fcc cobalt. (C) TEM micrograph of Co nanoparticles after dispersing in toluene. (D) SAED pattern of Co when redispersed in organic solvent.*

The main evidence for the formation of core shell nanoparticles is offered by TEM analysis of the samples shown in *Figure 6.34.* The TEM image of $Co_{core}Au_{shell}$ prepared with the Co:Au ratio as 15:1 shows a thin shell formation *(Figure 6.34A)* whereas *Figure 6.34B* shows a prominent thick coating of Au shell on top of the Co nanoparticles. In this case the Co to Au ratio was 50:1 *(Figure 6.34B)*. The inset of this figure portrays the SAED obtained from the core shell nano structures, which matches well with the fcc Au diffraction pattern *(Figure 6.34A and B)*. The most interesting feature is that when the amount of Co is increased with respect to Au^{3+} the chloroaurate ions seem to be reduced more effectively which can be rationalized by the fact that the availability of more sacrificial nanoparticles cause better reduction of all the chloroaurate ions present in the solution.

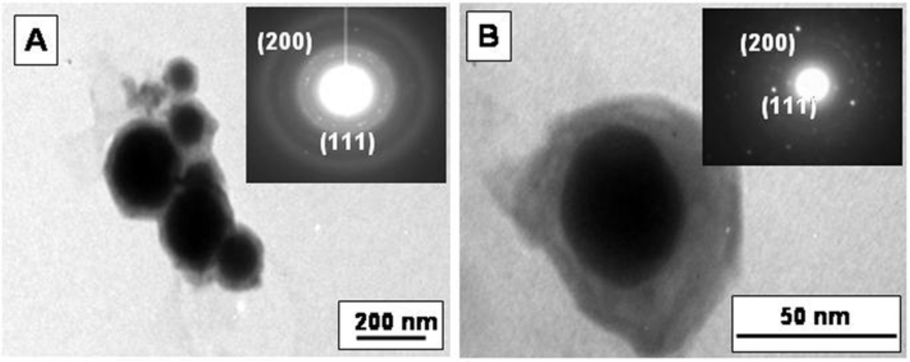

Figure 6.34. *(A) TEM micrograph of the similar core shell nanoparticle when the ratio was maintained as 15:1 and the SAED obtained from the particles was indexed as fcc Au confirming the formation of Au shell. (B) TEM picture representing the core shell nanoparticles with 50:1 proportion of Co and hydrophobized* $HAuCl_4$ *in organic medium. The shell thickness is observed to be maximum with this concentration ratio and the diffraction patterns taken from this nanocrystals are in good agreement with the fcc Au.*

6.5.4. X-RAY PHOTOELECTRON SPECTROSCOPY:

The proposition of formation of thicker Au-shell for Co:Au = 50:1 ratio, was further validated by XPS analysis of the three samples. *Figure 6.35A-D* illustrate the core level binding energy of Au 4f and Co 2p obtained from the core shell nanoparticles formed with different ratio of Co and $HAuCl_4$. In every combination of Co and chloroaurate ion to form core-shell nanoparticles, the Co $2p_{3/2}$ level of the core cobalt nanoparticles *(Figure 6.35A and C)* can be fit to a single peak centered at 781.4 eV BE with a characteristic satellite peak at 786.8 eV [44]. This feature is usual for Co^0 state, but there is an apparent increase in the background spectra of Co^0. Basically, the electron ejected from a point buried deeper from the surface experiences higher number of inelastic collisions than the surface electrons. This gives rise to a high Shirley background [33]. In our case, the electrons emanating from the core (Co nanoparticles) undergo more efficient inelastic collisions due to the presence of Au-shell. Thus the high background feature in the 2p core level spectra of Co clearly demands it to be present only in the core.

The XPS analysis of Au 4f core level spectra *(Figure 6.35B and D)* of core shell nanoparticles with different cobalt and chloroaurate ion ratio substantiate the variation in the Au-shell thickness. The spectra with Co:$HAuCl_4$ = 15:1 is broad suggesting the presence of Au(0) and Au(+1) states *(Figure 6.35B)* and a meaningful deconvolution is difficult. However in the other sample with higher fraction of Co nanoparticles, the curve can be fit into the Au $4f_{7/2}$ core level with distinct components centered at 84.7 eV BE that correspond to Au^0 state *(Figure 6.35D)*. This authenticates our proposition of partial completion of reduction of chloroaurate ions when surplus Co is absent in the solution.

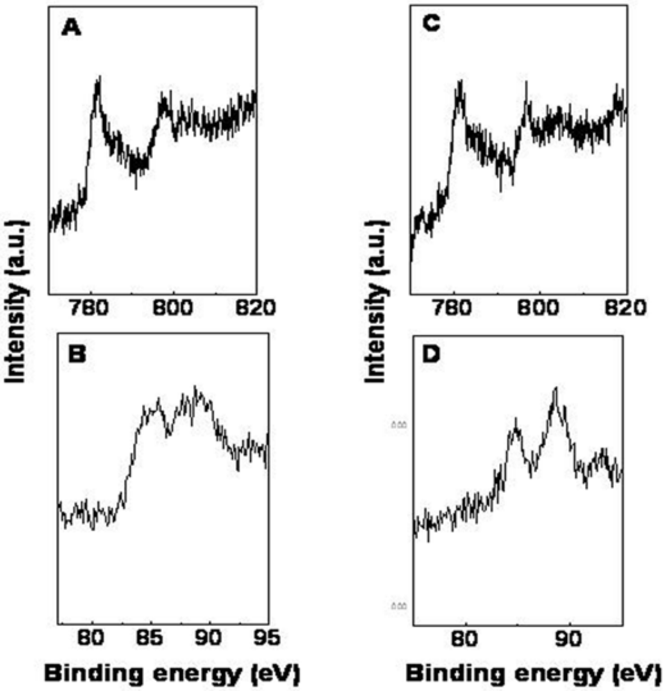

Figure 6.35. *XPS core level spectra recorded from the* $Co_{core}Au_{shell}$ *nanoparticles prepared with different ratio of Co:*$HAuCl_4$ *(A) Co 2p (B) Au 4f for 15:1 proportion and (C) Co 2p (D) Au 4f for 50:1 composition. All the samples were made on Si (111) substrate and the core level binding energy were aligned considering the C 1s binding energy as 285 eV.*

6.5.5. THERMOGRAVIMETRIC ANALYSIS:

It is expected that the transmetallation reaction is facilitated by the detachment of the surface bound oleic acid molecules on Co surface or due to flexible nature of oleic acid which allows easy diffusion of the Au^{3+} ions to access the surface Co atoms.

Moreover after the formation of Au shell on Co oleic acid molecules are in direct contact of Au-shell only. Acid groups are not recognized for their interaction with Au nanoparticles. Therefore the amount of organic matter is expected to decrease in amount subsequent to the formation of core shell nanoparticles. The surface bound organic matter is estimated from TGA of Co and $Co_{core}Au_{shell}$ system that is illustrated in *Figure 6.36A and B*. The curve in *Figure 6.36A* indicates the weight loss for only Co nanoparticles. The curve shows a steady loss of ~16% in the temperature range of 215-300^{0}C, probably due to desorption of surface bound oleic acid molecules. The core shell nanoparticles also show the known weight loss in the similar temperature zone but only to the extent of ~14% (*Figure 6.36 B*). It can thus be concluded that oleic acid molecules are not totally detached from the surface even after the shell formation.

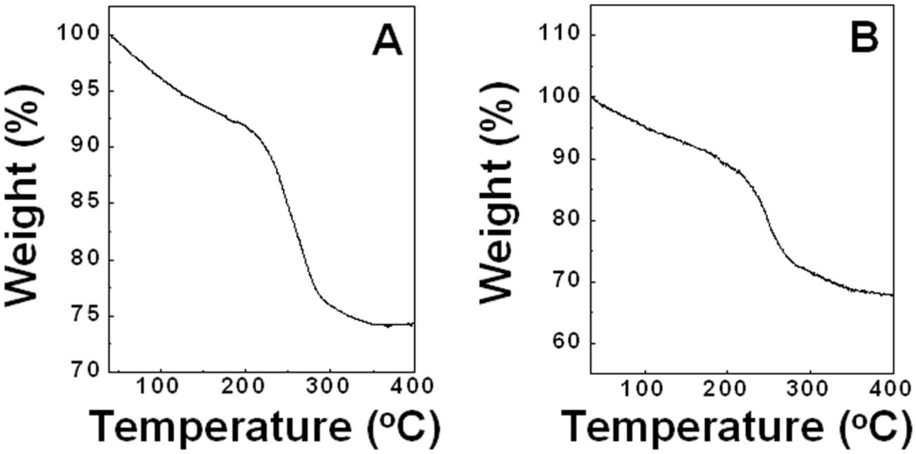

Figure 6.36. *(A) Thermogravimetric analysis of pristine oleic acid capped Co nanoparticles showing a small weight loss in the range of 100-120 ^{O}C and relatively larger weight loss of >16% in 200-300 ^{o}C. (B) TGA of core shell nanoparticles illustrating a similar behavior as the TGA curve of only Co nanoparticles but the weight loss is relatively lower (~14%).*

6.5.6. MAGNETIC MEASUREMENTS:

6.5.6-1. Temperature Dependent Magnetization measurements:

The temperature dependence of the magnetization for oleic acid capped Co nanoparticles and the core-shell systems are shown in *Figure 6.37A-C* respectively. In temperature dependent study, the applied magnetic field was 1000 Oe and the temperature was varied between room temperature and 2K. Curve 1 in *Figure 6.37A* corresponds to the M vs T plot for the pristine Co system in the zero-field-cooled (ZFC) mode while curve 2 is the measurement carried out in the field-cooled (FC) mode. As can be clearly seen, the curves of temperature dependent ZFC and FC magnetizations are typical of magnetic nanoparticles. For the pristine oleic acid capped cobalt nanoparticles, the ZFC curve shows a maximum at 5.0 K and the ZFC and FC curves show a divergence below this temperature revealing that the blocking temperature is 5.3 K. The blocking temperature is actually related to the size of the magnetic nanoparticles and the magnetocrystalline anisotropy constant (K) by the equation $K = 25k_BT_B/V$ where the k_B and V are the Boltzmann constant and the volume of single particle, respectively and T_B is the blocking temperature. By substituting the values for a ~35 nm particle we deduce K to be $0.77\text{x}10^3$ erg cm^{-3}, which is very low as compared to that of bulk cobalt ($45\text{X}10^5$ erg cm^{-3}) [45].

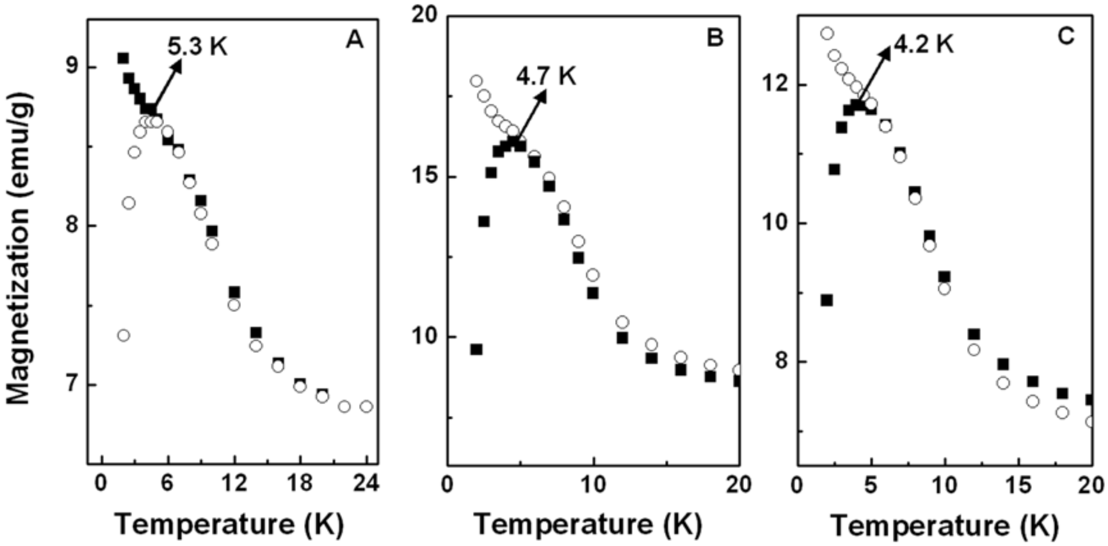

Figure 6.37. *(A) Temperature dependent magnetization of pristine oleic acid capped Cobalt nanoparticles in the zero field cooled (ZFC, curve 1) and field cooled (FC, curve 2) modes. The divergence between the two curves at 5.3 K is related to the blocking temperature (T_B). (B) and (C) The temperature dependent magnetization curves in zero field cooled (curve 1) and field cooled (curve 2) mode of the $Co_{core}Au_{shell}$ nanoparticles synthesized with 15:1 and 50:1 compositions of Cobalt and $HAuCl_4$ under the same external field as applied for Co nanoparticles. The T_B of this system is shifted from that of pure cobalt nanoparticles from 5.3K to 4.7K for sample A and to 4.2K for sample B due to loss of few surface Co atoms for the transmetallation reaction with chloroaurate. In every case the applied magnetic field was 1000 Oe.*

The curves in *Figure 6.37B and C* are the temperature dependence of ZFC and FC magnetization observed for the $Co_{core}Au_{shell}$ nanoparticle samples with two different ratio of Co:Au e.g. 15:1 and 50:1 respectively. The Au shell around Co nanoparticles is formed by an organic phase transmetallation reaction wherein a few layers of the surface cobalt atoms are oxidized to Co^{2+} in the process of reduction of the hydrophobized chloroaurate ions. This reduces the average particle size of core and in general the blocking temperature is expected to shift to lower temperatures as the particle size is reduced. Accordingly, a marginal shift in the T_B is observed for both the core shell nanoparticles towards the lower temperature regime as compared to pristine Co nanoparticles. The ZFC and FC curves for sample A diverge at 4.7K and hence considered as the T_B for these nanoparticles (*Figure 6.37B*). Similar analysis on sample B reveals the T_B as 4.2K (*Figure 6.37C*). So the gradual shift of T_B indicates the formation of thicker shell in case of sample B. The shift in the blocking temperature was marginal in case of pure Co and the two core-shell systems. This points towards the fact that expected number of Co atoms may not be depleted from the surface. Another possibility is the shell formed in case of Co-Au nanocomposites may not be of pure Au but an alloy of the two.

6.5.6-2. Field Dependent Magnetization measurements:

The field dependent magnetic behavior data for cobalt nanoparticles, measured at 300 K (above T_B, *Figure 6.38A*) and at 2 K (well below T_B, inset of *Figure 6.38A*) are in accordance with the expected features for superparamagnetic particles, i.e. i) no saturation was observed in the magnetization even at very high fields (actually up to our instrument limit); ii) magnetic hysteresis with a high coercivity and remnant magnetization below the blocking temperature and iii) disappearance of magnetic hysteresis above the blocking temperature.

The field dependent magnetizations of the core shell nanoparticles at the room temperature (300K) are displayed in *Figure 6.38.* The curve 1 in the figure is allied with the core shell formed with the Co to $HAuCl_4$ ratio as 15:1. The curve 2 is associated with the hysteresis for sample with Co:Au ratio 50:1. The saturation magnetization is noticed to decrease in case of 50:1 ratio of Co and chloroaurate ions than that of sample A. This also signifies that the shell formed in this case is thicker than the previous opus. The room temperature magnetization data for both the composition of the core-shell nanostructure is devoid of any hysteresis. But the field dependent magnetization of the both the samples i.e. 15:1 and 50:1 ratio at 2K (demonstrated in the inset I and II respectively in *Figure 6.38B*) undoubtedly illustrate an opening of the hysteresis loops below the blocking temperature of the samples. This observation supports that the core-shell nanocrystals are also superparamagnetic in nature. The shell formation on the surface of Co nanoparticles by transmetallation only results in the sacrifice of few layers of Co atoms without too much of impairment of their magnetic properties. The magnetic properties can thus be tuned depending on the thickness of the shell formed.

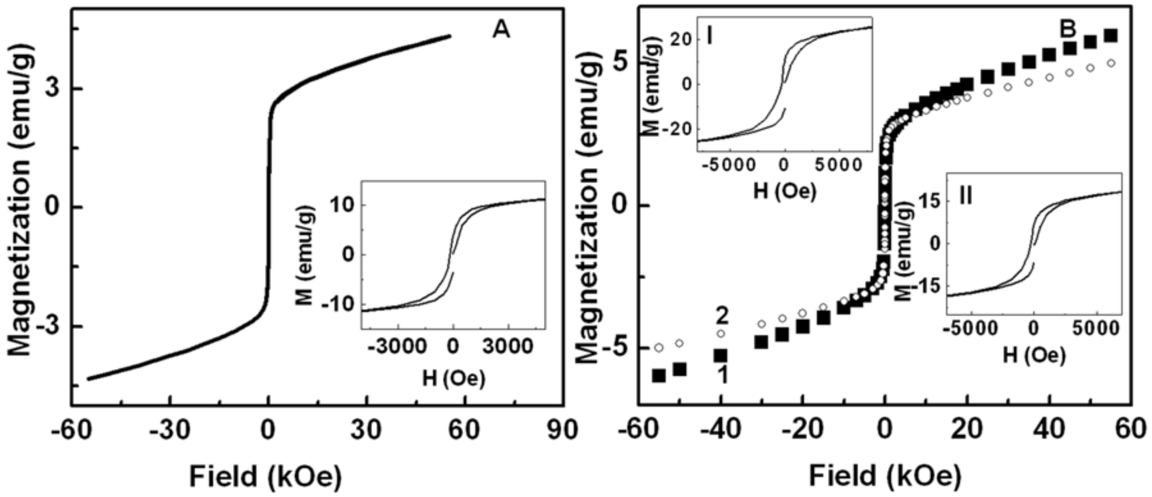

Figure 6.38. *(A) Field dependent magnetization of Co nanoparticles at room temperature (300 K) showing no hysteresis whereas below the blocking temperature (2K, inset) hysteresis loop opens up indicating superparamagnetic nature of the Co nanoparticles. (B) Field dependent hysteresis curves of* $Co_{core}Au_{shell}$ *nanoparticles at room temperature for 15:1 (curve 1) and 50:1 (curve 2) ratio of Cobalt to* $HAuCl_4$*. In both the systems the field dependent magnetization curves below* T_B *(2 K) show the hysteresis (inset I for 15:1 and inset II for 50:1 ratio) which recognized the core-shell particles to retain the superparamagnetic nature even after the shell formation.*

One interesting observation here is that the saturation magnetization of pristine oleic acid capped Co nanoparticles is lesser than both the core shell systems. This indicates that the shell formed in case of CoAu core-shell nanoparticles may not be of pure gold as contrary to the observation in the case Co-Ag core-shell nanoparticles discussed in details in Chapter IV. There are reports that Co and Au can be mixed effectively and easily to generate an alloy, which is quite difficult in case of Co and Ag.

So in this case also, formation of alloy on the shell cannot be totally ruled out. The presence of few magnetic Co atoms on the shell can cause incomplete alignment of the spins of Au-electrons, which can be a plausible reason for the enhancement of saturation magnetization of the core-shell composites.

6.5.7. SUMMARY:

In summary, an expedient method to fabricate $Co_{core}Au_{shell}$ nanoparticles with a tunable shell thickness by simple transmetallation reaction has been demonstrated. The Co nanoparticles are capped with oleic acid and thus conveniently dispersed in toluene. The transmetallation reaction was carried out with hydrophobized chloroaurate ions. The success of the synthesis lies in the fact that the formation of shell is taking place effortlessly as the whole of the reaction is only dependent on the redox potential of the pair selected. The Co nanoparticles and also the core shell nanoparticles can be stabilized in organic solvent as well as in powder form for long time without any deterioration. The introduction of the shell imparts the optical properties to the Co nanocrystals and also shields it from aerial oxidation. This in turn protects its magnetic characterizations making the composite more attractive for various purposes. The biocompatibility of Au shell can be judiciously exploited for the biological use of this core shell nanocrystals.

6.6. CONCLUSION:

In this chapter we have described different aspects of phase transfer of different nanoparticles mainly from aqueous to organic environment. In fact this field of work is of topical interest to the scientists for better understanding of the exact principle on which particles can be moved across the phase boundaries and also for the study of different physicochemical and optoelectronic properties that change due to the change in the environment of the nanoparticles before and after phase transfer. We have demonstrated here that the change in the orientation of the capping agents can be crucial in deciding the capability of phase transfer. Oleic acid and AOT both acted as good capping agent for Ag nanoparticles in aqueous medium, but slight alteration of their orientation on the surface can initiate the movement of the particles towards the organic medium. Again it has been depicted that the orientational flexibility of the surface bound organic molecule depends greatly on the surface element e.g. the oleic acid and AOT molecules showed orientational change on Ag surface but did not act similarly on Ni nanoparticles. So Ni nanoparticles enveloped in thin layer of Ag on the surface can exploit the orientational flexibility of oleic acid for the process of phase transfer. Phase transferred nanoparticles have always been utilized for generating ordered assembly by different techniques. Here we have shown the development of long-range assembly of such hydrophobized Ni nanoparticles by Langmuir-Blodgett method. The phase-transferred nanoparticles can also be employed for the production of core-shell nanoparticles in the organic phase. We have successfully made Co-core Au-shell nanocomposites in nonpolar organic solvents. Thus the first part of this chapter is mainly concerned with the method of phase transfer whereas in the later part emphasis has been given towards the application of this hydrophobized nanoparticles by assembling them at the air-water interface and by preparing core-shell nanomaterials with hydrophobized precursors.

6.7. REFERENCES:

[1]. Wei, G. T.; Yang, Z.; Lee, C. Y.; Yang, H.Y.; Wang, C. R. C. *J. Am. Chem. Soc.* **2004**, *126*, 5036.

[2]. Sastry, M. in: C.N.R. Rao, A. Muller, A.K. Cheetham (Eds.), The Chemistry of Nanomaterials, Wiley–VCH, Weinheim, **2004**, p. 31.

[3]. Cheng, W.; Wang, E. *J. Phys. Chem. B* **2004,** *108,* 24.

[4]. Sarathy, K. V.; Kulkarni, G. U.; Rao, C. N. R. *Chem. Commun.* **1997**, 537.

[5]. Sarathy, K. V.; Raina, G.; Yadav, R. T.; Kulkarni, G. U.; Rao, C. N. R. *J. Phys. Chem. B* **1997**, *101*, 9876.

[6]. Thomas, J. P.; Kulkarni, G. U.; Rao, C. N. R. *J. Phys. Chem. B* **2000**, *104*, 8138.

[7]. Sastry, M. Curr. Sci. **2003**, *85*, 1735.

[8]. Lala, N.; Lalbegi, S. P.; Adyanthaya, S. D.; Sastry, M. *Langmuir* **2001**, *17*, 3766.

[9]. Kumar, A.; Mandale, A. B.; Sastry, M. *Langmuir* **2000**, *62*, 9299.

[10]. Wang, W.; Efrima, S.; Regev, O. *Langmuir* **1998**, *14*, 602.

[11]. Wang, W.; Chen, X.; Efrima, S. *J. Phys. Chem. B* **1999**, *103,* 7238.

[12]. Sastry, M.; Kumar, A.; Mukherjee, P. *Colloids Surf. A* **2001**, *181*, 255.

[13]. Kumar, A.; Mandale, A. B.; Sastry, M. *Langmuir* **2000**, *16*, 9299.

[14]. Kumar, A.; Joshi, H.; Pasricha, R.; Sastry, M. *J. Colloid Interface Sci.* **2003**, *264*, 396.

[15]. Kumar, A.; Mandal, S.; Selvakannan, P. R.; Pasricha, R.; Mandale, A. B.; Sastry, M. *Langmuir* **2003**, *15*, 6277.

[16]. Hirai, H.; Aizawa, H.; Shiozaki, H.; *Chem. Lett.* **1992,** 1527.

[17]. Hirai, H.; Aizawa, H. *J. Colloid Interface Sci.* **1993**, *161*, 471.

[18]. Simard, J.; Briggs, C.; Boal, A. K.; Rotello, V. M. *Chem. Commun.* **2000,** 1943.

[19]. Gittins, D. I.; Caruso, F. *Angew. Chem. Int. Ed.* **2001**, *40*, 3001.

[20]. Wang, Y.; Wong, J. F.; Teng, X.; Lin, X. Z.; Yang, H. *Nano Lett.* **2003**, *3*, 1555.

[21]. Pellegrino, T.; Manna, L.; Kudera, S.; Liedl, T.; Koktysh, D.; Rogach, A. L.; Keller, S.; Radler, J.; Natile, G.; Parak, W. J. *Nano Lett.* **2004**, *4*, 703.

[22]. (a) Swami, A.; Kumar, A.; Sastry, M. *Langmuir* **2003**, *19*, 1168. (b) Swami, A.; Jadhav, A.; Kumar, A.; Adyanthaya, S. D.; Sastry, M. *Proc. Indian Acad. Sci. (Chem. Sci.)* **2003**, *115*, 679.

[23]. Zubarev, E. R.; Xu, J.; Sayyad, A.; Gibson, J. D. *J. Am. Chem. Soc.,* **2006,** *128,* 4958.

[24]. Creighton, J. A.; Eadon, D. G. *J. Chem. Soc., Faraday Trans.* **1991**, *87*, 3881.

[25]. (a) Whetten, R. L.; Khoury, J. T.; Alvarez, M. M.; Murphy, S.; Vezmar, I.; Wang, Z. L.; Stephens, P.W.; Cleveland, C. L.; Luedtke, W. D.; Landman, U. *Adv. Mater*. **1996**, *8*, 428. (b) Andrews, M. P.; Ozin, G. A. *J. Phys. Chem.* **1986**, *90*, 2929.

[26]. Badia, A.; Gao, W.; Singh, S.; Demers, L.; Cuccia, L.; Reven, L. *Langmuir* **1996**, *12*, 1262.

[27]. Park, J.-II.; Cheon, J. W. *J. Am. Chem. Soc.* **2001**, *123*, 5743.

[28]. Bala, T.; Armugam, S. K.; Pasricha, R.; Prasad, B. L. V.; Sastry, M. *J. Mater. Chem.* **2004**, *14,* 1057.

[29]. Ulman, A. An Introduction to Ultrathin Organic Films: From Langmuir– Blodgett to Self Assembly, Academic Press, New York, 1991.

[30]. Tao, Y. T. *J. Am. Chem. Soc.* **1993**, *115*, 4350.

[31]. Hostetler, M. J.; Stokes, J. J.; Murray, R. W. *Langmuir* **1996**, *12*, 3604.

[32]. PCPDF # 030931, a= b= c= 4.067, space group= fm3m.

[33]. Shirley, D. A. *Phys. Rev. B* **1972**, *5*, 4709.

[34]. Yang, D. Q.; Sacher, E. *J. Phys. Chem. B* **2005**, *109,* 19329.

[35]. Wagner, C. D.; Riggs, W. M.; Davis, L. E.; Moulder, J. F.; Muilenberg, G. E. *Handbook of X-ray Photoelectron Spectroscopy,* Perkin Elmer Corp., Publishers, Eden Prairie, MN, **1979**.

[36]. Wu, N.; Fu, L.; Su, M.; Aslam, M.; Wong, K. C.; Dravid, V. P. *NanoLett.* **2004**, *4*, 383.

[37]. Yim, K. S.; Brooks, C. F.; Fuller, G. G. *Langmuir* **2000**, *16*, 4325.

[38]. Seoane, R.; Monones, J.; Conde, O.; Minones, J. Jr.; Casas, M.; Iribarnegaray, E. *J. Phys. Chem. B* **2000**, *104,* 7735.

[39]. PCPDF file no.04-0850 CAS no.7440-02-0, Space group Fm3m with cell parameter *a* = 0.3523 nm.

[40]. Kiely, C. J.; Fink, J.; Zheng, J. G.; Brust, M.; Bethell, D.; Schiffrin, D. J. *Adv. Mater.* **2000**, *12*, 640.

[41]. Kiely, C. J.; Fink, J.; Brust, M.; Bethell, D.; Schiffrin, D.J. *Nature* **1998**, *396*, 444.

[42]. Hutchinson, T. O.; Liu, Y. P.; Kiely, C.; Kiely, C. J.; Brust, M. *Adv. Mater.* **2001**, *13,* 1800.

[43]. Petit, C.; Taleb, A.; Pileni, M. P. *J. Phys. Chem. B* **1999,** *103,* 1805.

[44]. Fu, L.; Liu, X.; Zhang, Y.; Dravid,V. P.; Mirkin, C. A. *Nano lett.* **2003,** *3*, 757.

[45]. Cullity, B. D.; Introduction to Magnetic Materials, Addison-Wesley Publishing, Reading, **1972.**

Chapter VII

Conclusions

This chapter details the salient features of the research work presented in this thesis and emphasizes on possible avenues for future work.

7.1. SUMMARY OF THE WORK:

Nanotechnology has become one of the fascinating branches of science for the generation of novel materials with new properties [1] and superior applications. Material scientists working at the interface of science and engineering have developed several strategies for the preparation of simple nanomaterials, composites along with the tools for thorough characterizations and applications [2-4]. This includes the studies on colloidal particles, biomolecules, polymers etc. and their interactions with each other. The establishment of efficient synthetic routes for the construction of nanometer-scale architectures/conjugates/materials is of paramount importance if the expectation of nanomaterials in the field of molecular electronics, sensing, catalysis etc. are to be realized. In this thesis we have highlighted the synthesis of different magnetic materials by some alternative avenues. Aqueous liquid foams served as one such template, which have shown to be effective for the synthesis of metallic as well as oxide nanoparticles. The success in the synthesis of Co and Ni nanoparticles and also multi-component ferrites like cobalt ferrite and magnesium ferrite in aqueous medium substantiated the great potential of the template. Stabilization of magnetic metallic nanoparticles has always been very crucial for their propensity towards aerial oxidation [5]. Different options are adopted to stabilize these magnetic nanoparticles among which the use of long chain organic molecules as capping agent is the simplest. In our work we have utilized oleic acid extensively to stabilize magnetic nanoparticles. We have also attempted to have an insight into the metal-COOH interaction by carrying out several detailed experimental investigations as well as utilizing theoretical calculations to estimate the strength of binding of different metal ions with –COOH group. These studies enabled us to address some of the long pending issues of enhanced interaction of few metal ions like Pb^{2+} with –COOH group over smaller metal ions such as Cd^{2+}.

Obtaining greater stability as well as gaining control over the surface chemistry of metallic magnetic nanoparticles has been a great concern for the scientists working in this area. To this effect we have shown that deposition of noble metal sheath over the magnetic metallic core can offer stability to the magnetic nanoparticles. Moreover it can fetch enhanced functionality to the composite systems besides preserving the magnetic character of the core. We have synthesized Co/Ni-core Ag-shell systems using very simple transmetallation reaction and the composite nanoparticles of $Ni_{core}Ag_{shell}$ could be phase transferred effortlessly from aqueous to organic phase using the orientational flexibility of oleic acid on the surface of Ag-shell. The success of such phase transfer process encouraged us to change the surface capping of Ag nanoparticles to another well-known surfactant AOT and to carry out the phase transfer in a similar manner. This process also enable us to produce Ag nanoparticles in powder form very easily, which can be re-dispersed in a number of organic solvents as well as in water. This opens up a vast range of application of these nanoparticles in both aqueous and organic media. The hydrophobized nanoparticles are particularly used for ordered assembly. In our work also we have demonstrated that hydrophobized Ni can be exploited for organizing the particles in the form of long domains at the air-water interface using Langmuir-Blodgett technique. Re-dispersion of magnetic Co nanoparticles in organic medium gave us the opportunity to carry out transmetallation reaction in organic medium too. In this case we utilized hydrophobized $HAuCl_4$ to form $Co_{core}Au_{shell}$ nanocomposites.

7.2. SCOPE FOR FUTURE WORK:

Foam based synthetic method has already proved to be a very convenient way to synthesize different nanoparticles. Though simple metal nanoparticles, inorganic compounds like CdS and $CaCO_3$ were already reported, the success in synthesis of magnetic oxides like cobalt ferrites and magnesium ferrite will obviously encourage us to move to the next step of multi-component oxides containing three or more cations, which are generally very difficult to synthesize.

Transmetallation reaction is another interesting aspect of this thesis work. Theoretically the transmetallation can be accomplished between Co^0/Ni^0 nanoparticles and lots of other cations, which have higher reduction potential than Co and Ni to produce new composites, some of them can be useful for catalytic applications. The proper choice of core and shell combination like Ni/Pt, could generate excellent catalysts as both of them are well known for their catalytic activities in hydrogenation reaction, the experiments are under investigations currently. In fact we are also trying to understand the exact mechanism of transmetallation by carrying out the reaction in a more controlled fashion. In this respect LB technique is found to be quite handy where we can study the transmetallation between hydrophobized Ni nanoparticles with H_2PtCl_6 subphase and the detailed characterization of the samples obtained at different time interval can enlighten us regarding the exact mechanism of the reaction.

We have used oleic acid for the capping of magnetic nanoparticles like Co and Ni. This is cis-octadecenoic carboxylic acid. It will also be quite interesting to study the effect of trans form of these acids both experimentally and theoretically. In theoretical study also there are further scope to modify the systems by taking into account some other effects like hydration of the cations in solution, interaction of near neighbors among the capping molecules etc that might give more accurate results quantitatively.

7.3. REFERENCES:

[1]. El-Sayed, M. A. *Acc. Chem. Res*. **2001**, *34*, 257.

[2]. Metal Nanoparticles: Synthesis, Characterization, and Applications. Edited by Feldheim, D. L.; Foss, C. A. *Marcel Dekker pulishers*, **2002**.

[3]. Nanoparticles: Building Blocks for Nanotechnology. Edited by Rotello, V. *Kluwer Academic/Plenum Publishers*, **2004**.

[4]. The Chemistry of Nanomaterials. Edited by Rao, C. N. R.; Muller, A.; Cheetham, A. K. *Wiley-VCH Verlag GmbH & Co. publishers*, **2004.**

[5]. (a) Glavee, G. N.; Klabunde, K. J.; Sorensen, C. M.; Hadjipanayis, G. C. *Langmuir*, **1992**, *8,* 771. (b) Son, S. U.; Lee, S. I.; Chung, Y. K.; Kim, S. W.; Hyeon, T. *Org. Lett.* **2002**, *4*, 277.

List of publications:

1. Foam-based synthesis of cobalt nanoparticles and their subsequent conversion to CocoreAgshell nanoparticles by a simple transmetallation reaction

Tanushree Bala, Sujatha K. Arumugam, Renu Pasricha, B. L. V. Prasad and Murali Sastry, *J. Mater. Chem.,* 14 (2004) 1057.

2. A facile liquid foam based synthesis of nickel nanoparticles and their subsequent conversion to NicoreAgshell particles: structural characterization and investigation of magnetic properties

Tanushree Bala, S. D. Bhame, P. A. Joy, B. L. V. Prasad and Murali Sastry, *J. Mater. Chem.,* 14 (2004) 294.

3. Phase transfer of oleic acid capped NicoreAgshell nanoparticles assisted by the flexibility of oleic acid on the surface of silver

Tanushree Bala, Anita Swami, B.L.V. Prasad and Murali Sastry, *Journal of Colloid and Interface Science* 283 (2005) 422.

4. Solvent-Adaptable Silver Nanoparticles

B. L. V. Prasad, Sujatha K. Arumugam, **Tanushree Bala,** and Murali Sastry, *Langmuir* 21 (2005) 822.

5. Cobalt and Magnesium Ferrite Nanoparticles: Preparation Using Liquid Foams as Templates and Their Magnetic Characteristics

Tanushree Bala, C. Raj Sankar, Marina Baidakova, Vladimir Osipov, Toshiaki Enoki, P. A. Joy, B. L. V. Prasad and Murali Sastry, *Langmuir* 21 (2005) 10638.

6. Assembly of Phase Transferred Nickel Nanoparticles At Air-Water Interface Using Langmuir-Blodgett Technique

Tanushree Bala, Bhagyashree Joshi, Neelima Iyer, Murali Sastry and B. L. V. Prasad *J. Nanosci. Nanotech.* 6 (2006) 3736.

7. $La_{0.7}Sr_{0.3}MnO_3$ nano-particles coated with fatty amine

Rajashree Rajagopal, M. Jani, S. N. Kale, **Tanushree Bala,** Renu Pasricha, Ponkaj Poddar, B. L. V. Prasad, Murali Sastry, Darshan C. Kundaliya and Satish B. Ogale, *J. Appl. Phys.* 89 (2006) 023107

8. Interaction of Different Metal Ions with Carboxylic Acid Group: A Quantitative Study

Tanushree Bala, B. L. V. Prasad, Murali Sastry, Mousumi Upadhyay Kahaly and Umesh V. Waghmare, *J. Phys.Chem. B* 2006 (communicated)

9. Ferromagnetic Resonance in Nanomagnetic Metal Core and Noble Metal Shell Systems

Tanushree Bala, T. Enoki and B. L. V. Prasad, *Chem. Phys. Lett*. 2006 (communicated)

10. An Organic Phase Transmetallation Approach For The Synthesis of $Co_{core}Au_{shell}$ Nanoparticles With A Tunable Shell Thickness

Tanushree Bala, Chika Katsuyama, Toshiaki Enoki, Murali Sastry and B. L. V. Prasad, 2006 (manuscript under preparation)

11. Highly monodisperse nickel and cobalt nanoparticles by a facile solution based methodology

Deepti S. Sidhaye, **Tanushree Bala,** S. Srinath, H. Srikanth, Pankaj Poddar, Murali Sastry and B. L. V. Prasad, *Langmuir* 2006 (communicated)

12. Synthesis of catalytically active porous platinum nanospheres by transmetallation reaction and proposition of the mechanism

2006 (manuscript under preparation)

13. Nano Structured Pt catalysts for preferential oxidation of CO at low temperatures in H_2 rich streams

Sachin Malwadkar, **Tanushree Bala,** B.L.V. Prasad and Satyanrayana Chilukuri, *Catalysis B* 2006 (communicated)